

**NOVEL SURFACE CHEMISTRY OF SINGLE MOLECULES AND SELF-ASSEMBLED  
STRUCTURES BY SCANNING TUNNELING MICROSCOPY**

by

**Petro Maksymovych**

B. Sc., Kiev Taras Shevchenko University, 2001

Submitted to the Graduate Faculty of  
Arts and Sciences in partial fulfillment  
of the requirements for the degree of  
Doctor of Philosophy

University of Pittsburgh

2007

UNIVERSITY OF PITTSBURGH  
FACULTY OF ARTS AND SCIENCES

This thesis was presented

by

Petro Maksymovych

It was defended on

April 25, 2007

and approved by

Prof. J. T. Yates, Jr., Department of Chemistry, University of Pittsburgh

Prof. D. H. Waldeck, Department of Chemistry, University of Pittsburgh

Prof. D. Pratt, Department of Chemistry, University of Pittsburgh

Prof. H. Petek, Department of Physics, University of Pittsburgh

Dissertation Advisor: Prof. J. T. Yates, Jr., Department of Chemistry, University of  
Pittsburgh

Copyright © by Petro Maksymovych  
2007

# **NOVEL SURFACE CHEMISTRY OF SINGLE MOLECULES AND SELF-ASSEMBLED STRUCTURES BY SCANNING TUNNELING MICROSCOPY**

Petro Maksymovych, Ph. D.

University of Pittsburgh, 2007

## **ABSTRACT**

This thesis demonstrates the richness of Scanning Tunneling Microscopy (STM) as a method to understand surface chemistry and physics and to explore the new frontiers in single-molecule surface reactions and molecular self-assembly. Organosulfur molecules on the Au(111) surface were studied to address unresolved and controversial issues about self-assembled monolayers of alkanethiol molecules on gold surfaces. The key new finding is that the thermal surface chemistry of alkanethiol molecules occurs in a dynamic chemical environment that involves reactive gold adatoms to which the alkanethiol molecules chemically bond. The problem of alkanethiol self-assembly is thus transformed from the realm of adsorption on a surface toward organometallic surface chemistry, which is anticipated to have broad implications for the field. Molecules containing a disulfide (S-S) bond were also found to be a spectacular model system for exploring electron-induced surface chemistry. In particular, the atomically-localized injection of electrons from the metal tip of the tunneling microscope is capable of producing highly delocalized chemical reactions by means of surface current of hot-electrons. Chemical reactions can therefore be a unique approach to the measurement of the local transport of hot-electrons on metal surfaces. Finally the concepts of self-assembly and electron-induced chemistry are combined through an observation of an unusual process that flips the chirality of molecules self-assembled on the surface by a radical-like chain reaction. This experiment demonstrates how self-assembly enables a new reaction coordinate by optimizing the steric factor of the chemical reaction.

## TABLE OF CONTENTS

### PREFACE

1.0	INTRODUCTION	1
1.1	Self-assembled monolayers of alkanethiols on gold surfaces.....	2
1.2	Electron-induced surface chemistry in scanning tunneling microscope.....	8
1.3	Surface structure and herringbone reconstruction of Au(111).....	15
1.3.1	Uniaxial compression of the hexagonal surface lattice.....	15
1.3.2	The herringbone reconstruction.....	18
1.4	Bulk and surface electronic states.....	20
1.4.1	STM studies of surface states.....	23
1.4.2	Where do electrons tunnel?.....	26
1.4.3	Lifetimes of excited states.....	27
2.0	EXPERIMENTAL.....	29
2.1	Scanning tunneling microscopy.....	29
2.2	Measurement modes in scanning tunneling microscopy.....	33
2.2.1	Topographic imaging.....	35
2.2.2	Electronic spectroscopy in STM.....	36
2.3	Auger electron spectroscopy.....	39
2.4	Ultra-high vacuum chamber.....	42
2.4.1	Preparation chamber.....	44
2.4.2	LT-STM chamber.....	45
2.5	Measurement of tunneling current.....	48
2.5.1	Electronic noise.....	49
2.5.2	Vibrational noise.....	49
2.5.3	Scanner calibration.....	50

2.6	STM-tip preparation.....	51
2.7	Preparation of Au(111) surface.....	54
<b>PART I. TIP-INDUCED DYNAMICS OF PHYSISORBED MOLECULES ON AU(111) SURFACE.....</b>		<b>56</b>
3.0	SURFACE BONDING AND DYNAMICAL BEHAVIOR OF THE CH <sub>3</sub> SH MOLECULE ON AU(111).....	57
3.1	Experimental methods and theoretical calculations.....	58
3.2	Hindered rotation of CH <sub>3</sub> SH on defect-free Au(111) surface.....	59
3.3	Adsorption site of CH <sub>3</sub> SH.....	62
3.4	DFT calculation of hindered rotation.....	64
3.5	Classical description of hindered rotation.....	66
3.6	Quantum-mechanical description of hindered rotation.....	67
3.7	Tip-effects in hindered rotation of CH <sub>3</sub> SH on Au(111) at 5K.....	72
3.8	Summary of results.....	75
4.0	ATTRACTIVE INTERACTION AND TIP-INDUCED DYNAMICS OF CO MOLECULES ON AU(111).....	77
4.1	Introduction.....	77
4.2	Experimental.....	79
4.3	Results and discussion.....	79
4.4	Conclusions.....	85
<b>PART II. STRESS EFFECTS IN ADSORPTION AND SELF-ASSEMBLY OF SMALL MOLECULES ON AU(111) SURFACE.....</b>		<b>86</b>
5.0	SELECTIVE ADSORPTION OF CO, CH <sub>3</sub> SH AND CH <sub>3</sub> SSCH <sub>3</sub> MOLECULES ON THE HERRINGBONE RECONSTRUCTION OF AU(111).....	87
5.1	Introduction.....	87
5.2	Experimental.....	90
5.3	Computational methods.....	91

5.4	Adsorption of single molecules on the herringbone reconstruction.....	91
5.5	Statistical analysis of CO adsorption on the fcc-region.....	95
5.6	Discussion.....	98
5.6.1	DFT calculations of CO adsorption on Au(111).....	99
5.6.2	Electronic effects in adsorption site selection on the herringbone reconstruction.....	100
5.7	Conclusion.....	103
6.0	MOLECULAR SELF-ASSEMBLY GUIDED BY SURFACE RECONSTRUCTION: CH <sub>3</sub> SH MONOLAYER ON THE AU(111) SURFACE.....	105
6.1	Introduction.....	105
6.2	Experimental.....	107
6.3	CH <sub>3</sub> SH monolayer modulated by the herringbone reconstruction.....	108
6.4	CH <sub>3</sub> SH monolayer formation imaged in real-time.....	111
6.5	Discussion.....	113
6.5.1	Structural differences between saturated molecular domains.....	113
6.5.2	CH <sub>3</sub> SH monolayer formation imaged in real-time.....	115
6.6	Conclusions.....	118

**PART III. ORIGIN OF ANCHOR-BOND IN SELF-ASSEMBLED ALKANETHIOLATE MONOLAYERS ON AU(111) SURFACE..... 120**

7.0	ADSORPTION SITE OF METHANETHIOLATE (CH <sub>3</sub> S) ON AU(111) SURFACE AT T = 5 K.....	122
7.1	Computational methods.....	122
7.2	Single CH <sub>3</sub> SH and CH <sub>3</sub> SSCH <sub>3</sub> molecules chemisorbed on the Au(111) surface.....	123
7.3	Electron-induced dissociation of CH <sub>3</sub> SSCH <sub>3</sub> and CH <sub>3</sub> SH.....	125
7.4	Adsorption energetics of the CH <sub>3</sub> S species by DFT calculations.....	128
7.5	Adsorption site of the CH <sub>3</sub> S species on the defect-free Au(111) surface.....	129
7.6	Lack of rotational motion of the bridge-bonded CH <sub>3</sub> S species.....	133
7.7	Summary.....	135

8.0	GOLD-ADATOM-MEDIATED BONDING IN SMALL ORGANOSULFUR MOLECULES SELF-ASSEMBLED ON AU(111) SURFACE.....	137
8.1	Adatom-bonded Stripe-phase of Methylthiolate on Au(111) surface.....	138
8.2	Herringbone reconstruction – source of reactive Au-adatoms.....	141
8.3	Conclusions.....	146
9.0	IMPLICATIONS OF AU-ADATOM BONDING IN ALKANETHIOLATE AND ARYLTHIOLATE SAMS ON AU(111).....	147
9.1	Au-adatoms in dissociation of S-S and S-H bonds on Au(111).....	147
9.2	Au-adatoms in self-assembly of benzenethiol on the Au(111) surface.....	149
9.3	Au-adatoms modify intermolecular interactions.....	155
9.4	Conclusions and outlook.....	156
<b>PART IV. ELECTRON-INDUCED SURFACE CHEMISTRY OF CH<sub>3</sub>SSCH<sub>3</sub> MOLECULE.....</b>		<b>159</b>
10.0	PROPAGATION OF CONFORMATION IN SURFACE-ALIGNED DISSOCIATION CH <sub>3</sub> SSCH <sub>3</sub> ON AU(111).....	160
10.1	Introduction.....	160
10.2	Results and discussion.....	161
11.0	CHAIN REACTION IN A MOLECULAR SELF-ASSEMBLY ON METAL SURFACE.....	165
11.1	Introduction.....	165
11.2	Results and discussion.....	166
12.0	NON-LOCAL HOT-ELECTRON SURFACE CHEMISTRY IN SCANNING TUNNELING MICROSCOPE.....	175
12.1	Introduction.....	175
12.2	Experimental.....	176
12.3	Non-local molecular excitation.....	178
12.4	Non-local reaction is driven by hot-electrons injected from the STM-tip....	180
12.5	Lateral attenuation of the non-local reaction.....	184
12.8	Eliminating tip-arifacts.....	186

12.8	Conclusions.....	186
APPENDIX A. STM STUDY OF WATER ADSORPTION ON $\text{TiO}_2(110)-(1 \times 2)$ SURFACE WITH UV-INDUCED DEFECTS.....		188
APPENDIX B. IMPROVED CRYSTAL GRINDING AND POLISHING HOLDER FOR METAL SINGLE CRYSTAL PREPARATION.....		205
BRIEF VITA.....		209
BIBLIOGRAPHY.....		212

## LIST OF TABLES

<b>Table 3.1.</b> Calculated equilibrium distances (Å) and adsorption energies for CH <sub>3</sub> SH adsorbed on Au(111) surface at different surface sites.....	63
<b>Table 7.1.</b> Structures and adsorption energies for CH <sub>3</sub> S adsorbed on the Au(111) surface at different coverages (Θ) determined from PAW-PW91 calculations (top-views of the structures are shown in Fig. 7.6).....	129

## LIST OF FIGURES

- Figure 1.1.** Mechanism of alkanethiolate self-assembly on Au(111) surface proposed by G. Poirier: (1)  $\alpha$  - disordered “lattice gas”; (2)  $\beta$  - 2D-stripe-phase; (3)  $\delta$  - 2D-3D stripe-phase; (4)  $\phi$  - 3D-saturated SAM.....5
- Figure 1.2.** Left: STM image of 2D self-assembled chains (stripe-phase) of n-propanethiolate ( $C_3H_7S$ ) on the Au(111) surface ( $7.6 \times 7.6 \text{ nm}^2$ ,  $U = 2 \text{ mV}$ ,  $I = 0.9 \text{ nA}$ ). Right: structural model of a single stripe-phase chain. In the model: Au-yellow, S-red, H-white, C-grey.....6
- Figure 1.3.** Structural model of the mixed ( $7.5/11.5 \times \sqrt{3}$ ) stripe-phase of dodecanethiolate on Au(111) surface where the transition from 2D to 3D-SAM begins.....7
- Figure 1.4.** Calculated adsorption geometries of  $CH_3S$  adsorbed on the Au(111) surface.....8
- Figure 1.5.** Two models of evolution of electronically excited states on surfaces: Menzel-Gomer-Redhead (MGR), bound-repulsive model and Antoniewicz bound-bound model. Bottom potential corresponds to the ground-state of a molecule in the vicinity of the surface, upper – to its electronically excited state. Arrows show the evolution of the nuclear wavepacket upon electronic excitation of the adsorbed molecule..... 10
- Figure 1.6.** Two mechanisms of electron-induced molecular excitation in STM.  $\pi$  is the HOMO and  $\pi^*$  is the LUMO of the adsorbed molecule;  $E_V$  – vacuum level,  $E_F$  – Fermi level..... 12
- Figure 1.7.** Four representative time-resolved traces of tunneling current during electron-induced dissociation of the  $CH_3SSCH_3$  molecule under the STM-tip on the Au(100) surface. The reaction event is seen as an abrupt drop due to dissociation of the S-S bond causing a corresponding change in the tunnel-barrier height. The current traces are offset along the y-axis for clarity. The dwell-time is different for each dissociation event. The reaction rate at a given tunneling current ( $1/\tau$ ) is obtained from an exponentially decaying probability distribution of

dwell-time ( $t$ ) obtained by averaging 100-200 current traces (right panel shows a representative distribution).....	13
<b>Figure 1.8.</b> $22\times\sqrt{3}$ reconstruction of the Au(111) surface. (a) atomically-resolved STM image, blue rectangle is the $22\times\sqrt{3}$ unit-cell; (b) structural model from Ref. [98]. (c) Variation of the lattice-constant in the unit-cell, which is anisotropically compressed along the $[\bar{1}10]$ direction. A1 and A2 are two close-packed rows in the unit-cell.....	16
<b>Figure 1.9.</b> Burgers vectors used to describe Shockley partial dislocations of the Au(111) surface lattice underlying the herringbone reconstruction. Yellow Shockley partial dislocations have matching Burgers vectors at the elbow site, while green and blue partial dislocations mismatch producing a perfect edge dislocation .....	17
<b>Figure 1.10.</b> Large-scale STM image of the Au(111) herringbone reconstruction showing elbow regions and defective/non-defective soliton lines.....	19
<b>Figure 1.11.</b> Atomically resolved pointed elbow site on the Au(111) surface. The blue circles mark lattice atoms in the vicinity of the perfect edge dislocation, where the number of gold atoms in the close-packed row (shown in the image) increases by one.....	20
<b>Figure 1.12.</b> Wavefunction of a surface state in the 1D-crystal potential (dashed line). $V_0$ is the work function, $a$ – crystal lattice constant.....	21
<b>Figure 1.13.</b> Bulk band structure projected onto 2D surface Brillouin zone of Au(111) surface along high-symmetry directions (schematic). Shaded areas are regions of $k$ -space where bulk states exist, white areas are projected band-gaps. Red curve is a surface state in the band-gap centered on the $\bar{\Gamma}$ -point. $E_F$ is the Fermi-level.....	22
<b>Figure 1.14.</b> STS recorded in the hcp-region of the Au(111) surface and on top of the adsorbate (Au-adatom bonded $\text{CH}_3\text{S}$ , Chapter 5). An abrupt onset of the surface state at -500 mV below Fermi level is clearly visible in the spectrum of the surface. The adsorbate quenches the surface state.....	23
<b>Figure 1.15.</b> Constant current STM image of sulfur islands on the Cu(111) surface. $280 \text{ \AA} \times 138 \text{ \AA}$ , $V = 0.24 \text{ V}$ , $I = 0.23 \text{ nA}$ . Sulfur islands act as static scatterers of surface state electrons producing wave-like fringes in the vicinity of the islands.....	24
<b>Figure 1.16.</b> Electron-electron (red line) and electron-phonon (blue line) lifetimes on Cu(111) at $T = 5\text{K}$ as function of energy within the Fermi-liquid theory and the Debye-model respectively ( $t_0=0.46 \text{ fs}$ , $E_0 = 7 \text{ eV}$ , $w_D = 27 \text{ meV}$ , $\lambda=0.15$ ) .....	27

**Figure 2.1.** Principal components of the scanning tunneling microscope. Voltage applied between a sharp-metal tip and a conducting sample will drive tunneling current across the 5-8 Å wide vacuum gap. The tip is positioned with sub-angstrom accuracy using piezo-electric scanners.....30

**Figure 2.2.** Formation of a rectangular tunnel-barrier in STM upon tip-approach: (a) tip and sample are infinitely far away; (b) tip-sample distance is 5-8 Å allowing electron tunneling; (c) tunneling junction under positive applied sample bias (U).....31

**Figure 2.3.** Two modes topographic imaging by STM. a) Constant current mode: while scanning the tip over the surface in the x- and y-direction, the height z of the tip is adjusted by the feedback loop to keep the current constant. b) Constant height mode: the height of the tip is kept constant while scanning the tip.....36

**Figure 2.4.** Scanning tunneling (left) and distance-voltage (right) spectroscopy. The spectroscopic measurement in both cases is accomplished by recording the first harmonic of the lock-in amplifier (dI/dV) during a ramp of tunneling voltage. The feedback loop is off in STS and on in z(V)-spectroscopy.....39

**Figure 2.5.** Schematic energy diagram of the final state of the  $KL_{II}L_{III}$  Auger transition..... 40

**Figure 2.6.** AES spectrum of Cu(110) surface obtained after 1 hr of Ar sputtering and 20 min annealing at 800 K..... 41

**Figure 2.7.** Overview of the Omicron LT-STM apparatus..... 43

**Figure 2.8.** Bare STM stage of the Omicron LT-STM (without cryoshields) in the suspended position ready for scanning..... 46

**Figure 2.9.** Temperature calibration for heating a Cu crystal in a wobble-stick after the crystal is extracted from the 5K-STM stage. The K-type thermocouple is attached to the surface of the crystal, which itself is mounted on a standard tantalum sample holder.....47

**Figure 2.10.** Lateral drift of the LT-STM at 5K. The drift causes a slow displacement of a single CO molecule in the STM image. Images on top were taken at the start and the finish of the drift measurement ( $3.4 \times 3.4 \text{ nm}^2$ ,  $U = -0.030 \text{ V}$ ,  $I = 30 \text{ pA}$ ).....50

**Figure 2.11.** Single CO molecule adsorbed on the Au(111) surface imaged by a metal- and a CO-functionalized STM-tip.....53

**Figure 2.12.** Atomically resolved STM images of the largest facet on the melted bead, which is the  $22 \times \sqrt{3}$ -reconstructed Au(111) surface ( $U = -0.12 \text{ V}$ ,  $I = 31 \text{ pA}$ ). Left: hexagonally close-

packed surface lattice of gold atoms.  $U = -0.12$  V,  $I = 31$  pA. Size:  $5 \times 5$  nm<sup>2</sup>. Right: common defects on the clean Au(111) surface - intrinsic edge-dislocation due to the herringbone reconstruction and a sub-surface defect, most likely an implanted Ar atom or a carbon atom. Size:  $10 \times 10$  nm<sup>2</sup>.....54

**Figure 3.1.** Low-resolution STM image of CH<sub>3</sub>SH molecules at 5K on the defect-free regions of the surface. ( $U = -0.16$ V,  $I = 0.2$  nA)..... 59

**Figure 3.2.** a) High-resolution STM image at 5K of a single rotating CH<sub>3</sub>SH molecule on the non-defective surface in a shape of a flower with six petals. ( $U = -0.01$ V,  $I = 0.04$  nA) The dashed lines correspond to the close-packed crystallographic directions determined from atomically-resolved STM images of the Au lattice in the vicinity of the molecule. b). A schematic model of the adsorption geometry inferred from the STM image..... 60

**Figure 3.3.** Direct evidence for the rotation of CH<sub>3</sub>SH molecules on Au(111) at 5K. ( $U = -1$  mV,  $I = 0.05$  nA). a). STM image of rotating molecules before the manipulation. The arrow shows the position where a pulse of +0.6V was applied in order to move molecule A toward molecule B. b). Molecular rotation stops as a result of proximity of two molecules. Molecules A and B form a zig-zag shaped dimer. The inset to Fig. 6b shows a possible (CH<sub>3</sub>SH)<sub>2</sub> head-to-tail dimer model..... 61

**Figure 3.4.** DFT optimized adsorption geometry of CH<sub>3</sub>SH on an unreconstructed Au(111) surface. The molecule adsorbs with the SH group on top of the Au atom, and the CH<sub>3</sub> group above the hollow site..... 63

**Figure 3.5.** Minimum energy path for rotation of CH<sub>3</sub>SH molecule around the S-Au bond as a function of the azimuthal angle  $f$  (Au1-Au2-S-C). The zero point corresponds to the geometry in Fig. 3.4..... 65

**Figure 3.6.** Rotational energy levels of a free and three hindered rotors. Lower panels show representative wavefunctions for the ground (left) and an excited (right) rotational state of CH<sub>3</sub>SH on Au(111)..... 68

**Figure 3.7.** Division of the arbitrary potential into small sections of constant potential for calculations using transfer-matrix method..... 70

**Figure 3.8.** Tunneling probability for the rotational motion of CH<sub>3</sub>SH across a barrier of 5.2 meV. Tunneling occurs between two neighbor minima of the six-fold sinusoidal potential barrier. Blue values are Boltzman factors for the energy levels at 5K..... 72

<b>Figure 3.9.</b> Tunneling probability for a rotating CH <sub>3</sub> SH molecule hindered by a potential barrier of 0.12 kcal/mol and 0.5 kcal/mol.....	73
<b>Figure 3.10.</b> Bias dependent imaging of rotating CH <sub>3</sub> SH molecules on Au(111) with a sharp metal tip. Four CH <sub>3</sub> SH molecules are imaged consecutively at -1 mV (a), -10 mV (b), -100 mV (c), -250 mV (d) and a constant tunneling current of 100 pA. Noticeable changes in the apparent shape of the molecule indicate tip-involvement in the dynamics of the molecule.....	74
<b>Figure 3.11.</b> Comparison of C <sub>3</sub> H <sub>7</sub> SH and C <sub>6</sub> H <sub>5</sub> SH adsorbed on Au(111) at T < 70K. Hindered rotation of propanethiol is clearly observed. The streakiness of the image indicates substantial tip-molecule interactions, and thus the likelihood of the rotation being tip-induced.....	75
<b>Figure 4.1.</b> Numeric nomenclature for neighbor surface sites on the close-packed (111) surface.....	78
<b>Figure 4.2.</b> Spontaneous CO clustering on Au(111) at T<20K (20x20 nm <sup>2</sup> , U= -30 mV, I = 30 pA).....	80
<b>Figure 4.3.</b> CO clusters on Au(111) surface that form spontaneously at T < 20 K.....	81
<b>Figure 4.4.</b> STM images of the tip-induced isomerization and decomposition of the CO dimers. a-d: U = -30 mV; scale = 4.1 x 2.7 nm <sup>2</sup> .....	82
<b>Figure 4.5.</b> Tip-induced motion of the CO clusters.....	83
<b>Figure 5.1.</b> (a) Side and (b) top views of the 22x√3 unit-cell of the reconstructed Au(111) surface obtained from first-principles. For visualization purposes the slab has been repeated by three units along the [11̄2] direction and the atoms in deeper layers have been represented by increasingly darker colors.....	89
<b>Figure 5.2.</b> Site-selective adsorption of CO on the Au(111) herringbone reconstruction at different adsorbate coverages. The STM images were acquired with a metal-tip (a) and a CO-functionalized tip (b,c).....	92
<b>Figure 5.3.</b> Site-selective adsorption of CH <sub>3</sub> SH and CH <sub>3</sub> SSCH <sub>3</sub> on the reconstructed Au(111) surface. The distribution of molecules dosed on the surface at 10K is nearly random (a) and becomes ordered after heating the surface to 90K (b,c).....	93
<b>Figure 5.4.</b> Distribution of 575 CO molecules within the fcc-region. The energy values correspond to decrease in the binding energy relative to its center calculated from the Boltzman distribution at T=20 K.....	94

**Figure 5.5.** CO binding energy as a function of the anisotropic lattice compression of the Au(111) surface along  $[\bar{1}\bar{1}0]$  direction calculated in the  $(3 \times 1)$  unit-cell with shown in the figure (the lattice vectors of the unit-cell run along  $[\bar{1}\bar{1}0]$  and  $[\bar{1}\bar{1}\bar{2}]$  directions).....96

**Figure 5.6.** Variation of the atomic coordinates in horizontal (a) and vertical (b) planes for the Au atoms in the top layer of the slab. Here x, y and z coordinates are taken along  $[1\bar{1}0]$ ,  $[\bar{1}\bar{1}\bar{2}]$  and  $[111]$  directions, respectively and  $Z_0$  denote the vertical coordinates of the atoms at the bottom of the slab. (c) The variation of the Au-Au distance along the chain in the top layer (along  $[\bar{1}\bar{1}0]$  direction).....97

**Figure 5.7.** Adsorption configuration of CO in the  $22 \times \sqrt{3}$  unit-cell of the reconstructed Au(111) surface. The surface Au atoms at increasingly deeper layers are depicted in darker colors. Configurations (a) is the CO molecule on the fcc-site, (b) on the soliton and (c) on the hcp site.....99

**Figure 5.8.** CO adsorption on Au(111) in the vicinity of the single-atom step. The oscillatory pattern of the Shockley surface state due to scattering at the step is clearly visible. The depletion region where no CO molecules are observed in the fcc-regions near the step is 1.7 nm wide, which is roughly one half of the Fermi wavelength of the Shockley surface state..... 101

**Figure 5.9.** Local density of states in arbitrary units of the surface Au atoms at the fcc, soliton and hcp sites.....102

**Figure 6.1.** STM images of clean Au(111) surface with  $22 \times \sqrt{3}$  herringbone reconstruction. ( $V = -0.143$  V,  $I = 43$  pA ). a) Atomically-resolved close-up image showing the regions of fcc- and hcp-stacking as well as the in-plane distortion of the surface lattice along the  $[\bar{1}\bar{1}\bar{2}]$  direction due to the uniaxial compression along the  $[\bar{1}\bar{1}0]$  direction. b) a large-scale image of rotational domains of the herringbone reconstruction. Yellow dashed lines mark the position of the rotational domain boundary where crystallographic direction of the anisotropic lattice compression is rotated by  $60^\circ$ ..... 107

**Figure 6.2.** A large scale STM image of  $\text{CH}_3\text{SH}$  monolayer on the Au(111) surface showing the modulation effect due to the herringbone reconstruction. ( $V = -0.013$  V,  $I = 30$  pA.). The yellow line marks the domain boundary of the  $\text{CH}_3\text{SH}$  monolayer. The blue lines is the rotational boundary of the herringbone reconstruction, where the C-direction of the anisotropic lattice compression turns by  $60^\circ$  to  $C'$ ..... 108

<b>Figure 6.3.</b> Molecular structure of the CH <sub>3</sub> SH monolayer on Au(111).....	109
<b>Figure 6.4.</b> Structural models of the A-, B- and C-oriented CH <sub>3</sub> SH monolayer domains. The domains are transformed into each other by 60° rotation in plane of the surface. C-orientation is the only one observed in the completed self-assembled monolayer. The white arrows show the unit-cell vectors of the monolayer domains. The matrix notation is based on the A- and C-substrate vectors following the standard convention.....	110
<b>Figure 6.5.</b> Real-time imaging of CH <sub>3</sub> SH monolayer ordering. Time interval between STM images is ~45 minutes. The right-hand side shows the Fourier-transforms of the STM images. The arrows mark the reflexes corresponding to a domain with C-orientation. U=-0.013 V, I=17 pA.....	112
<b>Figure 6.6.</b> Three consecutive STM images of a nearly-completed CH <sub>3</sub> SH monolayer showing the disappearance of A(B)-oriented domains with time (U = -0.013 V, I = 17 pA). Bottom graph shows the decay of the A-oriented island marked by white arrows.....	114
<b>Figure 6.7.</b> A model of a single CH <sub>3</sub> SH self-assembled domain demonstrating the different detachment trajectories available to molecules on different domain walls. The notation follows the text. The dots mark the available adsorption sites for a single molecule escaping the domain. Red (green) dots mark the sites where repulsive (small) interactions with the neighbors will exist.....	116
<b>Figure 6.8.</b> Sub-monolayer coverage of CH <sub>3</sub> SH on the Au(111) surface, where the preference of the C-orientation is observed on the length-scale of locally-saturated fcc-regions (U= -0.022V, I = 16 pA).....	117
<b>Figure 7.1.</b> CH <sub>3</sub> SSCH <sub>3</sub> molecule on Au(111) surface at T = 5 K.....	123
<b>Figure 7.2.</b> Topographic comparison of the products of tip-induced dissociation of CH <sub>3</sub> SH and CH <sub>3</sub> SSCH <sub>3</sub> .....	124
<b>Figure 7.3.</b> STM images of several single CH <sub>3</sub> SH molecules before and after tip-induced deprotonation, showing that the tip-induced rotation of CH <sub>3</sub> SH stops after reaction. Scale: 6.14 x 3.9 nm <sup>2</sup> , U = -0.010 V, I = 40 pA. The blue dashed line marks the rotating CH <sub>3</sub> SH molecule that was not pulsed.....	126
<b>Figure 7.4.</b> Triangulation of CH <sub>3</sub> S produced from CH <sub>3</sub> SSCH <sub>3</sub> by tip-induced dissociation at 5K. Scale: 4.8 x 5.2 nm <sup>2</sup> ; U = -0.04 V; I = 20 pA.....	127

**Figure 7.5.** Top-view ball models of the calculated adsorption configurations of CH<sub>3</sub>S described in Table 1. The CH<sub>3</sub>S coverage is 1/5 ML for each model..... 130

**Figure 7.6.** Structural models of representative adsorption configurations of CH<sub>3</sub>S species on the Au(111) surface for which the STM images were calculated. Side and top views are shown for each configuration..... 131

**Figure 7.7.** Experimental and calculated STM images of CH<sub>3</sub>S species. Experimental: a) CH<sub>3</sub>S species derived from CH<sub>3</sub>SSCH<sub>3</sub> (U = -0.010 V, I = 40 pA). Calculated: b) *br-fcc*; c) *fcc-t*; d) *fcc-v*; e) *top(1)*. Blue (experimental) and red dots (calculated) mark the position of Au atoms in the lattice.....132

**Figure 7.8.** Barrier to rotation of the *br-fcc* CH<sub>3</sub>S species calculated using DFT/NEB method. The Au atoms are colored according to their vertical position in the slab (Fig. 7.5)..... 134

**Figure 8.1.** CH<sub>3</sub>SSCH<sub>3</sub> chemistry on Au(111) surface. a) Single CH<sub>3</sub>S-SCH<sub>3</sub> molecule. b) Two CH<sub>3</sub>S fragments formed by dissociating CH<sub>3</sub>S-SCH<sub>3</sub> with a 1.0V pulse at 5K. c) Close-up of a single stripe-phase unit. The asymmetrical boundaries of the CH<sub>3</sub>S species are marked by dashed white lines. d) Chains of CH<sub>3</sub>S stripe-phase after heating CH<sub>3</sub>S-SCH<sub>3</sub> on Au(111) to 300K...138

**Figure 8.2.** Alkanethiolate stripe-phase SAM. Top-view models of the CH<sub>3</sub>S stripe-phase according to (a) Ref. [68], (b) Ref. [59] and (c) proposed here. Au<sub>a</sub> is the Au-adatom..... 139

**Figure 8.3.** Structure of CH<sub>3</sub>S-Au-SCH<sub>3</sub> on Au(111). (a), (b) Calculated structure of adatom-bonded pair-unit which forms the CH<sub>3</sub>S stripe-phase. (c) Triangulation of the CH<sub>3</sub>S stripe-phase relative to the underlying lattice using CO molecules as markers of the Au lattice atoms. The off-hollow position of the Au-adatom (blue circle) agrees well with the theoretical predictions presented in this work. (d) Perspective view of the S-atom showing its position above the lattice Au-atom..... 140

**Figure 8.4.** Correlation between self-assembly of the stripe-phase and lifting of the Au(111) herringbone reconstruction. (a) Typical large-scale sampling area of the Au(111) surface used for counting. Dashed line is the unfaulted soliton line. (b) Distribution of Au atoms (embedded herringbone atoms plus adatoms in the stripe-phase) as a function of stripe-phase coverage for stripe-phases produced from CH<sub>3</sub>SSCH<sub>3</sub>, CH<sub>3</sub>SH (marked) and C<sub>3</sub>H<sub>7</sub>SH (marked)..... 142

**Figure 8.5.** Step-etching by alkanethiolate self-assembly. (a) Au(111) surface with hexagonal etch-pits decorated by single-atom steps running along [1 $\bar{1}$ 0] directions. (b) After dosing a small amount of CH<sub>3</sub>SSCH<sub>3</sub> at room temperature. (c) Further dosing produces low-coverage of CH<sub>3</sub>S-

Au-SCH<sub>3</sub> stripe-phase on the terraces. Step-morphology is hardly changed in (b) and (c). (d) STM images of high CH<sub>3</sub>S-Au-SCH<sub>3</sub> stripe-phase coverage on the terraces: substantial erosion of previously hexagonal pits is observed. (e) Enlarged area inside the dashed square in (d)..... 144

**Figure 9.1.** Slow conversion of CH<sub>3</sub>SSCH<sub>3</sub> to CH<sub>3</sub>S-Au-SCH<sub>3</sub> on Au(111) at ~180K..... 148

**Figure 9.2.** Phenylthiol (PhSH) and phenylthiolate (PhS) adsorbed on Au(111) at 5K. PhS species in (b) was produced at 5K by applying a 2.7V pulse on top of PhSH molecules in (a). Au adatoms are not involved in these species because of the low temperature..... 150

**Figure 9.3.** Dimers of phenylthiolate (PhS-Au-PhS) observed after heating Au(111) with PhSH to 300K. (a) Large scale image showing dimers and the dominance of the dimer in the trans-configuration. (b) Close-up STM image showing trans- and cis-PhS-Au-SPh units. Schematic ball-models are shown on the left (the Au-adatom is blue).....151

**Figure 9.4.** Formation of PhS-dimers at room temperature causes partial lifting of the herringbone reconstruction: the periodicity of the reconstruction is 7.5 nm along  $\langle 1\bar{1}0 \rangle$  direction which is larger than 6.3 nm for the clean Au(111)..... 152

**Figure 9.5.** Pairing of PhSH molecules on the elbow-site at T~70K. The S-H groups are facing each-other. The overall geometry of the pair is closely-reminiscent of the PhS-Au-SPh unit formed at higher temperature (Fig. 9.3). Each pair in left panel was pulsed with a 2.7-3.0 V pulse. Pulsing converts PhSH to PhS (right panel) via S-H bond-scission..... 153

**Figure 9.6.** Intermolecular interactions modified by Au-adatoms. (a) A small coverage of CH<sub>3</sub>SSCH<sub>3</sub> molecules on Au(111) at T<170 K. The molecules are isolated indicating repulsive intermolecular interactions. (b) STM image obtained after heating the surface in (a) to 300K. The initial coverage of CH<sub>3</sub>SSCH<sub>3</sub> molecules is the same for (a) and (b). Most CH<sub>3</sub>S-Au-SCH<sub>3</sub> units aggregate into chains indicating attractive intermolecular interactions..... 155

**Figure 10.1.** Conformation of CH<sub>3</sub>SSCH<sub>3</sub> adsorbed on Au(111) surface. a) STM image of two CH<sub>3</sub>SSCH<sub>3</sub> molecules on Au(111). Both molecules are trans-conformers (see text); b) Line-profiles of several CH<sub>3</sub>SSCH<sub>3</sub> molecules taken along the white dashed line in (a); c) Triangulation of CH<sub>3</sub>SSCH<sub>3</sub> molecules using CO molecules on atop Au sites. The black dot in the upper molecule marks the position of the inversion center; d) Comparison of cis- and trans-symmetry for CH<sub>3</sub>SSCH<sub>3</sub>. In c) and e) the red line marks the direction of the S-S bond..... 161

**Figure 10.2.** Electron-induced dissociation of CH<sub>3</sub>SSCH<sub>3</sub> molecules on the Au(111) surface as seen by STM. The products retain the conformation and orientation of the parent molecules:

CH<sub>3</sub>SSCH<sub>3</sub> molecules 1 and 3 are identical producing identical CH<sub>3</sub>S *trans*-pairs. Molecules 1 and 2 are offset mirror images of each other, and so are the product *trans*-pairs of CH<sub>3</sub>S-species (dashed blue line is the mirror plane)..... 162

**Figure 10.3.** Propagation of conformation in CH<sub>3</sub>SSCH<sub>3</sub> dissociation. a) STM image and structural model of isolated CH<sub>3</sub>S-species adsorbed on the Au-Au bridge site. Blue dots mark Au atoms in the lattice; b) Undissociated CH<sub>3</sub>SSCH<sub>3</sub> molecule (red line is the direction of the S-S bond); c) The *trans*-pair of CH<sub>3</sub>S-species produced by electron-induced dissociation of (b). The models show the schematic of the surface-aligned dissociation of CH<sub>3</sub>SSCH<sub>3</sub>..... 163

**Figure 11.1.** STM images before and after electron-induced dissociation of a single CH<sub>3</sub>SSCH<sub>3</sub> molecule and its self-assembled chains on the Au(111) surface. Select structures are shown schematically in ball models (position of CH<sub>3</sub>S-fragments in models of chain reactions is one of two equivalent positions). (a) Conformation-retaining dissociation of CH<sub>3</sub>SSCH<sub>3</sub> producing two CH<sub>3</sub>S-fragments by a pulse of tunneling current at 1.4V. (b)-(d) Chain reactions of self-assembled chains of CH<sub>3</sub>SSCH<sub>3</sub> molecules induced by electron-induced dissociation of the terminal molecule (pulse voltage 0.9V). Voltage pulses were applied at a position marked by yellow circle. (e) Chain reaction of 15 CH<sub>3</sub>SSCH<sub>3</sub> molecules self-assembled on Au(100) surface: the reaction produces 9 flipped molecules.....167

**Figure 11.2.** Chain reaction scenario..... 169

**Figure 11.3.** Potential energy profile for dissociation of the CH<sub>3</sub>SSCH<sub>3</sub> dimer calculated using DFT CI-NEB method. The insert figure represents the variation of the S-S bond-lengths corresponding to the dissociating molecules (S1-S2, S3-S4) and the newly forming CH<sub>3</sub>SSCH<sub>3</sub> molecule (S2-S3). The ball models are initial, final and select intermediate optimized configurations along the reaction coordinate. The size of the surface Au atoms (shown in gray) corresponds to their vertical position in the slab, larger atoms being closer to the surface.....171

**Figure 11.4.** Potential energy profile for dissociation of the CH<sub>3</sub>SSCH<sub>3</sub> monomer calculated using DFT CI-NEB method. The insert figure represents the variation of the S-S bond-length. Coloring scheme is the same as in Fig. 11.3..... 172

**Figure 11.5.** Potential energy profile for the interaction of the CH<sub>3</sub>S-fragment with the CH<sub>3</sub>SSCH<sub>3</sub> molecule..... 173

**Figure 12.1.** Non-local electron-induced dissociation of CH<sub>3</sub>SSCH<sub>3</sub> molecules. Top: structural models of undissociated CH<sub>3</sub>SSCH<sub>3</sub> molecule on Au(111) and its dissociation products (CH<sub>3</sub>S).

Middle: STM images of the same surface area before (a) and after (b) a single pulse of tunneling current (2.0 V/1 nA/100 msec) applied at the marked position (blue circle) on the clean surface. Nearly all the molecules dissociated in the field of view (the undissociated molecules are highlighted). (c) STM image of non-local CH<sub>3</sub>SSCH<sub>3</sub> dissociation induced by a single 2.5 V/1.0 nA/200 ms pulse at the blue point. The inset shows a surface area (inside yellow square) located ~46 nm away from the pulse position. *u* marks unreacted and *r* - reacted CH<sub>3</sub>SSCH<sub>3</sub> molecules.

.....177

**Figure 12.2.** Reproducibility and energy threshold of non-local CH<sub>3</sub>SSCH<sub>3</sub> dissociation. (a) Total number of dissociation events per pulse plotted as a function of pulse number. The same current pulse (1.8 V/0.350 nA/150 ms) was repeated in 18 different areas on the surface. The red dashed line is the average number of events. (b) Total number of dissociation events per pulse as a function of pulse voltage. Each pulse is performed at 1.0 nA for 200 ms. The points are connected to guide the eye..... 179

**Figure 12.3.** Dependence of non-local CH<sub>3</sub>SSCH<sub>3</sub> dissociation on the bias-polarity of the tunneling junction during excitation. Hot-hole injection (left panel) is much less effective than hot-electron injection (right panel) in the non-local reaction..... 180

**Figure 12.4.** Non-local reaction from a current pulse applied to a nanocluster. (a) STM image of an artificially created metal cluster. The line-scan below the image was taken along the yellow dashed line. (b) Non-local dissociation of CH<sub>3</sub>SSCH<sub>3</sub> molecules induced by a current pulse (1.8V/0.5 nA/200 msec) applied to the metal cluster in the center. (c) Histograms of the CH<sub>3</sub>SSCH<sub>3</sub> dissociation events induced by the same current pulse (1.8V/0.5 nA/200 msec) applied to the cluster and to the Au(111) surface. (d) The effect of the pulse on the cluster and on the surface compared for three different clusters. Pulse conditions are 1.8V/0.5 nA/200 ms for experiment 1 and 2, and 1.8V/0.25 nA/250 ms for experiment 3.....181

**Figure 12.5.** Statistical analysis of non-local CH<sub>3</sub>SSCH<sub>3</sub> dissociation. (a) Linear scaling of non-local reaction rate with excitation current (Eq. 12.2) from two experiments using pulses at 1.8 V and 2.0 V. Each point is an average of two measurements. Red lines are linear fits to the data. (b) Attenuation function of the non-local chemistry from two experiments using pulses at 1.8 V (average of 15 measurements) and 2.2 V (average of 5 measurements). Red lines are exponential decay fits to the data. .... 182

**Figure A.1.** Three crystal structures of TiO<sub>2</sub>. Ti is grey, O – red..... 189

<b>Figure A.2.</b> TiO <sub>2</sub> (110)-(1x1) surface: n-Ti corresponds to the n-fold coordinated Ti atom; br-O is the bridging O-atom.....	190
<b>Figure A.3.</b> STM image of a clean TiO <sub>2</sub> (110)-(1x1) surface showing the two types of line defects. U=+1.9V, I=0.035 nA.....	191
<b>Figure A.4.</b> Close-up STM image of clean TiO <sub>2</sub> (110)-(1x1) surface displaying oxygen vacancies (10x10 nm <sup>2</sup> , U=2.5 V, I= 0.035 nA).....	193
<b>Figure A.5.</b> STM images of the TiO <sub>2</sub> (110)-(1x2) surface with links, obtained under the <i>reducing</i> conditions (UHV, annealing at 1200K). U=+3.05V, I=0.040nA.....	194
<b>Figure A.6.</b> DFT relaxed geometry of the added-row model for the TiO <sub>2</sub> (110)-(12x2) reconstructed surface. The stoichiometry of the added row is Ti <sub>3</sub> O <sub>5</sub> (according to Pang et.al.) Ti atoms are grey, O-atoms – red.....	195
<b>Figure A.7.</b> The structure of the crosslinks on the TiO <sub>2</sub> (110)-(1x2) surface. The STM image on the left was acquired at U=+3.2V, I=0.040 nA. The model on the left is adopted from Ref. [352]. Small black circles correspond to Ti atoms, large grey circles correspond to O atoms. The correspondence between the grey shading and the type of O atom is shown in the cross section of the model.....	198
<b>Figure A.8.</b> STM images of the same 100x100 nm <sup>2</sup> area of the TiO <sub>2</sub> (110)-(1x2) surface after consecutive H <sub>2</sub> O exposures at room temperature (scanning conditions for all images are U = 3.15 V, I = 0.035 nA): (a) clean surface after UV-irradiation before H <sub>2</sub> O exposure (arrow points to a UV-induced line defect); (b), (c) and (d), surface after H <sub>2</sub> O exposures of 0.3, 3 and 180 L correspondingly. The insets show the area within the dashed square. The black arrow in the insets (b) and (c) points to the same crosslink.....	200
<b>Figure A.9.</b> A room temperature STM image taken after exposing a clean UV-irradiated surface to 0.04L of H <sub>2</sub> O at 110K. (size 100×100 nm <sup>2</sup> , U=+3.5 V, I=0.035 nA.....	202
<b>Figure A.10.</b> A higher magnification STM image of the surface in Fig. A.9 (size 30×30 nm <sup>2</sup> , U=+3.5 V, I=0.035 nA). Shown in the insets are protrusions of group I (inset a), group II (inset b) and group III (inset c). Arrow points to the UV-induced line defect.....	203
<b>Figure B.1.</b> Schematic of crystal polishing equipment on a rotary polishing wheel. The crystal is glued to the adjustable plate of the Bond Barrel holder and oriented to the desired crystallographic direction using x-ray back reflection. The abrasive is supported on a cloth, which is attached to the polishing wheel.....	206

**Figure B.2.** Schematic drawing of the fixture for automatic crystal polishing with the Bond Barrel holder used to orient and hold the crystal.....207

**Figure B.3.** Interference pattern for an Al crystal polished using the designed fixture,  $\lambda=546$  nm..... 207

**Figure B.4.** Plot of air film thickness vs interference minima positions as determined from Fig. B-3. The error bars represent the standard deviation of the interference minima measurements along three different trajectories in Fig. B-3. The fitted curve around the 2 mm position corresponds to a 3.4 m radius, which increases to larger values as one moves toward the crystal edge.....208

## PREFACE

The course toward a degree in science is full of puzzle, surprise, difficulty and frustration. It is by no means a straight road without traffic. At first, there seem to be no directions either. Although gradually one realizes that a flag sprouts up here and there. Sometimes the flag shows the way, sometimes it points to a shortcut. The person waving the flag is one's scientific advisor. It is up to him to turn a Ph. D. into an average experience or make it a fascinating journey into the world of science. Without a shade of doubt, my graduate school was the wildest journey to remember and I would like to express my sincere and utmost gratitude to the person who made it all happen, my advisor Prof. John T. Yates, Jr.

John is a world famous scientist and a pioneer in the field of surface science. He has the deepest insight into the many questions of science and beyond. His intuition was at times not immediately obvious, and it was only weeks later that I would realize the greatness and value of his advice. One of John's qualities that I deeply appreciate is allowing me to explore some things on my own, which was at times costly and even useless, and yet a most pleasurable and educational experience.

Inspiration is the key to any scientific experiment, which is why I would like to thank the many wonderful people who helped and inspired me along the way: Dr. Dan Sorescu, whose theoretical work, humor and constructive criticism have built a profound part of my thesis, Prof. Jeremy Levy and Prof. Hrvoje Petek for their support and for not giving up on my endless inquiries into the more physical aspects of experiments, Prof. Jorge Cerda for mentoring me on the theoretical aspects of the tunneling microscopy. My sincere gratitude goes to all the members of the Surface Science Center, some of whom have become my dear friends. I would like to thank Dr. Sergey Mezheny, for teaching me a great deal about the instruments and the way of

the experimentalist, Dr. Daniel Dougherty, for being my partner the last two years and for his patient listening to my endless speeches on the philosophy of our work, Dr. Tykhon Zubkov, Dr. Izabela Rzezinicka, Dr. Junseook Lee and my fellow students Peter Kondratyuk, Gregg Morgan, Tracy Thompson, Olivier Guise and Oleg Byl for keeping me company when the going would get tough.

Little accomplishment would happen without the help of our dear granny, Margie Augenstein, who would also assist us on the administrative front. A huge word of thanks goes to the staff of the Department of Chemistry at the University of Pittsburgh, Thomas Gasmire, Dennis Sicher, Jeffrey Sicher, Roy Watters from the machine shop, Bob Muha, Chuck Fleishaker, David Emala, James McNerney from the electronics shop and Robert Greer from the glassblowing shop. Thanks guys for your expert skills, technical brilliance and the helping hand!

Finally, there are no words that would allow me to express deeply my gratitude and love to my parents Olexander and Nelli Maksymovych for raising me into a world of adventure and for being my firm and everlasting support in life.

I dedicate this thesis to my beloved fiancée Liliya Bykova, who is my very best friend, my most patient listener and most reliable partner and who has made a great many sacrifices to break away from home and join me on my American journey.

## 1.0 INTRODUCTION

Scanning Tunneling Microscopy (STM) is truly a pinnacle of our effort to understand nature by looking at objects with a magnification far exceeding our natural ability. The tunneling microscope operates on the principle of quantum-mechanical electron tunneling between a sharp-tip and a flat surface separated by several angstroms. This simple geometry produces astonishing atomic spatial resolution, which has made STM a technique of choice for the greatest variety of experiments in surface and materials science where direct microscopic information enlightens the physical and chemical processes at the atomic scale.

Scanning tunneling microscopy was born in 1983 in the hands of two researchers, Gerd Binnig and Heinrich Rohrer [1], at IBM in Zurich, Switzerland. The very first STM result widely accepted by the scientific community was the real-space image of the Si(111)-(7X7) surface with atomic resolution [2]. Most seminal applications of STM were focused on topographic imaging of clean metallic and semiconductor surfaces in order to understand their atomic structure, study various kinds of natural defects and analyze surface dynamics in real-space [3, 4]. Later, the development of Scanning Tunneling Spectroscopy (STS) introduced energy-resolved STM measurements [5]. STS has become a powerful technique for the local measurements of the electronic states of the surface, providing direct access to electron work function [6], surface band-structure [7], lifetime of charge carriers [8] and even magnetism of single atoms [9].

In late 1980's Wolkow and Avouris [10] were the first to demonstrate the ability of STM to image adsorbates on semiconductor surfaces, paving a way to a whole new era of atomically resolved chemistry, where single molecules can be visualized and chemical reactions can be triggered with atomic precision [11]. STM has become an indispensable tool in the studies of molecular adsorption [4, 12], catalysis [13], molecular diffusion [14], molecular self-assembly [15] and electronic structure of adsorbed molecules.

In this thesis the cryogenic scanning tunneling microscope is used to address a number of problems in surface chemistry on the scale of a single molecule as well as to carry-out new chemical reactions on metal surfaces. Two topics best reflect the scope of the experiments performed. The first topic is the atomic-scale understanding of the reaction of organosulfur compounds with the Au(111) surface (Part 4), which is at the heart of a tremendous field of today's nanoscience - self-assembled molecular monolayers [16]. The second topic can be termed "non-local chemistry" in a scanning tunneling microscope. It encompasses two experiments where atomically localized chemical excitation by the metal tip of the tunneling microscope produces delocalized chemical reactions on the surface. In one of the experiments delocalization of the chemical excitation happens by means of surface current of hot-electrons injected from the STM-tip (Chapter 12). In the other experiment, the STM excites a chain-reaction on the surface where the chemical excitation is transferred by radical-like reaction intermediates along the self-assembled chain of molecules (Chapter 11). Both experiments differ considerably from the well-known single-molecule chemistry in STM [11, 17], where the chemical transformation is localized only to the molecule excited by the STM-tip. The non-local chemistry in STM is largely an unexplored area and the potential of this approach for the future studies of surface chemistry is discussed.

In the following introductory section, the known facts about the chemistry of organosulfur molecules on gold surfaces are summarized, followed by a brief description of electron-induced chemistry in STM and a section on the structure and electronic properties of the Au(111) surface which was used in most of the presented studies.

## **1.1 SELF-ASSEMBLED MONOLAYERS OF ALKANETHIOLS ON GOLD SURFACES**

One of the milestones of nanoscience is to master the ability to make a nanoscale object with the desired structure and properties. It is no surprise that in this context biology is a source of inspiration for nanoscience. A wide variety of nanoscale chemical structures, such as enzymes, lipid bilayers, ion-channels, DNA etc. are mass-produced in nature via a universal principle of self-organization. Self-organization is the modular assembly of simple building blocks into

complex architectures, whose topology is determined by the kinetics and thermodynamics of the assembly process.

A simplified version of self-organization in natural systems is molecular self-assembly on crystalline surfaces, where the interplay of molecule-molecule and molecule-surface interactions spontaneously produces an ordered structure on the surface (in contrast to a random distribution of adsorbed molecules, or molecular overlayers that are only in registry with the underlying surface). Since structuring and functionalization of surfaces is of great technological interest, with potential applications in molecular (opto-) electronics, chemical sensing as well as heterogeneous catalysis, molecular self-assembly has become a rapidly developing branch of nanoscience [15, 16, 18-20]. Most of today's studies in molecular self-assembly investigate the self-assembled structure and the forces that produce the structure. Three common forces behind molecular self-assembly are van der Waals interaction, hydrogen-bonding, and metal-ligand interactions [21]. Atomistic understanding of the self-assembly mechanisms has been greatly advanced by scanning tunneling microscopy, which is capable of imaging self-assembled structures with atomic resolution and often observing the self-assembly process in real-time.

The self-assembled monolayer (SAM) of organosulfur molecules (e.g. alkanethiol) on noble-metal surfaces occupies a special place in the world of self-assembly. The organothiol molecule, that can be structurally described as having a headgroup (SH) and a tail (the organic residue), makes a strong covalent bond to the surface of noble-metals by the deprotonation of the SH-headgroup [15, 16, 22, 23]. A peculiar property of alkanethiol SAMs is self-organization in three dimensions rather than only two dimensions commonly observed in most other self-assembled monolayers. This property makes alkanethiol SAMs a convenient, flexible, and simple system with which to tailor the interfacial properties of metals, metal oxides, and semiconductors. The alkanethiol 3D-SAM is relatively inert (i.e. it can passivate reactive surfaces [24]), it can be used to attach virtually any functionality to a metal substrate ([16] and references therein) and it is an excellent host matrix for insertion of other molecules into a self-assembled layer [25, 26]. Electron transport through the SAM can be tuned by changing its chemical composition [27, 28]. Conducting, rectifying and switching behavior of the molecules in the SAMs has been demonstrated [28, 29]. An additional capability to pattern alkanethiol SAMs on the metal surface [30] makes them a promising candidate for the field of molecular electronics, where ensembles of molecules exhibit an electronic function. Finally, alkanethiol

SAM can be easily grown on noble-metal surfaces (in particular, Au(111)) and noble-metal nanoparticles allowing experiments to be done in the ambient environment.

The usefulness of the alkanethiol SAMs and numerous questions concerning their structure have stimulated an intense research effort to understand and control the self-assembly process. SAMs on Au(111) have been studied with virtually every surface science technique available: electron spectroscopy (e.g. X-ray, ultraviolet, two-photon photoemission spectroscopy [31-33]), diffraction techniques (X-ray diffraction [34, 35], X-ray standing waves [36, 37]), optical spectroscopy (infrared [38, 39], Raman [40], sum-frequency generation [41]), helium scattering spectroscopy [42, 43], temperature-programmed desorption [44-46] and scanning probe microscopy [47-49]. The analytical techniques specifically addressing the structure of the S-gold anchor bond are photoelectron diffraction (PhD) [50, 51], near-incidence X-ray standing wave-analysis (NIXSW) [52], grazing incidence x-ray diffraction (GIXRD) [53] and scanning tunneling microscopy. Unlike diffraction and standing wave techniques, STM is not able to provide the direct measurement of bond-lengths and angles. Structural assignments are made on the basis of the symmetry of molecular features in the STM images, their position relative to the underlying lattice and comparison of experimental and theoretical STM images. The sensitivity of the STM measurements to the structural details also depends on the strength of correlation between the structure and the electronic states of the adsorbed molecule.

The growth of three-dimensional alkanethiolate SAMs proceeds via a series of intermediate structures, including 2D-ordered SAMs, which were first reported by G. Poirier in 1996 [54]. To detect these intermediate structures, the gold surface was exposed to a controlled dose of alkanethiol vapor in UHV conditions. In solutions the reaction quickly proceeds toward the three-dimensional growth. According to Poirier's model (Fig. 1.1), which is still widely accepted, SAM growth starts with the dissociation of the S-H bond of alkanethiols or the S-S bond of alkanedisulfides on the Au(111) surface and formation of the thiolate species (R-S) [49, 54]. At a very low coverage, the R-S species are assumed to be weakly bonded to the surface (some authors also claim that thiols, R-SH, are still present at this coverage) and no ordered structures can be observed at room-temperature [49]. At a slightly higher coverage, ordered 2D-phases begin to form (these are often termed stripe-phases due to their visual appearance in the STM images, Fig. 1.2). As noted by Poirier, 2D-SAM-growth is correlated with the lifting of the herringbone reconstruction of the Au(111) surface [55]. The original proposal was that the strong

bonding of alkanethiolate to the Au(111) surfaces causes ejection of the extra Au-adatoms from the reconstructed surface layer on Au(111) [56], which are then embedded into single-atomic steps. In this thesis strong evidence is obtained to support a different mechanism, where the ejected Au-adatoms participate in the organometallic chemistry of alkanethiols on the surface.

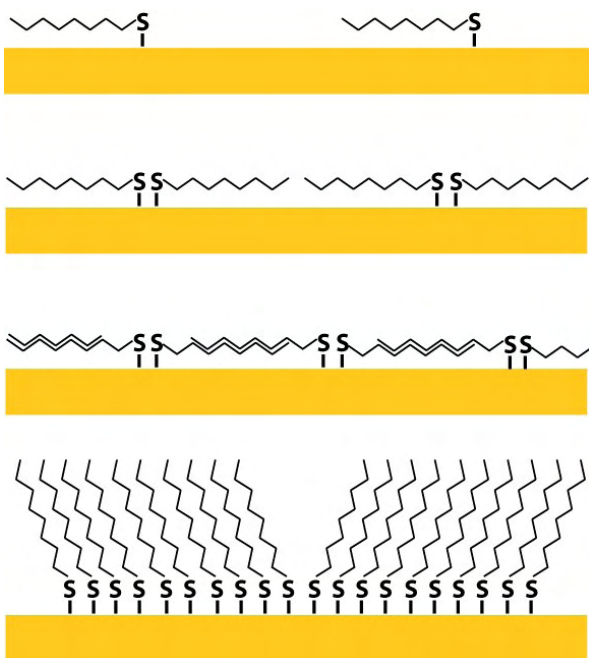


**Figure 1.1.** Mechanism of alkanethiolate self-assembly on Au(111) surface proposed by G. Poirier [57]: (1)  $\alpha$  - disordered “lattice gas”; (2)  $\beta$  - 2D-stripe-phase; (3)  $\delta$  - 2D-3D stripe-phase; (4)  $\phi$  - 3D-saturated SAM.

In the 2D-SAMs, the organic tails of the alkanethiolate species run nearly parallel to the surface (Figs. 1.1, 1.2). The S-headgroups dimerize and dimers assemble into extended chains along the  $[11\bar{2}]$  direction (up to 100 nm long) with the periodicity of  $\sim 5$  Å. The distance between the chains along the  $[11\bar{0}]$  direction is roughly twice the length of the alkane tail. The 2D-SAM continues to grow until the herringbone reconstruction of the Au(111) surface is completely lifted, and further on until saturation coverage. At an even greater thiol coverage the stripe-phase chains become more densely packed because of the thermodynamic gain due to S-headgroup bonding to Au(111). The alkane tails inevitably overlap, which causes them to buckle-up and “slide” onto each other (Fig. 1.1, 1.3). At this coverage the transition from the 2D-SAM to the 3D-SAM begins. A large number of mixed 2D-3D phases have been observed and they are all traditionally termed stripe-phase [58]. The 3D-SAM growth is complete when the S-headgroups bonded to the surface form a  $(\sqrt{3}\times\sqrt{3})R30^\circ$  superlattice. Due to van-der-Waals repulsion, the organic tails of the molecules lift off the surface (Fig. 1.1). In the case of alkanethiols, the alkane tails make an angle of  $\sim 30^\circ$  off-normal in the 3D-SAM.

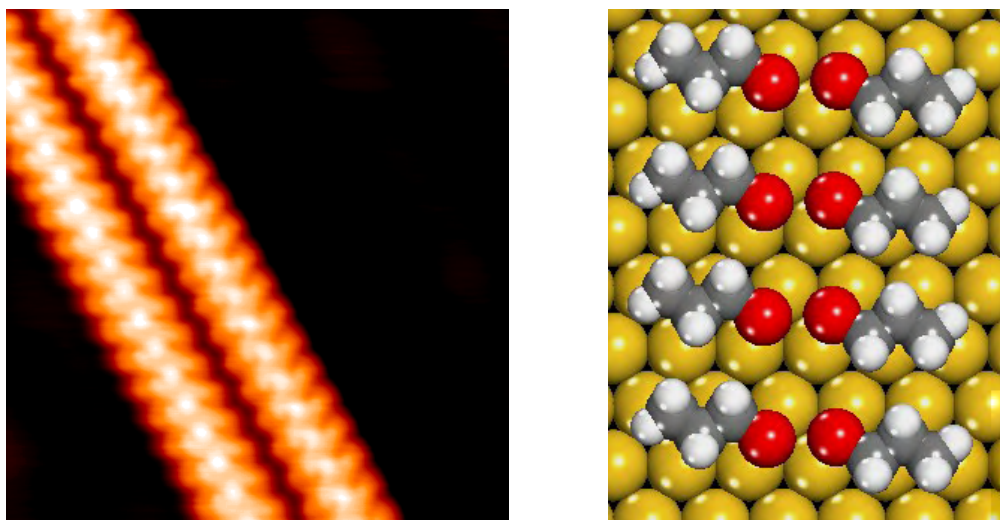


**Figure 1.2.** Left: STM image of 2D self-assembled chains (stripe-phase) of n-propanethiolate ( $C_3H_7S$ ) on the Au(111) surface ( $7.6 \times 7.6 \text{ nm}^2$ ,  $U = 2 \text{ mV}$ ,  $I = 0.9 \text{ nA}$ ). Right: structural model of a single stripe-phase chain after Ref. [59]. In the model: Au-yellow, S-red, H-white, C-grey.

The research of alkanethiol self-assembly on Au(111) has become very active already in the early 90's [60]. However, many aspects of the self-assembly process are still poorly understood today. The questions that are widely debated in the literature are the detailed mechanism of self-assembly [16, 54], the process and energetics of dissociation of thiol (RS-H) and dithiol (RS-SR) molecules on the Au(111) surface [15], the structural nature of the S-Au anchor bond [37, 47, 53], the morphological changes on the Au(111) surface that accompany self-assembly, such as lifting of the Au(111) herringbone reconstruction, formation of etch-pits in the surface layer, dramatic step erosion [16] and many others. Correct answers to these questions are crucial to understand the mechanism of alkanethiol self-assembly and to achieve control of the SAM structure and the properties of the self-assembled molecules. Furthermore the facile and reproducible growth of alkanethiolate SAMs on gold may serve as a prototype for the exploration of other molecule/substrate combinations in search of new, useful and functional SAMs.

The anchor-bond is an important, if not central structural property of the SAM. Nevertheless, the existing models of the S-headgroup bonding to the Au(111) surface only partially account for a wide-range of experimental observations. Uncertainty in this question translates into other unresolved SAM problems. The anchor-bond also has a profound effect on

the electronic properties of the molecule in the SAM. Changing the structure of the anchor-bond modifies the band-lineup at the metal-molecule interface [61] (i.e. the position of the HOMO-LUMO gap of the molecule relative to the Fermi level of the metal leads) and the electron-charging energy of the molecule [62]. New electronic states may also appear at the interface. All these effects may add up to an order of magnitude variation of molecular conductance [62, 63], which is certainly important for SAM applications involving electron-transfer, such as molecular electronics.

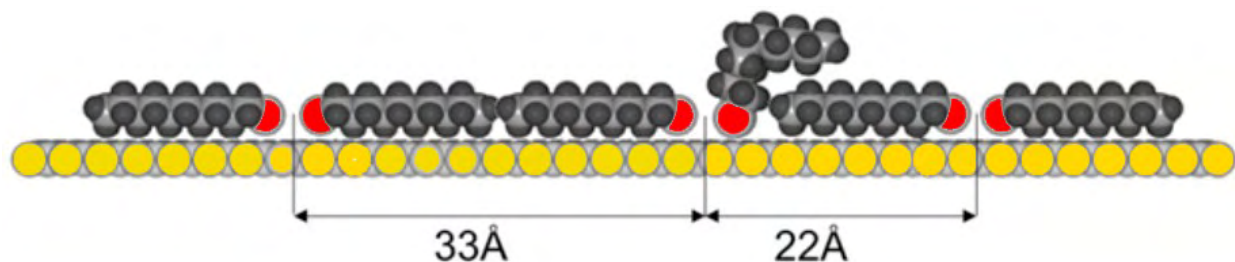


**Figure 1.3.** Structural model of the mixed  $(7.5/11.5 \times \sqrt{3})$  stripe-phase of dodecanethiolate on Au(111) surface where the transition from 2D to 3D-SAM begins [58].

The most intensely debated issue is the discrepancy between theoretical and experimental predictions of the adsorption site of the thiolate species on the Au(111) surface. DFT calculations predict that in the most stable adsorption geometry, the S-atom is two-fold coordinated, positioned on a bridge-site above two Au-atoms of the surface lattice with a slight shift toward a neighbor hollow-site (the so-called bridge-fcc, or bridge-fcc site, Fig. 1.4 [64-67]). Adsorption of the S-atom on 3-fold fcc- or hcp-hollow sites is less favorable by several kcal/mol, while the S-atom making a single bond to a Au-atom on an atop site (Fig. 1.4) is less stable by  $\sim 10$  kcal/mol [65, 67]. The preference of the bridge-fcc site was generally accepted in experimental and theoretical studies [16]; however, in a recent series of spectroscopic studies using photoelectron diffraction (PhD [50, 68]) and near-incidence x-ray standing-wave analysis (NIXSW [69]) it was conclusively shown that the S-atom in SAMs is adsorbed atop a Au-atom in a singly-coordinated configuration. To reconcile theory with experiment, deficiencies of the theoretical methods [50], coverage effects [35] and surface reconstruction at elevated temperatures [69] were proposed.

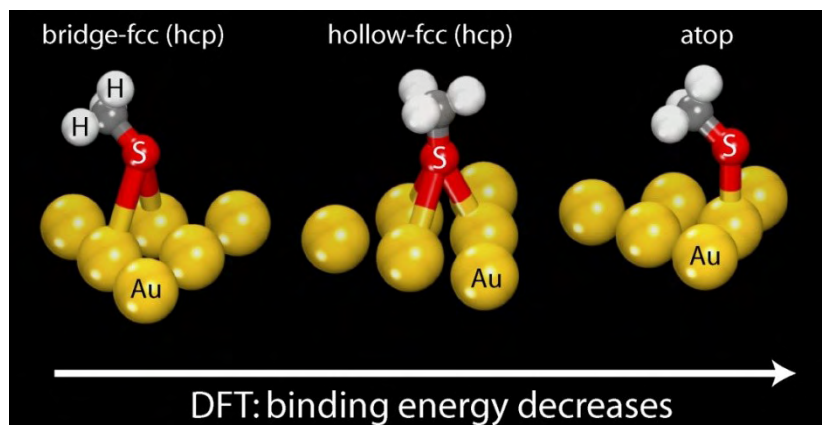


**Figure 1.4.** Calculated adsorption geometries of  $\text{CH}_3\text{S}$  adsorbed on the Au(111) surface.

The need to solve the problem of the sulfur-gold bonding in light of the growing interest in organosulfur SAMs on gold was our motivation to carry-out the experiments presented in Chapter 8. The key new finding is that the Au(111) surface acts as a dynamic support for alkanethiol chemistry, releasing reactive Au-adatoms that bind alkanethiol molecules into organometallic-like surface complexes. We proposed a new structural model for the stripe-phase 2D-SAM that involves Au-adatoms. It agrees well with the STM observations and the previously reported spectroscopic data. The model also accounts for the lifting of herringbone reconstruction of Au(111) by alkanethiolate self-assembly: the reconstructed surface layer provides reactive Au-adatoms at the early stage of 2D-SAM growth.

## 1.2 ELECTRON-INDUCED SURFACE CHEMISTRY IN SCANNING TUNNELING MICROSCOPE

Electronic excitation of adsorbed molecules can induce a wide-variety of processes, such as fluorescence, change of configuration, and chemical reaction. Its major advantage over the thermal excitation is the tunability of the excitation source. In addition to increasing the efficiency of the excitation process, this property enables mode-selective excitation of a specific reaction coordinate. This culminates in the ability to achieve coherent control of molecular dynamics, where the chemical reaction proceeds through a controlled preparation of coherent superposition of electronically excited states [70].

The first observation of desorption induced by electronic transition (DIET) dates back to the mid-60's [71, 72]. Experimentally, electronic excitation of adsorbates can be carried out using radiation sources, such as lasers [73] and synchrotron radiation [74] or by electron impact [75]. It is well-known that the lifetime of the electronically excited state of the adsorbate is very short due to its interaction with the underlying surface, which causes ultrafast relaxation of the excited state. The lifetime typically ranges from a few fs to a few picoseconds. It is much smaller on metal surfaces than on semiconductor surfaces, because of the efficient electron-hole pair excitation on the former. Because of the short lifetime, very little molecular dynamics occurs in the electronically excited state of the adsorbate. Instead, the transformations occur in the vibrationally excited ground state of the adsorbate into which the excited state relaxes [73]. These processes are described by the Menzel-Gomer-Redhead (MGR) model and its variants [71, 72].

The dynamics is described within a classical 1D two-electronic-state model, assuming that the excited state is repulsive in the adsorbate-substrate coordinate (Fig. 1.5). The excitation process projects the initial ground state onto the excited electronic surface. This sets the system into downhill motion on the repulsive potential. After a brief delay time, the electronic excitation relaxes, converting electronic energy into both kinetic and potential energies of the center-of-mass motion. If the system is displaced beyond a critical adsorbate-substrate distance, the amount of energy deposited into the translational degree of freedom is sufficient to overcome the desorption barrier.

In the early eighties, Antoniewicz [76] introduced a variant to the MGR scheme (Fig. 1.6), which assumes a bound excited state as opposed to the repulsive excited state in the MGR model. The excited state is assumed to be ionic. Once formed it is attracted to the surface by its image charge in the metal. Therefore the equilibrium configuration of the ionic state is shifted closer to the surface relative to the ground-state equilibrium. Due to the mismatch of potential minima, instantaneous excitation sets the system in the motion toward the surface. After a short delay, the system relaxes back to the ground state and appears on the repulsive wall of the

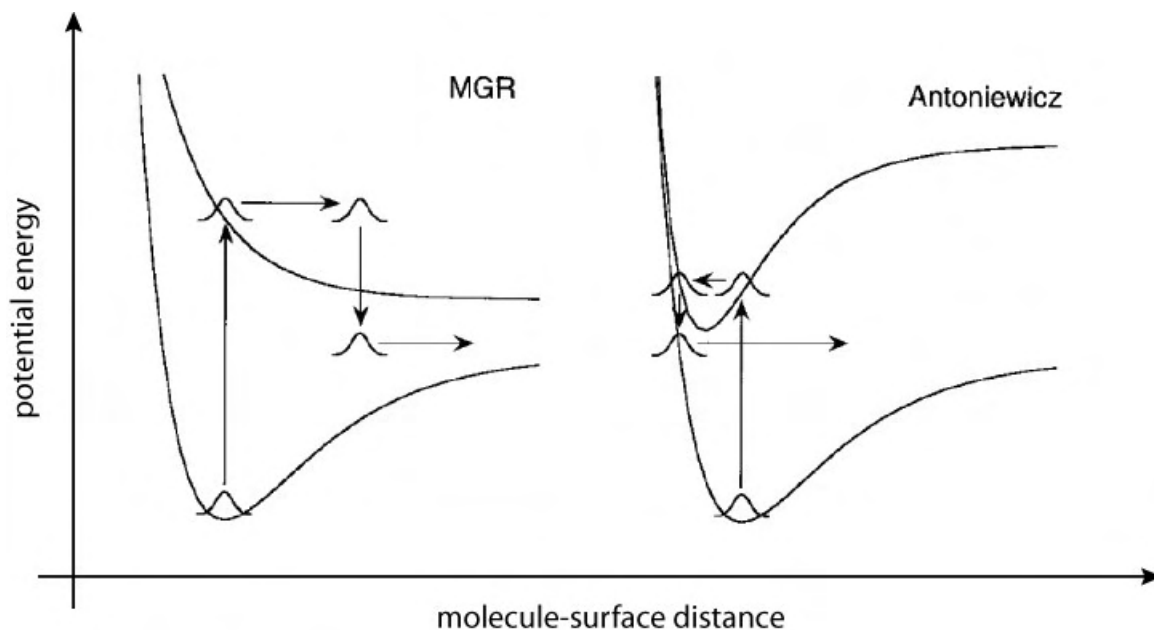


**Figure 1.5.** Two models of evolution of electronically excited states on surfaces: Menzel-Gomer-Redhead (MGR) [72], bound-repulsive model and Antoniewicz bound-bound model [76]. Bottom potential corresponds to the ground-state of a molecule in the vicinity of the surface, upper – to its electronically excited state. Arrows show the evolution of the nuclear wavepacket upon electronic excitation of the adsorbed molecule.

ground-state potential. Depending on the mismatch of the ground and excited potential curves and the lifetime of the excited state, the system may gain sufficient energy to desorb from the surface (or undergo any other transformation described by the 1D-potential, such as a chemical reaction or diffusion on the surface).

The 1D-approximation behind both models is not always sufficient to describe the evolution of the nuclear wave-packet, which may involve coupling of several reaction coordinates [77]. The second approximation is the assumption of the nearly instantaneous transitions. Nevertheless, MGR and Antoniewicz models predict the isotope effect of the electron-stimulated processes that factors in through the change of the shape of the potential curves. Also they capture the essential physics behind the excitation process.

The high spatial resolution scanning tunneling microscopy offer unique opportunities in electron-induced surface chemistry [11, 17, 78]. The STM-tip can be considered as a highly localized and energy-tunable electron gun. Therefore, the excitation can be limited to a single molecule and even parts of the molecule under the STM-tip. The current density achievable in the tunneling junction (of order  $10^6 \text{ A}\cdot\text{cm}^{-2}$ ) is superior to any other electron source by several

orders of magnitude, which allows one to excite dynamical processes with a yield as low as  $10^{-11}$  per electron. Naturally, the reagents and products of a surface chemical reaction, as well as the effect of the local surrounding, can be analyzed with atomic resolution.

STM-induced chemistry was first demonstrated in 1990 by desorbing hydrogen from Si(111)-(7x7) surface using pulses of tunneling current from the STM-tip [79]. Hydrogen desorption proceeds via excitation of the S-H  $\sigma^*$  anti-bonding orbital with the electron-threshold energy of  $\sim 4\text{V}$  [80]. A whole new direction in surface chemistry, termed single-molecule chemistry, was pioneered by the group of W. Ho in 1997 [81]. Inelastic-scattering of the tunneling electrons was shown to excite the vibration of the  $\text{O}_2$  molecule on the Pt(111) surface causing it to dissociate. Isotope effects and reaction kinetics were observed by the direct measurement of the single-molecule dissociation rate. Several recent reviews summarize the progress of single-molecule chemistry involving vibrational excitation of the molecules in the ground electronic state and electronic excitation of the adsorbed molecules [11, 17, 78, 82, 83]. Some of the biggest achievements in the field are the identification of the reaction products by single-molecule vibrational spectroscopy [84], controlled synthesis of single-molecules [85-87], observation of molecular diffusion on the surface by quantum tunneling [88, 89], mode-selective excitation by the tunneling current [90] and sub-molecular precision of electron-induced excitation [91].

All the STM-induced reactions on metal surfaces in this thesis are induced by electron-energies that are substantially (at least a factor of two or three) higher than the energies of the vibrational modes in the molecule (which are  $< 400\text{ mV}$ ). They are therefore likely to involve electronically excited molecular states [78]. Electronic excitation may proceed along one of the two mechanisms shown in Fig. 1.6, electron attachment to a molecular LUMO or excitation of the HOMO-LUMO transition by a tunneling electron. Using the STM it is possible to measure the threshold energy for the reaction as well as its kinetics. The former is determined from the voltage-dependent yield of the reaction, which is straightforward. The kinetic measurement requires some explanation.

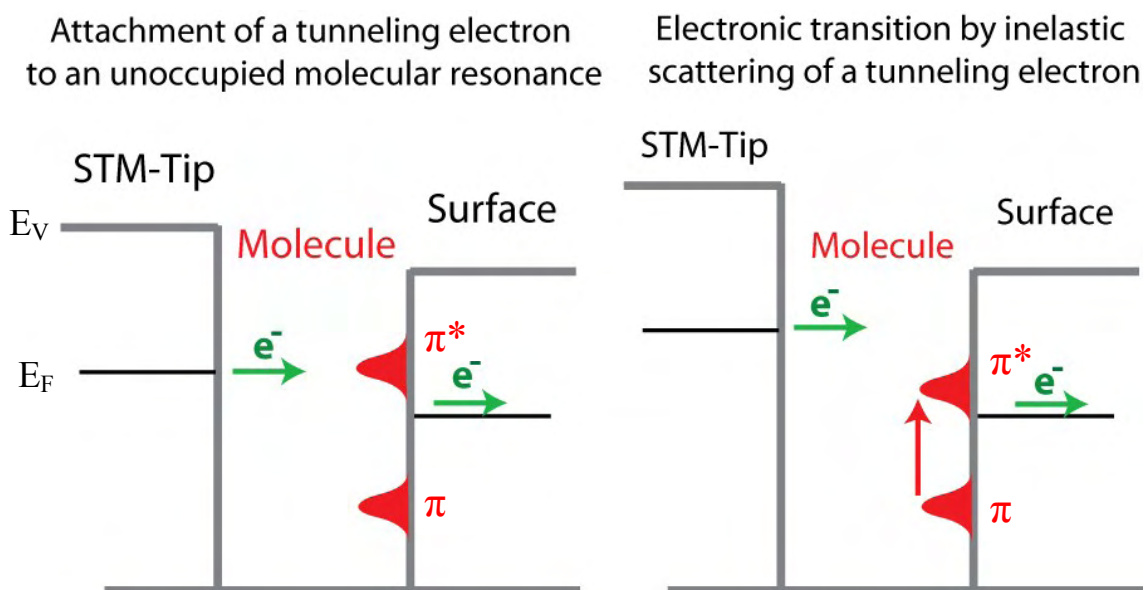


**Figure 1.6.** Two mechanisms of electron-induced molecular excitation in STM [78].  $\pi$  is the HOMO and  $\pi^*$  is the LUMO of the adsorbed molecule;  $E_V$  – vacuum level,  $E_F$  – Fermi level.

In order to induce a single-molecule reaction, the STM-tip is positioned above the molecule and the tunneling voltage is increased to a desired value. The feedback loop of the STM is open, i.e. the tip-surface distance is constant throughout the reaction. Tunneling current is simultaneously monitored with the time-resolution of  $\sim 10 \mu\text{s}$ . The reaction event is observed in the time-trace of the tunneling current as an abrupt step (either positive or negative, Fig. 1.7) occurring after a certain dwell-time. The step occurs because the product(s) of the reacted molecule is always different from the reagent causing a change of the tunneling barrier and therefore a change of the tunneling current. Both voltage and initial tunneling current have to be chosen so that the dwell-time of the molecule in the junction is sufficiently large to be detectable.

Single-molecule reaction is a quantum-mechanical process with a certain probability of occurring. Therefore, its rate (extracted from the dwell-time) cannot be determined from a single measurement (Fig. 1.7). To extract a true reaction rate the dwell-time must be measured on a large ensemble of molecules (100-1000). Further, the reaction events are subject to Poisson statistics because the probability of a reaction is constant at any given time of the measurement, which yields the exponentially decaying probability distribution of dwell-times as shown in Fig. 1.8. The decay-rate ( $1/\tau$ ) of the exponent is proportional to  $I^n k$  [92], where  $I$  – is the tunneling current,  $n$  – the number of electrons required to induce a single reaction event and  $k$  is the rate constant of the reaction. By measuring the decay-rate as a function of current, one can determine

both  $n$  and  $k$ . It should be mentioned that  $k$ -values are, in general, tip-dependent and are rarely pursued. However, the  $n$ -exponent is very important to understand reaction mechanism and has to be measured ideally with the exact same tip [11].

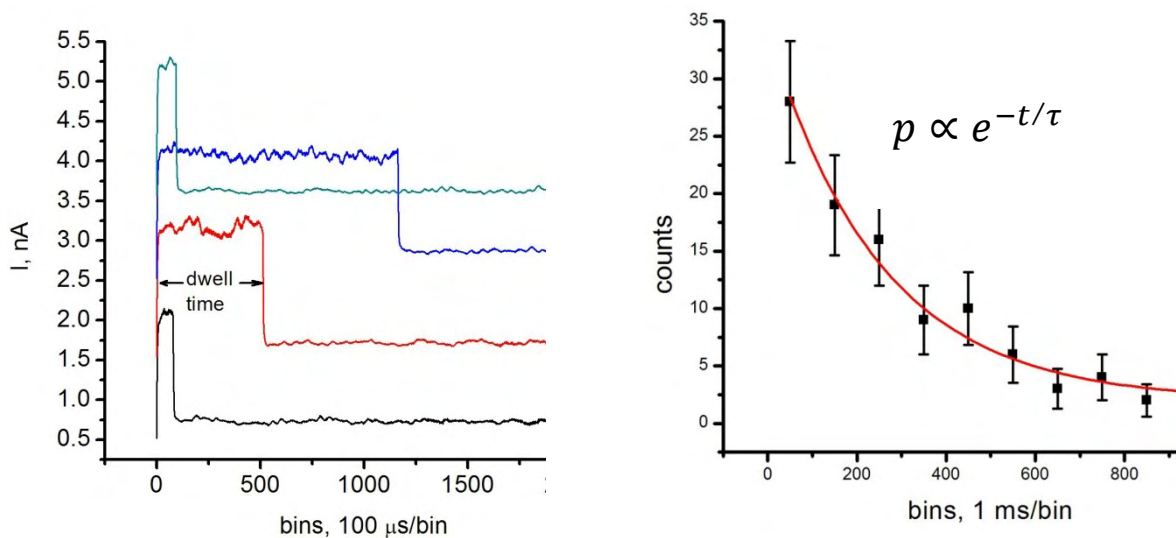


**Figure 1.7.** Four representative time-resolved traces of tunneling current during electron-induced dissociation of the  $\text{CH}_3\text{SSCH}_3$  molecule under the STM-tip on the Au(100) surface. The reaction event is seen as an abrupt drop due to dissociation of the S-S bond causing a corresponding change in the tunnel-barrier height. The current traces are offset along the y-axis for clarity. The dwell-time is different for each dissociation event. The reaction rate at a given tunneling current ( $1/\tau$ ) is obtained from an exponentially decaying probability distribution of dwell-time ( $t$ ) obtained by averaging 100-200 current traces (right panel shows a representative distribution).

One of the challenges in single-molecule chemistry is to demonstrate that the STM-tip itself does not influence the outcome of a chemical reaction initiated by the tunneling current [78]. The problem originates from the unknown shape, composition, electronic structure of the STM-tip and the tip-molecule separation. The STM-tip may affect the chemical process either by the electric field [93] always present in the tunneling junction or by the direct tip-molecule interactions. The latter occurs by direct overlap of the electronic wavefunctions (formation of a weak chemical bond) or the electric-field effect tip. The influence of the tip can be strong enough to allow manipulation of the molecule as a whole, which is a powerful methodology in its own right [94, 95]. The transition state of a molecule dissociating under the tip may also be affected. The degree of this undesirable effect will vary depending on the system being investigated. But for some applications of the electron-induced chemistry it may be detrimental to achieving understanding. One such application, termed surface-aligned chemistry or more specifically

patterned molecular reactions, was proposed by J. C. Polanyi [83]. Many molecules are oriented on solid surfaces because of the adsorbate-substrate and adsorbate-adsorbate interactions. When photo- or electron-induced fragmentation takes place in the adsorbed layer, it is possible for the fragments to collide with the surface and/or other molecules nearby. Therefore bimolecular reactions can be carried out with well-defined reactant alignment and impact parameters, eliminating the extensive averaging of the gas phase. Compared with gas-phase reactions in thermal conditions, surface-aligned chemistry has the potential to greatly improve reaction efficiency and control over product selectivity [83]. Atomically-resolved mapping of reactants and products using scanning tunneling microscopy is the ideal way to approach electron-induced surface-aligned reactions. However, the influence of the STM-tip should be minimized in such experiments. Surface-aligned chemical effects have also been studied by macroscopic methods, using the atomic steps on a Pt crystal to align adsorbed O<sub>2</sub> molecules which are photochemically dissociated [96].

In Chapter 12 of the thesis a novel, non-local approach to carry out electron-induced surface chemistry is presented. In this approach, electrons injected from the STM-tip excite a chemical reaction far outside of the tunneling junction (up to 100 nm) in contrast to directly underneath the STM-tip, as in the single-molecule chemistry. On the noble-metal surfaces the injected electrons transport toward the adsorbed molecules via the surface-state or surface resonance band and then scatter on adsorbed molecules, causing a chemical reaction. Tip-artifacts are eliminated in this case by the spatial decoupling of the STM-tip from the reacting molecules. Non-local excitation connects STM- and photo-induced surface chemistry on metal surfaces, because in the latter the chemical reactions are also caused by hot-electrons excited into various surface electronic states. Finally, it is shown that non-local chemistry can be used to measure the transport of hot-electrons on the surface, where the reaction probability is used as a measure of hot-electron current as a function of distance from the point of electron-injection.

### 1.3 SURFACE STRUCTURE AND HERRINGBONE RECONSTRUCTION OF AU(111)

Most of the experiments presented in this thesis were carried out on the Au(111) surface, the hexagonally close-packed termination of the gold single crystal. A distinct property of this surface is the so-called “herringbone” reconstruction [56], which occurs naturally for the atomically clean Au(111) surface to allow the surface layer to have a more close-packed structure than the bulk-terminated (111) plane. In this thesis it is shown that the herringbone reconstruction plays an important role in both physisorption and chemisorption of various molecules on the Au(111) surface. Minute variations of Au-Au bond distance across the surface layer produce a rich landscape of surface sites with different adsorption energies, which in turn influences molecular self-assembly of physisorbed molecules (Part 4). In the case of alkanethiol chemisorption leading to their self-assembly, the herringbone reconstruction surprisingly acts as a source of reactive Au-adatoms that are released at  $T > 200\text{K}$  and become incorporated into strongly-bonded organometallic-like complexes on the surface (Chapter 8).

#### 1.3.1 Uniaxial compression of the hexagonal surface lattice

The herringbone reconstruction on the Au(111) surface arises from the competition between two effects: (1) the surface atoms are under tensile stress, i.e. the surface bond length prefers to be smaller than that in the bulk; (2) the surface atoms seek potential minima due to underlying substrate atoms, which correspond to positions of maximum coordination with these atoms [97]. The bond-lengths between surface atoms are decreased by inserting extra Au atoms into the surface layer. In the case of Au(111), a single gold atom is added for each 22 surface atoms along one of the three  $\langle \bar{1}10 \rangle$  equivalent close-packed directions [56, 97, 98]. As a result,  $22 \times \sqrt{3}$  reconstruction is formed, with the reconstructed unit cell containing 2 added Au-atoms (and a total of  $44+2$  surface atoms), Fig. 1.8. The surface lattice is compressed by an average of 4% along the  $[\bar{1}10]$  direction.

Since gold is an fcc-metal, the surface Au atom on the [111] plane can occupy either the fcc- (ABCA..) or the hcp- (ABA..) hollow site. The hcp site is slightly less stable than fcc [97] which is why on the unreconstructed surface only the fcc-sites are occupied. When the  $22 \times \sqrt{3}$

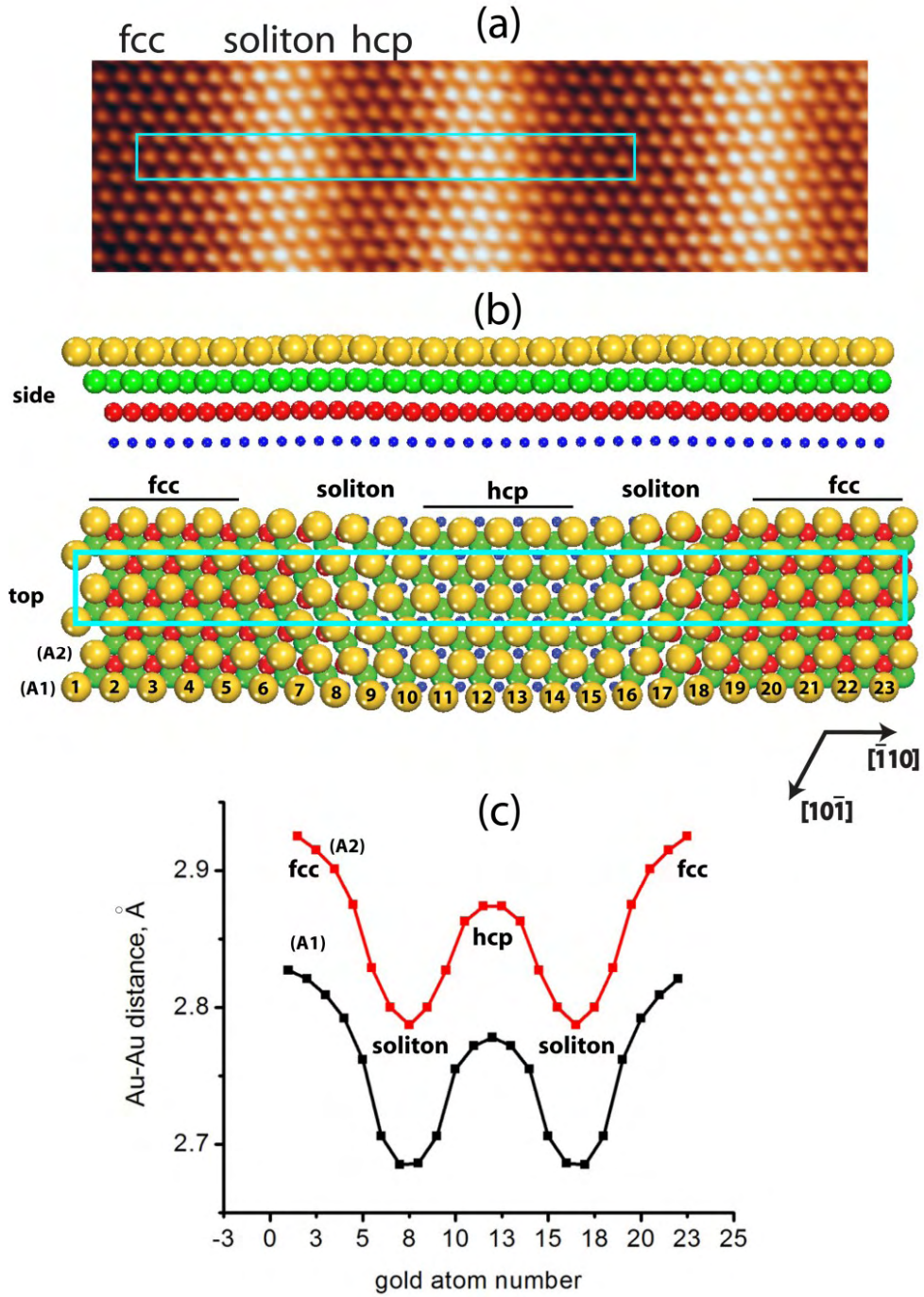


**Figure 1.8.**  $22 \times \sqrt{3}$  reconstruction of the Au(111) surface. (a) atomically-resolved STM image, blue rectangle is the  $22 \times \sqrt{3}$  unit-cell; (b) structural model from Ref. [97]. (c) Variation of the lattice-constant in the unit-cell, which is anisotropically compressed along the  $[\bar{1}10]$  direction. A1 and A2 are two close-packed rows in the unit-cell.

reconstruction is formed, the extra atom is accommodated by shifting a fraction of the surface atoms to the hcp sites. As a result, alternating domains of fcc- and hcp-stacking are formed (Fig. 1.8a,b). These domains are separated by narrow transition regions, termed soliton walls, where the atoms occupy “bridge” sites, mid-way between fcc and hcp sites (Fig. 1.8b). The in-plane distortion of the surface lattice is  $0.7 \text{ \AA}$  normal to the compressed close-packed direction. This is clearly seen in the atomically resolved STM image of the surface, Fig. 1.8a . In addition, a small out-of-plane relaxation of the surface takes place, raising the gold atoms in the soliton walls by  $0.2 \text{ \AA}$  relative to the fcc region. The elevated solitons produce a distinct “double-row” surface corrugation of the Au(111) surface in the STM images (Fig. 1.8).

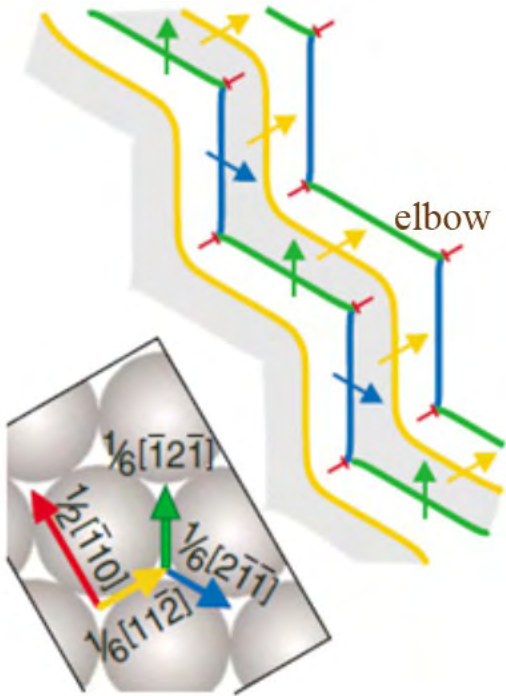


**Figure 1.9.** Burgers vectors used to describe Shockley partial dislocations of the Au(111) surface lattice underlying the herringbone reconstruction. Yellow Shockley partial dislocations have matching Burgers vectors at the elbow site, while green and blue partial dislocations mismatch producing a perfect edge dislocation [99].

An important but rarely emphasized property of the herringbone reconstruction is the variation of the interatomic Au-Au distance in the surface layer along the compressed  $[\bar{1}10]$  direction (Fig. 1.8c). From the model calculation of the  $22\times\sqrt{3}$ -reconstructed Au(111) surface [97], the Au-Au distance varies gradually from  $\sim 2.83 \text{ \AA}$  in the center of the fcc-region, to  $2.67 \text{ \AA}$  in the middle of the soliton and has an intermediate value of  $2.78 \text{ \AA}$  in the middle of the hcp-region. The variation of the interatomic distance is reflected in change of the surface stress on the

Au-atoms from tensile in the fcc-region to compressive on the soliton lines to vanishingly small in the hcp-region [97].

In the terms of the dislocation theory, the anisotropic lattice compression of the Au(111) surface is described by two Shockley partial dislocations  $[100]$  (Figure 1.9). Insertion of an extra atom in principle requires a shift of the atomic row by one lattice spacing along the close-packed direction, producing a perfect dislocation: the corresponding Burgers vector is  $\frac{1}{2}[\bar{1}10]$  or its  $60^\circ$  equivalent, Fig. 1.9. The same result can be achieved by dissociating the perfect dislocation into two imperfect dislocations (also called Shockley partial dislocations):  $\frac{1}{2}[\bar{1}10] \Rightarrow \frac{1}{6}[\bar{1}1\bar{2}] + \frac{1}{6}[\bar{2}\bar{1}\bar{1}]$  (Fig. 1.9). The total norm of two Shockley partials is  $\frac{2a^2}{3}$ , which is smaller than the norm of the perfect dislocation,  $a^2$  ( $a$  is the lattice constant). Therefore partial dislocations will be favored following Frank's energy criterion [101]. As seen in Fig. 1.9, a  $\frac{1}{6}[\bar{1}1\bar{2}]$  partial dislocation translates the fcc-hollow site into the hcp-hollow site, and the  $\frac{1}{6}[\bar{2}\bar{1}\bar{1}]$  partial dislocation translates the hcp-hollow site back into the fcc-site, which is exactly what is observed in the herringbone reconstruction on Au(111). The soliton walls (Fig. 1.8, 1.10) are the Shockley partial dislocations.

### 1.3.2 The herringbone reconstruction

Anisotropic lattice compression caused by the  $22\times\sqrt{3}$  reconstruction of Au(111) produces long-range elastic forces that increase the surface energy [102]. To compensate for this effect, the vector of anisotropic compression is rotated by  $60^\circ$  from  $[\bar{1}10]$  direction to an equivalent  $[01\bar{1}]$  or  $[10\bar{1}]$  directions with a period of  $\sim 15$  nm, generating the characteristic herringbone pattern of soliton lines (Fig. 1.11). The surface region at the point of rotation is usually referred to as an elbow site. As seen in Fig. 1.9, the Burgers vectors of only one of the two Shockley partial dislocations (yellow arrow) can be matched at the elbow. The other Shockley partial dislocation (blue arrow) meets its analogue (green arrow) with the Burgers vectors rotated by  $120^\circ$ . This produces a perfect edge dislocation in each elbow site [99, 103], which is the point where an extra atom is inserted. The mismatch of the Burgers vectors also explains why there are two types of elbows – termed rounded and pointed according to their shape. Indeed, the structure of

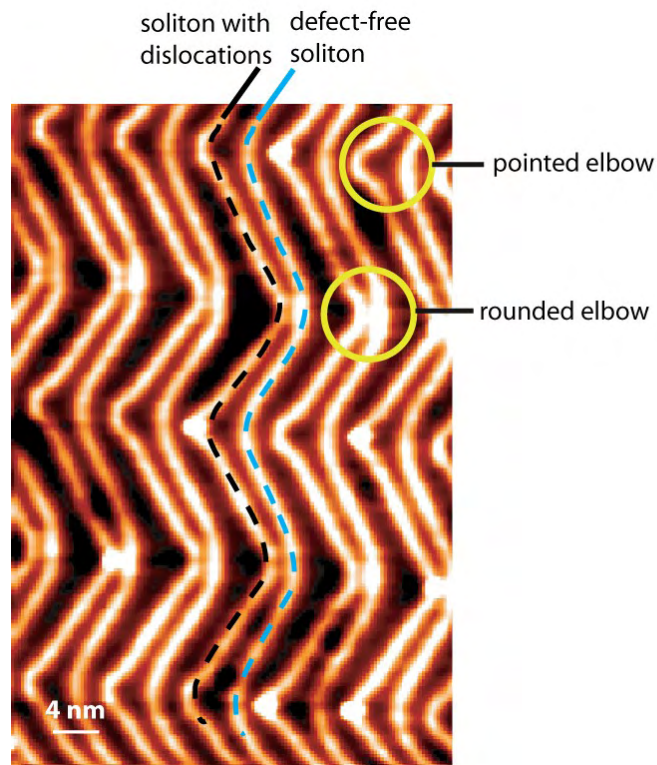


**Figure 1.10.** Large-scale STM image of the Au(111) herringbone reconstruction showing elbow regions and defective/non-defective soliton lines.

the edge dislocation will depend on whether the blue-arrow meets the green one or the other way around in Fig. 1.10.

A large scale STM image of the Au(111) herringbone reconstruction is shown in Fig. 1.10. The soliton pairs, rounded and pointed elbows are clearly seen. Again, only one soliton wall in each pair contains dislocations at the elbow sites. Fig. 1.11 shows an atomically-resolved STM image of the pointed elbow with the perfect edge dislocation. The blue atoms in the vicinity of the dislocations have a significantly distorted coordination suggesting that this site will have an increased reactivity towards atomic and molecular adsorbates. Indeed, this is the preferential adsorption site on Au(111) for all molecules studied in this thesis, as well as for a number of other cases reported in the literature [104, 105]. Furthermore, Chapter 5 presents preliminary evidence that the elbow sites act as local sources of reactive Au-adatoms in the organometallic chemistry of alkanethiolate molecules on the Au(111) surface.

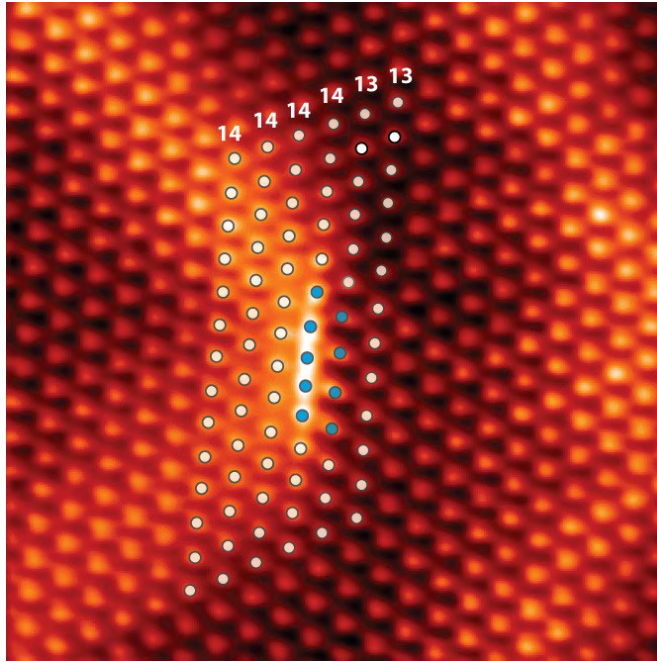


**Figure 1.11.** Atomically resolved pointed elbow site on the Au(111) surface. Blue circles mark lattice atoms in the vicinity of the perfect edge dislocation, where the number of gold atoms in the close-packed row (shown in the image) increases by one.

## 1.4 BULK AND SURFACE ELECTRONIC STATES

The electronic states in solids are commonly divided into bulk states that extend across the whole volume of the sample and surface states, which are localized near the surface termination of the bulk and extend exponentially both into the bulk and the vacuum region. Since surface states do not propagate perpendicularly to the surface, they usually behave as a two-dimensional electron gas [106]. There is also a third type of state – a surface resonance. These are extended into the bulk similar to bulk states, but they have an enhanced probability amplitude on the surface [107]. The overall density of bulk states is  $\sim 10^8$  larger than the surface states, which is why surface states are neglected when one deals with bulk properties of the material. However, the free-electron character of the surface state and their increased local density of states on the surface makes their contribution often dominant in various surface phenomena, such as the formation of Schottky barriers [108], long-range interactions between adsorbates [109], molecular self-assembly [110, 111], epitaxial growth [104], surface magnetism [112], lifetime of charged

surface species [113], etc. Surface states can also be used to study the properties of various electron scatterers, such as single-atom high steps and adsorbates [114, 115]. In this work, the surface states are shown to act as an efficient transport medium for hot-electrons that induce chemical reactions of adsorbed molecules.

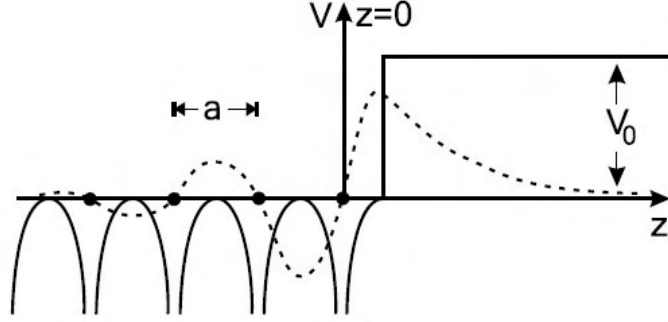


**Figure 1.12.** Wavefunction of a surface state in the 1D-crystal potential (dashed line).  $V_0$  is the work function,  $a$  – crystal lattice constant.

Surface states were predicted by Igor Tamm [116, 117] and William Shockley [110] in the 1930's. In the one-dimensional model of the solid (infinite chain of atoms along the  $z$ -coordinate), the electron potential can be expressed as:

$$V(z) = -V_0 + 2V_g \cos(g \cdot z) \quad (1.1)$$

Where  $V_0$  is the work function of the metal surface,  $V_g$  is the atomic corrugation potential and  $g = \frac{2\pi}{a}$  is the reciprocal lattice vector;  $a$  = lattice constant of the solid (Fig. 1.12). Electron states are obtained by solving the Schrödinger equation in one dimension:

$$\left[ -\frac{\hbar}{2m} \frac{d^2}{dz^2} + V(z) \right] \psi(z) = E\psi(z) \quad (1.2)$$

The solutions are the well-known Bloch states, which are plane-waves modulated by the periodicity of the bulk potential:

$$\psi(z) = e^{ikz} \cos\left(\frac{gz}{2} + \delta\right) \quad (1.3)$$

where  $\sin(2\delta) = \frac{\hbar}{2m} \frac{kg}{V_g}$ . Note that the quantum number  $k$  can only be real in the bulk. Complex solutions would exponentially decay for plane-waves propagating to the right and would diverge for plane-waves propagating to the left. However, complex solutions can exist on the surface

(termination of the 1D-chain) because the state can exponentially decay into both, bulk and the vacuum regions:

$$\Psi(z) = e^{ik'z} \cos\left(\frac{gz}{2} + \delta\right), z < \frac{a}{2}$$

$$\Psi(z) = e^{-qz}, z > \frac{a}{2}, q = \sqrt{V_0 - E} \quad (1.4)$$

$k'$  values are chosen so that they match the decaying exponential in the vacuum region. The resulting wavefunction is shown in Fig.1.12 and is termed a Shockley surface state. Since  $k'$  has no solutions in the bulk, Shockley states exist only in the projected bandgaps of the bulk. At the same time, the periodicity in-plane of the surface persists, and therefore the Shockley states have dispersion parallel to the surface that is characterized by a vector of  $k_{\parallel}$ . The surface state energy scales quadratically with  $k_{\parallel}$  reflecting the nearly-free character of surface state electrons:

$$E_{SS} = E_{\min} + \frac{\hbar^2 k_{\parallel}^2}{2m} \quad (1.5)$$

where  $E_{\min}$  is the energy of the surface state band minimum relative to the metal's Fermi level.

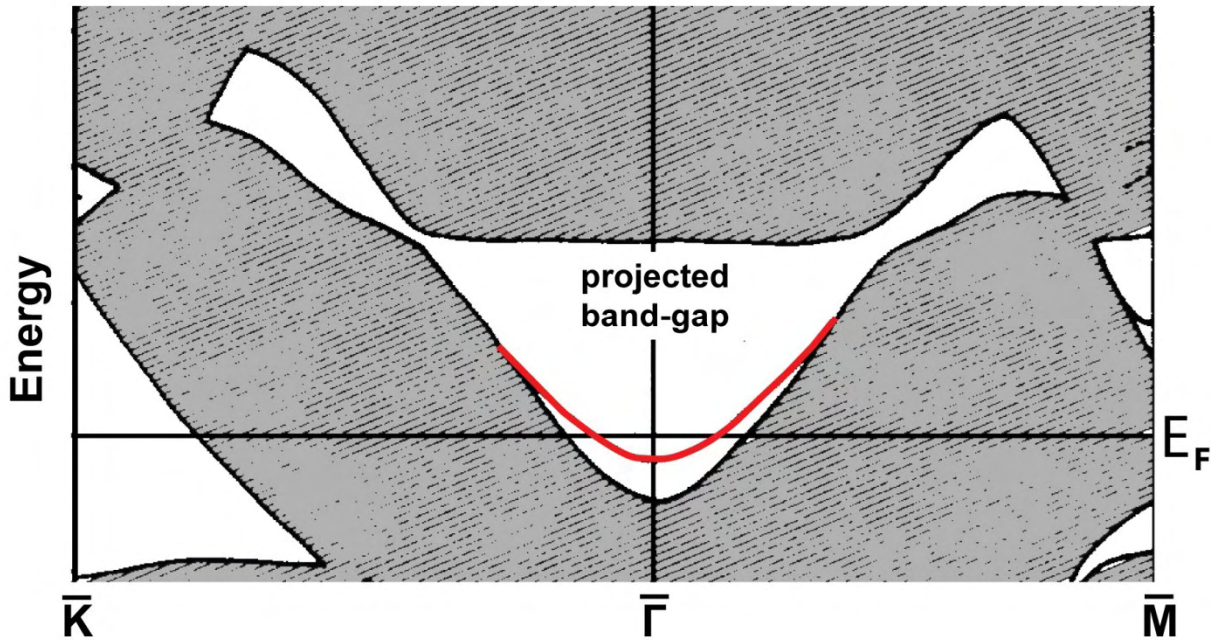


**Figure 1.13.** Bulk band structure projected onto 2D surface Brillouin zone of Au(111) surface along high-symmetry directions (schematic). Shaded areas are regions of  $k$ -space where bulk states exist, white areas are projected bandgaps. Red curve is a surface state in the band-gap centered on the  $\bar{\Gamma}$ -point.  $E_F$  is the Fermi-level.

All the noble metals – Cu, Ag and Au show a bandgap in the  $\Gamma$ L projected band-structure (Fig. 1.13). The bandgap, centered on the  $\bar{\Gamma}$  point in the surface Brillouin zone, is the result of s-p band crossing in these materials and the surface state existing in this gap is therefore an s-p Shockely surface state. There are many more surface states on the (111) surfaces, such as an s-d Shockley surface state at  $\bar{\Gamma}$  ([118] and references therein), but they are located relatively far away from the Fermi level and therefore have been much less studied by STM and other techniques.

### 1.4.1 STM studies of surface states

The most straightforward STM measurement that reveals the presence of the surface state is scanning tunneling spectroscopy near the Fermi level [119-121]. As seen in Fig. 1.14, the

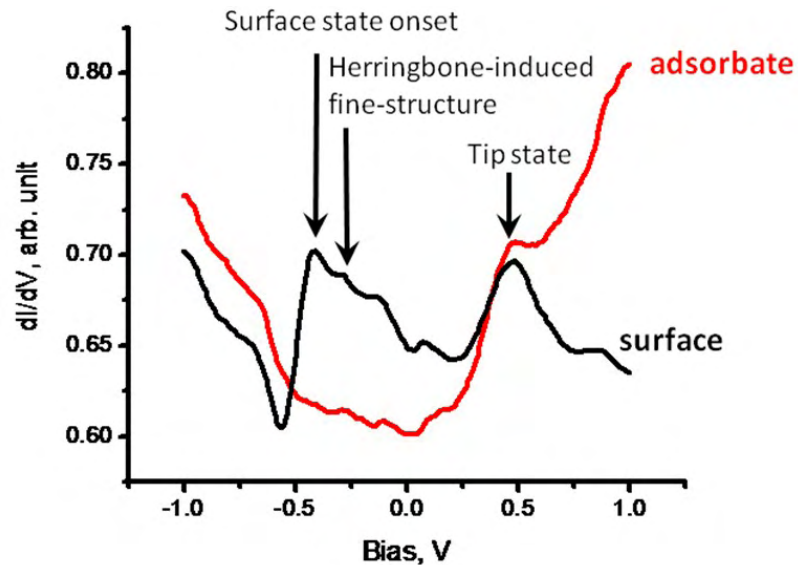


**Figure 1.14.** STS recorded in the hcp-region of the Au(111) surface and on top of the adsorbate (Au-atom bonded  $\text{CH}_3\text{S}$ , Chapter 5). An abrupt onset of the surface state at -500 mV below Fermi level is clearly visible in the spectrum of the surface. The adsorbate quenches the surface state.

conductance of the tunneling junction increases abruptly at the onset of the surface state on Au(111), which is  $\sim 500$  mV below  $E_f$ . There are two experimental indications that the observed onset is indeed due to the surface state. One is that the measured onset matches well the energy

of the surface state band minimum obtained by angular resolved photoelectron spectroscopy (ARPES) [122]. The other indication is that the peak intensity drops at the single atom high step sites and most adsorbates, particularly adatoms and adatom-bonded complexes. Both steps and strongly bonded adsorbates break the translational symmetry of the surface allowing mixing of the surface state with the bulk states, which is ideally forbidden [123-125]. The surface state DOS is substantially broadened which is measured as the drop in STS intensity.

However, the most striking signature of the surface state in the STM images are the wavelike fringes around defects (e.g. Fig. 1.15) [120, 126]. The fringes are periodic oscillations of the local density of surface state (surface state LDOS) that are analogous to Friedel oscillations of total charge density. The oscillations occur because of the interference of the electron wave travelling towards the defect with the one that is backscattered from the defect [127]. Using  $di/dv$  mapping, i.e. spatially resolving the surface LDOS at a chosen energy, the

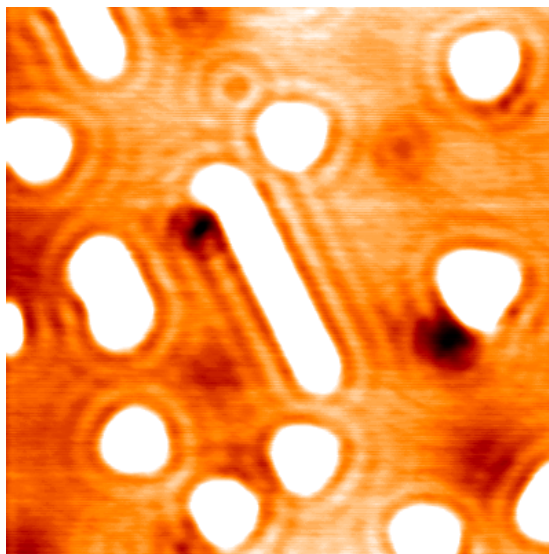


**Figure 1.15.** Constant current STM image of sulfur islands on the Cu(111) surface (white patches).  $280 \text{ \AA} \times 138 \text{ \AA}$ ,  $V = 0.24 \text{ V}$ ,  $I = 0.23 \text{ nA}$ . Sulfur islands act as static scatterers of surface state electrons producing wave-like fringes in the vicinity of the islands.

period and amplitude of surface state oscillations can be measured as a function of energy. Burgi et. al. have published a series of elegant studies of surface state scattering at straight steps on Ag(111), Au(111) and Cu(111) surfaces [8, 114, 128-130]. Surface state LDOS oscillations in

the direction normal to a straight step are fitted by the probability density integrated over all possible in-plane momenta ( $k_x, k_y$ ) at a given energy ( $E_{||} = E_{\bar{\Gamma}} + \frac{\hbar^2(k_x^2 + k_y^2)}{2m}$ ) and  $m$  is the effective electron mass:

$$\rho_s(E, x) \approx \rho_b + L_0 \left[ 1 - r(E) e^{-2\left(\frac{x}{L_\phi}\right)} J_0(2k_E x) \right] \quad (1.6)$$

where  $\rho_s$  is the spatially and energy resolved surface state LDOS,  $\rho_b$  is the bulk density of states (usually it is just an offset in the STS spectra),  $L_0 = \frac{m}{\pi\hbar^2}$  is the density of the 2D electron gas,  $r(E)$  is energy dependent reflection coefficient of the step (it is nearly unity at the surface state minimum at decreases to  $\sim 20\%$  at 2.0 eV above  $E_f$  [114]),  $L_\phi$  is the coherence length of the surface state electron on the *clean* surface (the exponential factor accounts for a decay of surface state electrons due to inelastic electron-electron or electron-phonon scattering, the factor of 2 in the exponential accounts for the fact that the electrons travels the same distance to and from the scatterer) and  $J_0(2k_E x)$  is the zero-order Bessel function that is oscillatory and that accounts for the wavelength of the surface state electron. Spatial mapping of the surface states therefore allows one to measure the coherence length  $L_\phi$  of surface state electrons on the clean surface and the reflection probability of surface state electrons from the single-atom steps.

#### 1.4.2 Where do electrons tunnel?

Electrons tunneling from the STM-tip can in-principle couple into the electronic states of the surface (bulk and surface states) with an arbitrary value of parallel momentum,  $k_{||}$ . However, the probability of tunneling into these states will depend dramatically on the value of  $k_{||}$ . The transmission coefficient of the planar tunneling barrier in the WKB approximation is given by [107]:

$$T(E, V, z) \propto \exp\left(-2z \sqrt{\frac{2m}{\hbar^2} \left(\Phi + \frac{eV}{2} - E_{\perp}\right)}\right) \quad (1.7)$$

For a free-electron gas  $E_{\perp} = E - E_{||} = E - \frac{\hbar^2 k_{||}^2}{2m}$ . Therefore electrons with a larger value of parallel momentum,  $k_{||}$ , experience a higher tunneling barrier and contribute less to the tunneling current. Going back to Fig.1.13 it is clear that on Au(111) surface there are no available states with  $k_{||} = \mathbf{0}$  above Fermi level due to the L-gap. At any electron energy above -0.5 V and below ~2.0V, the surface state band has the lowest values of  $k_{||}$  and will therefore dominate tunneling conductance. The largest fraction of the tunneling conductance due to the surface state is ~64% at the onset of the surface-state band ( $k_{||} = \mathbf{0}, E = -500 \text{ mV}$ ) [128]. At electron energies exceeding 2.0V, the surface state crosses with the bulk-states becoming a surface resonance. Since the probability amplitude of the surface resonance is still relatively large on the surface, it continues to be an efficient tunneling channel. The requirement for the finite value of parallel momentum also explains why the trajectories of tunneling electrons injected into the bulk states on Au(111) always form a hollow cone with an angle of ~30° off-normal [131, 132].

### 1.4.3 Lifetimes of excited states

An electron in a conducting medium is characterized by two length-scales (and correspondingly two time-scales): momentum-relaxation length (elastic mean-free path) and energy-relaxation length (inelastic mean-free path) [133]. Mean-free path determines how far an electron travels before its momentum (energy) is changed. On clean metal surfaces there are two main sources of energy relaxation of a hot-electron (electron with energy above Fermi level): electron-electron and electron-phonon scattering. Electron-electron scattering occurs because the electron charge of the excess electron is screened by the Fermi-sea of the metal creating a fluctuating Coulomb potential which ultimately results in inelastic electron scattering with a creation of an electron-hole pair. The hot-electron lifetime due to electron-electron scattering is well described in many cases by the Fermi-liquid theory [108]:

$$\tau_{e-e}(E) \mu \left( \frac{E_0}{E - E_F} \right)^2 \quad (1.8)$$

$E_0$  is the Fermi energy and  $n$  – electron density. In short, the lifetime drops off quadratically with energy of the hot-electron. This dependency is valid only for energies much smaller than  $E_0$ .

The relaxation time of hot-electrons due to electron-phonon interactions is given by the Debye model, which for  $k_B T \gg \hbar \omega_D$  (**the Debye energy**) [134]:

$$\frac{\hbar}{\tau_{e-ph}(E_F, T)} = 2\pi\lambda k_B T \quad (1.9)$$

The electron-electron and electron-phonon relaxation times are compared in Fig. 1.16 for a Cu surface. At 5K, which is the temperature where most STM experiments from this thesis were carried out, the electron-phonon interaction dominates the lifetime of hot-electrons below  $\sim 0.5$  eV, while above 1 eV the relaxation due to electron-electron interaction is much faster.

In this work, hot-electrons injected from the STM-tip into the metal surface are found to transport on the surface and cause chemical reactions of adsorbed molecules in the range of up to 100 nm (Chapter 12). The adsorbate molecules are certainly an additional source of hot-electron relaxation, both elastic and inelastic (the evidence for the latter are chemical reactions). For

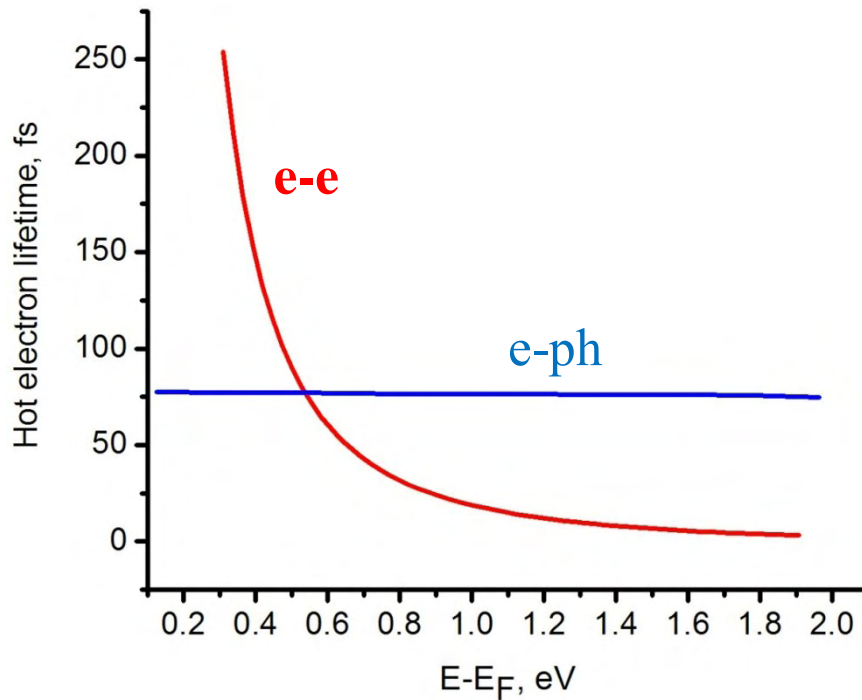


**Figure 1.16.** Electron-electron (red line) and electron-phonon (blue line) lifetimes on Cu(111) at  $T = 5\text{K}$  as function of energy within the Fermi-liquid theory and the Debye-model respectively ( $t_0=0.46$  fs,  $E_0 = 7$  eV,  $\omega_D = 27$  meV,  $\lambda=0.15$ ) [127].

reference, the group velocity of hot-electrons in the surface resonance on Au(111) is 1.7 nm/fs at the energy of 1.8 eV above Fermi level. Assuming the hot-electron lifetime of 10 fs due to electron-electron scattering, a hot-electron will travel a distance of 18 nm if the transport is ballistic (elastic mean-free path much longer than inelastic mean-free path).

## 2.0 EXPERIMENTAL

### 2.1 SCANNING TUNNELING MICROSCOPY

The phenomenon of quantum-mechanical tunneling has been known for more than seventy years. The earliest observation of electron tunneling was done by Esaki [135] in p-n junctions and by Giaever in planar metal-oxide-metal junctions [136]. The first observation of metal-vacuum-metal tunneling was reported by Young et. al in 1971 [137] using a device called a topographiner, which closely resembled the generic design of a scanning tunneling microscope. However, due to poor vibrational isolation, the topographiner had a limited vertical resolution of 3 nm and lateral resolution of 400 nm. The scanning tunneling microscope was demonstrated by Binnig and Rohrer in 1981 [1], when the authors obtained a topographical image of the Au(100) surface with a vertical resolution of  $\sim 0.02$  nm.

The principle of STM operation is strikingly simple. If a sharp tip (usually made of W or Pt-Ir) is brought to within 5 – 10 Å from the surface and a small voltage is applied between the tip and the conducting sample, the current of tunneling electrons will flow through the junction (Fig. 2.1). Tunneling current is used to probe the physical properties of the surface on the subatomic scale, as well as to control tip-surface distance. The tip can be scanned laterally over the surface while keeping the tunneling current constant and recording the vertical tip displacement (constant current mode). Alternatively one can keep the tip-sample distance constant and map out the tunneling current (constant distance or constant-z mode).

In contrast, the theoretical description of STM is rather complicated. The complexity arises due to the need to join macroscopic and microscopic physical concepts in the correct description of the STM junction. The macroscopic description applies to the sample and the tip electrodes, while the microscopic analysis is required for the atomic structure of the tip apex and

the peculiarities of the local surface states, as well as the dynamic electronic effects that occur when the tunneling junction is formed.

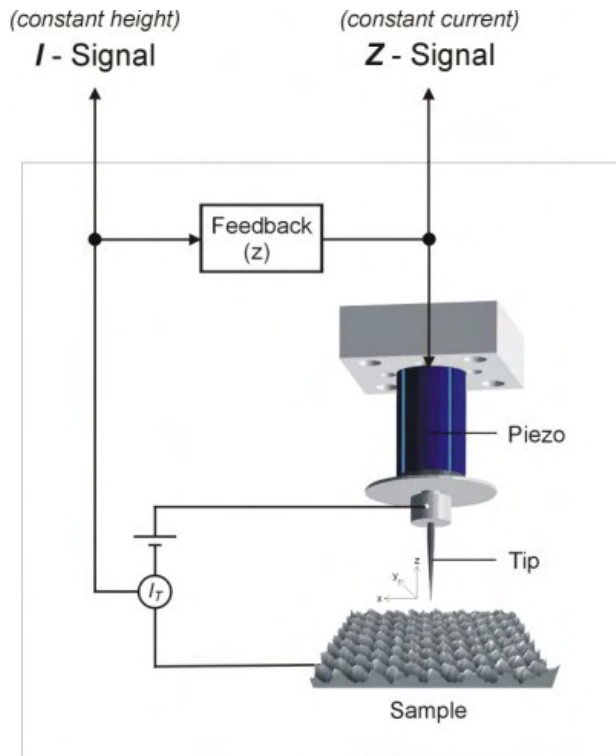


**Figure 2.1.** Principal components of the scanning tunneling microscope. Voltage applied between a sharp-metal tip and a conducting sample will drive tunneling current across the 5-8 Å wide vacuum gap. The tip is positioned with sub-angstrom accuracy using piezo-electric scanners.

The simplest description of the energy levels in the tunneling junction is the rectangular tunnel-barrier model. The formation of the tunnel-barrier between the tip and the surface is schematically shown in Fig. 2.2. The local density of electronic states (LDOS) on the sample surface is structured, while the LDOS of the tip is assumed to be constant. The energy bands of tip and sample are filled with electrons up to the Fermi energies  $E_{Ft}$  and  $E_{Fs}$ , respectively. The difference between the vacuum energy levels and the Fermi levels are the work functions  $\Phi_t$  and  $\Phi_s$ . When the tip and the sample are separated, the vacuum energy levels  $E_{Vac}$  are the same (Fig. 2.2a). Upon approach, the wavefunctions of the tip partially overlap with the surface states. The Fermi levels  $E_{Fs} =$  and  $E_{Ft}$  are adjusted to each other by charge transfer, which forms the rectangular potential barrier in the junction with the average height of  $\frac{\Phi_t + \Phi_s}{2}$  (Fig. 2.2b). When a

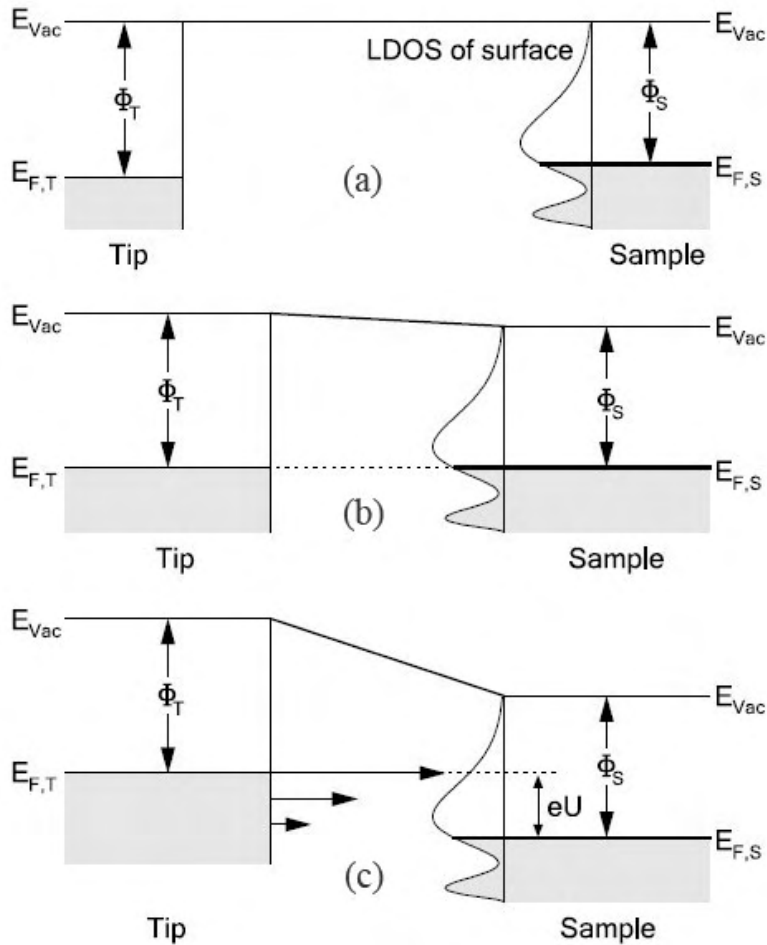


**Figure 2.2.** Formation of a rectangular tunnel-barrier in STM upon tip-approach: (a) tip and sample are infinitely far away; (b) tip-sample distance is 5-8 Å allowing electron tunneling; (c) tunneling junction under positive applied sample bias ( $U$ ). (Adapted from [138])

positive voltage  $U$  is applied between tip and sample, the electrons tunnel from the occupied states of the tip to the unoccupied states of the sample (Fig. 2.2c). Due to the energy-dependence of the transmission coefficient  $T$ , tunneling current is dominated by electrons from the Fermi level of the tip for positive sample bias (the current flows from tip to surface) and electrons from the Fermi-level of the surface for negative sample bias.

The key to the ultimate resolution of the STM is the exponential dependence of the tunneling current on tip-sample separation. Consider an electron with kinetic energy  $|E|$  that impinges onto a potential barrier of width  $W$  and height  $U$ , with  $|U| > |E|$ . The wavefunction of the electron in the classically forbidden barrier region is exponentially decaying with distance  $z$ :

$$\Psi_n(z) = \Psi_n(0)e^{-\kappa z}, \quad \kappa = \frac{\sqrt{2m(U-E)}}{\hbar} \quad (2.1)$$

The probability of the electron to be on the other side of the barrier is proportional to  $|\Psi_n(W)|^2$ . In the first approximation, tunneling current is proportional to the probability of all electrons within the  $eU$  energy window (Fig. 2.2) to tunnel across the barrier [107]:

$$I \propto \sum_{E_n=E_f-eV}^{E_f} |\Psi_n(0)|^2 e^{-2\kappa W} \quad (2.2)$$

The decay constant  $\kappa$  is  $\sim 1.0 \text{ \AA}^{-1}$ , which corresponds to about 7-fold decrease of the tunneling for an additional  $1 \text{ \AA}$  of the tip-surface separation. Therefore minor variations of the surface topography yield pronounced and measurable changes of the tunneling current which made the STM the first instrument to achieve atomic lateral resolution in surface imaging.

The first successful theory of STM was based on a modified method of Bardeen [139], using first-order time-dependent perturbation theory. Tunneling current is given by

$$I = \frac{2\pi e}{\hbar} \sum_{\mu, \nu} [f_s(E_\mu - eV)][1 - f_t(E_\nu)] |M_{\mu\nu}|^2 \delta(E_\mu - E_\nu) \quad (2.3)$$

where indices  $s$  and  $t$  correspond to the sample and the tip,  $f$  is the Fermi-Dirac distribution function, and  $M_{\mu\nu}$  is a tunneling matrix element between states  $\chi_\nu$  of the tip and  $\psi_\mu$  of the sample. The delta function accounts for the condition of elastic tunneling.

In the limit of low bias (so that the density of electronic states on the tip and the sample is roughly constant in the tunneling energy window of width  $eU$ , Fig. 2.2) and zero temperature (the Fermi distribution becomes a step function) the expression simplifies to

$$I = \frac{2\pi e^2}{\hbar} V \sum_{\mu, \nu} |M_{\mu\nu}|^2 \delta(E_\mu - E_f) \delta(E_\mu - E_f) \quad (2.4)$$

The tunneling matrix element is the central term in the equation:

$$M_{\mu\nu} = -\frac{\hbar^2}{2m} \int_{\Sigma} (\chi_\nu^* \nabla \psi_\mu - \psi_\mu \nabla \chi_\nu^*) \cdot dS \quad (2.5)$$

It is evaluated on the separation surface between the tip and the sample, which completely encompasses the tip body. The physical meaning of the matrix element is the energy lowering due to the overlap of the two states.

The most widely used implementation of this approach is the Tersoff-Hamann theory [140, 141], where the tip state is assumed to have spherical symmetry and the vacuum tail of this state beyond the separation surface is given by the spherical modified Bessel function:

$$C \frac{1}{\kappa r} e^{-\kappa r} \quad (2.6)$$

In this approximation the matrix element (Eq. 2.5) becomes proportional to the value of the sample wavefunction at the center of the tip apex. Hence,

$$I = Const * R^2 e^{2\kappa R} \sum_{\nu} |\Psi_{\nu}(0)|^2 \delta(E_{\nu} - E_f) \quad (2.7)$$

$R$  = the radius of curvature of the s-wave tip. In other words, the tunneling current follows the density of sample states at the Fermi level in the center of the curvature of the tip.

Tersoff-Hamann theory suffers from several approximations: a low-bias limit, a spherically symmetric tip, and non-self-consistent tip and sample states. In addition, the choice of the tip-sample separation is often arbitrary. However, the method is still a workhorse for the theoretical STM, and many popular ab-initio codes allow quick estimation of the STM image in this approximation. Calculated STM images presented in this thesis were obtained using the Tersoff-Hamann approach implemented in the p4VASP code ([http://cms.mpi.univie.ac.at/odubay/p4vasp\\_site](http://cms.mpi.univie.ac.at/odubay/p4vasp_site)).

A more rigorous description, which is inherently non-pertubative, can be derived from Keldysh's theory of non-equilibrium processes [142]. The STM junction is described by a certain number of independent ideal one-dimensional conductors, which are referred to as channels (each described by the quantum state,  $u_{\alpha}$ ). Electrons propagate through these channels without dissipation from the reservoirs to their respective surfaces, and vice versa. When the propagating electrons (both from the sample and the tip bulk volumes) scatter on the tunneling junction, they have a certain probability of forward scattering, i.e. transmission through the junction. The transmission probability matrix element is given by:

$$\mathcal{T}_{m',m}^{\pm}(E) = |\langle u_{\alpha'}^{\pm m'}(E) | \mathcal{S}^{\pm}(E) | u_{\alpha}^{\pm m}(E) \rangle|^2 \frac{v_{\alpha'}^{m'}}{v_{\alpha}^m} \quad (2.8)$$

$u_a$  is the group velocity of electrons in state  $u_a$ ; the plus and minus signs determine the direction of propagation; and  $S$  is the scattering matrix in the channel basis. The tunneling current is given by the generalized multichannel Landauer-Buttiker formula [143]:

$$I(V) = \frac{e}{\pi\hbar} \int_0^{-eV} dE \sum_{mm'} \mathcal{T}_{m',m}^{\pm}(E + \mu_s) \quad (2.9)$$

$\mu_s$  is the chemical potential of the sample. Its presence and the integration limits mean that the transmission matrix elements are integrated over tip and sample states only in the energy window defined by the applied external bias.

All the physics of tunneling is therefore included in the scattering matrix, which must be evaluated to derive the transmission matrix. The scattering matrix can be solved using the non-equilibrium Green's function formalism [143]. The most common quantum description of both the tip and sample is provided by the tight-binding approximation, using extended-Huckel Hamiltonian. The important difference between the scattering and the perturbative approach, is a straight-forward inclusion of the finite bias in the former. Using this approach, a number of successful predictions of STM images of surface reconstructions, adsorbates and sub-surface impurities have been made [144-147].

## 2.2 MEASUREMENT MODES IN SCANNING TUNNELING MICROSCOPY

Various instrumental modes of the STM are best discussed in terms of equations for a particle tunneling across a rectangular barrier (Fig 2.2). The expression for the tunneling current is:

$$I = \frac{2\pi e}{\hbar} \left(\frac{\hbar^2}{2m}\right)^2 \int_{-\infty}^{\infty} T(E, V, z) (f_t(E - eV) - f_s(E)) \rho_t(E + eV) \rho_s(E) dE \quad (2.10)$$

where  $T(E, V, z)$  is the transmission coefficient, which is commonly expressed in the WKB approximation:

$$T(E, V, z) \propto \exp\left(-2z \sqrt{\frac{2m}{\hbar^2} \left(\Phi + \frac{eV}{2} - E_{\perp}\right)}\right) \quad (2.11)$$

$\Phi$  is the average workfunction of the two electrodes;  $E_{\perp}$  is the component of electron kinetic energy in the tunneling direction. Therefore, the tunneling current depends on the height (and shape) of the potential barrier as well as the density of states of the sample and the STM-tip. Again, assuming a low-temperature limit, the difference of the Fermi occupation functions will either be unity (between  $E_f$  of the sample and  $E_f + eU$  of the tip, Fig. 2.2) or zero. Furthermore, the density of states of the tip is often assumed to be constant (in reality tip states often observed to influence STM images and tunneling spectra). Equation 2.10 then simplifies to

$$I \propto \int_{E_f}^{E_f + eV} \rho_s(E) T(E, V, z) dE \quad (2.12)$$

### 2.2.1 Topographic imaging

STM is mostly recognized in the world due to its ability to produce astonishing atomically resolved images of crystalline surfaces, molecules and nanoscale objects. The basic principle of topographic imaging is shown in Fig. 2.3. The tip is rastered over the surface by x- and y- piezo-drivers and tunneling current between the tip and the sample is measured at each point of the raster. In the *constant current* mode, the tip is also moved in the z-direction to maintain constant current throughout the scan. The z-coordinate is recorded as a function of x- and y- to produce a classic STM image. The electronic unit responsible for maintaining constant current is called the *feedback loop*. Alternatively the tunneling current is recorded as a function of tip position keeping the tip at a constant height (or more exactly maintain constant z, with the feedback loop open). This mode of topographic imaging is called *constant height imaging*. Constant-height images can be obtained much faster because the tip does not have to be displaced along the z-direction. However, there is always a risk of crashing the tip into a tall feature on the surface.

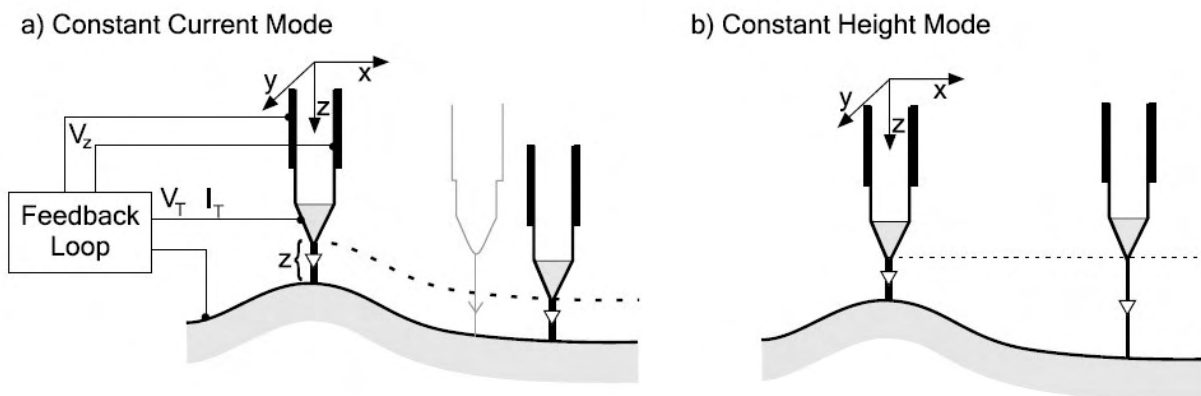


**Figure 2.3.** Two modes topographic imaging by STM. a) Constant current mode: while scanning the tip over the surface in the  $x$ - and  $y$ -direction, the height  $z$  of the tip is adjusted by the feedback loop to keep the current constant. b) Constant height mode: the height of the tip is kept constant while scanning the tip.

In both imaging modes the signal comes from the exponential dependence of the tunneling current on the distance to the surface (or surface features, such as steps, molecules etc.). Eq. 2.12 shows that the “topographic” measurement in STM is, in fact, imaging of the local variation of the density of states on the sample. Therefore, the STM images yield purely topographic information only when the all the objects in the image are electronically identical. This is the case for a single atomic step on the surface, because both upper and lower terrace are the same material. In general, however, the STM image is a convolution of topographic and electronic information Lang [148, 149]. For example, adatoms on the surface can appear in STM images as protrusion, depressions [150] or may even remain unnoticed [149] depending on their electronic configuration.

### 2.2.2 Electronic spectroscopy in STM

Spectroscopic information is obtained from the dependence of the tunneling current on the tip-sample voltage ( $I$ - $V$  curves).  $I$ - $V$  curves and their derivatives are obtained by positioning the STM-tip above a chosen point on the surface and ramping the voltage in a given range while recording the tunneling current and (sometimes) its derivative. The tip-sample separation is maintained constant during the voltage ramp.

### Scanning Tunneling Spectroscopy ( $dI/dV$ )

The first derivative of the WKB-expression for the tunneling current (Eq. 2.12) is

$$\begin{aligned} \frac{dI}{dV} = e \frac{dI}{dE} \propto e \rho_s(V) T(eV + E_f, V, z) + \int_{E_f}^{E_f + eV} \rho_s(E) \frac{dT(E, V, z)}{dV} dE \\ + \int_{E_f}^{E_f + eV} \rho_s(E) \frac{dT(E, V, z)}{dz} \frac{dz}{dV} dE \end{aligned} \quad (2.13)$$

The last term in the equation equals zero, because the tip-sample separation is constant. The transmission coefficient is a smooth function of voltage. The remaining integral term (second term in the equation) will then produce only a gradually varying background in the STS spectra. This term is often neglected. Also, the variation of the transmission coefficient does not change the position of peaks produced by sharp variations of the DOS ( $\rho_s(E)$ ). Therefore the derivative signal is well-approximated by  $e \rho_s(V) T(eV + E_f, V, z)$ , which makes it directly proportional to the local density of states of the surface (or a surface object). Typically, peaks in STS curves correspond to the electronic states of the surface or the adsorbed object. Despite the unknown shape and composition of the STM tip, STS is routinely used to measure the electronic structure of surfaces and adsorbates on metals and semiconductors. STS can also yield the spatial distribution of the electronic state (e.g. a molecular orbital of an adsorbate [151]) and its lifetime [121].

Substantial noise reduction in STS measurements is commonly achieved by using modulation (lock-in) techniques. An AC voltage  $\Delta V = V_L \cos(\omega_L t)$  with a small amplitude  $U_L$  ( $\sim 20$  mV) and frequency  $\omega_L$  is added to the tunneling voltage. The modulation period is typically chosen to be much larger than the response time of the feedback loop, to assure constant-current condition of the tunneling junction. The effect of the small AC voltage on the tunneling current is seen by expanding the tunneling current in the Taylor series:

$$\begin{aligned} I(V + \Delta V) &= I(V) + \frac{dI(V)}{dV} \Delta V + \frac{1}{2} \frac{d^2 I(V)}{dV^2} (\Delta V)^2 + \dots \\ &= I(V) + \frac{dI(V)}{dV} V_L \cos(\omega_L t) + \frac{1}{2} \frac{d^2 I(V)}{dV^2} (V_L \cos(\omega_L t))^2 + \dots \end{aligned} \quad (2.14)$$

The signal is detected by a lock-in amplifier. When it is tuned to the first harmonic of the signal, the output of the amplifier is directly proportional to  $\frac{dI(U)}{dU}$ . The advantage of the lock-in amplifier is a substantial narrowing of the measurement bandwidth around the chosen modulation frequency, which dramatically reduces electronic (and other) noises inherent in the system. The second harmonic measurement yields  $\frac{d^2I(U)}{dU^2}$ , which is proportional to the probability of inelastic scattering of tunneling electrons in the junction, in particular due to vibrational excitation of adsorbed molecules. Second-harmonic STS can therefore be used as the single-molecule vibrational spectroscopy [11].

#### *Distance-voltage Spectroscopy (dz/dV)*

It is possible to do STS with the feedback loop engaged during the voltage ramp. In this case, the STM tip will retract away from the surface to maintain constant current. From Eq. 2.12 (neglecting the second term), STS signal at constant current is given by:

$$\begin{aligned} \frac{dI}{dV} &= e \frac{dI}{dE} \propto e \rho_s(V) T(eV + E_f, V, z) + \int_{E_f}^{E_f+eV} \rho_s(E) \frac{dT(E, V, z)}{dz} \frac{dz}{dV} dE & (2.15) \\ &= e \rho_s(V) T(eV + E_f, V, z) + \frac{dz}{dV} \int_{E_f}^{E_f+eV} k \rho_s(E) T(E, V, z) dE \\ k &= -2 \sqrt{\frac{2m}{\hbar^2} \left( \Phi + \frac{eV}{2} - E_{\perp} \right)} \end{aligned}$$

The STS spectrum at constant current will then be dominated by the second term in Eq. 2.15, because  $\frac{dz}{dV}$  is a large value when the tunneling voltage approaches a state with high spectral density in the vacuum gap. Such states are usually image-potential states or quantum well states [152, 153], but even molecular orbitals can be seen [154]. The retraction coordinate (z) exhibits a series of large steps (Fig. 2.4) while dI/dV signal yields a corresponding set of peaks.

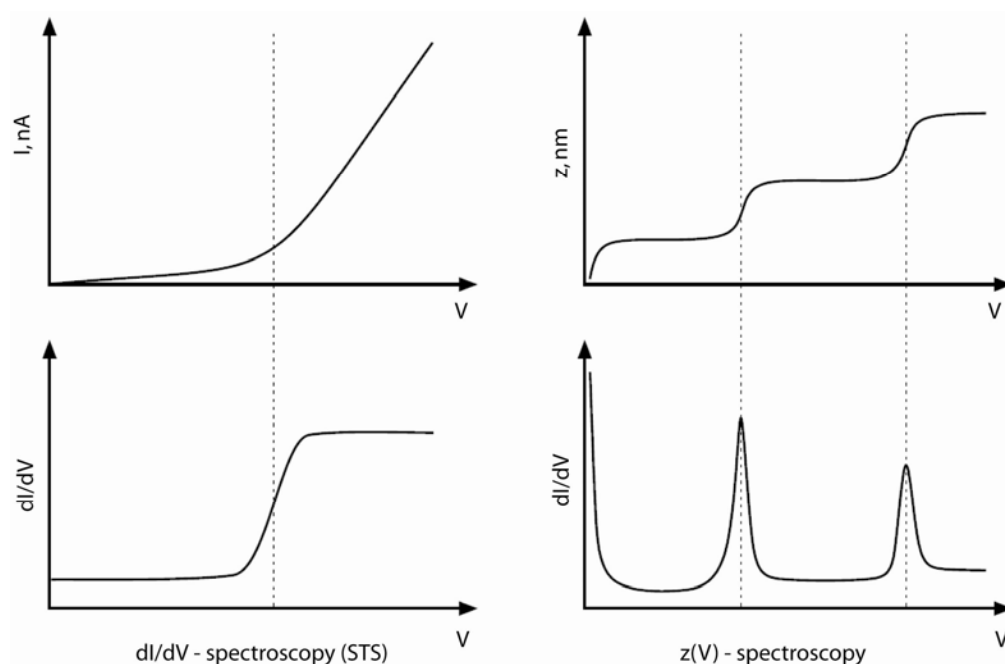


**Figure 2.4.** Scanning tunneling (left) and distance-voltage (right) spectroscopy. The spectroscopic measurement in both cases is accomplished by recording the first harmonic of the lock-in amplifier ( $dI/dV$ ) during a ramp of tunneling voltage. The feedback loop is off in STS and on in  $z(V)$ -spectroscopy.

The major advantages of the distance-voltage spectroscopy is a significantly broader voltage range of the measurement (without saturation of the current preamplifier) and the ability to minimize the tunneling current to a few pA preventing surface damage at high voltage. However, not all molecular or adsorbate states have a high density in the vacuum gap. For example, Shockley surface states are easily detectable in STS but are not observed in the  $dz/dv$  spectra.

### 2.3 AUGER ELECTRON SPECTROSCOPY

Auger Electron Spectroscopy (AES) is an analytical technique used to determine the elemental composition and, in some cases, the valence state of the atoms in the surface region. An AES spectrum is a plot of the number of electrons emitted from the sample in the Auger transition process versus electron energy.

Auger electron emission is initiated when a high-energy electron (2-10 keV) strikes the atom and creates a core-shell vacancy. The Auger transition (Fig 2.5) is the relaxation of the excited ion with a core hole, during which an electron from a higher lying level fills the inner shell vacancy with simultaneous energy-conserving emission of an Auger electron from another higher level. Simultaneous Coulomb rearrangement of two electrons results in a final state with two vacancies (Fig. 2.5).

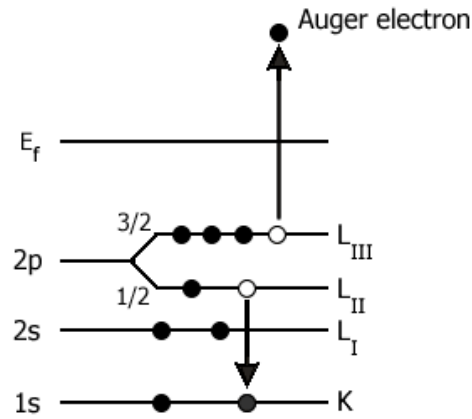


**Figure 2.5.** Schematic energy diagram of the final state of the  $KL_{II}L_{III}$  Auger transition.

The kinetic energy of an Auger electron is equal to the energy difference of the singly ionized initial state and the doubly ionized final state. For example, the energy of the transition in Fig. 2.5 for an atom of atomic number  $z$  can be written as

$$E_{KLL}(z) = E_K(z) - E_{L_{II}}(z) - E_{L_{III}}^*(z) - \varphi_s \quad (2.16)$$

where  $E_i$  is the binding energy of level  $i$  for a neutral atom measured with respect to the Fermi level  $E_f$ ;  $\varphi_s$  is the spectrometer work function. The star in  $E_{L_{III}}^*$  is the binding energy in the presence of the core hole, i.e. it is greater than for the corresponding energy in a neutral atom.

A more rigorous treatment of the Auger energy requires inclusion of terms corresponding to hole-hole repulsion and intra- and extra-atomic relaxations. The intensity of Auger peaks is given by the following transition matrix element:

$$\frac{2\cdot\pi}{h} \left[ \int \int \Psi_f^*(r_1) \Psi_f(r_2) V \Psi_i^*(r_1) \Psi_i(r_2) dr_1 dr_2 \right] \quad (2.17)$$

where  $\Psi_i$  represent the initial state wave functions of the two electrons in an atom with an initial core vacancy, and  $\Psi_f$  are the wave functions of the final state the electrons. The coupling potential  $V$  is the Coulomb operator.

The Auger transition peaks mostly have small intensity, which is comparable to the intensity of the background of secondary electrons. That is why the experimental procedure for recording the Auger spectrum is to take a first derivative of the current emitted from the sample via a lock-in technique. A typical Auger spectrum of a clean Cu(111) surface is shown in Fig. 2.6. The surface sensitivity of AES is determined by the escape depth of electrons from the surface. The escape depth is <5 nm, which makes the technique so valuable for surface science. The detection limit of AES is ~0.1 at. %.

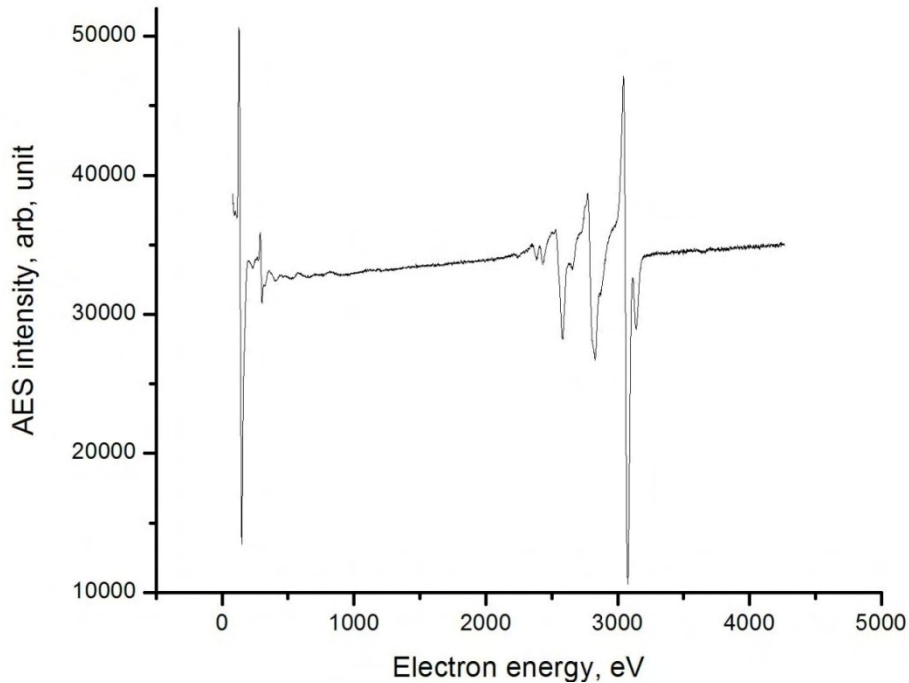


**Figure 2.6.** Derivative AES spectrum of Cu(110) surface obtained after 1 hr of Ar sputtering and 20 min annealing at 800 K.

## 2.4 ULTRA-HIGH VACUUM CHAMBER

The bulk of the experimental work presented in this thesis was done using a commercial UHV low-temperature STM from Omicron Nanotechnology (LT-STM/XA). The schematic of the apparatus is shown in Fig 2.7. The UHV chamber consists of two parts – the STM chamber and the preparation chamber. A fast-entry lock is attached to the preparation chamber. The system is mounted on a stainless-steel table, which can be suspended by three pneumatic supports from *Integrated Dynamics Engineering*. Pneumatic suspension is one of three types of vibrational isolation of the low-temperature STM. The LT-STM and the preparation chamber are each equipped with a triode ion-pump by *Varian Inc.* and a titanium-sublimation booster pump. The preparation chamber also has a turbomolecular pump from *Pfeiffer*, which is used for initial pump-down, bake-out and  $\text{Ar}^+$  sputtering of the metal surfaces. The turbo-pump, which is an active source of vibrations, is off during STM measurements. Due to an excellent conductance and pumping capability, the base-pressure at room temperature is  $<5 \cdot 10^{-11}$  in the LT-STM chamber and  $5 \cdot 10^{-10}$  in the preparation chamber. When the LT-STM is cooled with liquid nitrogen and liquid helium, the base pressure in the chamber decreases to a value that is below the sensitivity of a standard ion-gauge. The LT-STM chamber is separated from the preparation chamber by a well 0.5 m long/5 cm in diameter and a 2 3/4" viton-sealed gate-valve (VAT). The well has a small pneumatic conductance which provides poor pumping speed. While the latter is disadvantageous during system bakeout, the well prevents relatively poor pressure in the preparation chamber from deterring the excellent UHV conditions in the STM chamber during normal operation.

All the manipulators and the 6-slot carousel in the system are adapted for the standard Omicron sample holder, which is a 1 cm thick Ta plate with a small eye used for sample transfer. Metal crystals are mounted on the sample holder by two Ta wires (0.1 mm thick running through the slots in the crystal. The wires are spot-welded to the Ta plate. This mounting provides very good electrical and thermal contact, therefore allowing fast cool-down of the crystal. The sample is introduced from air into the preparation chamber via the fast entry-lock, which is pumped by the main turbo-pump. It can then be placed into the XYZ-manipulator (*Vacuum Generators*) in the prep-chamber or into one of the slots of the carousel located in the STM-chamber. The

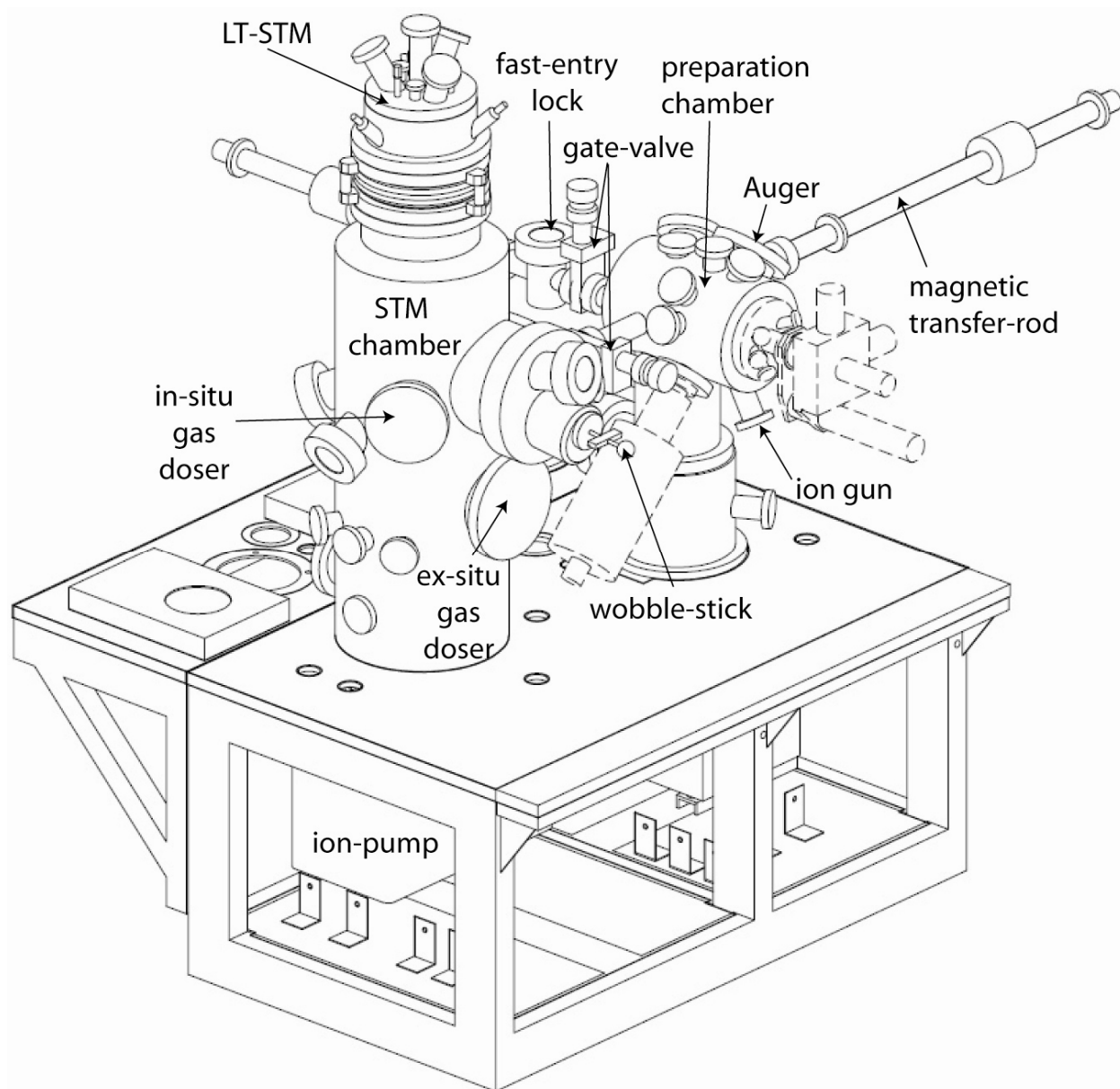


**Figure 2.7.** Overview of the Omicron LT-STM apparatus.

wobble-stick in the STM chamber is used to extract the sample from the carousel and insert it into the STM stage. The only cryo-cooled sample position in the chamber is the STM-stage. Two in-situ gas-dosers were designed and attached to the STM chamber to allow dosing of molecules onto cold surfaces at a minimum temperature of 10 K. Most of the molecules studied here did not chemically react on the metal surfaces at  $T < 90$  K, which made many interesting experiments possible. Among other home-built parts attached to the commercial chamber are the retractable STM-tip preparation manipulator, retractable room-temperature gas-doser in the preparation

chamber and a high-vacuum gas-line (base pressure < 1mTorr) for dosing up to five different gases through in-situ and ex-situ dosers.

### 2.4.1 Preparation chamber

The preparation chamber provides the capabilities of Ar sputtering and annealing of single crystals, AES, STM-tip preparation by electron-bombardment, and ex-situ dosing of non-volatile molecules (such as benzoic acid and C<sub>60</sub>) on the crystal surfaces at 300 K. The sample is translated in a modified XYZ manipulator (originally by Vacuum Generators). Sample transfer in and out of the preparation chamber is carried out using magnetic transfer-rods with a turn-and-lock mechanism designed for Omicron sample holders. The main turbo-pump and the load-lock are also connected to the preparation chamber. The focusable ion-gun and the Auger spectrometer are both commercial instruments from Omicron Nanotechnology. Ar sputtering was typically done at the Ar pressure of  $2 \times 10^{-6}$  Torr, ion-energy of 1 kV and ion-current of 3  $\mu$ A measured at the sample holder. The beam-diameter of the ion-gun was adjusted to  $\sim 2$  cm to assure uniform sputtering (maximum dimensions of metal crystals used here were 2x8 mm). Ar<sup>+</sup> sputtering was also used to form hexagonal nanopits on the Au(111) surface. The surface was first sputtered for 15 minutes, then heated to  $\sim 800$  K. Upon cooldown, the surface was sputtered for 0.5-2 more minutes at an ion current of 0.2  $\mu$ A and a surface temperature of 400-500 K. Under these conditions sputtering proceeds via a layer-by-layer mechanism, where vacancies created by sputtering diffuse on the surface and coalesce into one-atom-deep pits. The pit coverage, pit size and pit depth could be reasonably well controlled by adjusting sputtering conditions. Equilibrium pits have a symmetric hexagonal shape due to energy equivalence of A and B  $\langle \bar{1}10 \rangle$ -oriented steps of the Au(111) surface.

All Omicron STMs are designed for quick tip-exchange without breaking vacuum. This is especially valuable for the Low-Temperature STM, where chamber bake-out and cool-down take about a week. The tips (W-wire) are mounted in cylindrical tip-holders that are compatible with the STM-scanner. The apex of the STM scanner contains a magnet that holds the tip in place. Outside the STM, the tip is stored in a modified sample-holder that is also used to transport the tip inside the chamber. STM-tips were etched from a 0.1 mm tungsten wire using a

custom-built tip-etching apparatus. The procedure for ex-situ and in-situ tip preparation is described in Sec. 2.8.

### 2.4.2 LT-STM chamber

The STM chamber is coupled to the preparation chamber by a  $1\frac{3}{8}$ " diameter tube, through which the samples and tips are transferred from the preparation chamber. The rotatable carousel with six slots for tip and sample holders is located at the end of the well in the STM chamber. The samples are inserted into the carousel from the preparation chamber using the magnetic transfer rod.

The STM with the cryostat and all electrical wiring is mounted on a single 12" flange. The cryostat consists of the outer cryostat that holds 15 l of liquid nitrogen and the inner cryostat that holds either 4 l of liquid helium or 4 l of liquid nitrogen. The wiring (36 wires total) runs through three holes between the nitrogen and helium cryostats and are firmly attached to helium-cooled walls. Gold covered rotatable radiation shields are firmly attached to the bottom the cryostat. The inner shield (attached to the helium cryostat) has a rotatable door to access the STM; the shield itself is not-rotatable because it holds 12 magnets for the eddy-current vibrational damping of the STM stage.

The STM-stage is shown in Fig. 2.8. The sample is inserted facing down into the grounded molybdenum springs. The segmented piezo-electric tube scanner is mounted on a slip-stick z-slider for coarse-motion. Coarse positioning of the scanner (accuracy of  $\sim 50$  nm) is achieved by slip-stick motion of the z-slider and the slip-stick motion of the x-y table, which holds the scanner assembly. The range of the x-y coarse motion is  $\sim 8$  mm, while that of z coarse motion is 1 cm. The fine x-y-z motion (for scanning in STM) achieved by biasing the piezo-electric tube with up to 150V providing the range of  $\sim 1\mu\text{m}$  at 5K. The coarse-approach of the tip to the sample surface is monitored by a CCD-camera outside the chamber through one of three double-windows in the cryo-shields of the STM.

One of the big advantages of the LT-STM for surface-chemistry studies is the ability to freeze adsorbates in the weakly-bound precursor states on the surface. The mechanism of thermal chemistry can then be studied by gently heating the crystal while observing changes on the

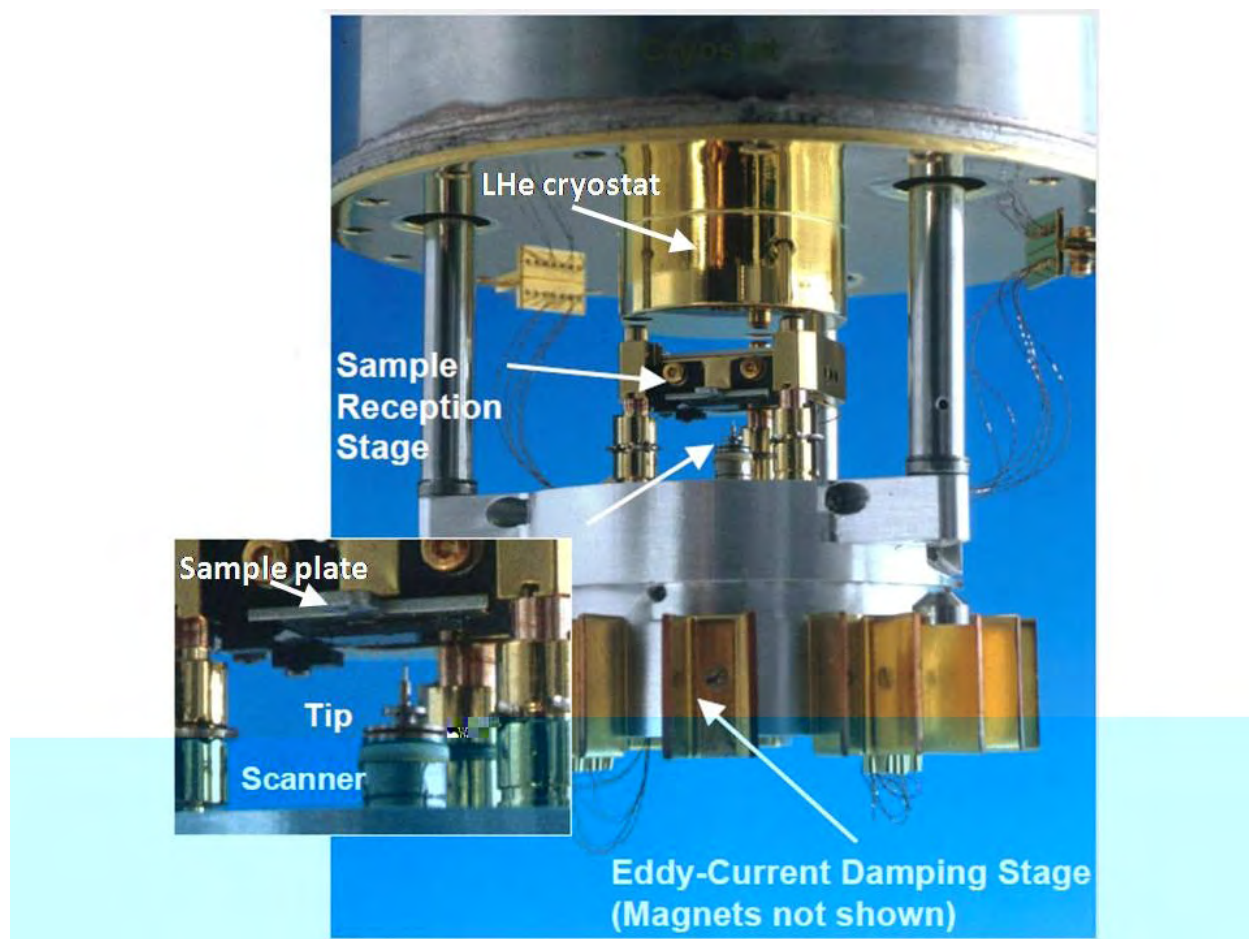


**Figure 2.8.** Bare STM stage of the Omicron LT-STM (without cryoshields) in the suspended position ready for scanning.

surface in real-time. To accomplish this goal, the adsorbates must be dosed onto a cold surface, which requires an in-situ gas-doser. Two such dosers were built.

The first doser is a retractable 0.25" stainless-steel tube bent and attached to a leak-valve at one of the 6" ports (Fig. 2.7, position: in-situ doser) on the LT-STM chamber. The leak-valve is mounted on two linear micro-positioners at a 90° angle allowing for two-dimensional translation of the doser. The doser is introduced into the cryo-shielded area toward the STM-stage through the same port that is used for tip- and sample-exchange. First, the doser is positioned at the center of the port by 1.5" translation. Then it is inserted by 4" toward the STM-stage, crossing the external and internal cryo-shields. The distance from the doser hole to the crystal surface during gas-dosing is several inches. The flux of gas from an external gas-line is regulated using a leak-valve. Since both cryo-shields are open during dosing, the sample temperature rises to 10K

as measured by the silicon-diode in the sample stage (the true temperature is likely to be slightly higher than 10K).

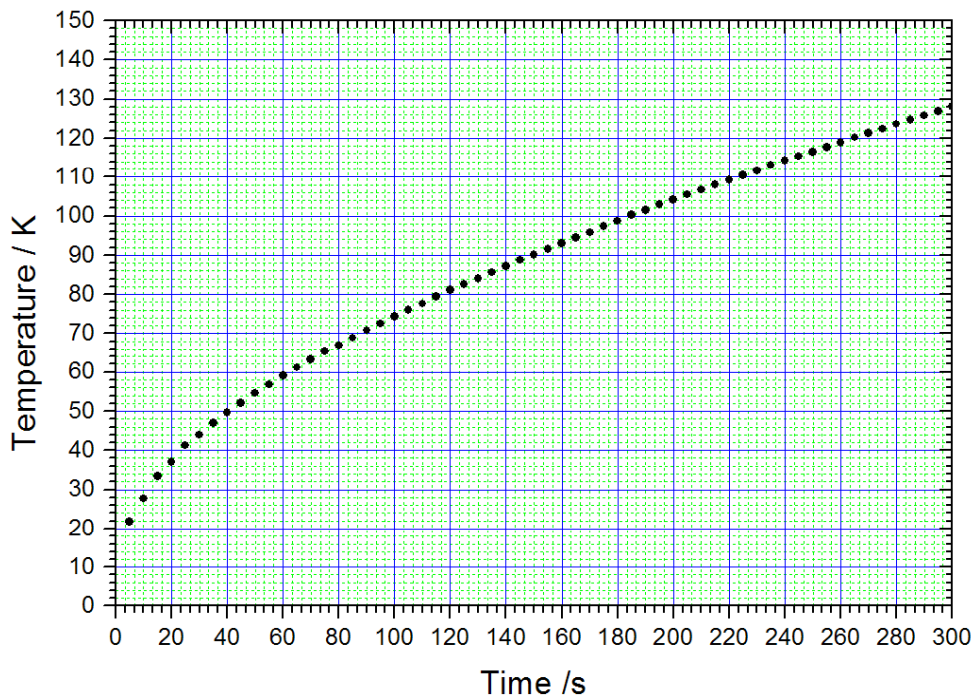


**Figure 2.9.** Temperature calibration for heating a Cu crystal in a wobble-stick after the crystal is extracted from the 5K-STM stage. During this measurement the K-type thermocouple was attached to the surface of the crystal mounted on a standard tantalum sample holder [155].

In addition, a tungsten-wire heater was mounted in the middle of the doser tube. The purpose of the heater is to raise the temperature of the doser tube (to a maximum of 100°C) allowing molecules with small vapor pressure (strong intermolecular interactions or large molecular weight) to pass through the doser. The tungsten wire is insulated from the metal by two halves of a glass-tube similar to the doser described in Ref. [156]. The wire terminals are further attached to an external electrical feedthrough by two copper wires.

The second doser is simply a stainless-steel tube mounted underneath the wobble-stick port (Fig. 2.7, position: ex-situ doser) with a leak-valve for regulating the gas flux. The sample is extracted from the STM-stage and positioned in front of the doser using a wobble-stick. Because of large ratio of the size of the Omicron sample-holder to the area in contact with the pincer of the wobble-stick, the crystal is heated slowly from 10 to 70K for  $\sim 3$  min even after it is

completely removed from the liquid-helium cooled stage (Fig. 2.9) This delay provides ample time for dosing from the ex-situ doser. The same procedure is used to heat the crystal from 4 to 250K in order to observe gross chemical changes on the surface (e.g. Chapter 8, 9). Since the heat-capacity of the materials increases with temperature, the heating rate decreases (Fig. 2.9) improving the accuracy of the heating procedure.

## 2.5 MEASUREMENT OF TUNNELING CURRENT

In the standard set-up the sample stage is grounded by one of the 36 wires to a wall of the blank flange on top of the STM. The tunneling current is measured through a shielded wire that makes contact to the magnetic apex on the tube-scanner. The current preamplifier is located outside the vacuum chamber (because of the low-temperatures in the STM-stage). The first stage is a standard feedback picoammeter, which has a variable gain of  $3 \times 10^7$  and  $3 \times 10^9$  (the corresponding feedback resistors are 30 M $\Omega$  and 3 G $\Omega$ ). The lowest measurable current is 2 pA, while the maximum current is 333 nA at low-gain and 3 nA at high gain. The maximum bandwidth of the preamplifier is limited by the time-constant  $R_{\text{feedback}}C_{\text{parasitic}}$  because operational amplifiers always have parasitic capacitance across the feedback resistor. The bandwidth is 40 kHz at low gain and only 800 Hz at high gain. Nonetheless, the excellent drift-stability of the LT-STM (estimated as a shift of the position of a single CO molecule in a series of STM images taken at 5K with an interval of several minutes, Fig. 2.10) allows for reproducible scanning tunneling spectroscopy with an acquisition time of up to 1 minute. The voltage across the tunneling junction is applied by biasing the non-inverting input of the operational amplifier by a dual-range potentiostat with a range  $\pm 1\text{V}$  (accuracy  $\sim 1\text{ mV}$ ) and a range of  $\pm 10\text{V}$  (accuracy  $\sim 10\text{ mV}$ ). The non-inverting input of the operational amplifier (i.e. tunneling current) is also connected to two potentiostats, which are used for compensation of the zero-current offset (inherent in such picoammeters) and for the compensation of the capacitive cross-talk due to small external ac bias used for scanning tunneling spectroscopy with a lock-in amplifier. The second stage of current amplification consists of the another feedback preamplifier, a logarithmic amplifier that linearizes the variation of the tunneling current with tip-sample separation, and low-pass filters. The output of the preamplifier box is fed into the Omicron STM controller.

### 2.5.1 Electronic noise

The largest source of noise in a vibrationally isolated tunneling microscope is the electronic noise. The current preamplifier has a gain of  $\sim 10^9$  (the op-amp has a feedback resistor of 1 G $\Omega$ ). The Johnson noise at room temperature (the preamplifier is located outside of the cryogenic regions) is  $0.13 \cdot R(\Omega) \frac{nV}{\sqrt{Hz}} = 4.11 \frac{\mu V}{\sqrt{Hz}}$ .

In topographic mode, the signal is essentially integrated over the full bandwidth of the preamplifier, which is 200 Hz to 3 kHz in most measurements presented here. Therefore the Johnson noise amounts to 0.06-0.23 mV of rms noise, which translates into 0.06-0.23 pA of effective current noise. This is generally not a problem in topographic mode where the current setpoint current is  $>10$  pA. In  $dI/dV$  spectroscopic mode, the Johnson noise is further reduced by limiting the measurement bandwidth to a narrow band around the frequency of bias voltage modulation. Typically the effective width of this band with feasible averaging times is  $\sim 100$  Hz. The noise decreases to  $\sim 0.04$  pA. These values correspond to the lowest limit, because a large number of elements as well as imperfections in the electronics produce a higher current noise.

### 2.5.2 Vibrational Noise

Overcoming the interference of the vibrations in the positioning of the STM-tip relative to the surface was essentially a key step toward realization of the STM back in 1983. Vibrations can affect the STM measurement in two ways: (1) cause a change in the tip-sample separation, which is amplified exponentially in the tunneling current, and (2) move the wire carrying the tip current, which capacitively couples to its environment and therefore causes current spikes when moved. The latter issue can be addressed by carefully clamping all of the wires in place, so that they cannot move with respect to each other due to helium boiling vibrations or external building vibrations.

The LT-STM uses a three-stage vibration-isolation technology: the whole UHV chamber is floating on three pneumatic support-legs; the STM-stage is suspended on soft springs; the STM-

stage is additionally equipped with an Eddy-current damper, which counteracts the swinging motion and vertical oscillations of the STM-stage. The springs and pneumatic suspension have

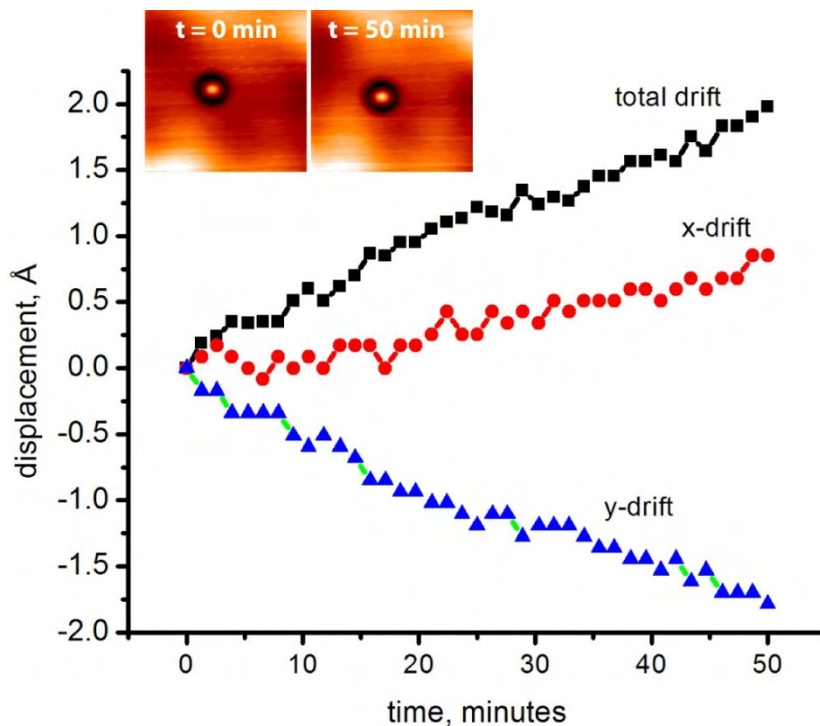


**Figure 2.10.** Lateral drift of the LT-STM at 5K. The drift causes a slow displacement of a single CO molecule in the STM image. Images on top were taken at the start and the finish of the drift measurement ( $3.4 \times 3.4 \text{ nm}^2$ ,  $U = -0.030 \text{ V}$ ,  $I = 30 \text{ pA}$ ).

natural vibrational frequencies of  $\sim 1\text{-}2 \text{ Hz}$ . They act as a low-pass filter, efficiently blocking external vibrations that are much higher than the natural frequencies.

### 2.5.3 Scanner calibration

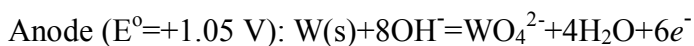
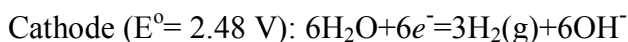
Scanner calibration is a crucial part of the STM measurement, and it is particularly important in the case of the LT-STM, because the piezo-coefficient of the scanner ceramics decreases roughly linearly with temperature. Being a microscopic technique with atomic resolution the STM uses the best standards for lateral and vertical calibration available: x-y dimensions are calibrated using atomically resolved images of the clean metal surface (or Si(111)) with the known values of lattice-constants; z-motion is similarly calibrated using single-atomic steps on the surface.

## 2.6 STM-TIP PREPARATION

Preparation of atomically sharp tips (diameter < 5 nm) for STM has become a routine procedure and there is a variety of ways to accomplish this task [157, 158]. Nonetheless reproducibility of the process is extremely poor and the exact shape of the tip is rarely known. The tips used in these studies were prepared via a 2 step procedure:

1. electrochemical etching of a 0.25 mm tungsten wire in air;
2. electron bombardment/annealing/field emission cycle performed in vacuum.

The home-built electrochemical tip etcher was detailed elsewhere [159]. The process starts with quick etching of a tungsten wire mounted on a micrometer screw and dipped into a droplet of 3M aqueous KOH solution supported in a loop of grounded Ir wire (cathode). The tip is biased positively up to +12 V so the anodic dissolution process occurs, and the net electrochemical reaction is:



After initial thinning of the tungsten wire to 0.1mm, it is submerged into a droplet of ~0.03M KOH solution to etch out a neck, which is almost invisible by an optical microscope. The final etching step is performed using the analog feedback electronics. The circuit amplifies a step change in the etching current, which occurs when the neck is completely etched off the tip apex. The electrochemical cell is then automatically opened using a fast switch (~500ns) to prevent further etching. The remaining KOH solution is rinsed away by a stream of hot water immediately after the breaking of the neck.

Freshly-etched tips are covered by a thick layer of  $\text{WO}_3$  which is insulating and unacceptable for the STM measurements. In order to remove tungsten oxide, the author built a mini-manipulator that is used to extract the tip from the sample-holder in the preparation chamber and process the tip by electron-bombardment. It consists of a linear translator with 100

mm travel, which translates a hollow stainless steel tube 0.25" OD/ 0.17" ID. The hollow tube is adapted with the CF-mini flange on one end and an electrically insulated magnetic tip-acceptor on the other. A thin Cu wire insulated by ceramic-beads runs through the length of the hollow-tube from the tip-acceptor to the CF flange, where it is connected to a medium-high-voltage electrical feedthrough with a BNC adapter. The tip is extracted from its holder by the combined motion of the mini-manipulator and the XYZ manipulator in the preparation chamber (Fig. 2.7). After tip-extraction, the tip-holder in the XYZ manipulator is replaced with a custom-made sample holder containing an electrically wired tungsten filament. The tip is then brought close to the filament using the mini-manipulator (separation is usually 1-2 mm).

The first tip-processing step is electron-bombardment, where 1.8-2.0 A electrical current runs through the filament referenced to the ground while the tip is biased at +0.5 kV using the BNC feedthrough. The current through the filament is increased to achieve ~5 mA of emission current. After 10 seconds of electron-bombardment, the set-up is rewired so that the tip is grounded through the picoammeter and the filament can be biased up to +2 kV. At this bias electrons are field-emitted from the sharp tip into vacuum (the electric field in the vicinity of the tip-apex must distort the vacuum-barrier to allow electron tunneling from the Fermi-level of the tip into vacuum). The bias on the filament is slowly increased until 0.1 nA of field-emission current from the tip is detected. Sharp STM-tips commonly have a 300-400 V threshold in such a set-up.

The final tip processing step is performed in-situ while scanning the sample surfaces in STM. It consists of a series of voltage and current pulses ( $t \sim 10$  ms) applied to the tip with the open feedback-loop. Commonly voltage pulses of 5 to 10 V in magnitude and current pulses up to 2 nA are used. It is suggested that during such procedure surface atoms are transferred onto the tip forming a sharp microtip [160]. The microtip is rarely stable and repetition of the procedure is required. In addition, weakly bound impurities on the tip apex may be removed in the course of pulsing.

On soft metal surfaces such as Au(111) and Ag(111), the STM tip can also be prepared by direct contact to the surface. The tip is first positioned  $\sim 0.5$  nm away from the surface. The feedback loop is open and the bias-voltage is decreased to zero (in reality the biased current preamplifier always produces a small non-zero bias voltage of  $<1$  mV). The z-piezo is slowly ( $\sim 0.5$  nm/s) extended by 2-3 nm toward the surface causing a gentle tip crash. Then the tip is

retracted by 5 nm away from the surface, moved away onto a clean surface region and the feedback loop is closed again. The variation of the tunneling current during approach and retraction of the STM tip exhibits a series of sharp jumps, which corresponds to the changes of the tunneling conductance that is a multiple of a single quantum of conductance ( $2e^2/h$ ) [161]. This is attributed to formation of an ultrathin metal neck between the tip and the surface. Upon retraction the neck breaks forming a sharp whisker on the tip apex, which is often a good STM-tip.

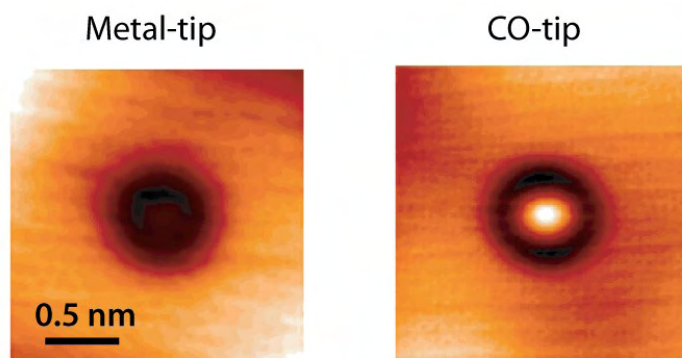


**Figure 2.11.** Single CO molecule adsorbed on the Au(111) surface imaged by a metal- and a CO-functionalized STM-tip.

Yet another technique routinely used in LT-STM measurements to increase the resolution of the STM images is the transfer of a single molecule from the metal surface to the STM-tip apex. CO is by far the most common choice in this case. To lift a single CO molecule off the Au(111) surface, the STM-tip is positioned above it and a voltage pulse of  $\sim 500$  mV is passed through the tunneling junction. It is argued that during this procedure, the CO molecule is not only lifted from the surface but also rotated, so that it is bonded to the tip-apex via the carbon atom, which is the same way it is bonded to the metal surface [162]. A successful transfer is indicated by the inversion of the STM-contrast of other CO-molecules adsorbed on the surface (Fig. 2.11). The contrast inversion was explained by the intermolecular interaction between CO molecules adsorbed on the STM-tip and the metal surface, which causes a strong modification of the scattering channels (or tunneling pathways) from the STM-tip to the metal surface [163]. The STM-contrast of other adsorbates usually remains the same, but the resolution is often improved.

## 2.7 PREPARATION OF AU(111) SURFACE

The Au(111) surface used in this thesis is a flat facet of a gold bead obtained by melting thin gold-wire of a rather low initial purity of  $\sim 92\%$  (Goodfellow, 0.3 mm thick) in a hydrogen flame [164, 165]. The major advantage of the bead-crystal compared to mechanically-cut single crystals is the zero-miscut angle the bead-facets, which provides extraordinary flat surfaces. The terrace width can be as large as several microns in the center of a facet. On the other hand, the edges of the facet approach the curved surface of the bead, which provides a variety of vicinal Au(111) surfaces, where single-atom steps form a regular superlattice.

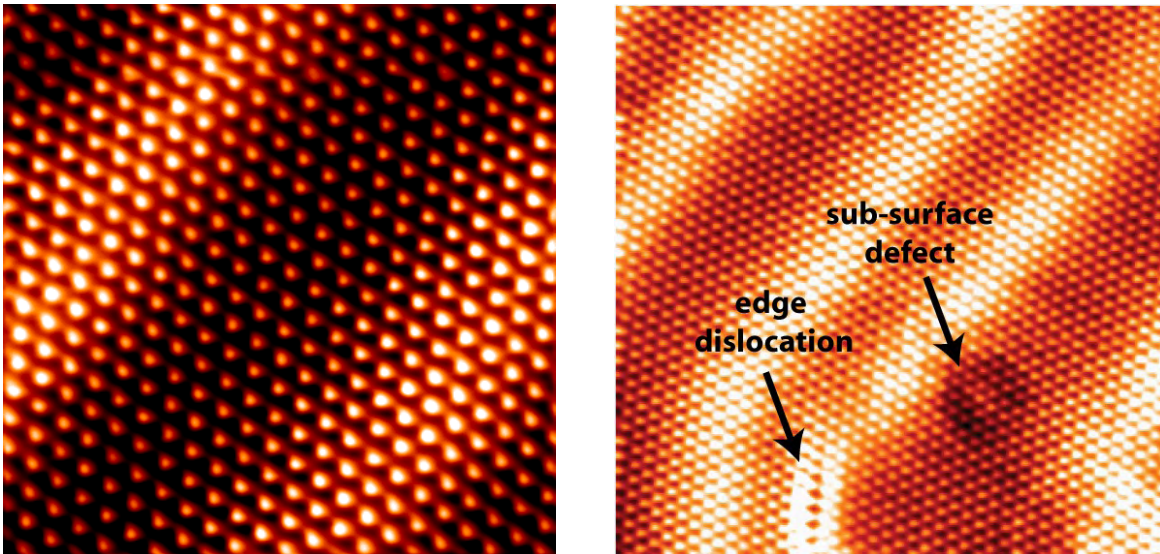


**Figure 2.12.** Atomically resolved STM images of the largest facet on the melted bead, which is the  $22 \times \sqrt{3}$ -reconstructed Au(111) surface ( $U = -0.12$  V,  $I = 31$  pA).

Left: hexagonally close-packed surface lattice of gold atoms.  $U = -0.12$  V,  $I = 31$  pA. Size:  $5 \times 5$  nm<sup>2</sup>.

Right: common defects on the clean Au(111) surface - intrinsic edge-dislocation due to the herringbone reconstruction and a sub-surface defect, most likely an implanted Ar atom or a carbon atom. Size:  $10 \times 10$  nm<sup>2</sup>.

The gold wire is first cleaned in piranha solution (3:1 mixture of concentrated H<sub>2</sub>SO<sub>4</sub> with 30% H<sub>2</sub>O<sub>2</sub>) to remove organic impurities and in boiling concentrated HNO<sub>3</sub> to remove transition metals. The impurities from the bulk of the wire are removed by melting (which is very similar to zone-melting in the semiconductor industry). When the wire is melted, impurities tend to segregate on the wire surface and in the melting front (separation line between melted

and solid gold). A region of very clean gold can be formed by slowly moving the melting front along the length of the wire and repeating the melting cycle several times. In addition, the contaminated surface of the wire can be dissolved in “aqua regia” (3:1 mixture of concentrated HCl and HNO<sub>3</sub>). After cleaning, the wire is slowly melted to produce a nearly spherical gold-bead. The bead is further cleaned by several melting cycles.

The bead is a single crystal of pure gold. When it becomes large enough (~5 mm in diameter), small flat facets form on the bead surface. The largest facets are <111> oriented surfaces following the Wulf construction for the fcc-crystal, which predicts the close-packed surfaces to have the smallest surface energy and therefore the largest relative size. The <111> orientation is, of course, confirmed directly in atomically resolved STM-images of the facets (Fig. 2.12). Melting/cleaning cycles and bead growth are continued until the facets become sufficiently large and the surface of the facet has no segregated contaminants visible in an optical microscope.

The bead is mounted on a tantalum sample holder using spot-welding and a small piece of tantalum foil. One of the facets is oriented roughly parallel to the surface of the sample holder. The bead is then transferred into a UHV chamber, where the clean Au(111) surface is prepared by cycles of Ar<sup>+</sup> sputtering and annealing to 773 K. The cleaning procedure is complete when the STM images of the surface show extended regions of the herringbone reconstruction and little or no adsorbates in the elbows of the reconstruction [56, 166]. The most common impurity is seen in STM images as a dark spot, 1-3 nm in diameter (Fig. 2.12). Atomically resolved images show that the surface lattice is virtually unperturbed within the dark spot. These impurities are attributed to residual subsurface Ar atoms implanted during sputtering cycles or to subsurface carbon atoms [167, 168].

**PART I. TIP-INDUCED DYNAMICS OF PHYSISORBED MOLECULES  
ON AU(111) SURFACE**

### 3.0 SURFACE BONDING AND DYNAMICAL BEHAVIOR OF THE CH<sub>3</sub>SH MOLECULE ON Au(111)\*

Bonding of alkanethiols on gold surfaces has been a controversial issue in many aspects. Even the question of S-H bond dissociation upon adsorption of alkanethiols and formation of the SAM has been a matter of active debate. By now it is firmly established that in most cases the S-H bond does dissociate at high temperatures on Au(111) surface [16]. CH<sub>3</sub>SH, however, is an exception to the rule. Being the smallest member of the alkanethiol family, CH<sub>3</sub>SH desorbs from the surface at ~185K, which is just under the temperature onset of the thermally activated dissociation of the S-H bond on Au(111). Non-dissociative adsorption of CH<sub>3</sub>SH has been confirmed both experimentally [44] and theoretically [169]. This chapter describes the adsorption of CH<sub>3</sub>SH on the Au(111) surface in the temperature range from 5 K to 80 K. Understanding the behavior of CH<sub>3</sub>SH on Au(111) was a starting point and an important step toward solving the thiol bonding problem at higher temperatures.

A spectacular manifestation of the physisorbed nature of CH<sub>3</sub>SH on the Au(111) surface is the hindered rotation of the molecule around the singly-coordinated S-Au anchor-bond at T = 5 K. The STM image of the rotating molecule is shaped as a flower with six petals, each petal corresponding to the position of a local potential minimum of the CH<sub>3</sub>-group along the rotational trajectory. Molecular manipulation was used to obtain a direct proof of CH<sub>3</sub>SH's hindered rotation and discard the possibility of an imaging artifact. The rotation is quenched on defects and strongly bonding surface sites provided by the structural distortions of the Au(111) herringbone reconstruction. Hindered rotation was also observed for C<sub>3</sub>H<sub>7</sub>SH, a longer-chain

---

\*Reproduced in part with permission from: P. Maksymovych, D. C. Sorescu, J. T. Yates, Jr., *Journal of Physical Chemistry B*, 110 (2006) 21161. Copyright 2006 American Chemical Society. Calculations done by D. C. Sorescu.

analogue of CH<sub>3</sub>SH, adsorbed on Au(111) (Fig. 3.11). The binding energy and rotational barrier of CH<sub>3</sub>SH on the Au(111) surface were calculated using DFT. Further analysis with classical and quantum mechanical models suggests that hindered rotation of the CH<sub>3</sub>SH molecule (by hopping or rotational tunneling) can be thermally driven already at 5K due to a small potential barrier of ~5 meV. However, the electric-field of the STM tip is likely to be an additional and possibly dominating energy-source to drive CH<sub>3</sub>SH rotation at 5K. The site location of the physisorbed CH<sub>3</sub>SH on Au(111) was determined from the six-fold symmetry of its rotational pattern. On the defect-free surface CH<sub>3</sub>SH molecules bind to atop Au sites via a singly-coordinated SH-Au bond. The S-C bond is nearly parallel to the surface.

### 3.1 EXPERIMENTAL METHODS AND THEORETICAL CALCULATIONS

The experiments were conducted on the Au(111) bead-crystal at 5K or 77K where specified. CH<sub>3</sub>SH was deposited on the surface through the in-situ doser while the crystal was in the STM imaging position at <10 K. The STM images were taken at a temperature of ~5K or at 77K where specified.

DFT calculations were done in the slab model using the Vienna *ab initio* simulation package (VASP) [170]. The electron-ion interaction has been described using the projector augmented wave (PAW) method of Blöchl [171] in the implementation of Kresse and Joubert [172]. All the calculations have been done using the PW91 generalized gradient approximation (GGA) of Perdew *et al.* [173]. The k-points were obtained from the Monkhorst-Pack scheme [174], with the cutoff energy of 400 eV. Electron smearing was employed via the Methfessel-Paxton technique [175], with a smearing width of  $\sigma = 0.1$  eV, in order to minimize the errors in the Hellmann-Feynman forces due to the entropic contribution to the electronic free energy [172]. All energies were extrapolated to T=0 K. The value of  $E_{\text{cut}}$  and the k-point grid were chosen to ensure the convergence of energies and structures. In particular, using a 8x8x8 k-point mesh for the bulk unit cell of Au, we obtained a lattice dimension of  $a_{\text{calc}}=4.1744$  Å and a cohesive energy of  $E_{\text{coh,calc}}=3.21$  eV. These values agree well with the corresponding experimental data of  $a_{\text{exp}}= 4.078$  Å and  $E_{\text{coh}}= 3.81$  eV as well as with the values determined in other theoretical studies [65, 176]. An equally good representation has been obtained for the

geometric parameters of the isolated CH<sub>3</sub>SH molecule. Based on optimizations performed in a cubic box of size 12 Å, we have determined the following equilibrium bond lengths:  $r(\text{S-C})=1.820$  Å,  $r(\text{S-H})=1.349$  Å,  $r(\text{C-H})=1.095\text{-}1.096$  Å, and the bond angle  $\theta(\text{C-S-H})=96.8^\circ$ . These values are in close agreement with the experimental values reported in Ref. [177]:  $r_{\text{exp}}(\text{S-C})=1.819$  Å,  $r_{\text{exp}}(\text{S-H})=1.340$  Å,  $r_{\text{exp}}(\text{C-H})=1.090$  Å and  $\theta_{\text{exp}}(\text{C-S-H})=96.5^\circ$ .

### 3.2 HINDERED ROTATION OF CH<sub>3</sub>SH ON DEFECT-FREE AU(111) SURFACE

CH<sub>3</sub>SH molecules preferentially adsorb on step-edges and elbow sites due to the presence of under-coordinated Au atoms in these sites (see *Introduction*). Molecular adsorption on the defect-free surface, such as the fcc- or hcp-domains and the soliton walls of the Au(111) herringbone reconstruction is observed at a higher coverage, when the defective sites are saturated. Figure 3.1 shows an STM image obtained after dosing  $\sim 0.05$  ML of CH<sub>3</sub>SH on a clean Au(111) surface at  $<10\text{K}$ . The molecules are imaged as nearly round protrusions 8 Å in diameter and  $0.9\pm 0.1$  Å in height. Brighter molecules in the image are adsorbed on topographically higher soliton walls.

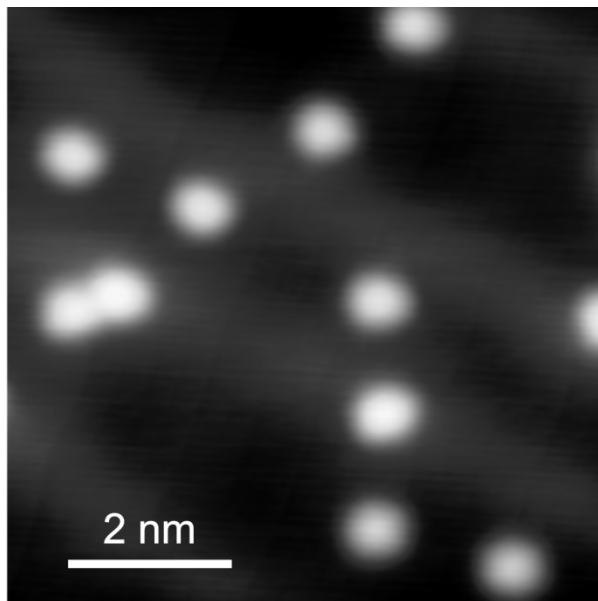


**Figure 3.1.** Low-resolution STM image of CH<sub>3</sub>SH molecules at 5K on the defect-free regions of the surface. ( $U = -0.16\text{V}$ ,  $I = 0.2$  nA).

The diameter of the CH<sub>3</sub>SH molecules as seen by STM is about twice as large as the van-der-Waals radius of the molecule. This discrepancy is resolved by inspecting high resolution STM images (Fig. 3.2) obtained by sharpening the tip via gentle crashes into the gold surface and scanning at low tunneling resistance (reduced tip-molecule distance). As seen in Fig. 3.2a, the CH<sub>3</sub>SH image has a shape of a flower with six petals around a bright dot in the center. The average apparent diameter of the flower, along the petal-center-petal line, is 8 Å, which is identical to the diameter of the molecular image seen at lower resolution in Fig. 3.1.

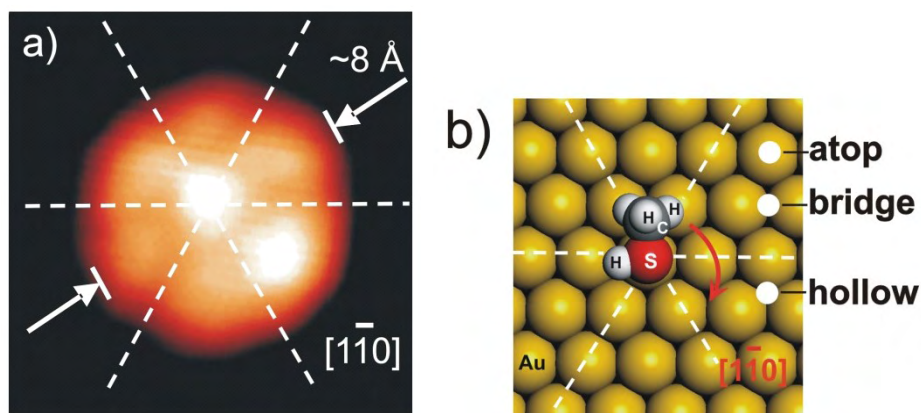
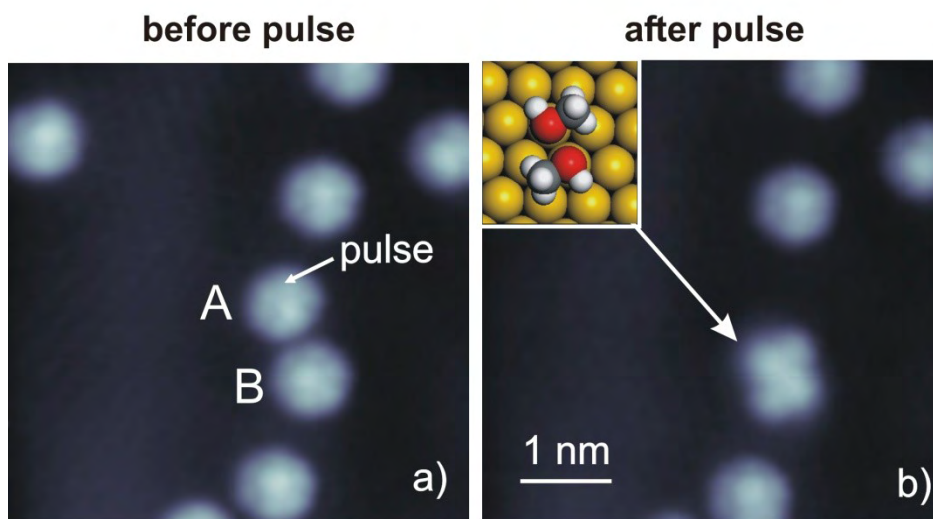


**Figure 3.2.** a) High-resolution STM image at 5K of a single rotating CH<sub>3</sub>SH molecule on the non-defective surface in a shape of a flower with six petals. ( $U = -0.01\text{V}$ ,  $I = 0.04\text{ nA}$ ) The dashed lines correspond to the close-packed crystallographic directions determined from atomically-resolved STM images of the Au lattice in the vicinity of the molecule. b). A schematic model of the adsorption geometry inferred from the STM image.

The flower-shaped appearance of the CH<sub>3</sub>SH image can be explained by assuming that the molecule undergoes hindered rotation on the surface. In this case, the STM image taken at the time-scale of seconds represents a time-averaged picture of the rotating molecule. The azimuthal directions of the petals correspond to the potential minima along the rotational coordinate, where the residence time of the molecule. Conversely, the potential maxima on the rotational coordinate correspond to the close-packed Au-Au azimuths shown by dashed lines in Fig. 3.2a. Previously, benzenethiol molecules were seen to rotate on Cu(111) surface producing similar STM images [178].

Direct evidence for the rotation of the molecule was obtained from the STM-tip-assisted manipulation of CH<sub>3</sub>SH molecules. In Fig. 3.3a all the molecular images have a flower-shape

## $(\text{CH}_3\text{SH})_2$ Dimer Formation. $T=5\text{K}$



## $(\text{CH}_3\text{SH})_2$ Dimer Decomposition

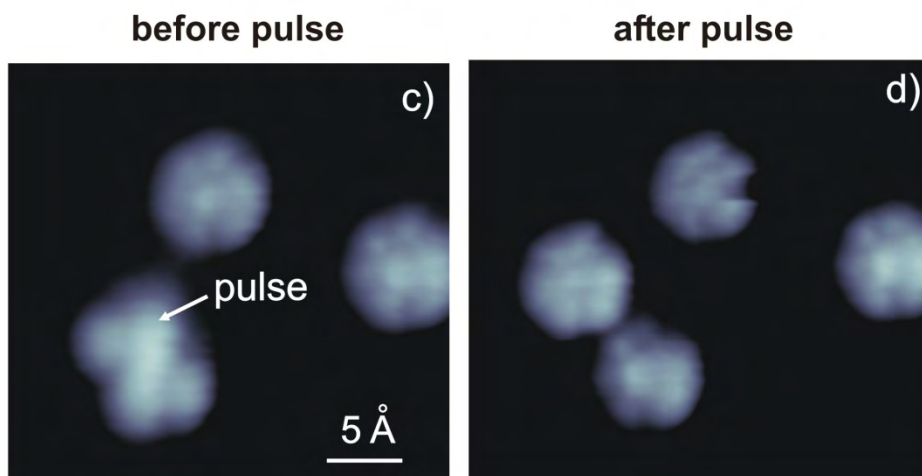


**Figure 3.3.** Direct evidence for steric hindrance of the rotation of  $\text{CH}_3\text{SH}$  molecules on  $\text{Au}(111)$  at 5K. ( $U = -1$  mV,  $I = 0.05$  nA). a). STM image of rotating molecules before the manipulation. The arrow shows the position where a pulse of +0.6V was applied in order to move molecule A toward molecule B. b). Molecular rotation stops as a result of proximity of two molecules. Molecules A and B form a zig-zag shaped dimer. The inset to Fig. 6b shows a possible  $(\text{CH}_3\text{SH})_2$  head-to-tail dimer model.

due to hindered rotation. The STM tip was positioned above molecule A, and a pulse of -0.6V was applied to move it toward molecule B. As seen in Fig. 3.3b the manipulation produces a single entity which has a zig-zag shape composed of identical two-lobed shapes in an anti-parallel orientation. Each two-lobed shape has a node separating the lobes of slightly different

size. The geometry of the zig-zag species implies that it is a dimer of two CH<sub>3</sub>SH molecules and each two-lobed shape corresponds to an individual CH<sub>3</sub>SH molecule. A possible model for the CH<sub>3</sub>SH dimer corresponding to the STM image is shown in the inset to Fig. 3.3b.

The rotation of individual molecules in the dimer will be unfavorable due to steric hindrance, which is consistent with the observations. The rotational motion is restored when the molecules are moved apart by an STM pulse as seen in Fig. 3.3c and 3.3d. This also implies that CH<sub>3</sub>SH dimerization does not involve formation of chemical bonds between CH<sub>3</sub>SH adsorbate molecules.

### 3.3 ADSORPTION SITE OF CH<sub>3</sub>SH

The six-fold symmetry of the flower-shape of the rotating molecule immediately testifies that there are six equivalent orientations of the molecule around its center of rotation. This in-turn requires the surface potential around adsorption site of the molecule to have six-fold symmetry. Since the length of the C-S bond (~1.8 Å) is smaller than the Au lattice constant (~2.8 Å), only the nearest-neighbor lattice atoms surrounding the CH<sub>3</sub>SH adsorption site on Au(111) will determine the symmetry of the surface potential sensed by the molecule.

The only surface site with the six-fold symmetry in the topmost surface layer is the atop site, which is surrounded by six hollow sites and six neighbor atoms (Fig. 3.2b). The hcp and fcc hollow sites have three-fold symmetry, and the bridge site has only two-fold symmetry in the topmost layer. Therefore we assign the atop site as the preferential adsorption site for the CH<sub>3</sub>SH molecule on the defect-free Au(111) surface. In Fig. 3.3a the dashed lines correspond to the close-packed directions on the Au(111) surface, inferred from atomically resolved STM images of the surface area around the molecule. The petals of the flower shape, which correspond to the preferential direction of the molecule along its rotational coordinate, are seen to be located in between these lines. This means that the molecule during its rotation is preferentially oriented toward the hollow sites around the Au atom on which the molecule is adsorbed.

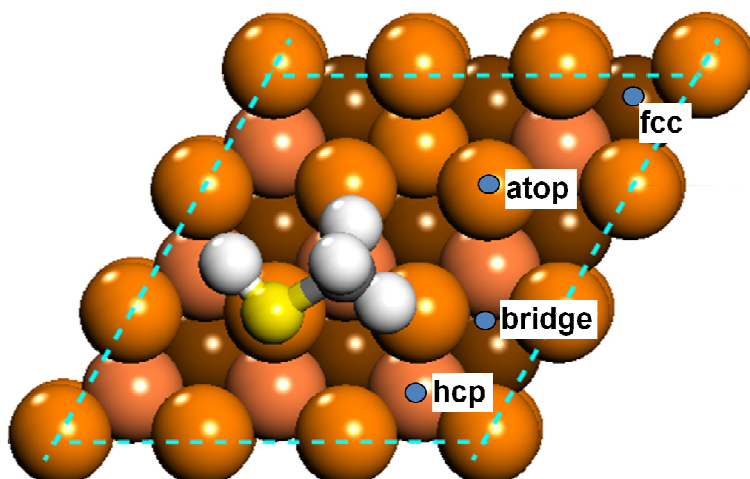


**Figure 3.4.** DFT optimized adsorption geometry of CH<sub>3</sub>SH on an unreconstructed Au(111) surface. The molecule adsorbs with the SH group on top of the Au atom, and the CH<sub>3</sub> group above the hollow site.

**Table 3.1. Calculated equilibrium distances (Å) and adsorption energies for CH<sub>3</sub>SH adsorbed on Au(111) surface at different surface sites**

	Configuration	$r(\text{Au}_T\text{-S})^a$	$r(\text{S-C})$	$r(\text{S-H})$	$E_{\text{ads}}$ , kcal/mol
Gas Phase		1.821	1.350		
<b>top</b>	2.668	1.822	1.352	<b>8.6</b>	
fcc	3.303	1.824	1.352	2.9	
hcp	3.472	1.825	1.352	2.7	

---

<sup>a)</sup>  $r(\text{Au}_T\text{-S})$  is the shortest distance from the S to the Au<sub>T</sub> atoms in the first layer.

In order to verify the experimental assignment of the adsorption and to estimate the barrier to rotation, we have carried out DFT slab calculations with CH<sub>3</sub>SH adsorbed on the unreconstructed Au(111) surface. Several adsorption configurations of the CH<sub>3</sub>SH molecule on Au(111) unreconstructed surface have been studied using a 3x3 supercell model with 4 Au layers. The two top layers of the slab model together with the adsorbed molecule were allowed to optimize, while the two bottom layers of the slab were frozen in the bulk configuration.

Table 3.1 summarizes the binding energies and representative geometric parameters obtained for different adsorption sites of the CH<sub>3</sub>SH molecule. The adsorption sites refer to the position of the S atom of the CH<sub>3</sub>SH molecule on the surface. According to these data, the atop

adsorption configuration (Fig. 3.4) is indeed the most stable with the binding energy that is nearly 3 times as large as that of the hollow fcc or hollow hcp configurations. This is in good agreement with the STM results, where the absolute majority of the molecules exhibit a six-fold symmetrical pattern due to molecular rotation. We have also analyzed the case when adsorption takes place at the bridge site, but the corresponding configuration was found to be unstable, and the molecule moved to the atop site during energy minimization.

In the atop configuration the molecule is tilted toward the surface (Au-S-C angle of  $108^\circ$ ), and the Au-S bond length is about  $2.664 \text{ \AA}$  (Fig. 3.4). The S-C molecular axis is in a plane bisecting the  $60^\circ$  angle formed by two surface Au atoms nearest to the Au atom on which the molecule is adsorbed and the methyl group is positioned above the hollow site. This is also consistent with the STM image (Fig. 3.2a) of the  $\text{CH}_3\text{SH}$  molecule, where the petals of the flower shape have the same orientation.

In summary, the  $\text{CH}_3\text{SH}$  molecule preferentially binds to the atop adsorption site with the SH-group directly above the Au atom, and the methyl group directed toward the neighbor hollow site. In the flower-shaped STM image of the rotating  $\text{CH}_3\text{SH}$  molecule, the petals are due to the  $\text{CH}_3$  groups, and a bright feature in the center marks the position of the SH group.

### 3.4 DFT CALCULATION OF HINDERED ROTATION

The minimum energy path for  $\text{CH}_3\text{SH}$  rotation around the S-Au bond between successive equilibrium configurations (Fig. 3.5) was determined by use of the nudged elastic band (NEB) method of Jónsson and co-workers [179, 180]. In this approach, the rotational coordinate is split into several configurations (images) between the potential minima. The images are connected by elastic springs with a certain force-constant to prevent them from sliding to the global minimum during the optimization. The energies of the intermediate states along the reaction path are simultaneously minimized but the atomic motion is restricted to a hyperplane perpendicular to the rotational coordinate. Five images were distributed in increments of 10 degrees between the neighbor equilibrium configurations along the rotation path.

The results plotted in Fig. 3.5 represent the minimum energy path versus the azimuthal angle of rotation  $f$ . In the initial and final configurations the  $\text{CH}_3$  group is located above the

hollow hcp or fcc site, respectively. In the least favorable orientation the CH<sub>3</sub> group is located in the direction of the near neighbor Au atom ( $f=30^\circ$  in Fig. 8). The maximum barrier height to rotation is  $\sim 0.1$  kcal·mol<sup>-1</sup>. The small calculated energy of the rotational barrier is at the limit of the accuracy of DFT, so we assign it as the upper limit of the true barrier. The barrier is slightly asymmetric around the direction to the near neighbor Au atom ( $f=30^\circ$ ) due to the difference in the surface structure when approaching this direction from the side of the fcc site and the hcp site.

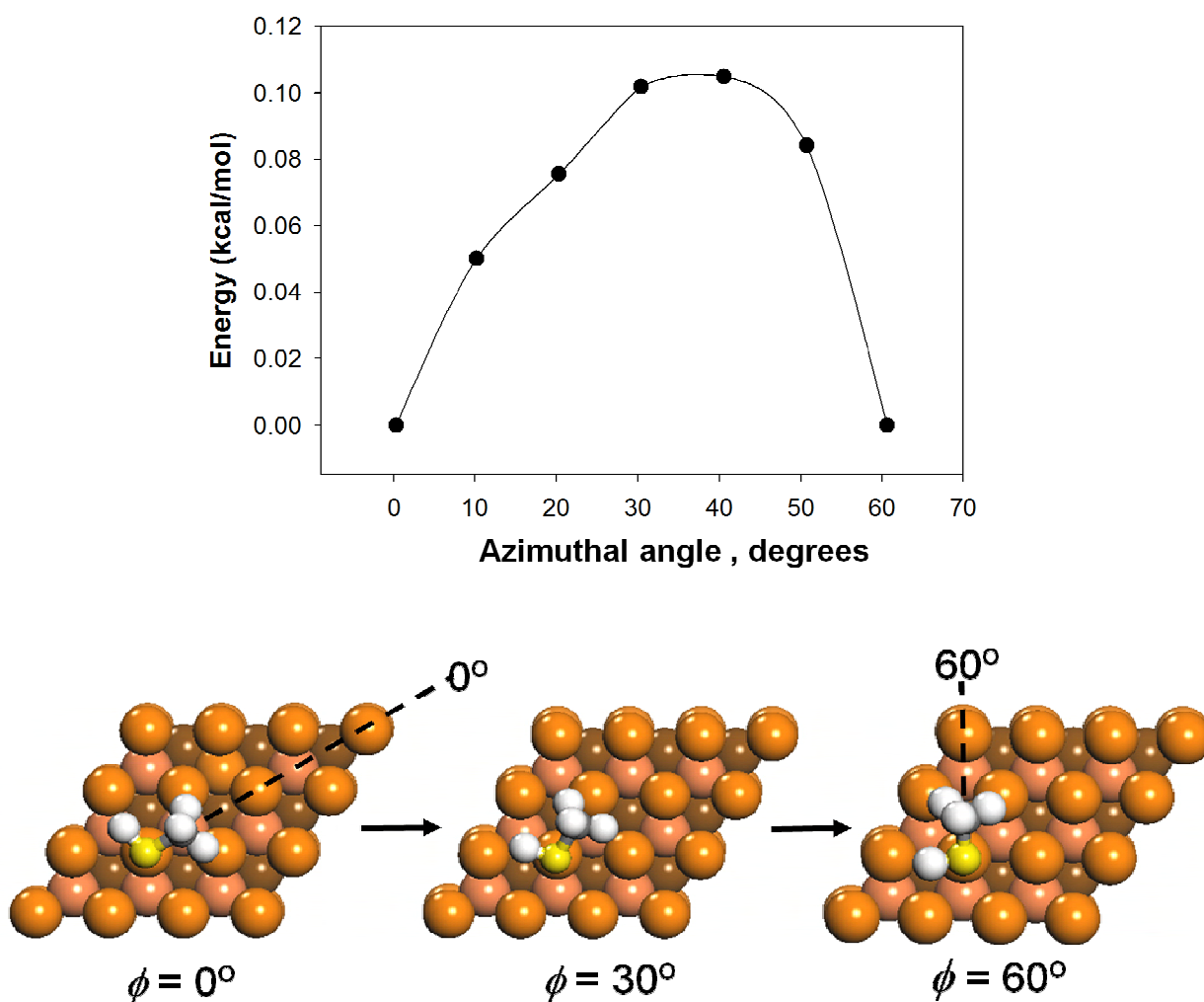


**Figure 3.5.** Minimum energy path for rotation of CH<sub>3</sub>SH molecule around the S-Au bond as a function of the azimuthal angle  $f$  (Au1-Au2-S-C). The zero point corresponds to the geometry in Fig. 3.4.

### 3.5 CLASSICAL DESCRIPTION OF HINDERED ROTATION

Since the rotation of the CH<sub>3</sub>SH molecule is imaged by the STM tip, the tip itself may influence the rotational motion. Quantitative description of the tip-molecule interaction in the presence of applied field can in principle be done using sophisticated density-functional calculations [181]. However, given a small barrier to CH<sub>3</sub>SH rotation, we shall first examine the problem excluding any tip-influence in order to estimate the feasibility of the thermally-driven rotation of the CH<sub>3</sub>SH molecule at 5K.

In the simplest, classical model a hindered rotor undergoes diffusive motion across the potential barrier [182]. The rate of molecular hopping across the barrier is given by the Arrhenius equation:

$$\text{Rate} = w \times \exp\left(\frac{-W}{kT}\right)$$

Here  $W$  is the barrier height and  $\omega$  is the librational frequency of the molecule in the potential well given by

$$w = \sqrt{\frac{n^2 W}{2I}}$$

with  $I$  being the molecule's moment of inertia and  $n$  – the symmetry number for the rotational potential (which is 6 in the case of CH<sub>3</sub>SH on Au(111)). Using 0.12 kcal·mol<sup>-1</sup> for the rotational barrier ( $E_{\text{rot}}$ ) the hopping rate is  $\sim 10^7$  hops/sec at 5K. Since one full rotation takes 6 hops, the molecule makes  $\sim 10^6$  full rotations per second at this temperature. Therefore the molecule would appear to rotate in the STM measurement given that the average time of an STM measurement of a single molecule is several seconds.

The natural shortcoming of the classical model is that the molecule is not allowed to tunnel through the potential barrier. This results in a very strong dependence of the hopping rate on the barrier height. Hopping across a barrier of 0.3 kcal/mol is nearly forbidden (0.3 hops per second). At the same time, the intrinsic error of the DFT calculated value of the potential barrier may well be as much as 0.1-0.2 kcal/mol.

### 3.6 QUANTUM-MECHANICAL DESCRIPTION OF HINDERED ROTATION

The energy eigenvalues and wavefunctions for molecular rotation in a periodic potential of the surface are obtained from the Schrodinger equation for a particle on a ring ( $\phi$  is the polar angle in the XY-plane):

$$-\frac{\hbar^2}{2I} \frac{d^2\Psi}{d\phi^2} + \frac{W}{2} [1 - \cos(6\phi)]\Psi = E\Psi \quad (1)$$

The procedure for solving this equation was detailed in [183] and [184]. It was successfully applied to describe the rotation of PF<sub>3</sub> adsorbed as an inverted umbrella on the Ni(111) surface [184]. The wavefunction of the rotational motion is assumed to be a superposition of plane-waves:

$$\Psi(\phi) = \sum_{\tau=-\infty}^{\infty} a_{\tau} \exp(i\tau\phi) \quad (2)$$

Equation (1) can then be reduced to a recursion formula for the Fourier coefficients of the eigenfunction corresponding to a particular energy eigenvalue.

$$\frac{S}{2(R-\tau^2)} a_{\tau-6} + a_{\tau} + \frac{S}{2(R-\tau^2)} a_{\tau+6} = 0; \quad S = \frac{IW}{\hbar^2}; \quad R = \frac{I}{\hbar^2} (2E - W) \quad (3)$$

The recursion formula is numerically solved using the method of continued fractions. Because of the six-fold symmetry of the hindering potential there are six equations with continued fractions. Combined solutions of these equations provide the complete set of rotational energy eigenvalues. Continued fractions are also used to obtain the Fourier coefficients of the rotational wavefunction corresponding to each eigenvalue. The numerical code used to solve the problem for CH<sub>3</sub>SH is detailed in the Appendix.

It was assumed that the surface potential is sinusoidal with the amplitude of 0.12 kcal/mol, which is the potential barrier height obtained from DFT calculations. Although the shape of the DFT-calculated barrier is slightly asymmetric, sinusoidal approximation is often very good [184] because the solutions do not depend strongly on the exact shape of the barrier. The moment of inertia of the CH<sub>3</sub>SH molecule was calculated from its DFT-optimized geometry

(Fig. 7) by projecting the bond-lengths onto X-Y plane and assuming that the axis of rotation goes through

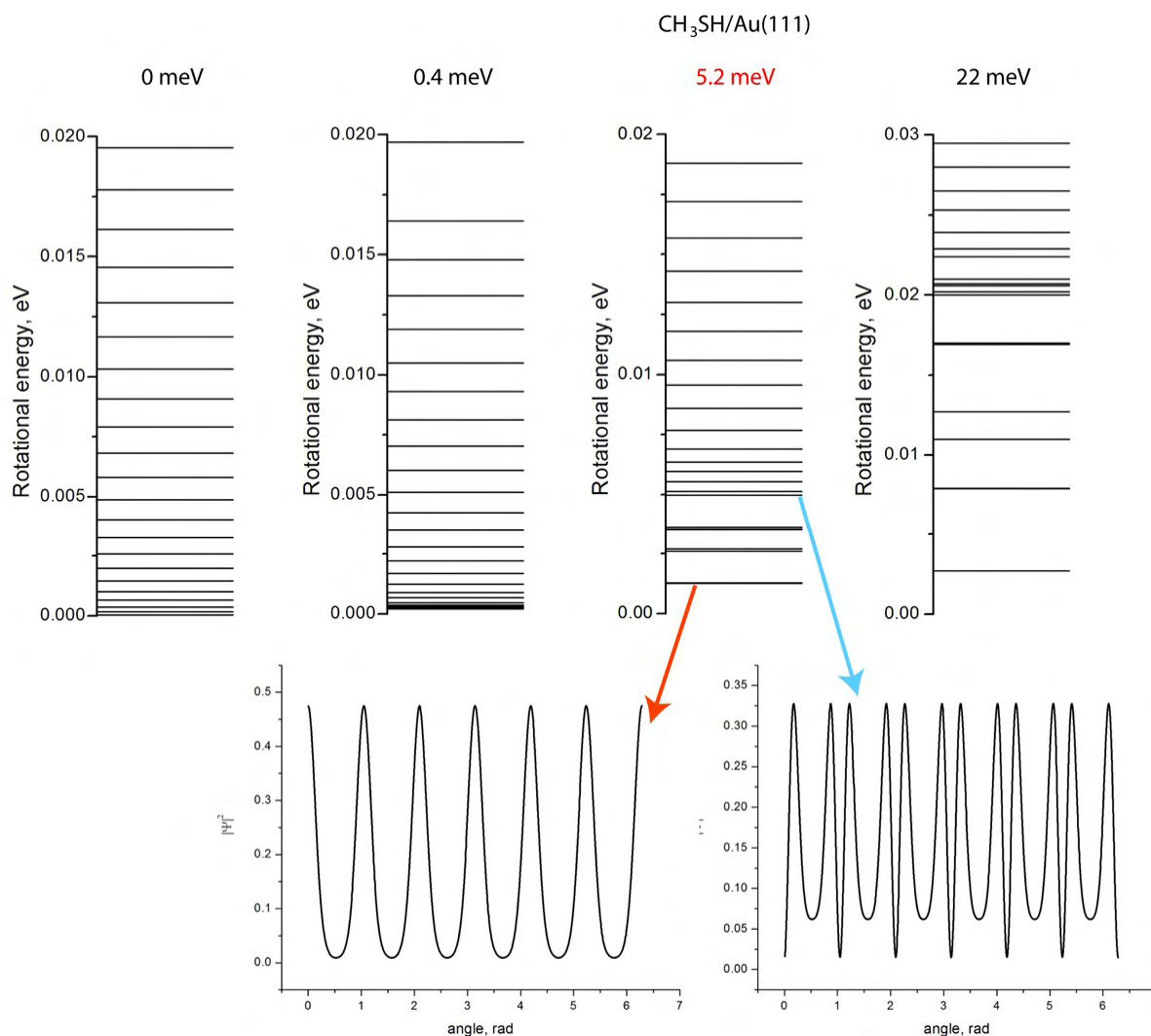


**Figure 3.6.** Rotational energy levels of a free and three hindered rotors. Lower panels show representative wavefunctions for the ground (left) and an excited (right) rotational state of CH<sub>3</sub>SH on Au(111).

the center of the S-atom. The internal dynamics of the CH<sub>3</sub> group will not affect the moment of inertia, but it may slightly influence the shape and the height of the potential. These effects were assumed to have only a weak effect.

The energy levels were calculated for the 0.12 kcal/mol barrier height as well as two other barriers (0.01 kcal/mol and 0.5 kcal/mol) and a free rotor for comparison. The results are shown in Fig. 3.6. Six-fold symmetric hindered rotor is, in essence, a combination of six

harmonic oscillators coupled to each other by energy-barriers of finite height. Therefore, the rotational energy levels of the hindered rotor are reminiscent of the free rotor above the barrier height and approach those of the harmonic oscillator below the barrier height. This is clearly seen in Fig. 3.6. The transition from the free rotor to the harmonic oscillator causes not only the shift of energy levels, but also increased degeneracy of the rotational level. The free-rotor levels are two-fold degenerate (except the  $E=0$ ), while in the limiting case of infinite barrier height the six-fold hindered rotor turns into six harmonic oscillators with six-fold degeneracy of each energy level.

The first energy level of the hindered rotor with a barrier of 5.2 meV (the DFT calculated value for CH<sub>3</sub>SH on Au(111)) is at 1.2 meV. It is six-fold degenerate. The next two energy levels are at 2.6 meV and at 3.5 meV. The Boltzmann factors for these levels at 5K are  $7 \cdot 10^{-2}$ ,  $4 \cdot 10^{-3}$  and  $2 \cdot 10^{-5}$  respectively. The contribution of any level but the lowest to the partition function is therefore negligible, and most of the CH<sub>3</sub>SH molecules are expected to be in their ground rotational state at 5K. In the free-rotor case the lowest rotational energy is zero, i.e. the rotor does not rotate [185]. However, the harmonic oscillator character of the hindered rotor results in a non-zero value of lowest-energy level (zero-point energy), therefore potentially allowing it to rotate even at 0K. The feasibility of such rotation can be estimated from the probability of molecular tunneling between two lowest energy levels in the neighbor potential wells along the rotational coordinate.

In order to calculate the tunneling probability of a rotating particle, let us compare the Schrödinger equations for the rotational and translational motion:

$$\text{Translation: } -\frac{\hbar^2}{2m} \frac{d^2\Psi}{dx^2} + U\Psi = E\Psi \quad \text{Rotation: } -\frac{\hbar^2}{2I} \frac{d^2\Psi}{d\phi^2} + U\Psi = E\Psi$$

Since these equations are equivalent, the solutions for the tunneling probability of the rotating particle can be obtained by substitution of  $\{m, x\}$  for  $\{I, \phi\}$  in those of the translating particle.

The probability of tunneling through a potential barrier of arbitrary shape (including the sinusoidal barrier in our problem) is then calculated using the transfer-matrix algorithm [186]. Here the tunneling coordinate is subdivided into  $n$  small sections where the potential is assumed to be constant (Fig. 3.7). The true potential is thus approximated by a piecewise constant

potential. Within each section the particle is then tunneling through a rectangular barrier, and the solutions for this problem are well-known.

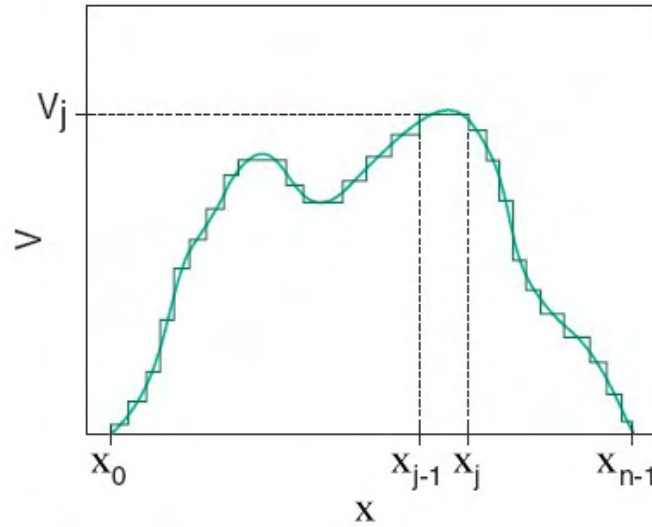


**Figure 3.7.** Division of the arbitrary potential into small sections of constant potential for calculations using transfer-matrix method.

The transmission through the whole barrier in one-dimension is described by the following matrix equations (the moment of inertia of the rotor is assumed to be constant throughout the barrier):

$$\begin{pmatrix} A_0 e^{ik_0 x_0} \\ B_0 e^{-ik_0 x_0} \end{pmatrix} = M \begin{pmatrix} A_n e^{ik_n x_n} \\ B_n e^{-ik_n x_n} \end{pmatrix}$$

$$M = M^{(0)} \cdot N^{(1)} \cdot M^{(1)} \cdot N^{(2)} \dots M^{(n-1)} \cdot N^{(n)}$$

$$M^{(j)} = \frac{1}{2} \begin{pmatrix} 1 + \frac{k_{j+1}}{k_j} & 1 - \frac{k_{j+1}}{k_j} \\ 1 - \frac{k_{j+1}}{k_j} & 1 + \frac{k_{j+1}}{k_j} \end{pmatrix}$$

$$N^{(j)} = \begin{pmatrix} e^{-ik_{j+1} \Delta z_{j+1}} & \mathbf{0} \\ \mathbf{0} & e^{ik_{j+1} \Delta z_{j+1}} \end{pmatrix}$$

$A_j$  ( $B_j$ ) are the amplitudes of the plane-wave impinging onto (departing from) the potential barrier in section  $j$  (barrier height is  $V_j$ ) and  $k_j$  is its wavevector given by

$$k_j = \sqrt{\frac{2m(E - V_j)}{\hbar^2}}$$

The transmission probability is the ratio of the squared amplitude of the outgoing wave (at point  $n$ ) to that of the impinging wave (at point  $0$ ). Furthermore, it is assumed that the amplitude of the wave impinging on the whole barrier from the right (i.e.  $B_n$ ) is zero, i.e. the particle always tunnels from left to right. This implies that  $A_n = 1$  and the transmission probability is calculated from the  $M$ -matrix as follows:

$$T = \frac{|k_n| |A_n|^2}{|k_0| |A_0|^2} = \frac{|k_n|}{|k_0|} \frac{1}{|A_0|^2} = \frac{|k_n|}{|k_0|} \frac{1}{|M_{11}|^2} = \frac{1}{|M_{11}|^2}$$

The very last potential step assumes a symmetric barrier so that  $k_0 = k_l$ , or alternatively  $V_0 = V_l = 0$ .

As seen in Fig. 3.8, the probability of the CH<sub>3</sub>SH molecule to tunnel between two neighbor potential wells along the rotational coordinate is  $4 * 10^{-5}$  for the lowest-energy level. It is very similar to the classical probability of the molecule to hop across the barrier at 5K (Section 2.1.6). The physical meaning of the tunneling probability is the ratio of the flux of the particles that tunnel through the barrier to the total flux of the impinging particles. In the context of the hindered rotor problem, the impinging flux can be assumed to be the librational frequency of the CH<sub>3</sub>SH molecule (Section 3.5),  $\sim 6 \cdot 10^{12}$  Hz. The molecule will then undergo  $\sim 10^7$  full rotations per second (6 hops per rotation on average). Therefore the hindered rotation of CH<sub>3</sub>SH at 5K is also expected from the quantum-mechanical point of view.

For completeness, the tunneling probabilities were also estimated for the higher sinusoidal potential barrier of 0.5 kcal/mol. As seen in Figure 3.9, the tunneling probability for the lowest energy level decreases dramatically to  $\sim 10^{-11}$ , meaning that the rotational motion will not be observed in this case. The tunneling probability quickly approaches unity when the energy of the rotor approaches the height of the hindering barrier, which is consistent with the harmonic-oscillator/free-rotor transition mentioned above.

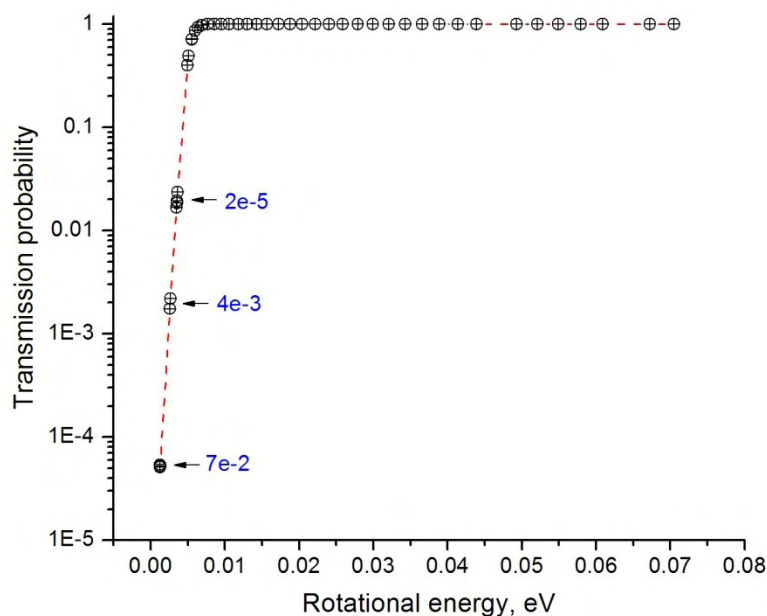


**Figure 3.8.** Tunneling probability for the rotational motion of CH<sub>3</sub>SH across a barrier of 5.2 meV. Tunneling occurs between two neighbor minima of the six-fold sinusoidal potential barrier. Blue values are Boltzmann factors for the energy levels at 5K.

### 3.7 TIP-EFFECTS IN HINDERED ROTATION OF CH<sub>3</sub>SH ON Au(111) AT 5K.

Although rotational tunneling of the CH<sub>3</sub>SH molecule on Au(111) at 5K seems to be plausible, the effect of the STM-tip is very important. Qualitatively this can be seen from the voltage-dependence of the STM images of rotating CH<sub>3</sub>SH molecules obtained with the same sharp tip and at the same tunneling current. The STM images in Fig. 3.10 were taken with at 50 pA tunneling current and at a bias of 1 mV (a), 10 mV (b), 100 mV (c), 250 mV (d). Visually, the STM images of CH<sub>3</sub>SH molecules taken at a vanishingly small bias of 1 mV appear as almost round symmetric doughnuts, which would technically correspond to a nearly-free rotor. As the bias increases, the doughnut shape evolves into the hindered image with six-petals, and, finally, into an asymmetric nearly-elliptical image in Fig. 2d. At the same time, the STM image of the non-rotating CH<sub>3</sub>SH molecule (e.g. in the dimers or on the elbows) hardly

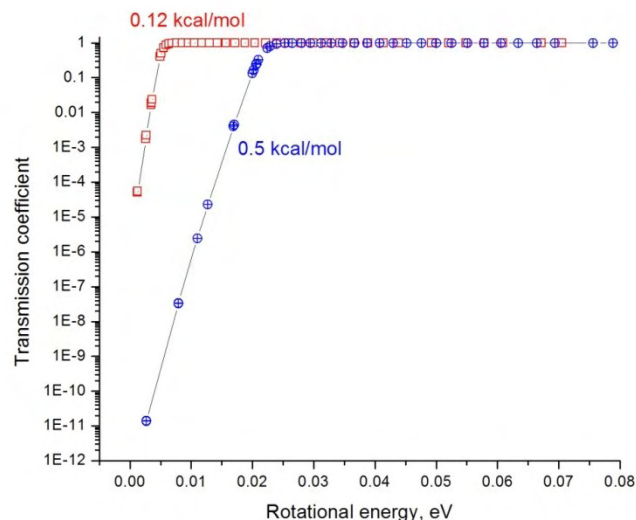


**Figure 3.9.** Tunneling probability for a rotating CH<sub>3</sub>SH molecule hindered by a potential barrier of 0.12 kcal/mol and 0.5 kcal/mol.

depends on the tunneling condition. Therefore the evolution of the shape in Fig. 2 can indeed be due to varying freedom of the molecule to rotate. This implies that the rotation may be driven by the STM-tip [182].

Tunneling current at small bias voltage can be expressed as [107]:

$$I \propto V \rho_s(\mathbf{0}, E_F) e^{-1.025 \sqrt{\varphi} Z}$$

where  $V$  is the bias,  $\rho_s(\mathbf{0}, E_F)$  is the Fermi LDOS at the sample surface,  $\varphi$  is the sample workfunction and  $Z$  is the tip-sample separation. From this equation the difference in the tip-sample separation in the STM images of Fig. 2 can be estimated. Assuming a 0.50 nm separation at 250 mV in Fig. 2d, the tip sample distance is estimated to be 0.29 nm in Fig. 2a, 0.39 nm in Fig. 2(b) and 0.46 nm in Fig. 2(c). In the simplest linear approximation, the electric field is given by  $E = \frac{V}{Z}$ , which amounts to  $3.4 \cdot 10^{-3}$  V/nm for (a),  $2.6 \cdot 10^{-2}$  V/nm for (b), 0.22 V/nm for (c) and 0.50 V/nm for (d). At the same time, the rotation becomes more and more hindered going from (a) to (d). Therefore, it seems likely that the rotation is caused by direct tip-sample interaction (similar to atomic manipulation using STM) rather than electric field effect. These conclusions, however, are qualitative and tentative. Fully ab-initio analysis would be desirable to clarify the effect of the tip on molecular rotation.

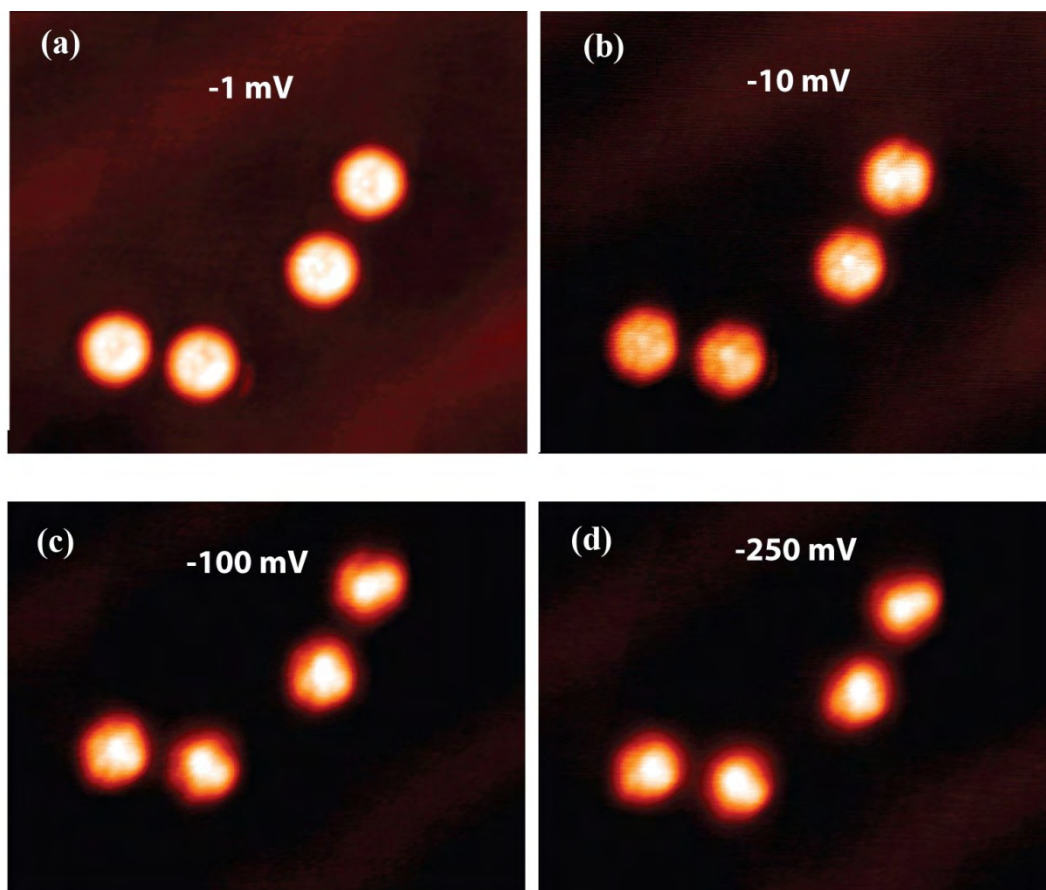


**Figure 3.10.** Bias dependent imaging of rotating CH<sub>3</sub>SH molecules on Au(111) with a sharp metal tip. Four CH<sub>3</sub>SH molecules are imaged consecutively at -1 mV (a), -10 mV (b), -100 mV (c), -250 mV (d) and a constant tunneling current of 100 pA. Noticeable changes in the apparent shape of the molecule indicate tip-involvement in the dynamics of the molecule.

Finally, CH<sub>3</sub>SH molecules adsorbed on undercoordinated Au-atoms in atomic step and herringbone elbow sites do not undergo hindered rotation under any tunneling conditions. CH<sub>3</sub>SH molecules adsorbed on these sites are always imaged smaller than the molecules adsorbed on the terraces. This is consistent with stronger binding of CH<sub>3</sub>SH molecules on these sites on one hand and lattice distortion on the other. Both of these factors will tend to increase the barrier to rotation.

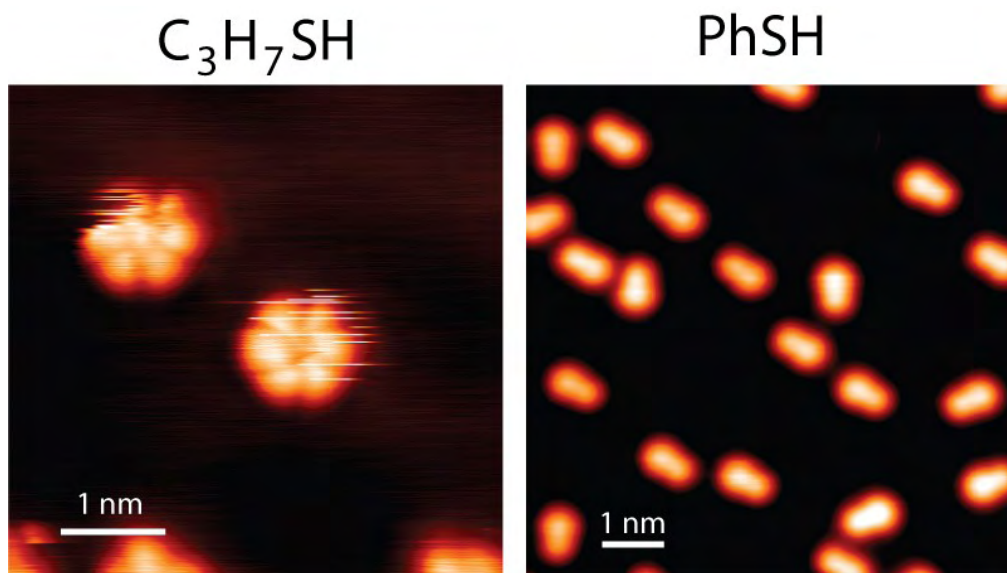


**Figure 3.11.** Comparison of  $C_3H_7SH$  and  $C_6H_5SH$  adsorbed on Au(111) at  $T < 70K$ . Hindered rotation of propanethiol is clearly observed. The streakiness of the image indicates substantial tip-molecule interactions, and thus the likelihood of the rotation being tip-induced.

### 3.8 SUMMARY OF RESULTS

The adsorption site and the dynamics of rotational motion of chemisorbed  $CH_3SH$  species at low coverages on Au(111) have been studied using STM and by DFT calculations. The following results have been obtained:

1. The undissociated  $CH_3SH$  molecule binds to an atop Au(111) site on a defect-free Au(111) surface. The calculated binding energy is  $8.6 \text{ kcal}\cdot\text{mol}^{-1}$  at this site.
2. The isolated molecule undergoes hindered rotation at 5K on this site; an upper bound of  $\sim 0.1 \text{ kcal}\cdot\text{mol}^{-1}$  has been calculated for the rotational barrier. The potential minima along the rotational coordinate occur in the direction of the six hollow sites around the Au adsorption site, as indicated by the STM measurements and by DFT calculations.

3. Rotational motion of chemisorbed  $\text{CH}_3\text{SH}$  is impeded by the presence of a neighbor  $\text{CH}_3\text{SH}$  molecule, which forms a head-to-tail dimer,  $(\text{CH}_3\text{SH})_2$ , at 5K. Dimers can be formed or broken by manipulating molecules with the STM tip.

4.  $\text{CH}_3\text{SH}$  does not exhibit rotational freedom at 5K when adsorbed at random step defect or at vacancy defect sites present at the herringbone elbows.

In addition to  $\text{CH}_3\text{SH}$ , the rotational motion was observed for  $\text{C}_3\text{H}_7\text{SH}$  adsorbed on Au(111) (Fig. 3.11) However, PhSH does exhibit any rotational motion, which is likely due to increased molecule-surface interaction. Tip-induced dynamics was very useful when assigning the adsorption site of the rotating species. In the next section tip-induced dynamics is used to describe intermolecular interactions.

## 4.0 ATTRACTIVE INTERACTION AND TIP-INDUCED DYNAMICS OF CO MOLECULES ON AU(111)\*

Spontaneous formation of clusters between CO molecules adsorbed on the Au(111) surface was observed at 5 K using STM. In all the  $(\text{CO})_n$  clusters ( $n = 2-5$ ), the CO molecules are bonded to the nearest-neighbor gold atoms in characteristic arrangements. The CO dimer was found to exhibit an unusual tip-induced motion, where one molecule orbits around its neighbor. The clusters could be translated and manipulated without decomposition using the STM tip. These results demonstrate that the interaction between CO molecules bonded in particular cluster geometries to the nearest-neighbor Au atoms is attractive rather than repulsive as commonly assumed.

### 4.1 INTRODUCTION

The adsorption of CO has been studied extensively on noble metals [187-190], in light of their catalytic activity in CO oxidation [191, 192]. The description of the bonding of CO to the noble metals and the CO-CO interactions is still incomplete [190, 193]. The sign of intermolecular interaction between adsorbed CO molecules exhibits oscillatory character on (111)-terminated metal surfaces. It is repulsive between CO molecules adsorbed atop of the nearest neighbor metal atoms according to experimental and theoretical studies [194-196], and becomes slightly attractive in  $\sqrt{3}$ -configuration (Fig. 4.1) [197].

---

\*Reproduced in part with permission from: P. Maksymovych, J. T. Yates, Jr., Chemical Physics Letters 421 (473) 2006. Copyright 2006 Elsevier.

Previously adsorption of CO on Au(111) surface by STM was studied under high pressure conditions [198] and in HClO<sub>4</sub> solution under variable potential at room temperature [199]. In both studies the herringbone reconstruction of the Au(111) surface was lifted. Here the first scanning tunneling microscopy study of CO adsorbed on the Au(111) surface is presented. No evidence for the lifting of the reconstruction even in the saturated layers in UHV is found, which suggests that the CO interaction with the gold surface was strongly influenced by the experimental conditions in previous studies and possibly by the presence of impurities. The key new result of the present work is the *spontaneous* formation of small stable clusters of CO molecules at 5-20 K when the adsorbate coverage is very low. We identify isolated close-packed dimers, trimers, tetramers and higher order clusters of CO molecules on the Au(111) surface, in which the molecules are adsorbed on top of the nearest neighbor surface atoms. This is unexpected in light of the existing picture of the repulsive CO-CO interactions [197] on the nearest neighbor sites.

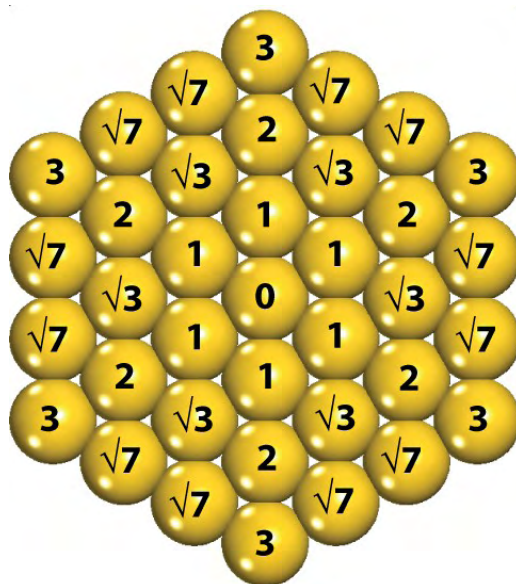


**Figure 4.1.** Numeric nomenclature for neighbor surface sites on the close-packed (111) surface.

Very recently CO islands and clusters were observed at high adsorbate coverage on the Ag(111) surface [200]. Although their stoichiometry and structure were not determined, we believe that they are topologically similar to the clusters in our studies, because of the similarity of adsorption behavior expected for CO on Au(111) and Ag(111) surfaces [190].

## 4.2 EXPERIMENTAL

The surface temperature in this experiment did not exceed 8K during exposure to CO gas. This was achieved through the use of a retractable effusive beam doser, which can dose molecules onto the crystal located directly in liquid-helium cooled STM-stage. All the STM measurements were done at 5K with a tungsten tip that was intentionally modified with a CO molecule to improve the imaging resolution. It was verified that this chemical modification of the tip did not introduce any artifacts except for an overall contrast reversal, which is not essential for the presented analysis. Single adsorbed CO molecules were used as markers of the positions of Au atoms in the surface lattice in order to triangulate the site locations of adsorbed molecules and their dissociation products. A similar procedure was described in Ref. [201].

## 4.3 RESULTS AND DISCUSSION

The behavior of isolated CO molecules on the Au(111) surface is identical to that on Cu(111) [202], where occupancy of atop sites occurs [203, 204]. With a bare metal tip the isolated molecules are imaged as round dark depressions. A CO molecule can be controllably transferred to the tip. Imaging a single CO molecule on the surface with the CO-coated tip reveals a bright protrusion surrounded by a dark halo (Fig. 2.10), which is similar to the Cu(111) case [202]. Thus we conclude that an isolated CO molecule on the Au(111) surface also occupies an atop adsorption site. Moreover, by triangulating the position of isolated CO molecules using other adsorbed CO molecules as markers, it was determined that all CO molecules occupy the same atop Au adsorption site.

At a very small CO coverage of  $\sim 2$  molecules per  $100 \text{ nm}^2$ , all of the adsorbed molecules are observed to be isolated for sampling areas of  $\sim 400 \times 400 \text{ nm}^2$ . Surprisingly, clusters form spontaneously upon increasing the coverage to only  $\sim 4$  molecules per  $100 \text{ nm}^2$  (Fig. 4.2). An observable effect of the herringbone reconstruction of the Au(111) surface is that at low coverage both isolated CO molecules and CO clusters are adsorbed within the fcc-stacked region, where the Au lattice spacing is largest. This can be explained using the d-band centroid argument [205], because increasing the lattice constant leads to an upward energy-shift of the d-

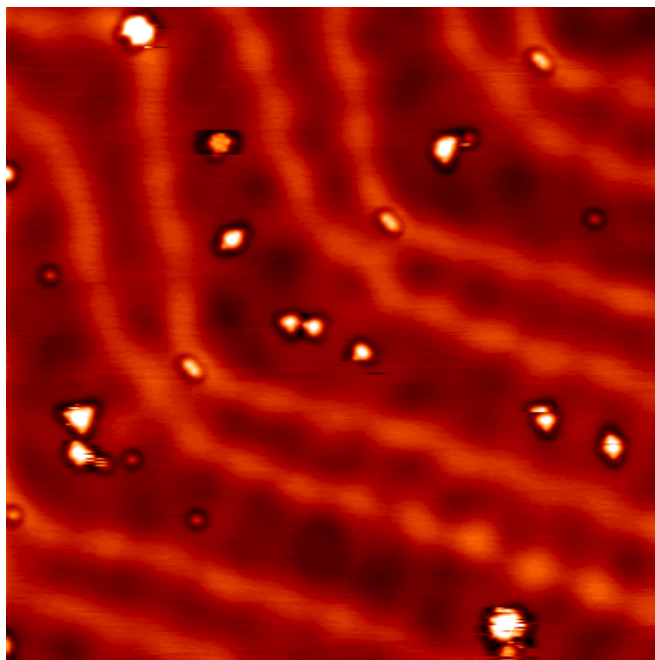


**Figure 4.2.** Spontaneous CO clustering on Au(111) at  $T < 20\text{K}$  ( $20 \times 20\text{ nm}^2$ ,  $U = -30\text{ mV}$ ,  $I = 30\text{ pA}$ ).

band center, which, in turn, increases the reactivity of the surface (a detailed discussion is presented in Chapter 5).

The observed small CO clusters have one of the following characteristic shapes as shown in Fig. 4.3: an ellipse (Fig. 4.3b); a pinwheel (Fig. 4.3c); a triangle (Fig. 4.3d); a triangle+dot (Fig. 4.3e) and a sombrero (Fig. 4.3f). All the clusters are surrounded by a dark halo, which is reminiscent of the halo observed around an isolated CO molecule. The green arrows in Fig. 4.3 show the pathways for the tip-induced cluster isomerization (see below) that were observed experimentally. The red arrows represent  $n$  to  $n+1$  synthetic pathways, that can be deduced from the comparison of the STM images. Based on the cluster transformations and the triangulation of STM images, we have determined that the ellipse and the pinwheel clusters are isomers of the CO dimer; the triangle corresponds to the CO trimer; the sombrero and the triangle+dot are isomers of the CO tetramer. Schematic models of the clusters are shown on the right in Fig. 4.3. Higher order clusters (up to a hexamer) also exhibit a characteristic shape, but their structure is perturbed by the STM tip resulting in streaked or fuzzy STM images.

The apparent shape of the pinwheel dimer (Fig. 4.3c) is noteworthy in that a six-fold symmetry of the pattern is observed for a cluster that contains only two molecules. The six components of the pinwheel shape are aligned in the  $\langle 1\bar{1}0 \rangle$  azimuthal directions on the Au(111)

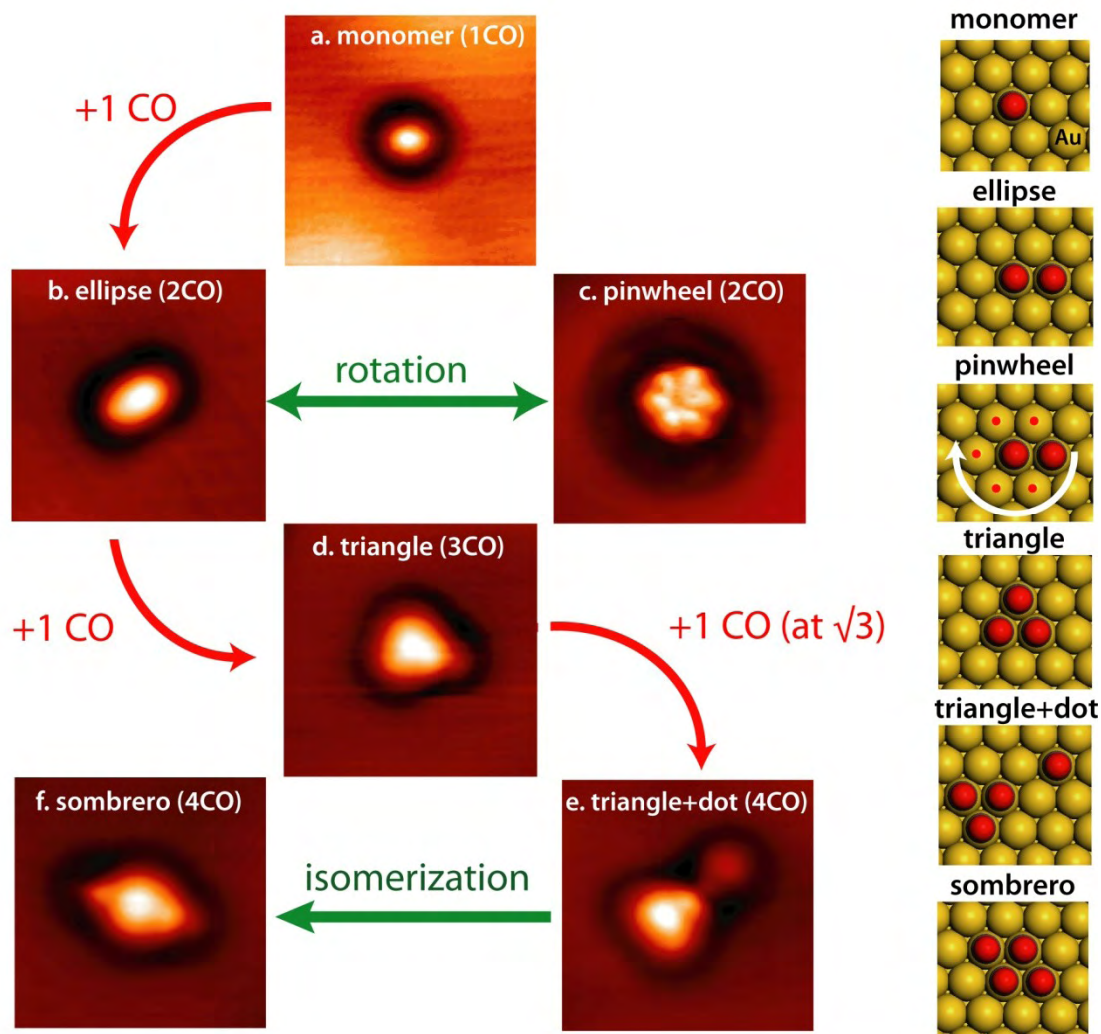


**Figure 4.3.** CO clusters on Au(111) surface that form spontaneously at  $T < 20$  K. STM images ( $U = -30$  mV,  $I = 25$  pA) of the CO clusters were obtained with a CO-covered tip. Scale:  $2.0 \times 2.0$  nm<sup>2</sup>. The green arrows show isomerization pathways of the cluster, that were observed experimentally. The red arrow is a logical connection derived on the basis of the STM images. a) Isolated upright CO molecule shown for reference; b) Elliptical dimer; c) Pinwheel-shaped dimer of CO molecules; d) Close-packed CO trimer. Addition of a single CO molecule at a  $\sqrt{3}$  position with respect to one vertex of the trimer leads to a triangle-with-a-dot tetramer; e) Triangle-with-a-dot CO tetramer; f) Sombrero-shaped CO tetramer, which is the isomer of e.

Right: structural models of the observed clusters derived from the STM images. The red circles mark the position of CO molecules. Small red dots in the pinwheel dimer mark the adsorption sites occupied by the orbiting CO molecule causing the dimer to rotate.

surface, and the six-fold pattern is centered on top of a Au atom (Fig. 4.4a). Occasionally we observed isomerization between the pinwheel dimer and the elliptical dimer (Fig. 4.4b). The elliptical dimer can further decompose into two isolated CO molecules (Fig. 4.4 c,d). The

composition, orientation, spacing and the apparent contrast of the elliptical dimer (Fig. 4.4b) unambiguously identify it as two CO molecules bonded to nearest neighbor Au atoms. Then, based on the triangulation of the pinwheel dimer and the similarity of the maximum apparent

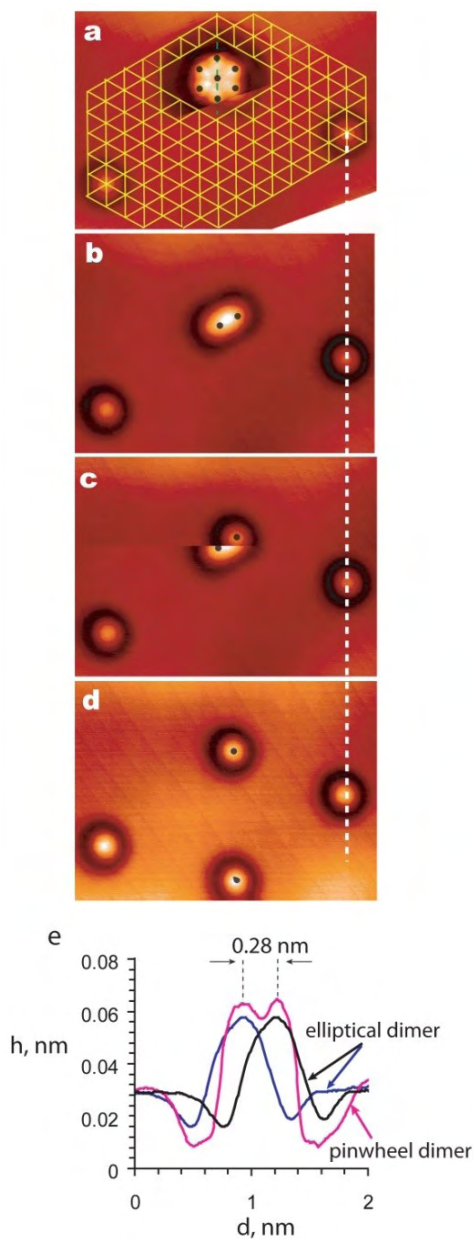
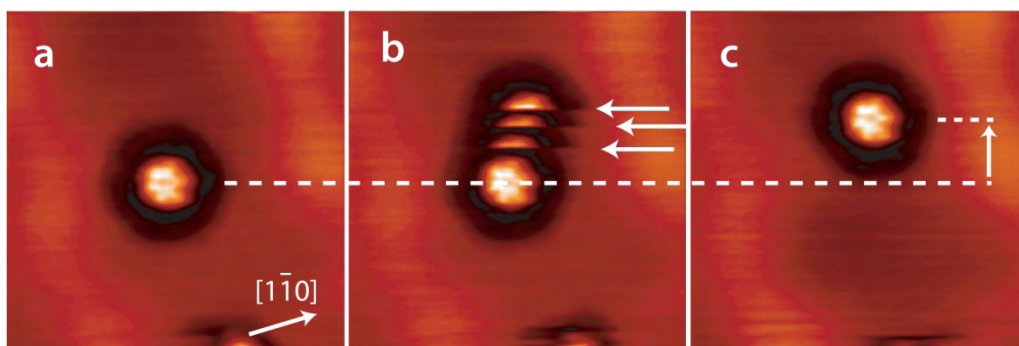


**Figure 4.4.** STM images of the tip-induced isomerization and decomposition of the CO dimers. a-d:  $U = -30$  mV; scale =  $4.1 \times 2.7$  nm<sup>2</sup>. a) Pinwheel-shaped CO dimer. Lattice mesh was derived on the basis of two isolated CO molecules in the corners of the image. Black dots mark positions of Au atoms derived from the lattice mesh. b) The pinwheel dimer spontaneously converts to an elliptical dimer where two CO molecules occupy nearest-neighbor Au atoms. c) The elliptical dimer further dissociates into two isolated CO molecules. The cut-off of the ellipse occurs at the instant of the dissociation. d) Two isolated CO molecules are the dissociation products of both dimers. e) Red: STM line-profile of the pinwheel dimer measured along the green dashed line in (a); Blue and Black: STM line-profiles of the elliptical dimer shifted by  $0.28$  nm (one lattice spacing on the Au(111) surface [56]) with respect to each other to mimic the profile across the pinwheel image. The apparent maximum of the elliptical dimer is located in the center between two CO molecules due to tip-interference effects [163].

height between the elliptical and the pinwheel dimers (Fig. 4.4e), we conclude that the pinwheel dimer image results from an unusual dynamic motion of a pair of CO molecules where one CO molecule acts as a center of rotation, and the other one orbits around it, by changing its adsorption site between the six Au atoms surrounding the central CO molecule.

## Controlled manipulation of CO-dimer



## Walking of triangle+dot CO-tetramer

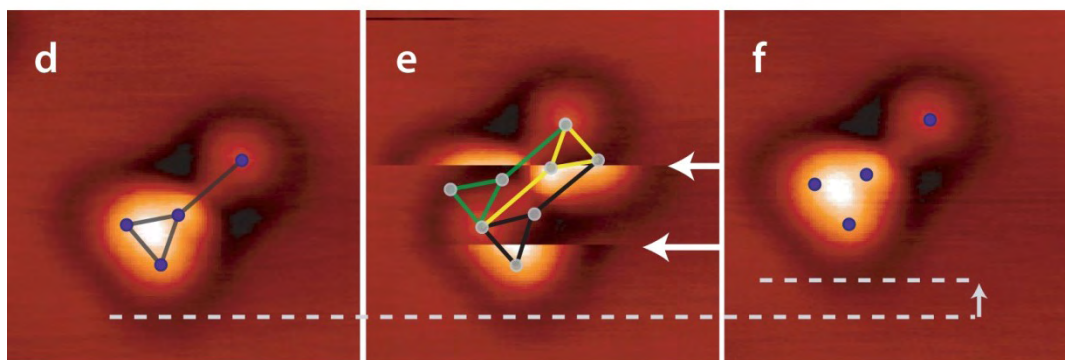


**Figure 4.5.** Tip-induced motion of the CO clusters.

**Controlled manipulation of the pinwheel CO dimer (scale:  $4.1 \times 4.1 \text{ nm}^2$ ).**

a) Before manipulation. b) Three pulses of +0.3 V were applied at an off-center position in the dimer image. Each pulse causes a shift of one lattice-spacing along the  $[\bar{1}01]$  direction. A white arrow marks the instant of the pulse in the imaging raster. c) After manipulation.

**Walking of the triangle+dot CO tetramer (scale:  $2.6 \times 2.6 \text{ nm}^2$ ).** The dots in the images mark the position of CO molecules on atop Au sites. d) Cluster before the motion ( $U = -30 \text{ mV}$ ). e) Images during cluster motion caused by two pulses ( $U = -50 \text{ mV}$ ). An overall shift of the cluster symmetry axis by  $\frac{1}{2}$  lattice spacing along the  $[11\bar{2}]$  direction occurs after each pulse. The event occurs twice, as marked by white arrows. The grey dots mark the positions of CO molecules that were occupied before both pulses (connected by black line); after the first pulse (connected by yellow line); and after the second pulse (connected by green line). f) Undecomposed triangle+dot cluster after two walking events in e ( $U = -30 \text{ mV}$ ).

So far tip-induced molecular rotation was reported only for single adsorbed molecules, such as alkanethiols on Au(111) (Chapter 3) and Cu(111) [178] surfaces. In these systems the hindered rotation of a relatively weakly-bound molecular species occurs around the metal-molecule bond at the surface. The case of the CO dimer is different in that: a) no chemical bonding exists between the CO molecules; b) chemical bonding of equal strength exists between each molecule and the metal substrate. Observation of the orbiting motion indicates that there is substantial attractive interaction between the CO molecules. Although the orbiting motion is tip-induced, the mechanism of the rotation may involve tunneling of the CO molecule between Au atop sites, similar to the case of single CO molecules on the Cu(111) surface at 5 K [89]. direction. The manipulation does not destroy the dimer, suggesting that either both CO molecules move as a whole structure or that one molecule is moved by the tip and the other one follows it restoring the initial dimer structure. Additional proof of the significant CO-CO attraction in the pinwheel dimer was obtained from the tip-assisted manipulation of the pinwheel dimer (Fig. 4.5a-c). The dimer could be shifted by applying a voltage pulse of +0.3 V at an off-center position within the bright part of the dimer image. Each pulse caused a shift of one lattice spacing ( $\sim 0.3$  nm) in the  $\langle \bar{1}01 \rangle$  direction.

The concerted motion of CO molecules leading to cluster motion occurs not only in the pinwheel dimer, but also in trimers and tetramers of CO. The cluster motion is observed when scanning the clusters at a bias of -50 mV (stable STM images were obtained at -30 mV bias). The cluster motion results in either the shift of the CO cluster a whole or its isomerization into a different cluster. An example is shown in Fig. 4.5d-f, where the triangle+dot CO cluster “walks” intact over the surface.

The spontaneous formation of CO clusters, the ability to manipulate the CO dimer without its decomposition, and the observation of the motion of intact clusters through the concerted motion of their component CO molecules, provide surprising evidence that the interaction between the CO molecules in their clusters is attractive, despite the fact that the molecules are adsorbed in a close-packed manner on the nearest-neighbor Au atoms. Moreover, observation of a particular arrangement of CO molecules in the clusters and preservation of this arrangement during cluster motion, imply that attractive interaction is characteristic of only particular cluster geometries. For example, inline cluster geometry for clusters larger than a dimer was never observed.

The origin of repulsion between CO molecules on the nearest-neighbor adsorption sites is commonly assumed to be due to electrostatic interaction of intrinsic and image dipole moments of the neighbor molecules. The degree of repulsion on the Au(111) surface (and the Ag(111) surface) is likely to be smaller than on the Cu(111) surface, since the lattice spacing on the Au(111) surface (0.284 nm on the fcc area of the herringbone reconstructed Au(111) [97]) is larger than on the Cu(111) surface (0.255 nm). This will reduce the repulsion between intrinsic CO dipole moments on Au(111) [206]. In addition, the small charge transfer between CO and Au(111) [190], compared to Cu(111), will reduce the dipole moment and its image for CO/Au(111), also reducing CO-CO repulsion energy. The resulting decrease in repulsive dipole-dipole forces between CO molecules on Au(111) may then enable close-range attractive interactions to dominate. One possible origin of the attractive interaction arises from the partial depletion of the d-electron density in the nearest-neighbor Au atoms around the adsorbed CO molecule [4], which should increase the binding energy of other CO molecules on top of these atoms. Another possibility is the modification of the van-der-Waals interaction between the adsorbed CO molecules as a result of adsorption on the Au(111) surface (the potential minimum for two gas-phase molecules is observed only at a larger distance of  $\sim 0.38$  nm [206]).

#### 4.4 CONCLUSIONS

In conclusion, we have shown that CO spontaneously forms distinct and stable clusters on the Au(111) surface, where the CO molecules are adsorbed on the nearest-neighbor Au atoms. The attractive interaction underlying the cluster formation leads to the ability to manipulate the clusters without their decomposition. Furthermore, the interaction between two CO molecules on the neighbor Au atoms results in an unusual dynamic behavior of the pair, where one CO molecule orbits around its partner during imaging by the STM tip, occupying six nearest-neighbor Au sites. These findings provide new insight into the fundamental question of the sign of the intermolecular interaction between CO molecules on a weakly-binding surface.

**PART II. STRESS EFFECTS IN ADSORPTION AND SELF-ASSEMBLY  
OF SMALL MOLECULES ON AU(111) SURFACE**

## 5.0 SITE-SELECTIVE MOLECULAR ADSORPTION OF CO, CH<sub>3</sub>SH AND CH<sub>3</sub>SSCH<sub>3</sub> MOLECULES ON THE HERRINGBONE RECONSTRUCTION OF Au(111)

The effect of the  $22\times\sqrt{3}$  herringbone reconstruction of the Au(111) surface on the adsorption of several small molecules was studied using scanning tunneling microscopy and density-functional theory (DFT). At low adsorbate coverage on the surface, CO, CH<sub>3</sub>SH and CH<sub>3</sub>SSCH<sub>3</sub> molecules preferentially occupy the fcc-stacked regions of Au(111). In case of the CO molecule, local saturation of the fcc-regions occurs prior to adsorption in other areas of the surface. Regions of the hcp-stacking exhibit intermediate affinity to all the studied molecules, and molecular adsorption is least preferential on the soliton walls of the herringbone reconstruction. From the quantitative analysis of CO adsorption from the STM data and the first principles calculations, we conclude that the adsorption site preference is well-correlated with the Au-Au interatomic distance in the lattice, with stretched surface regions being preferential for molecular adsorption.

### 5.1 INTRODUCTION

Straining of metal surfaces provides a way to control their chemical reactivity. In general, the binding energy of the adsorbed molecules is higher on the expanded lattice of a *d*-metal surface. The most successful concept that accounts for this trend is the d-band centroid theory by J. K. Nørskov et. al. [205]. Expanding the surface-lattice decreases the overlap of d-orbitals between neighbor metal atoms which results in an upward shift of the metal's d-band toward the Fermi level and increased surface reactivity. The d-band centroid theory explains the preferential adsorption of molecules on the Ru(0001) surface stretched by sub-surface implantation of argon [207], the Cu(100) surface strained by nitrogen-induced surface reconstruction [208] etc. The

theory also describes the trends in the chemical reactivity of bimetallic alloys [209, 210], where the top metal surface is strained to maintain registry with the underlying substrate.

Recent interest in strained metal surfaces was stimulated by the continuing search for ways to control molecular self-assembly on metal surfaces. Indeed, naturally occurring surface reconstructions as well as surface deformations in pseudomorphic metal alloys are potentially useful templates for molecular self-assembly [211, 212] due to a rich landscape of surface sites with varying reactivity.

The anisotropic compression of the Au(111) surface leading to the herringbone reconstruction [56] makes it a natural model-system to study the effect of lattice compression on surface reactivity. The surface layer of gold atoms is anisotropically compressed along one of three close-packed directions by the addition of one extra gold atom per 22 surface atoms. The average 4.5% lattice compression [56] produces uniaxial domains of fcc- and hcp- vertical stacking separated by soliton lines (discommensurate regions). The Au-Au interatomic distance is largest on the fcc-stacked areas and smallest on the soliton lines. Model calculations have shown that the surface stress on the gold atoms is tensile in the fcc-domain, compressive in the soliton and vanishingly small in the hcp-domain [97].

A varying affinity of adsorbed molecules for the fcc- and hcp-stacked regions of the herringbone reconstruction was reported several times. Preferential adsorption on the fcc-regions was observed for nitronaphthalene clusters on Au(111) [213], for C<sub>60</sub> [211, 214] as well as hexabenzocoronene on the atomic step sites that terminate the fcc-regions [212]. From the statistical analysis of benzene adsorption on Au(111) it was concluded that the soliton is the least reactive area on the surface [215]. Very recently NO<sub>2</sub> islands were reported to form preferentially in the fcc-regions of the reconstruction [105]. Thus chemically different adsorbates preferentially adsorb in the fcc-regions of the reconstruction.

In this paper we show that the preferential molecular adsorption on various sites of the Au(111) surface takes place in the limit of a vanishingly small adsorbate coverage (i.e. single-molecule level) provided the surface is first heated to a temperature when the adsorbate is mobile. Previously only molecular clusters or high adsorbate coverages were investigated, where there is an additional contribution due to intermolecular interactions. The single-molecule analysis presented here gives a more precise description of site preference on the Au(111) surface in the absence of intermolecular forces. In particular, the most strongly bonding sites are

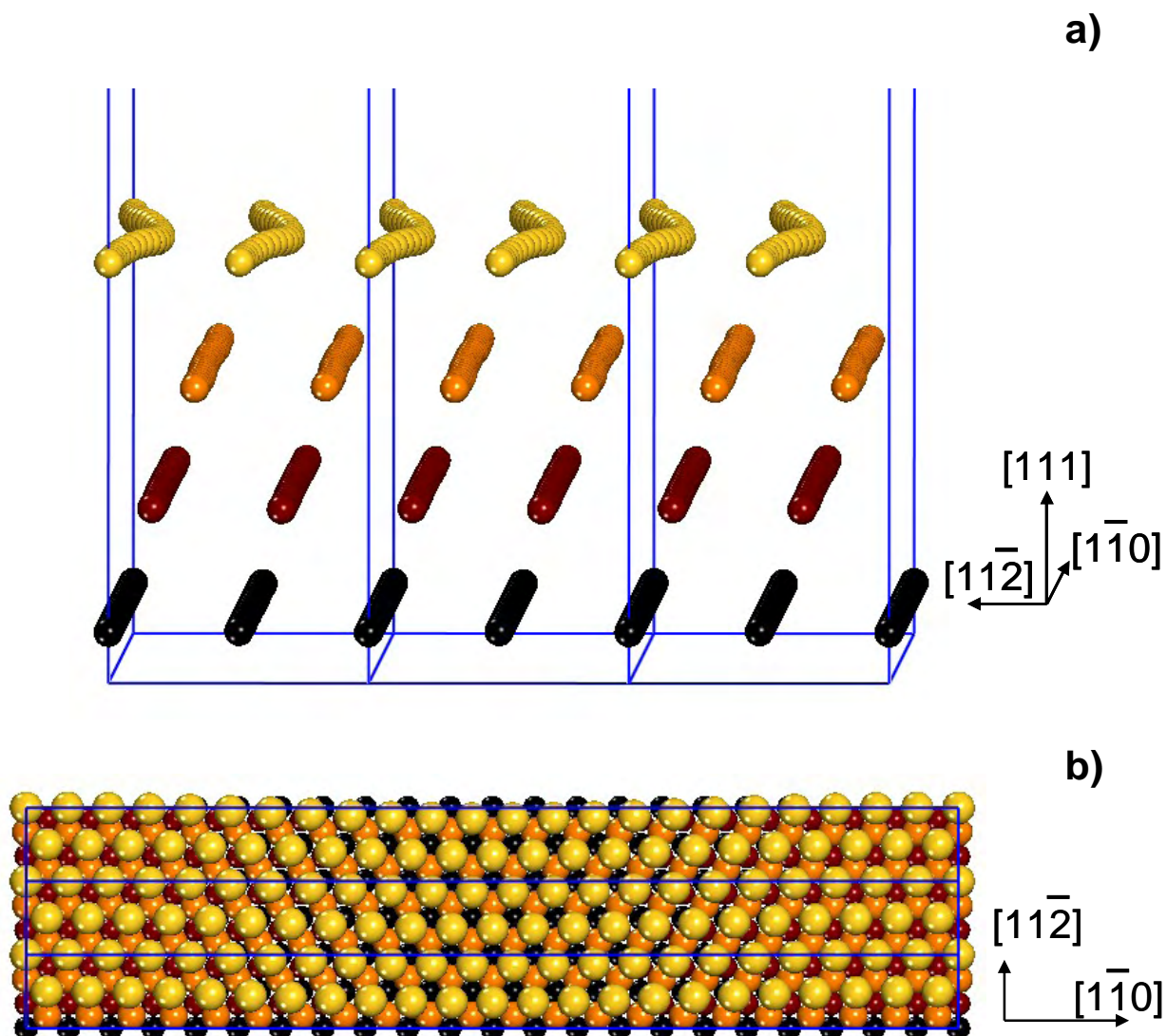


**Figure 5.1.** (a) Side and (b) top views of the  $22 \times \sqrt{3}$  unit-cell of the reconstructed Au(111) surface obtained from first-principles. For visualization purposes the slab has been repeated by three units along the  $[1\bar{1}2]$  direction and the atoms in deeper layers have been represented by increasingly darker colors.

at the *middle* of the fcc-region (the region is  $\sim 1.5$  nm wide). Also, the small expanded areas of the hcp-regions at the pointed elbows of the herringbone reconstruction are as preferential in molecular adsorption as the fcc-regions. Thus, minute variations of the lattice-spacing ( $< 1\%$  in the fcc-region) can produce observable changes of the adsorbate binding energy.

In the previous studies, the preferential adsorption in the fcc-regions was tentatively assigned to either the variation of the vertical stacking across the surface (e.g. Au atoms in the

hcp hollow sites are less reactive) or the anisotropy of the surface electron potential on the Au(111) surface [212, 215]. It is likely that both of these effects contribute to the variation of the adsorbate binding energy. We propose that the reactivity of the various regions of the Au(111) surface can be correlated with the Au-Au interatomic distance in the surface lattice. Local stretching or compression of the surface lattice affects the electronic states (in particular, the Shockley surface state and the d-band states) causing the variation of the adsorbate binding energy.

It is anticipated that the adsorption site-selection driven by small changes of the lattice constant across the surface will be observable for other surfaces with the herringbone reconstruction such as Ag/Ru(0001) [216] and Cu/Ru(0001) [209] as well as other surface reconstructions with anisotropic surface lattice [217], e.g. (5x20) reconstruction of Au(100) and Pt(100).

## 5.2 EXPERIMENTAL

Scanning tunneling microscopy experiments were conducted with a commercial Low Temperature STM (Omicron Nanotechnology) operating in an ultrahigh vacuum (UHV) chamber (background pressure  $< 5.0 \times 10^{-11}$  Torr). The Au(111) facet of the bead-crystal, melted from the gold wire, was cleaned by Ar<sup>+</sup> sputtering and annealing to 773 K. The Au(111) surface exhibited the well-known herringbone reconstruction. CH<sub>3</sub>SSCH<sub>3</sub> and CH<sub>3</sub>SH were purified using several freeze-pump-thaw cycles. CH<sub>3</sub>SH, CH<sub>3</sub>SSCH<sub>3</sub> and CO were deposited on the surface through an effusive beam doser while the crystal was in the STM imaging position at ~ 10 K. The crystal was subsequently heated using a PBN heater in the STM stage or simply by extracting the crystal from the STM stage for a short period of time. To increase imaging resolution, a single CO molecule was often picked up by the STM-tip. An adsorbed CO molecule is imaged as a protrusion with a halo with the CO-modified tip [218].

### 5.3 COMPUTATIONAL METHODS

The calculations were done using the Vienna *ab initio* simulation package (VASP) [219-221] based on density-functional theory and the pseudopotential approximation. The electron-ion interaction was described using the projector augmented wave (PAW) method of Blöchl [222] in the implementation of Kresse and Joubert [223]. All calculations were done using the PW91 generalized gradient approximation (GGA) of Perdew *et al.* [173, 224]

The calculations reported in this study were done using a slab model containing 256 Au atoms distributed over four layers (see Fig. 5.1). The surface layer is overpacked with two extra Au atoms. The surface vectors were taken along  $[1\bar{1}0]\times[11\bar{2}]$  directions of the  $22\times\sqrt{3}$  reconstructed surface. The adsorbate and the surface atoms in the topmost three layers were allowed to relax during optimizations while the bottom atoms of the slab were frozen at the bulk optimized positions.

Periodic boundary conditions were used, with the one electron pseudo-orbitals expanded over a plane wave basis set with a cutoff energy of 400 eV and a  $1\times 4\times 1$  ( $1\times 2\times 1$ ) Monkhorst-Pack grid of k-points for the (1x2) ((1x4)) slabs models [174]. In our previous study [166] we have shown that computations performed at this theoretical level were able to provide an accurate description of both the Au crystallographic parameters and the chemisorption properties of CH<sub>3</sub>SH on the Au(111) surface.

### 5.4 ADSORPTION OF SINGLE MOLECULES ON THE HERRINGBONE RECONSTRUCTION

All the molecules studied here (CO, CH<sub>3</sub>SH and CH<sub>3</sub>SSCH<sub>3</sub>) adsorb only weakly on Au(111). The surface temperature did not exceed ~10 K during gas dosing. To assure the observation of equilibrium distribution of molecules on the surface the crystal was annealed for several minutes at 40-80K after dosing. The STM images were taken after slowly cooling the crystal back to 5K. Since neither of the S-containing molecules dissociate in these experimental conditions [16, 44],

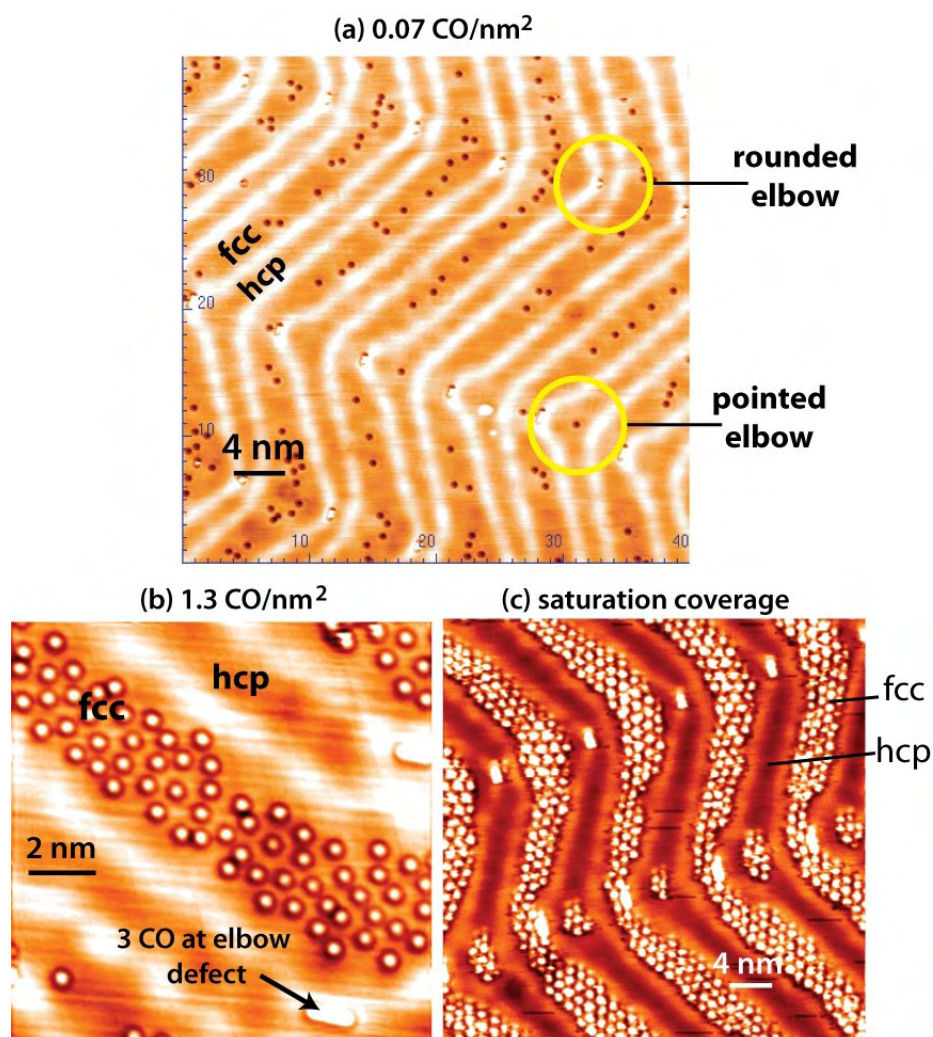


**Figure 5.2.** Site-selective adsorption of CO on the Au(111) herringbone reconstruction at different adsorbate coverages. The STM images were acquired with a metal-tip (a) and a CO-functionalized tip (b,c).

the herringbone reconstruction of the Au(111) surface remains intact. This is in contrast to the experiments at higher temperatures, where the S-containing molecules chemisorb on Au(111) via S-H and S-S bond dissociation, lifting the herringbone reconstruction [16]. Our discussion is centered on the CO adsorption because it is the smallest molecule considered here, binding atop of a gold atom and making it possible to compare the reactivity of different adsorption sites atom-by-atom. The calculated energy of CO adsorption on atop sites of the unreconstructed Au(111) surface is only 5.53 kcal/mol as determined in Ref. [190] at the PW91 exchange-correlation level and a 700 eV cutoff energy.

At very low coverage of  $<0.1$  molecules/nm<sup>2</sup>, CO molecules are observed only at the atomic steps and elbows of the herringbone reconstruction. Both of these sites contain coordinatively unsaturated Au atoms [166] which causes their higher reactivity. Each elbow site adsorbs up to three CO molecules. At a slightly higher adsorbate coverage of  $\sim 0.07$  molecules/nm<sup>2</sup>, preferential adsorption of CO in the fcc-stacked regions of the herringbone

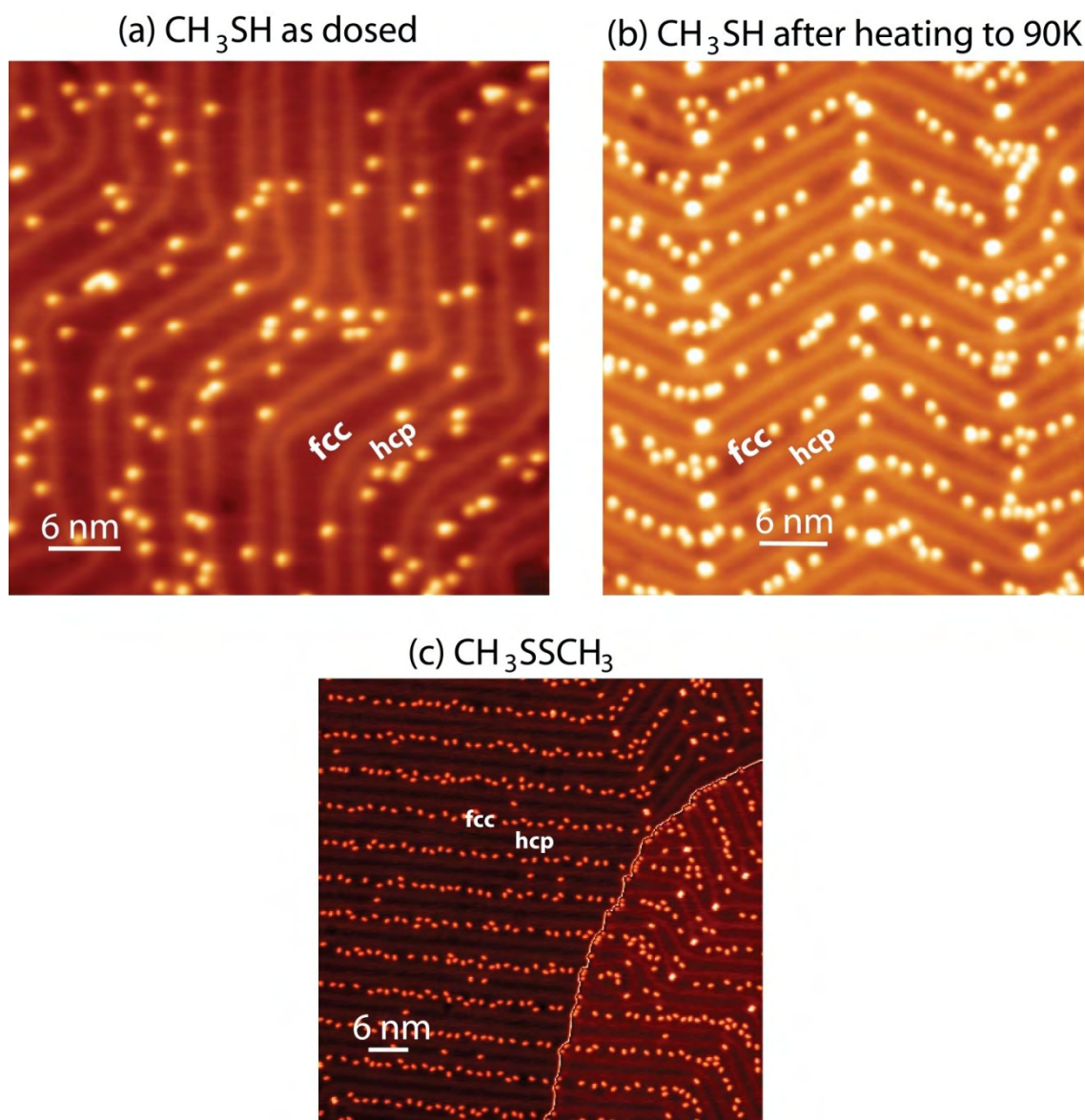


**Figure 5.3.** Site-selective adsorption of CH<sub>3</sub>SH and CH<sub>3</sub>SSCH<sub>3</sub> on the reconstructed Au(111) surface. The distribution of molecules dosed on the surface at 10K is nearly random (a) and becomes ordered after heating the surface to 90K (b,c).

reconstruction can be clearly seen (Fig. 5.2a). The soliton lines and the hcp-regions are nearly free of CO molecules. However, CO molecules are also adsorbed in hcp-region of the pointed elbow (Fig. 5.2a).

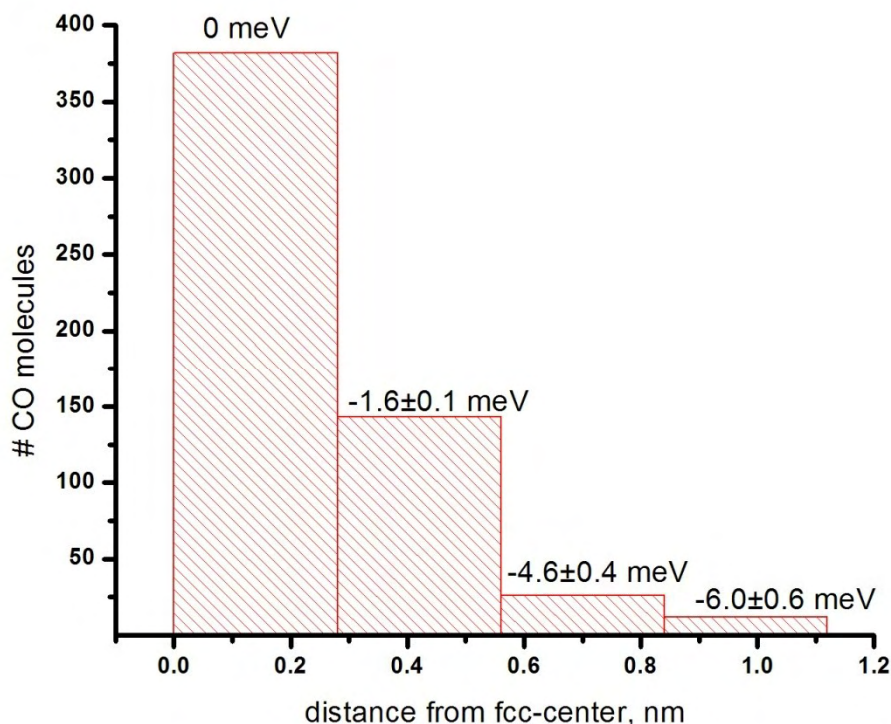


**Figure 5.4.** Distribution of 575 CO molecules within the fcc-region. The energy values correspond to decrease in the binding energy relative to its center calculated from the Boltzman distribution at  $T=20$  K.

Preferential adsorption of CO in the fcc-regions of Au(111) is rather dramatic and extends to higher coverages. As seen in Fig. 5.2b, the local CO coverage in the fcc-regions can increase by more than an order of magnitude to  $\sim 1.3$  molecules/nm<sup>2</sup>, without any substantial population of the hcp-regions or the soliton lines. At this coverage, the minimum CO-CO intermolecular separation decreases to  $\sim 5$  Å ( $\sqrt{3}$  – configuration). Finally, the fcc-regions can be locally saturated (Fig. 5.2c). The number of CO molecules is difficult to establish reliably at this coverage, because the molecules aggregate into clusters [200, 218] which then form a

superlattice. Nevertheless, most of the hcp-regions are still clean except for the hcp-patch in the pointed elbow, which is also saturated by CO-clusters (Fig. 5.2c).

The other molecules studied here, CH<sub>3</sub>SH and CH<sub>3</sub>SSCH<sub>3</sub>, behave similarly to CO. The binding energies for the molecules on an unreconstructed Au(111) surface calculated here are 0.37 eV for CH<sub>3</sub>SH and 0.45 eV for CH<sub>3</sub>SSCH<sub>3</sub>. The temperature onset of substantial surface diffusion for both molecules is at 50-60K. When the molecules are dosed on the Au(111) surface at 10K, the distribution of molecules is nearly random (Fig. 5.3a) After heating to 90K and cooling back to 5K for imaging, both molecules are seen to preferentially occupy fcc-regions and hcp-regions at the pointed elbows (Fig. 5.3b,c).

## 5.5 STATISTICAL ANALYSIS OF CO ADSORPTION ON THE FCC-REGION

To explore the correlation between the lattice constant and the chemical reactivity on the Au(111) surface, the positions of isolated CO molecules in the fcc-region were determined relative to the soliton walls. The width of the uniform fcc-region is commonly assumed to be ~1.5 nm because the variation of the Au-Au distance amounts to <1% within this area [97]. Nevertheless, it is easy to see that CO molecules are not uniformly distributed in the fcc-region and tend to adsorb in *the middle* of the fcc-region at very low coverages (Fig. 5.2a). The statistical distribution of molecular locations was obtained from the analysis of 575 isolated CO molecules. The middle of the fcc-region was determined as an equidistant point between the soliton lines decorating the fcc-region. Most of the data was obtained with a tip that clearly images the center of an adsorbed CO molecule. The lateral resolution of the raw STM images is 1 Å and it was digitally increased for more accurate image processing. The offset data were distributed among 2.8 Å-wide bins which is roughly the average calculated Au-Au lattice spacing along direction. The exact choice of the bin-size does not substantially affect the conclusions derived here. CO-molecules spaced by < 1 nm were not counted to exclude the effect of the intermolecular interactions.

The resulting distribution is shown in Fig. 5.4. The preference for the fcc-centered position of the CO molecule is rather striking. The variation of the binding energy along the fcc-region can be estimated from Fig. 5.4 using the Boltzmann distribution [225]:

$$\frac{n_i}{n_0} = \exp\left(-\frac{\Delta E}{kT}\right) \quad (5.1)$$

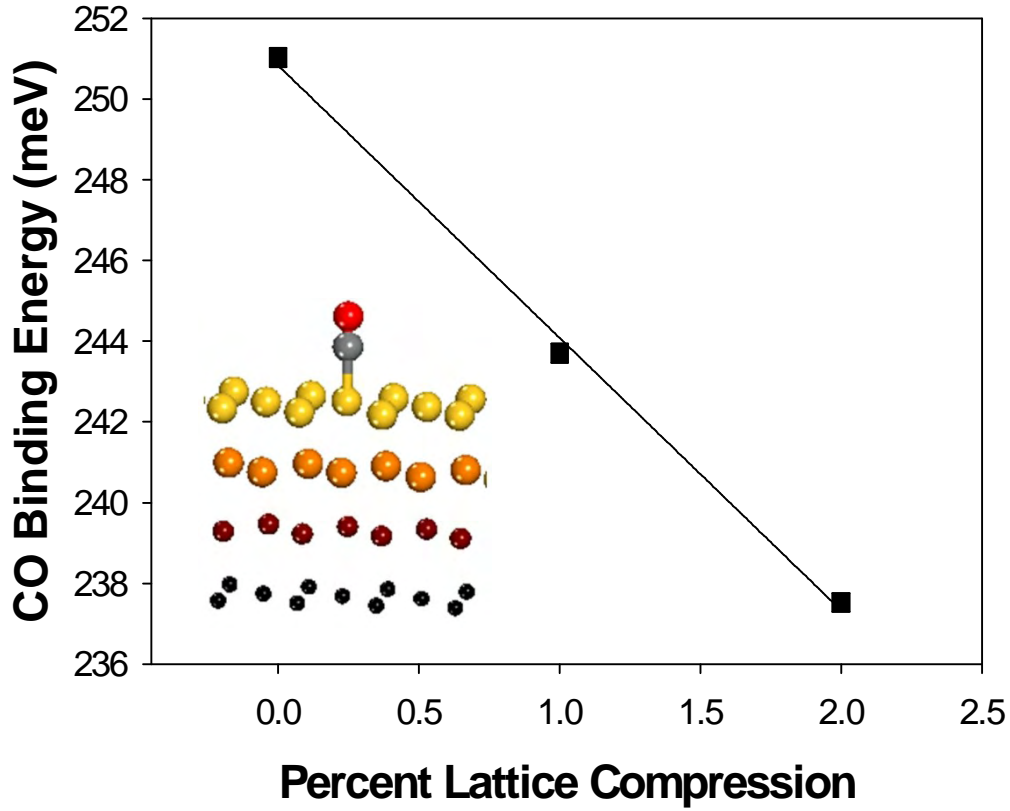


**Figure 5.5.** CO binding energy as a function of the anisotropic lattice compression of the Au(111) surface along  $[1\bar{1}0]$  direction calculated in the  $(3 \times 1)$  unit-cell with shown in the figure (the lattice vectors of the unit-cell run along  $[1\bar{1}0]$  and  $[11\bar{2}]$  directions).

where  $n_i$  is the number of molecules in bin- $i$ ,  $n_0$  is the number of molecules in bin-0 in the center, and  $\Delta E$  is the difference in adsorption energy between molecules adsorbed in bin- $i$  and bin-0.  $T$  is the temperature onset of molecular diffusion, which is  $\sim 20\text{K}$  [218]. As seen in Fig. 5.4, the

binding energy of CO molecules decreases by  $\sim 5$  meV at the edge of the fcc-region, which is located 7-8 Å angstroms from the center. Qualitatively similar behavior is observed for CH<sub>3</sub>SH

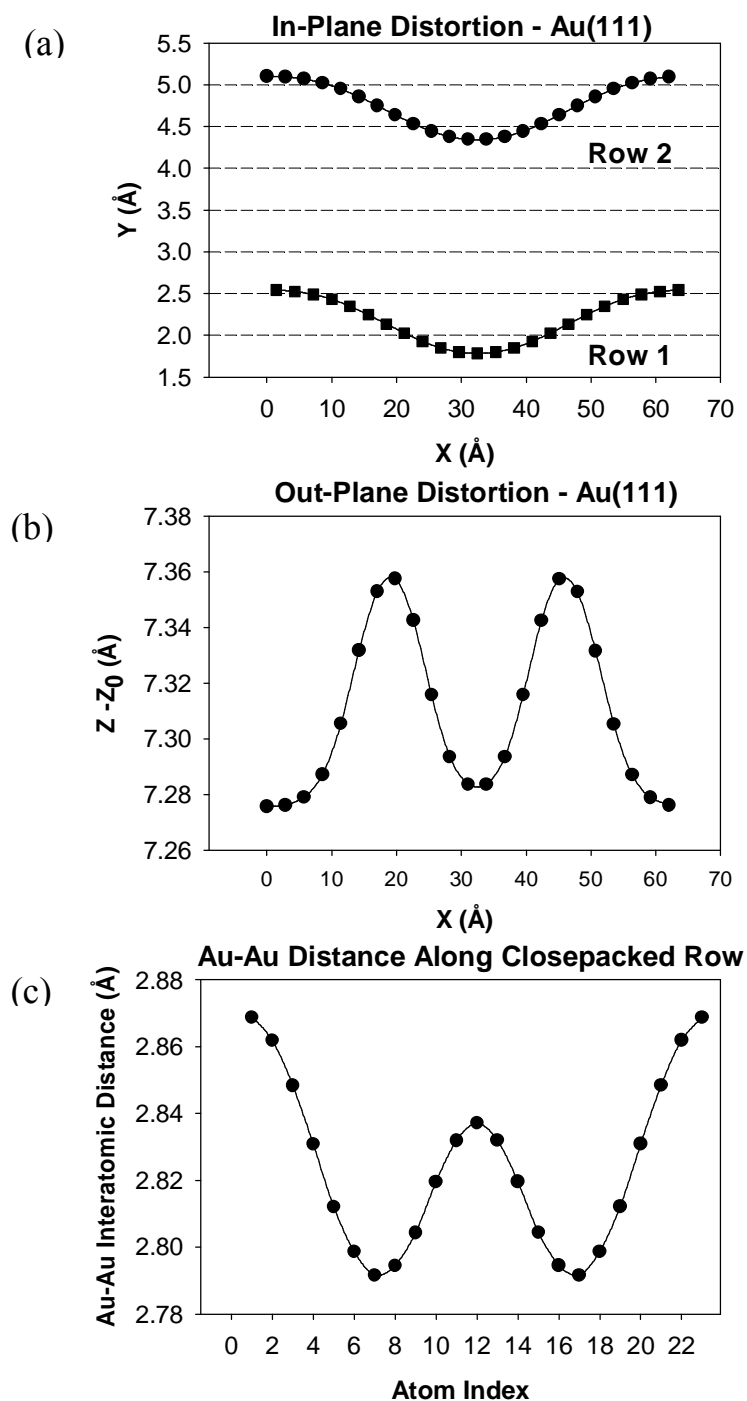


**Figure 5.6.** Variation of the atomic coordinates in horizontal (a) and vertical (b) planes for the Au atoms in the top layer of the slab. Here x, y and z coordinates are taken along  $[\bar{1}\bar{1}0]$ ,  $[1\bar{1}\bar{2}]$  and  $[111]$  directions, respectively and  $Z_0$  denote the vertical coordinates of the atoms at the bottom of the slab. (c) The variation of the Au-Au distance along the chain in the top layer (along  $[\bar{1}\bar{1}0]$  direction).

and  $\text{CH}_3\text{SSCH}_3$  (Fig. 5.3), although the higher temperature onset for molecular diffusion (these molecules are more strongly bound than CO) produces a more uniform distribution of molecules within the fcc-region.

## 5.6 DISCUSSION

The structural difference between the fcc- and the hcp-region is two-fold: (1) the vertical stacking of surface Au atoms is different; (2) the surface lattice in the hcp-region is compressed relative to the fcc-region. Both of these are likely to affect the binding energies of molecular adsorbates. From the experimental observations it is possible to identify the effect of lattice expansion. There is a clear tendency for CO molecules to adsorb in the middle of the fcc-region, where the Au-Au lattice spacing is largest. In addition, all three molecules studied here, CO,  $\text{CH}_3\text{SH}$  and  $\text{CH}_3\text{SSCH}_3$  molecules preferentially adsorb in the hcp-region at the rounded elbow even at a small adsorbate coverage. The hcp-stacked domain expands in the pointed elbow (Fig. 5.2a) and the Au-Au interatomic distance is increased. Conversely, the hcp-stacked domain is narrowest in the rounded elbow (Fig. 5.2a) and the molecules do not adsorb there up to near-saturation coverage (not shown). Therefore stretching of the Au(111) surface lattice increases its reactivity, in agreement with the d-band centroid theory [205]. Nevertheless, the effect of vertical stacking cannot be ruled out from the experimental observations. DFT calculations were employed to gain further understanding of the problem.

### 5.6.1 DFT Calculations of CO Adsorption on Au(111)

The effect of lattice compression of the Au(111) surface on the binding energy of CO and  $\text{CH}_3\text{SH}$  molecules was calculated using a slab model with 4 atomic layers and a (3x1) supercell (Fig. 5.5). The lattice vectors of the supercell run along  $[1\bar{1}0]$  direction (periodicity  $3 \times 2.951 \text{ \AA}$ ) and along  $[11\bar{2}]$  direction (periodicity  $1 \times 5.112 \text{ \AA}$ ). Gold atoms in the bottom layer were frozen

at their bulk-optimized positions. Anisotropic compression was introduced by varying the periodicity of the supercell along  $[1\bar{1}0]$  direction. The binding energy of CO molecules was calculated at 1% and 2% lattice compression. As seen in Fig. 5.5, the binding energy decreases almost linearly for compressed lattices with a slope of 6 meV/% compression. Experimentally the CO binding energy decreases by  $\sim 5$  meV upon 0.8% lattice compression, which is very close to the calculated values. Therefore, the correlation between the adsorbate binding energy and the Au-Au lattice spacing on the reconstructed Au(111) surface is supported experimentally and theoretically.

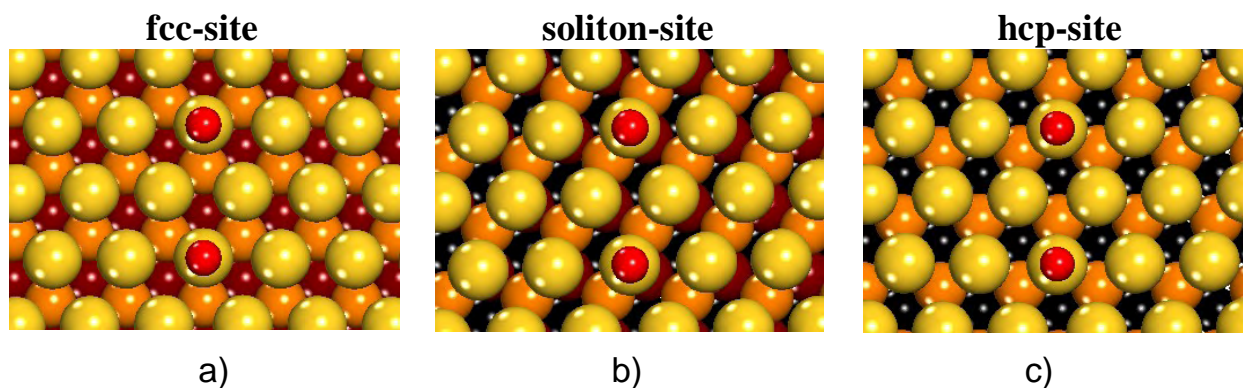


**Figure 5.7.** Adsorption configuration of CO in the  $22\times\sqrt{3}$  unit-cell of the reconstructed Au(111) surface. The surface Au atoms at increasingly deeper layers are depicted in darker colors. Configurations (a) is the CO molecule on the fcc-site, (b) on the soliton and (c) on the hcp site.

A second calculation was carried out involving a full unit-cell of the herringbone reconstruction. As described in Section 3, the size of the slab was a very large 256 Au atoms. To our knowledge this is the first ab-initio calculation of the “herringbone” reconstructed surface. At first, the bare surface slab was constructed as a  $22\times\sqrt{3}$  super-cell of the 4 layer-thick bulk terminated slab. The optimized structure is shown in Fig. 5.1. The lateral distortion of the surface along the  $[1\bar{1}0]$  direction and the presence of the fcc- and hcp-stacked regions are well-reproduced as can be seen from Figures 5.6 (a,b) where the variation of the atomic coordinates is shown both in plane (Fig. 5.6a) and normal to the surface (Fig. 5.6b). The buckling of the lattice normal to the surface (Fig. 5.6b) is 0.08 Å, which is smaller than the experimentally observed value of 0.2 Å [56]. Most likely this is due to a slight overestimation of the lattice dimensions commonly observed in DFT plane-wave calculations of 5d-metals and some other materials using the GGA functional [226, 227]. In qualitative agreement with the previous report [97], the

interatomic Au-Au distance along  $[1\bar{1}0]$  direction in the surface layer is largest in the fcc-region (2.868 Å), intermediate in the hcp-region (2.837 Å) and smallest in the soliton-region (2.791 Å) (Fig. 5.6c). The maximum theoretical local compression of the interatomic distance is therefore 2.68% for the soliton region relative to the fcc region.

After surface optimization, the adsorption configurations of CO on the  $22\times\sqrt{3}$ -reconstructed surface were determined in three separate calculations, where the molecule was adsorbed atop of a Au atom in the center of the fcc-region, hcp-region and the soliton (see Figure 5.7a-c). The corresponding bonding energies were calculated to be 0.22, 0.19 and 0.17 eV for the fcc, hcp and soliton regions, respectively. The CO binding energy in the fcc-region is therefore  $\sim 30$  meV higher compared to the hcp-region and 50 meV higher compared to the soliton-region. If lattice compression were the only influential effect, the binding energy of the CO molecule in the hcp region would be expected to be only 6 meV smaller than in the fcc-region (according to Fig. 5.5 and considering  $\sim 1\%$  lattice compression), while the calculated difference is 5 times larger. Although the small binding energies approach the limit of computational accuracy, we still consider the difference to be significant and attribute it to the effect of the hcp-stacking. Similar reasoning applies to the low CO binding energy calculated for the soliton region.

### 5.6.2 Electronic effects in adsorption site selection on the herringbone reconstruction

The projected bandgap centered on the  $\bar{\Gamma}$ -point in the surface Brillouin zone of the Au(111) surface supports a Shockley surface state, with a minimum energy at 450 mV below the Fermi level. The electrons in the surface state form a highly polarizable 2D electron-gas. Adsorbed CO molecules are expected to interact repulsively with the surface state electrons (in the sp-bands) [225] because of the reduced back-donation of electrons [228] from the  $5\sigma$  orbital of CO to the sp-band. If the surface state density becomes inhomogeneous due to a strong scattering center (e.g. atomic step) or varying surface potential (as on Au(111)), molecular adsorption will preferentially occur in the regions of surface state depletion. This was experimentally observed for CO molecules adsorbed on the Ag(111) surface, although the energetic effect of the surface state repulsion was  $\sim 1$  meV and did not cause long-range ordering of the adsorbate [225].

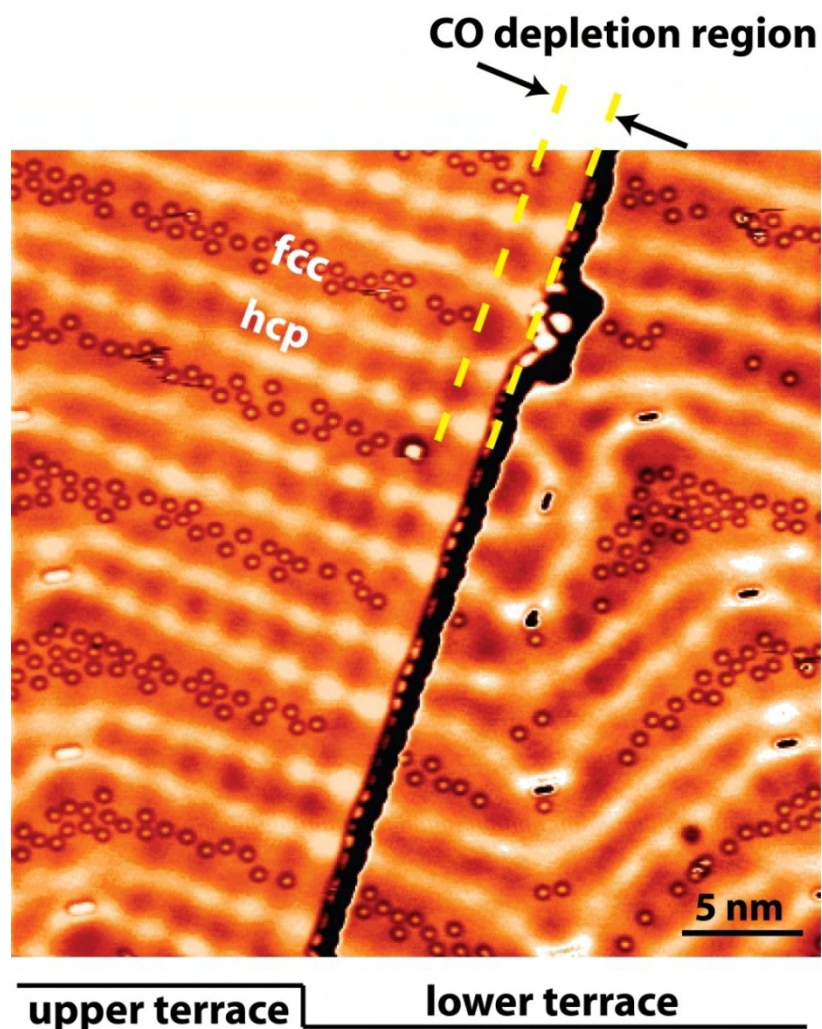


**Figure 5.8.** CO adsorption on Au(111) in the vicinity of the single-atom step. The oscillatory pattern of the Shockley surface state due to scattering at the step is clearly visible. The depletion region where no CO molecules are observed in the fcc-regions near the step is 1.7 nm wide, which is roughly one half of the Fermi wavelength of the Shockley surface state.

The anisotropic compression of the Au(111) surface causes a periodic variation of the surface electronic potential, which modifies the surface-state distribution [128]. In particular, the surface state density is highest on the soliton walls and smallest in the fcc-regions. The surface state is essentially concentrated in the regions of compressive stress. Therefore the preferential adsorption of adsorbates in the fcc (and other) regions of the herringbone reconstruction can also contain a surface-state contribution.

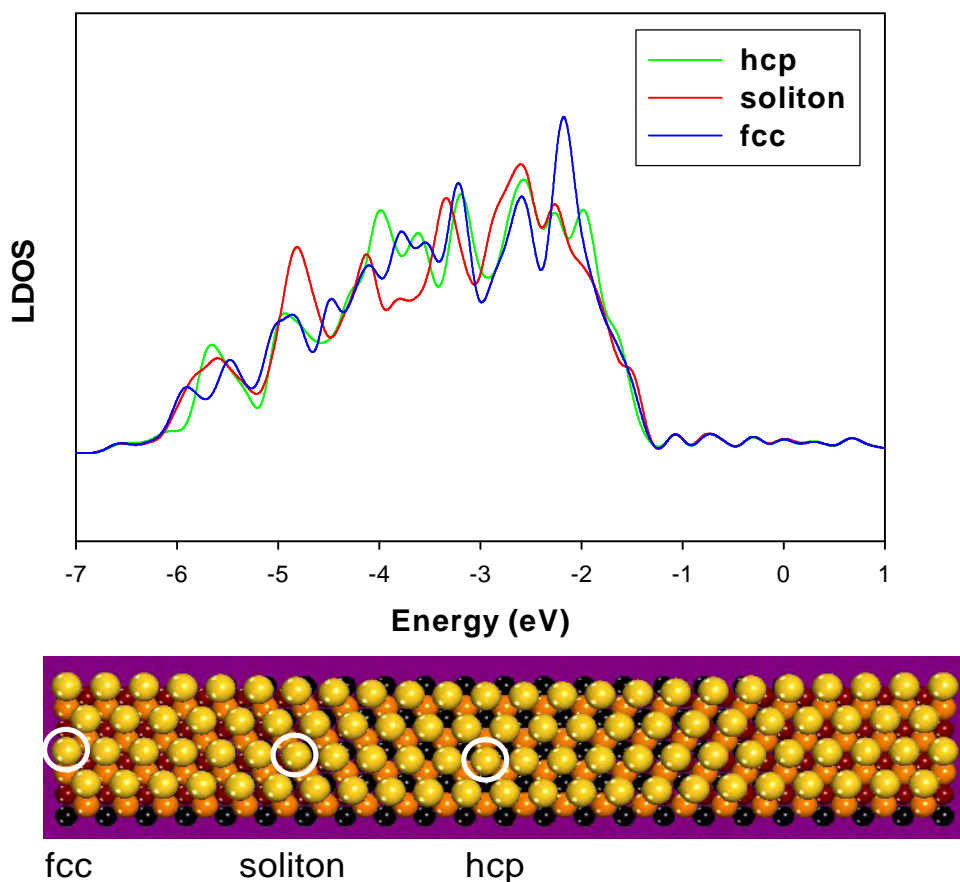


**Figure 5.9.** Local density of states in arbitrary units of the surface Au atoms at the fcc, soliton and hcp sites.

The sign of interaction of adsorbed CO molecules with the surface-state electrons can be qualitatively determined from the molecular distribution in the vicinity of the single-atom step, where the surface state is significantly perturbed [225]. The STM image of the single-atom step in Fig. 5.8 was taken at a small tunneling voltage of -10 mV (sample negative) to measure the spatial variation of the density of electronic states near the Fermi level of the metal surface. Periodic oscillations of the topography are observed in the vicinity of the step, which are due to Friedel oscillations of the local density of surface state due to scattering at the step [127, 229]. The CO molecules repel from the surface state on Au(111). The repulsive interaction is manifested in the depletion of CO molecules from the fcc-region (Fig. 5.8) within a distance of  $\sim 1.7$  nm normal to the step. This distance also matches closely one half of the Fermi wavelength of the surface state on Au(111) [230]. Therefore, local enhancement of the surface state density near the atomic step decreases the binding energy of CO molecules.

However, we suggest that the local variation of the surface-state density across the herringbone reconstruction cannot fully account for the preference of adsorption sites. From the detailed theoretical analysis, Gajdos et.al. [190] established that the major orbital interaction for CO bonded on top of the gold atom in the Au(111) surface is the overlap of  $5\sigma$  CO-orbital and  $d_{z^2}$ Au-orbital. Therefore stress-induced variations in the surface  $d$ -band must influence the adsorption energy of the molecule. According to the  $d$ -band centroid theory [205], stretching of the metal surface lattice will increase its reactivity, which would make the fcc-regions preferential for molecular adsorption. This argument is not directly applicable to the Au(111) surface because the small energy shift of the  $d$ -band centroid between different regions of the surface. However, our calculation of the  $d$ -band DOS for the gold atoms in the fcc, hcp and the soliton regions shows a significant variation of the fine-structure of the  $d$ -states (Fig. 5.9), which may affect the binding energy of the adsorbates.

Furthermore, both theoretical calculations presented here agree well with the experimental observations despite the fact that only thin surface slabs with four atomic layers were used. Such thin slabs do not provide a correct description of the surface-states [231]. The surface state penetrates into the bulk region by as much as several nanometers, while the width of the 4-layer slab is only  $\sim 8$  Å. Therefore the surface states of the top and the bottom slab surfaces will interact substantially producing a large energy splitting of the two states [231] (the splitting was calculated to be as much as 1.5 eV for 4-layer slabs of Ag(111) [231]). Neither of these split states correctly describes the true surface state. Proper description of the surface state requires thicker slabs of 10-17 layers [232] which are difficult to calculate in first principles calculations given the already large size of the herringbone supercell.

## 5.7 CONCLUSION

We have presented a detailed study of adsorption of several small molecules (CO, CH<sub>3</sub>SH and CH<sub>3</sub>SSCH<sub>3</sub>) on Au(111) surface with herringbone reconstruction. Previously reported preferential adsorption on the fcc-stacked domains of the reconstruction was explored in the limit of small adsorbate coverage, where intermolecular interactions are negligible and the reactivity of individual gold atoms can be analyzed. We developed a more detailed picture of site-selection

on the herringbone reconstruction: the CO molecules preferentially adsorb in the *center* of the fcc-stacked regions; the hcp-stacked regions in the pointed elbows of the herringbone reconstruction are as preferential as the fcc-stacked regions. CO-adsorption is remarkably site-selective, and local saturation of the fcc-regions can be achieved without substantial population of the rest of the surface. Altogether, molecular adsorption is found to be preferential on the stretched surface lattice. To support this hypothesis CO and CH<sub>3</sub>SH adsorption was analyzed by DFT on artificially compressed slab-models and good agreement with experiment was obtained. The preference of the stretched regions is likely to be a combined electronic effect of the Shockley surface state and the d-band states. Theoretical calculations also show that changes of the vertical stacking order from fcc to hcp across the surface may have an additional contribution to the site-preference on the reconstructed Au(111) surface.

## **6.0 MOLECULAR SELF-ASSEMBLY GUIDED BY SURFACE RECONSTRUCTION: CH<sub>3</sub>SH MONOLAYER ON THE AU(111) SURFACE**

Self-assembly of methanethiol (CH<sub>3</sub>SH) on Au(111) was studied using scanning tunneling microscopy at  $T < 150$  K when the S-H bond is intact. The CH<sub>3</sub>SH monolayer assumes a commensurate structure with a  $\begin{pmatrix} 6 & 2 \\ 0 & 2 \end{pmatrix}$  unit-cell. Only one of three possible azimuthal domains of the monolayer was observed, with domain walls pinned at the rotational boundaries of the herringbone reconstruction. From a real-time observation of monolayer formation at  $T = 60$  K we propose a phenomenological model for the growth of preferential domains, which is based on the interplay between molecular detachment from domain boundaries and surface mass transport anisotropy on Au(111) due to its herringbone reconstruction.

### **6.1 INTRODUCTION**

Molecular self-assembly is among the most promising methods for the future nanotechnology of controlled bottom-up construction [15, 16, 22, 233]. It involves the spontaneous formation of an ordered molecular overlayer that results from the balance of the molecule-substrate and molecule-molecule interactions. Although a great variety of self-assembled structures have been studied to date, new ways of self-assembly are constantly being discovered [213, 234-237].

Au(111) surface is a widely used substrate for molecular self-assembly on metals because it is relatively inert and stable in the ambient environment [16, 22, 233]. The periodic variation of the sign and magnitude of surface stress on the gold atoms produced by the herringbone reconstruction [238] may have an effect on molecular self-assembly. In most cases this effect was found to be insignificant: Au(111) acts as a nearly perfect close-packed hexagonal substrate.

Therefore the domain orientation of the self-assembled molecular layers exhibits little or no coherence with the underlying structural features of the herringbone reconstruction (such as elbows and rotational domains) [239-241].

In several reports the lattice distortion caused by the herringbone reconstruction was shown to influence molecular self-assembly. The long chain alkanes conformationally adapt to the distorted lattice in order to maintain the maximum binding strength of the chain carbon atoms to the surface [242]. The strength of hydrogen-bonding between the molecules of an aromatic carboxylic acid was predicted to vary by as much as 30% depending on the orientation of the molecular domain relative to the underlying lattice [239]. Various intermediate close-packed structures of azobenzene were shown to be influenced by the structural features of the herringbone reconstruction [243]. Self-assembled structures in some cases were reported to grow selectively in the fcc-stacked regions of the herringbone reconstruction [105, 213, 244].

We investigated the self-assembly of methanethiol ( $\text{CH}_3\text{SH}$ ) on the Au(111) surface, which is significantly influenced by the herringbone reconstruction.  $\text{CH}_3\text{SH}$  forms a commensurate monolayer with an oblique unit-cell, where the smallest vector *always* coincides with the vector of anisotropic compression of the gold surface lattice. Therefore the  $\text{CH}_3\text{SH}$  monolayer is composed of only one domain instead of expected three rotationally equivalent domains. On a larger scale the periodic rotation of the vector of anisotropic compression translates into the periodic rotation of the preferred  $\text{CH}_3\text{SH}$  monolayer domain, with sharp domain boundaries spaced by  $\sim 15$  nm. To the best of our knowledge, only one other molecular system, 2,2'-bipyridine on the Au(111) surface [245], was reported to have a similar self-assembly behaviour as  $\text{CH}_3\text{SH}$ . We propose a connection between  $\text{CH}_3\text{SH}$  and 2,2'-bipyridine monolayers indicating that the observed effect might be generic for a large number of molecules.

Specifically, we argue that the observed modulation of the  $\text{CH}_3\text{SH}$  monolayer by the herringbone reconstruction has a kinetic rather than thermodynamic origin that stems from the interplay between molecular detachment rates at molecular domain walls and the anisotropy of surface stress on the Au(111) surface [238]. We establish this based on the real-time observation of the ordering process, as well as the detailed knowledge about the adsorption of a single  $\text{CH}_3\text{SH}$  molecule on the Au(111) surface [166].

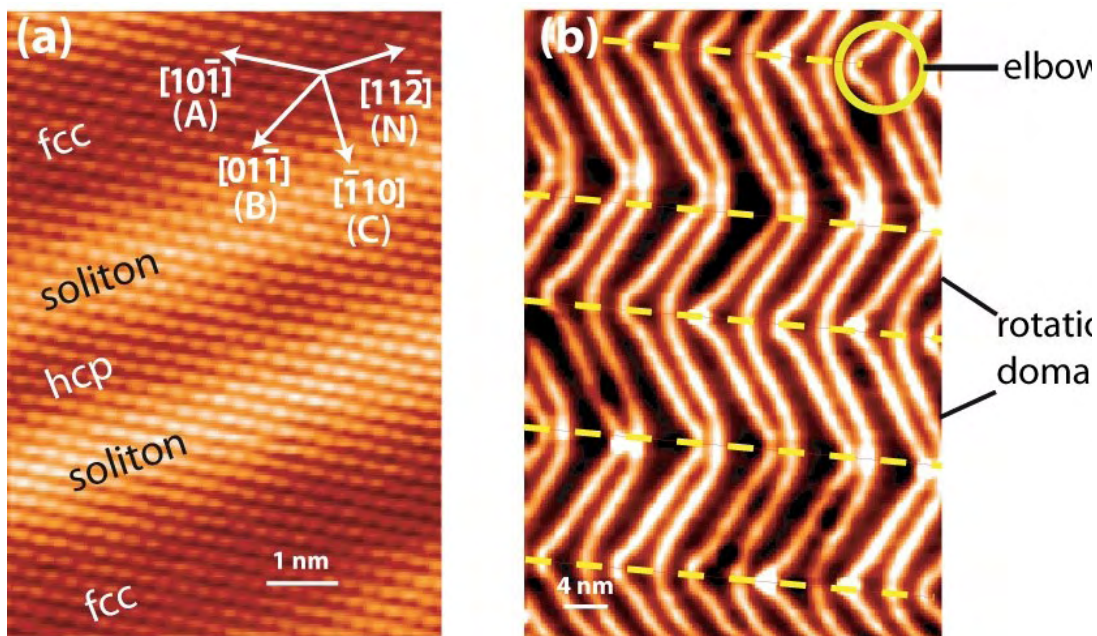


**Figure 6.1.** STM images of clean Au(111) surface with  $22\times\sqrt{3}$  herringbone reconstruction. ( $V = -0.143$  V,  $I = 43$  pA ).

- a) atomically-resolved close-up image showing the regions of fcc- and hcp-stacking as well as the in-plane distortion of the surface lattice along the  $[11\bar{2}]$  direction due to the uniaxial compression along the  $[\bar{1}10]$  direction.
- b) a large-scale image of rotational domains of the herringbone reconstruction. Yellow dashed lines mark the position of the rotational domain boundary where crystallographic direction of the anisotropic lattice compression is rotated by  $60^\circ$ .

## 6.2 EXPERIMENTAL

$\text{CH}_3\text{SH}$  was deposited on a clean Au(111) surface through an effusive beam doser while the crystal was in the STM imaging position at  $T < 10$  K. The STM images presented here were taken in the temperature range from 5-60K. Scanning at temperatures above 5K was accomplished using counter-heating via a PBN heater located close to the sample in the STM stage. The sample temperature was monitored using a Si-diode installed in the STM stage.

### 6.3 CH<sub>3</sub>SH MONOLAYER MODULATED BY THE HERRINGBONE RECONSTRUCTION

For the clarity of presentation, we will label the surface lattice directions as shown in Fig. 6.1:  $C$  –  $[\bar{1}10]$  close-packed direction of anisotropic compression,  $N$  –  $[11\bar{2}]$  direction normal to  $C$ -direction,  $A$  or  $B$  – close-packed directions at  $60^\circ$  relative to  $C$ -direction. The lattice spacing between two gold atoms along  $C$ -direction is contracted on average by 4% to  $\sim 2.75 \text{ \AA}$  [238], while the lattice spacing along  $A$ - and  $B$ -directions – by 2% to  $\sim 2.82 \text{ \AA}$ .

All the experiments were done at low temperatures ( $T < 150\text{K}$ ) where the S-H bond in the CH<sub>3</sub>SH molecule remains intact on Au(111) [16]. CH<sub>3</sub>SH adsorbs only weakly in this case, with a binding energy of  $< 10 \text{ kcal/mol}$  [166]. Self-assembly of alkanethiols at high temperatures is a very different, much more reactive process that lifts the herringbone reconstruction [15, 16, 47] (also Chapter 5).

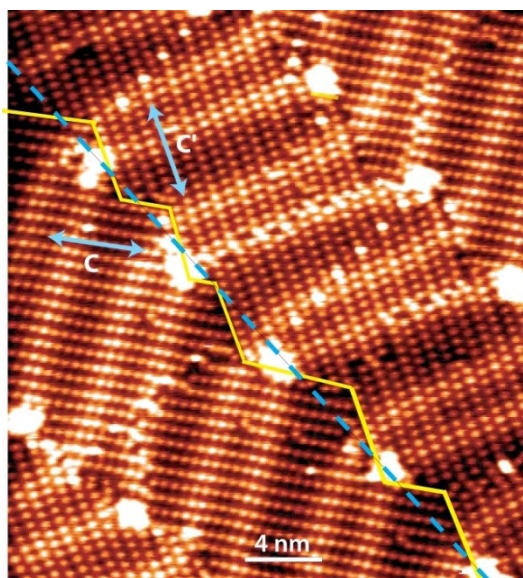


**Figure 6.2.** A large scale STM image of CH<sub>3</sub>SH monolayer on the Au(111) surface showing the modulation effect due to the herringbone reconstruction. ( $V = -0.013\text{V}$ ,  $I = 30 \text{ pA}$ ). The yellow line marks the domain boundary of the CH<sub>3</sub>SH monolayer. The blue lines is the rotational boundary of the herringbone reconstruction, where the  $C$ -direction of the anisotropic lattice compression turns by  $60^\circ$  to  $C'$ .

The ordered monolayer of CH<sub>3</sub>SH molecules was formed after heating the crystal with high adsorbate coverage to  $\sim 110\text{K}$  (Fig. 6.2). The CH<sub>3</sub>SH monolayer does not lift the

herringbone reconstruction on the Au(111) surface. The elbow sites are decorated with large molecular clusters, where no distinct order is observed.

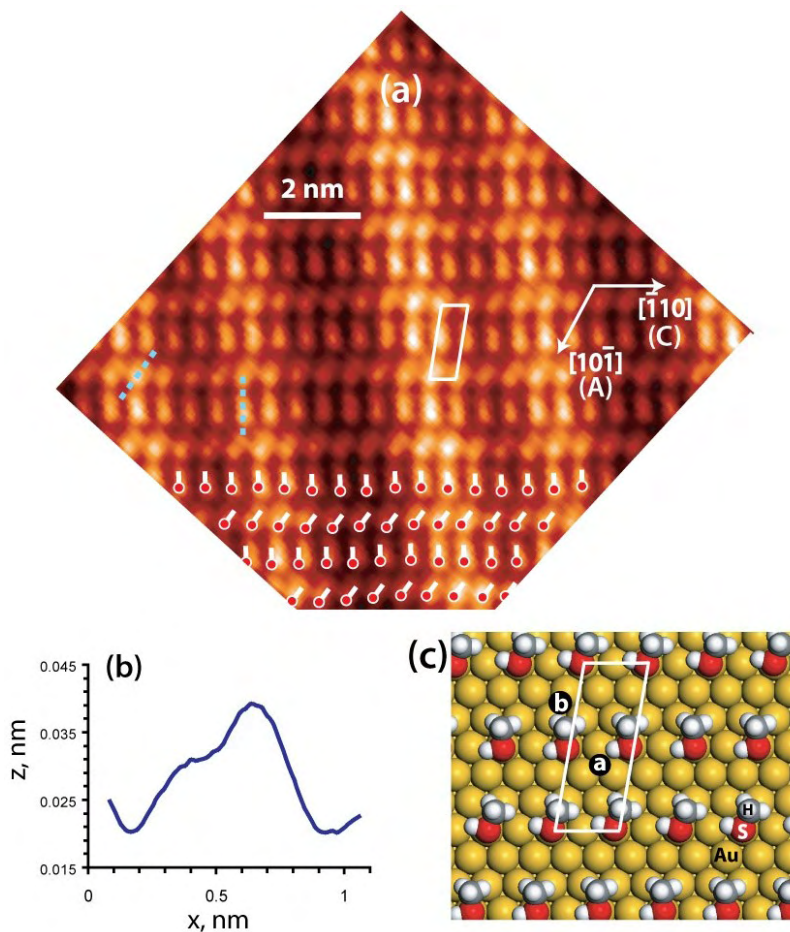


**Figure 6.3.** Molecular structure of the CH<sub>3</sub>SH monolayer on Au(111).

- a) STM image with individual CH<sub>3</sub>SH molecules resolved ( $V = -0.013\text{V}$ ,  $I = 30\text{ pA}$ ). The arrangement on the bottom was derived on the basis of apparent height and distance measurements.
- b) STM line-profile of a single CH<sub>3</sub>SH molecule taken along the yellow-dashed line. Higher lobe corresponds to the CH<sub>3</sub> group.
- c) Structural model of the CH<sub>3</sub>SH self-assembled monolayer derived from STM images.

The most distinct property of the CH<sub>3</sub>SH monolayer is revealed on the length scale of the herringbone reconstruction ( $\sim 15\text{ nm}$ ). As seen in Fig. 6.2, the CH<sub>3</sub>SH monolayer is composed of domains that alternate *in unison* with the rotation of the C-direction (vector of anisotropic compression of the gold lattice). The position of the domain boundary in the CH<sub>3</sub>SH monolayer (zig-zag yellow line in Fig. 6.2) is always pinned close to the point where the C-vector turns by

60° (dashed blue line in Fig. 6.2). The domain structure of the CH<sub>3</sub>SH monolayer is therefore modulated by the herringbone reconstruction.

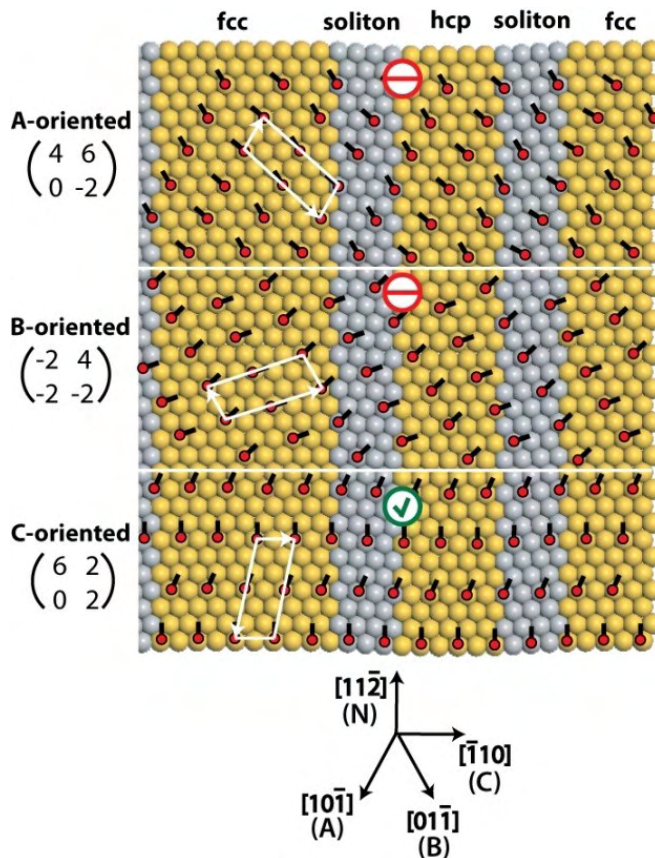


**Figure 6.4.** Structural models of the A-, B- and C-oriented CH<sub>3</sub>SH monolayer domains. The domains are transformed into each other by 60° rotation in plane of the surface. C-orientation is the only one observed in the completed self-assembled monolayer. The white arrows show the unit-cell vectors of the monolayer domains. The matrix notation is based on the A- and C-substrate vectors following the standard convention [246].

In order to describe the modulation effect on the molecular scale, we first need to visualize the microstructure of the CH<sub>3</sub>SH monolayer. Individual CH<sub>3</sub>SH molecules are imaged as ellipses (Fig. 6.3a) [166]. The line-scan along the major axis of the ellipse (Fig. 6.3b) reveals two peaks with the apparent height difference of ~ 0.2 Å. We assign the taller peak to the SH group and the smaller one – to the CH<sub>3</sub> group. The SH group binds on top of an Au atom [166].

A structural model of the CH<sub>3</sub>SH monolayer that is geometrically consistent with the STM images, is shown in Fig. 6.3c. CH<sub>3</sub>SH molecules are arranged in a zig-zag pattern, with the major axis of the ellipse inclined at either 90° or ~58° relative to the C-direction. The

intermolecular separation along the *C*-direction is  $\sim 5.4$  Å. The molecular rows are equispaced by  $\sim 7.3$  Å along the *N*-direction irrespective of the tilting angle of the molecular ellipses. The unit cell for the CH<sub>3</sub>SH monolayer is shown in Fig. 6.3a. According to the standard convention [246] it is described in matrix notation as  $\begin{pmatrix} 6 & 2 \\ 0 & 2 \end{pmatrix}$  using the substrate crystallographic directions  $[10\bar{1}]$  and  $[\bar{1}10]$ .

The large-scale domain modulation is observed because the smaller (0 2)-vector in the CH<sub>3</sub>SH monolayer always coincides with the *C*-vector of the Au(111) surface and is never aligned with the nearly equivalent *A*- and *B*-vectors (Fig. 6.4). The rotation of the *C*-vector by 60° therefore causes the same rotation of the CH<sub>3</sub>SH molecular domain and occurrence of a sharp domain boundary at the turning point of the herringbone reconstruction (Fig. 6.2).

Since *A*- or *B*-alignment is never observed, all the CH<sub>3</sub>SH domains on the surface are structurally equivalent in terms of intermolecular separations and molecular packing order. The 3-fold orientational degeneracy, expected for the molecular overlayer on a (111) surface, is thus lifted by the herringbone reconstruction, giving preference to only one domain with a particular orientation. There exist subtle variations between coexisting *C*-oriented domains across the surface, such as an offset of the registry between molecular rows along the *N*-direction or the tilting angle of individual CH<sub>3</sub>SH molecules. However, the unique feature of the CH<sub>3</sub>SH monolayer (the molecular packing order dictated by the herringbone reconstruction) is independent of these variations in the microstructure.

## 6.4 CH<sub>3</sub>SH MONOLAYER FORMATION IMAGED IN REAL-TIME

To gain further insight into why *C*-oriented domains are preferential, we have performed real-time measurement of the molecular ordering process. The motion of CH<sub>3</sub>SH molecules and evolution of the monolayer could be tracked at surface temperatures of 40-50 K. The Au(111) surface was first exposed to a saturation coverage of CH<sub>3</sub>SH molecules at 10 K and then warmed up to 40-48 K while imaging in STM.

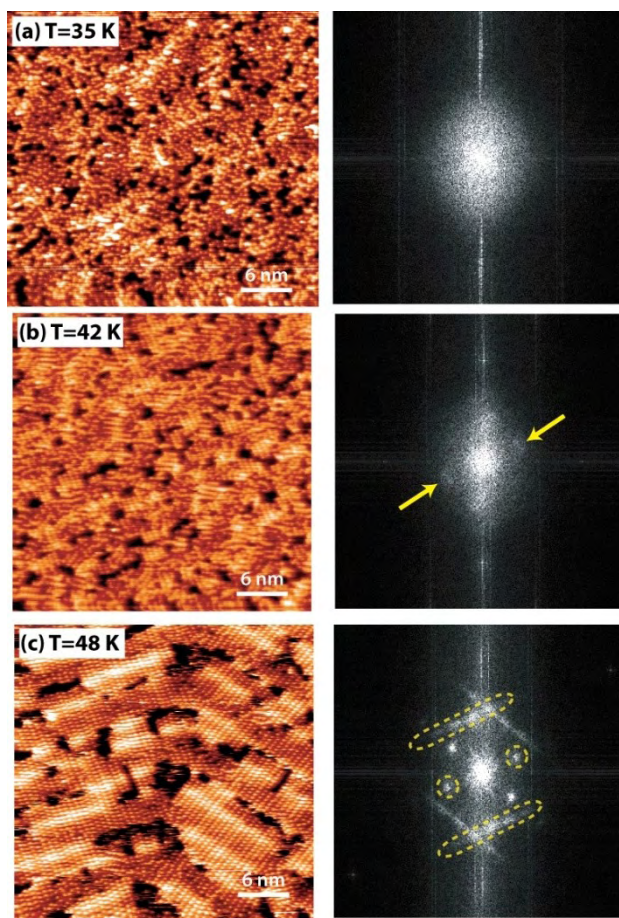


**Figure 6.5.** Real-time imaging of CH<sub>3</sub>SH monolayer ordering. Time interval between STM images is ~45 minutes. The right-hand side shows the Fourier-transforms of the STM images. The arrows mark the reflexes corresponding to a domain with C-orientation.  $U=-0.013$  V,  $I=17$  pA.

As seen in Fig. 6.5a, and its essentially uniform Fourier transform (right panel), there is no apparent order occurring in the CH<sub>3</sub>SH overlayer up to ~40 K. Slow ordering of CH<sub>3</sub>SH molecules starts at  $T > 40$  K. The ordering proceeds through the growth of single or nested lines of molecules along the *A*, *B* and *C* directions (Fig. 6.5b). According to the Fourier transform of the STM image, some preference of the *C*-oriented domains is observed already at this initial stage of the monolayer growth (Fig. 6.5b). The ordering is complete at ~48K after several hours. The Fourier transform (Fig. 6.5c) shows two groups of equivalent spots, produced by two *C*-oriented CH<sub>3</sub>SH domains at 60° to each other.

The time evolution of the nearly-ordered monolayer is very informative. Fig. 6.6 shows six out of 30 STM images taken with a time interval of several minutes at ~48K when the

monolayer ordering nears completion. Although most of the surface is covered by the *C*-oriented monolayer, several patches of the *A(B)*-orientations can also be seen. As time goes on, these patches shrink, and finally disappear, being displaced by the growing *C*-oriented domains. The time-resolved decay of one particular *A*-oriented island (marked by white-arrow) is plotted at the bottom of Fig. 6.6. The decay is linear suggesting that it occurs via detachment-limited kinetics, i.e. the rate-limiting step in island decay is molecular detachment from the island-boundaries [247]. Initial formation of all three domain orientations (*A*, *B*, *C*) and the detachment-limited island-decay during the formation of the CH<sub>3</sub>SH monolayer directly support the kinetic preference of the *C*-oriented monolayers on the reconstructed Au(111) surface as discussed below.

## 6.5 DISCUSSION

To understand the reason why a particular domain orientation becomes preferential in the presence of the herringbone reconstruction on the surface, we need to consider both structural (thermodynamic) and kinetic differences between different orientations of the self-assembled domains of CH<sub>3</sub>SH molecules.

### 6.5.1 Structural Differences Between Saturated Molecular Domains

*A*-, *B*- and *C*-oriented domains in Fig. 6.4 are equivalent on an unreconstructed (111) surface lattice. However, the anisotropic compression of the gold surface lattice (leading to the herringbone reconstruction) produces subtle structural differences between three orientations. Naturally, the intermolecular separations are slightly different within three domains. The shortest intermolecular distance will be observed in the *C*-domain because the lattice spacing (hence, the

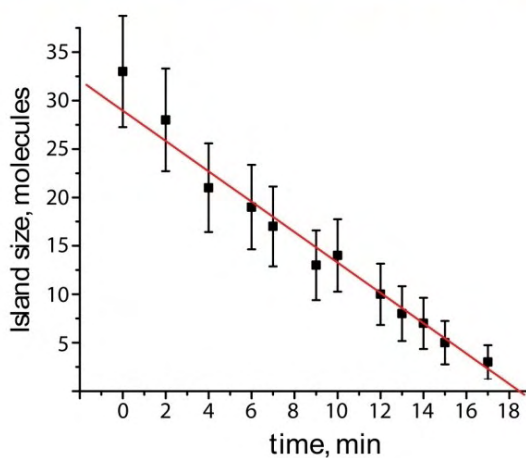
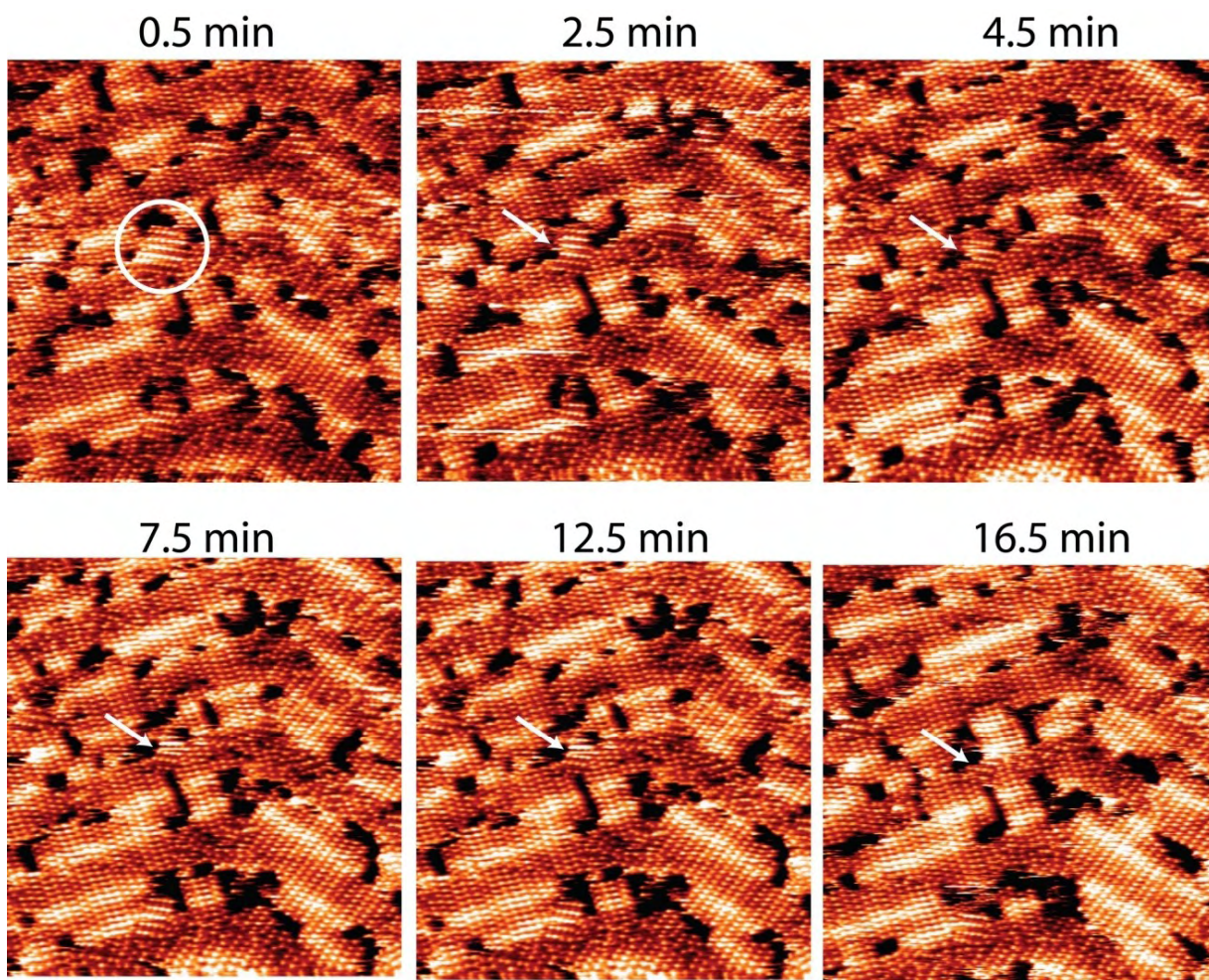


**Figure 6.6.** Three consecutive STM images of a nearly-completed  $\text{CH}_3\text{SH}$  monolayer showing the disappearance of A(B)-oriented domains with time ( $U = -0.013 \text{ V}$ ,  $I = 17 \text{ pA}$ ). Bottom graph shows the decay of the A-oriented island marked by white arrows.

2a separation) is smallest along the C-direction. However, it seems unlikely that the intermolecular separations play a dominant role in determining the preferential domain orientation. This is mainly due to large overall distances between the CH<sub>3</sub>SH molecules in all the domains. As seen in Fig. 6.2 the molecules are separated by ~5.5 Å head-to-tail along the N direction and by ~4.5 Å tail-to-tail along the C direction. These separations are almost two times as long as the typical chemical bond, including the hydrogen bond [248], and small changes in the separations when going from A(B)- to C-oriented domains will hardly change the strength of intermolecular interactions (mostly electrostatic in nature). We can also disregard the elastic substrate-mediated interactions between the neighbour molecules due to adsorption-induced shifting of lattice atoms, because these effects are characteristic of strongly binding adsorbates [195] while the binding energy of the CH<sub>3</sub>SH molecule on Au(111) is only ~10 kcal/mol. The expected similar energetics among the three domains is also consistent with the fact that all three types of domains are initially observed in the real-time STM movies of the CH<sub>3</sub>SH monolayer formation taken at ~50 K (Fig. 6.6). The packing density of CH<sub>3</sub>SH molecules among three domains does not exhibit big differences either (only ~2% of the surface area). In addition it is larger for the A(B)-oriented domain than for the C-oriented domain, which makes it impossible to attribute the preference for C domains to the tendency to maximize surface coverage.

Altogether, purely structural considerations do not provide a convincing rationale for the observed preference of the C-domain. Therefore, the driving force for the formation of this uniquely-favored domain must lie in the kinetics of overlayer assembly.

### 6.5.2 Kinetics of CH<sub>3</sub>SH Monolayer Formation

The kinetic origin of the C-domain preference can be discerned from the time-dependent STM images in Fig. 6.6 in which A and B domains shrink while C domains grow. In this section we describe how this process is governed by molecular detachment rates from domain walls with different structures. The orientation of these domain walls with respect to the anisotropic landscape of the reconstructed gold substrate provides a unique kinetic stability to the C-oriented domains that eventually allows them to exist across the whole surface.

The anisotropic unit cell of the CH<sub>3</sub>SH monolayer produces domain boundaries with very different molecular-packing density as seen in Fig. 6.7. This affects the probability for any single

CH<sub>3</sub>SH molecule to escape the close-packed domain through its domain wall. In order to escape through domain wall 1, a molecule must hop onto the neighbor gold sites labelled *a* and *b*. No other molecular trajectory will displace the molecule outside of the domain wall. The intermolecular interaction between the escaping CH<sub>3</sub>SH molecule and its neighbors in the domain will be repulsive on both of these sites because the shortest intermolecular spacing will decrease from  $2a$  to  $\sqrt{3}a$  when the molecule hops onto site *a* or *b*. Since  $\sqrt{3}a$  spacing is never observed at any coverage of CH<sub>3</sub>SH on Au(111) including saturation, it is reasonable to assume that the interaction between two CH<sub>3</sub>SH molecules at this separation is repulsive [249]. This implies the presence of a significant detachment barrier from wall 1 since the energy increase due to the repulsive  $\sqrt{3}$  spacing represents the minimum energy barrier.

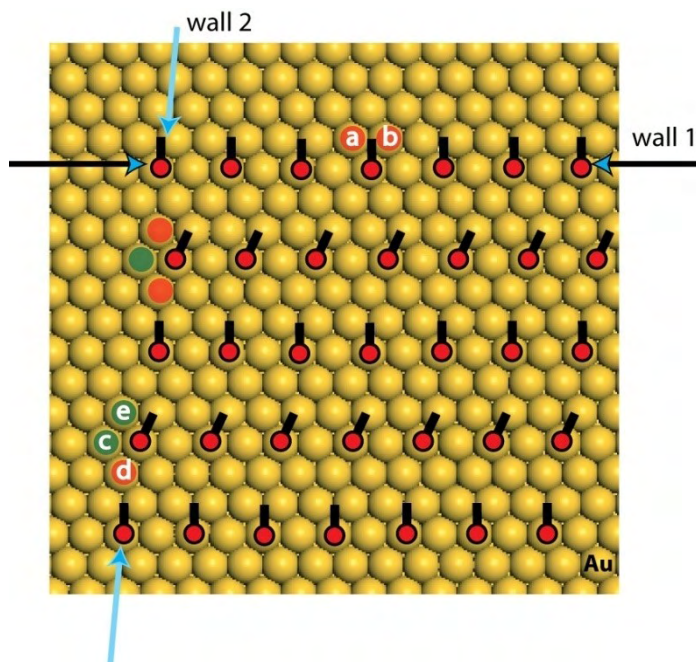


**Figure 6.7.** A model of a single CH<sub>3</sub>SH self-assembled domain demonstrating the different detachment trajectories available to molecules on different domain walls. The notation follows the text. The dots mark the available adsorption sites for a single molecule escaping the domain. Red (green) dots mark the sites where repulsive (small) interactions with the neighbors will exist.

On the other hand, a CH<sub>3</sub>SH molecule detaching from wall 2 can hop onto any of three nearest neighbour sites, labelled *c*, *d* and *e* in Fig. 6.7. Although hopping onto site *d* produces the repulsive  $\sqrt{3}$ -configuration (Fig. 4.1), a molecule moving to sites *c* or *e* will experience hardly any change in intermolecular interactions because of the large molecule-molecule

distances of  $2a$  or more. Therefore the energetic barrier to detachment should be significantly reduced for sites c and e and the rate of detachment from domain-wall 2 should be significantly larger than that from domain-wall 1. Domain wall 2 is hereafter referred to as a “leaky” wall.

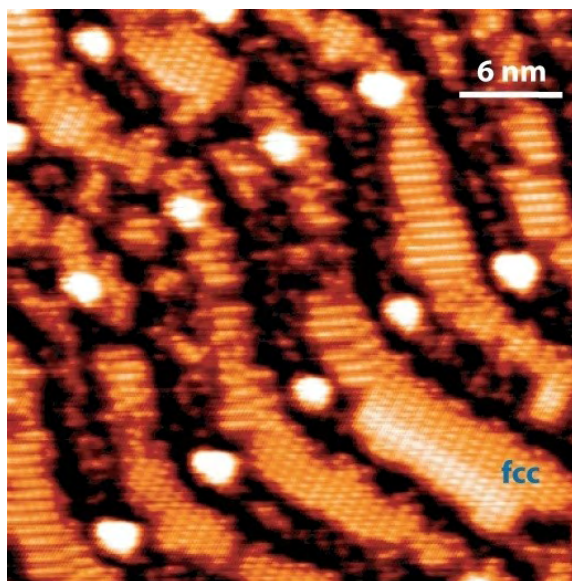


**Figure 6.8.** Sub-monolayer coverage of  $\text{CH}_3\text{SH}$  on the  $\text{Au}(111)$  surface, where the preference of the C-orientation is observed on the length-scale of locally-saturated fcc-regions ( $U = -0.022\text{V}$ ,  $I = 16\text{ pA}$ ).

To see how this stabilizes the C-oriented domain, it is necessary to consider how each domain wall aligns with the Au herringbone reconstruction.  $\text{CH}_3\text{SH}$  molecules bind most strongly on the fcc-stacked domains of the herringbone reconstruction, more weakly on the hcp-stacked domains, and most weakly on the soliton walls (maximum difference of binding energy fcc-to-soliton  $\sim 2$  kcal/mol, Section 4.1.). The variation of the binding energies directly reflects the anisotropy of surface stress inherent in the herringbone reconstruction. This produces a further constraint on the escape-probability of a  $\text{CH}_3\text{SH}$  molecule from a monolayer domain because the escape rate from the domain boundary to a soliton wall must be significantly lowered by the reduced binding energy on these sites. The C-oriented domains of  $\text{CH}_3\text{SH}$  are stabilized with respect to the A or B oriented domains because their “leaky” walls happen to run parallel to the soliton walls of the herringbone reconstruction thus severely reducing the rate of molecular detachment.

Consider a single monolayer island of  $\text{CH}_3\text{SH}$  molecules nucleating in the middle of an fcc-region of the  $\text{Au}(111)$  surface (Fig. 6.4). Initially the size of the domain is small compared to

the width of the fcc-region so that the effect of the soliton lines is negligible. When the linear dimension of the island reaches 6-7 molecules, the domain walls will approach the soliton lines of the herringbone reconstruction. If the island has *C*-orientation (Fig. 6.4), both of its leaky walls (wall 2 in Fig. 6.7) will be aligned with the soliton lines impeding detachment of molecules from these walls. The *A*- or *B*-oriented islands, on the other hand, will not be very sensitive to the presence of the soliton because their leaky walls are exposed mostly to the fcc-regions (Fig. 6.4) and molecules can still detach at a significant rate.

Further experimental support for this picture is seen in Fig. 6.8, where the preference for *C*-oriented domains is established at submonolayer coverages that are just large enough to allow growing domains to sense the soliton walls. Local saturation occurs on the fcc areas, and the *C*-orientation is maintained across all of the overlayer. This observation further verifies that the domain energetics is not responsible for formation of preferential domains. This is because it is unlikely that the stability the domains with different orientation will vary strongly on the length scale of a structurally uniform fcc area (width of  $\sim 1.1$  nm, and maximum compression of  $<2\%$  [238]).

It is worth mentioning that a single domain monolayer similar to  $\text{CH}_3\text{SH}$  was previously observed for 2,2'-bipyridine on the Au(111) surface [245]. Although the behaviour of isolated bipyridine molecules has not been investigated on Au(111), the anisotropic unit-cell of its monolayer is similar to that of  $\text{CH}_3\text{SH}$ . Anisotropy is crucial to our picture of the assembly process because it produces variations in the rate of mass-transport across domain walls of the overlayer. The similar behaviour of such different molecules as  $\text{CH}_3\text{SH}$  and 2,2'-bipyridine on Au(111) suggests that the phenomena described in this paper may be generic for anisotropic self-assembled molecular monolayers on substrates with herringbone reconstructions [216, 217] (or other reconstructions that produce large-scale anisotropy similar to the herringbone reconstruction).

## 6.6 CONCLUSIONS

In conclusion, using scanning tunnelling microscopy we have found that the self-assembly of  $\text{CH}_3\text{SH}$  on the Au(111) surface is distinctly modified by its herringbone reconstruction. The unit-

cell orientation in the CH<sub>3</sub>SH monolayer is determined by the anisotropic compression of the Au(111) surface. Therefore the monolayer is composed of molecular domains with only one of three possible azimuthal orientations. We propose a phenomenological model for the observed effect, where the growing molecular domain of a certain orientation is kinetically stabilized by the interference of the soliton lines of the herringbone reconstruction with molecular detachment from domain walls. This model is supported by the real-time observation of molecular ordering on the surface using scanning tunnelling microscopy.

**PART III. ORIGIN OF ANCHOR-BOND IN SELF-ASSEMBLED  
ALKANETHIOLATE MONOLAYERS ON AU(111) SURFACE FIRST  
PARAGRAPH**

This part of the thesis presents a solution to one of the most controversial problems in the field of molecular self-assembly, the chemical bond at the interface of alkanethiol self-assembled monolayers and Au(111) surface. Scanning tunneling microscopy is the most popular technique to study alkanethiol SAMs [22], and it was used many times to address this specific problem. The key novelty of the present work was to study the surface chemistry of two precursor molecules on Au(111), CH<sub>3</sub>SH and CH<sub>3</sub>SSCH<sub>3</sub>, prior to addressing the bonding in CH<sub>3</sub>S-SAMs on Au(111), which are formed by thermal dissociation of the precursor molecules.

In Chapter 7 the adsorption and electron-stimulated dissociation of the CH<sub>3</sub>SSCH<sub>3</sub> molecule is discussed in detail based on the STM measurements and DFT calculations. Electron-stimulated decomposition of CH<sub>3</sub>SSCH<sub>3</sub> (and CH<sub>3</sub>SH) on Au(111) at 5K produces a “cold” CH<sub>3</sub>S species, which binds to a Au-Au bridge site in complete agreement with DFT calculations. Today’s prevalent opinion is that the bridge-bonded S-headgroup is also the anchor group in self-assembled CH<sub>3</sub>S species produced at room temperature.

It turns out that the CH<sub>3</sub>S species produced by thermal decomposition of CH<sub>3</sub>SSCH<sub>3</sub> is strikingly different from the “cold” CH<sub>3</sub>S species as well as from the parent CH<sub>3</sub>SSCH<sub>3</sub> molecule (Chapter 8). This difference was ultimately traced to the involvement of Au-adatoms in the bonding and self-assembly of the thiolate species when thermal excitation is involved. New Au-adatom-bonded models of the CH<sub>3</sub>S-SAMs proposed here develop a consistent picture that agrees with theory, STM measurements *and* prior spectroscopic results [68, 69] for the first time. The adatom-concept also explains the lifting of the herringbone reconstruction (another controversial issue in organosulfur SAMs on Au(111)) which accompanies alkanethiolate self-assembly.

The analysis presented here is limited to the low-coverage two-dimensional self-assembly [16, 59] of alkanethiols on Au(111) where STM is best suited to understand the structure. However, 2D-SAMs are precursors to the saturated 3D-SAMs [16] making the new models relevant to the big picture of the self-assembly of organosulfur molecules on the Au(111) surface. Shortly after the publication of our findings, the signature of Au-adatoms in 3D-SAMs was reported in two independent studies using spectroscopic techniques [37, 53].

## 7.0 ADSORPTION SITE OF METHANETHIOLATE (CH<sub>3</sub>S) ON AU(111) SURFACE AT T = 5 K\*

The chemisorptive bonding of methanethiolate (CH<sub>3</sub>S) on the Au(111) surface has been investigated at a single-molecule level using Low-Temperature Scanning Tunneling Microscopy (LT-STM) and density-functional theory (DFT). CH<sub>3</sub>S species were produced by STM-tip induced dissociation of methanethiol (CH<sub>3</sub>SH) or dimethyldisulfide (CH<sub>3</sub>SSCH<sub>3</sub>) at 5K. The adsorption site of an isolated CH<sub>3</sub>S species was assigned by comparing the experimental and calculated STM images. The S-headgroup of the chemisorbed CH<sub>3</sub>S adsorbs on the two-fold coordinated bridge-site between two Au-atoms, consistent with theoretical predictions on the defect-free surface. The assignment of the adsorption site is also supported by the freezing of the tip-induced rotational motion of the CH<sub>3</sub>SH molecule upon its conversion to CH<sub>3</sub>S via deprotonation.

### 7.1 COMPUTATIONAL METHODS

DFT calculations of the adsorption geometries were done using VASP with parameters similar to Chapter 3. The surface coverage of the CH<sub>3</sub>S species in the calculations was either 1/3 ML or 1/5 ML (1ML corresponds to the ( $\sqrt{3}\times\sqrt{3}$ )R30° structure [22]). The rotational motion of the CH<sub>3</sub>S species was analyzed using the nudged elastic band (NEB) method of Mills *et al.* [180] STM

---

\*Reproduced in part with permission from: P. Maksymovych, D. C. Sorescu, J. T. Yates, Jr., *Journal of Physical Chemistry B* 110 (2006) 21161. Copyright 2006 American Chemical Society. Calculations done by D. C. Sorescu.

images for select adsorption configurations of the  $\text{CH}_3\text{S}$  on  $\text{Au}(111)$  were calculated using the Tersoff-Hamman approach [140]. The STM image was approximated by the iso-surface of charge density around the Fermi level within the energetic interval from  $-0.5$  to  $0.5$  eV, similar to the tunneling voltage used experimentally. The calculated constant charge density iso-surfaces were directly compared to the measured constant current STM images.

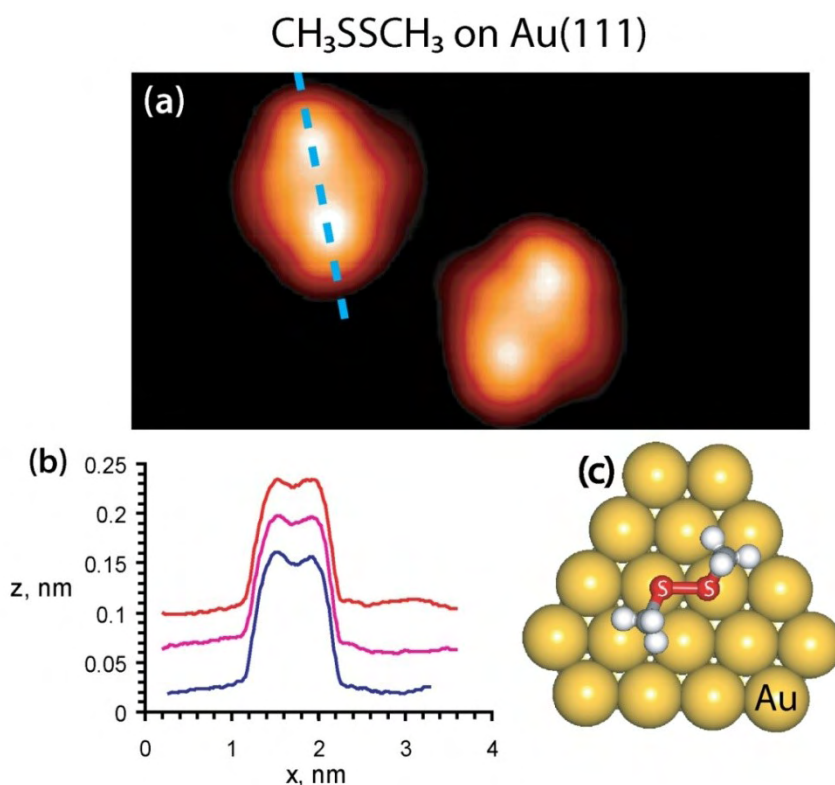


**Figure 7.1.**  $\text{CH}_3\text{SSCH}_3$  molecule on  $\text{Au}(111)$  surface at  $T = 5$  K. a) STM image of  $\text{CH}_3\text{SSCH}_3$  molecules adsorbed on the  $\text{Au}(111)$  surface. Scale:  $1.8 \times 3.6 \text{ nm}^2$ ;  $U = -0.04 \text{ V}$ ;  $I = 20 \text{ pA}$ . b) Representative line profiles of several adsorbed  $\text{CH}_3\text{SSCH}_3$  molecules taken along the direction of the blue dashed line in (a). c) Ball model of a  $\text{CH}_3\text{SSCH}_3$  molecule on the  $\text{Au}(111)$  surface.

## 7.2 SINGLE $\text{CH}_3\text{SH}$ AND $\text{CH}_3\text{SSCH}_3$ MOLECULES CHEMISORBED ON THE $\text{Au}(111)$ SURFACE

The adsorption behavior of  $\text{CH}_3\text{SH}$  on  $\text{Au}(111)$  at low temperatures was described in detail in Chapter 3. The S-H bond does not dissociate up to the maximum  $\text{CH}_3\text{SH}$  desorption temperature

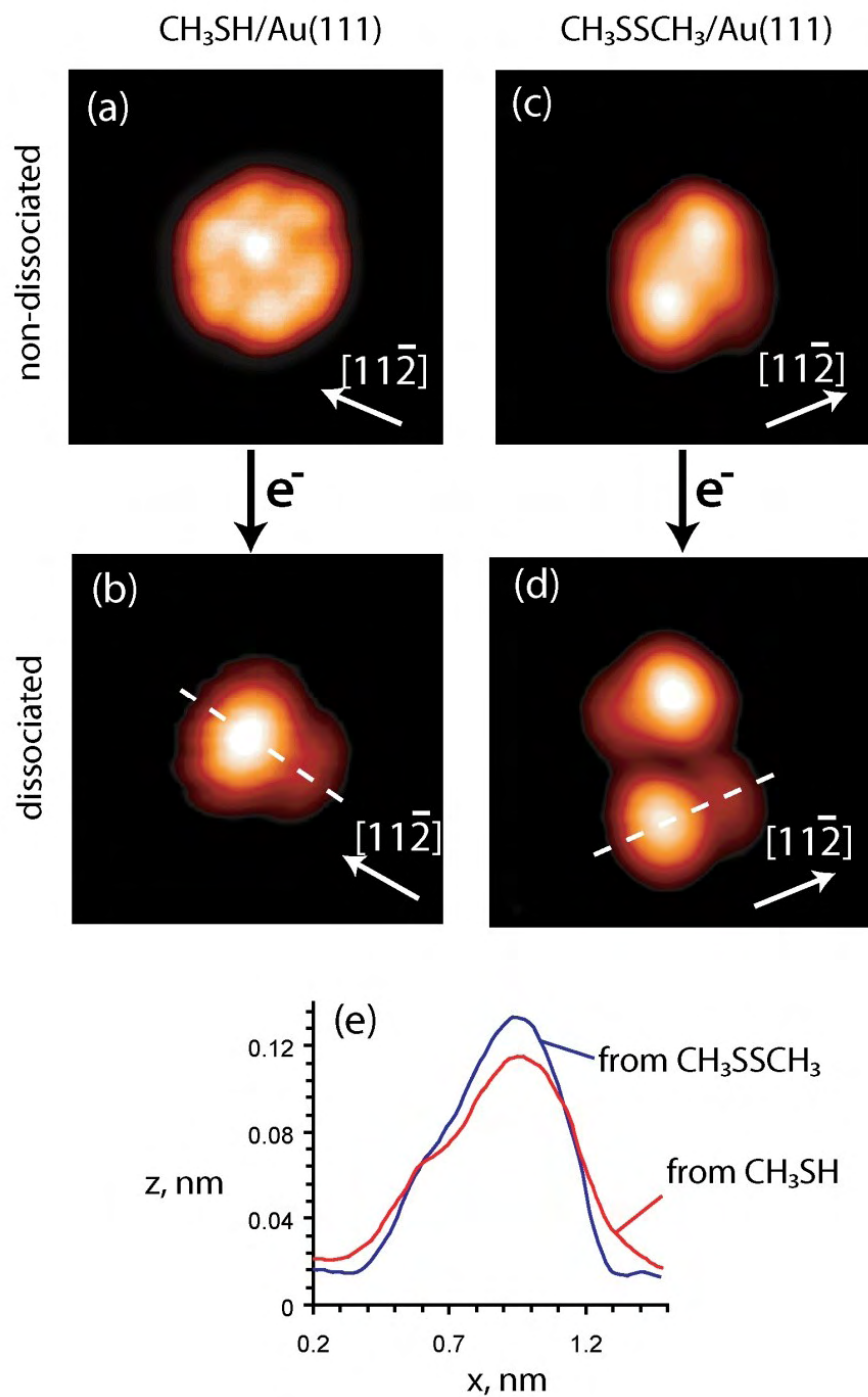


**Figure 7.2.** Topographic comparison of the products of tip-induced dissociation of  $\text{CH}_3\text{SH}$  and  $\text{CH}_3\text{SSCH}_3$ . All images: Scale:  $1.8 \times 1.8 \text{ nm}^2$ ; (a,b):  $U = -0.010 \text{ V}$ ,  $I = 40 \text{ pA}$ ; (c,d):  $U = -0.04 \text{ V}$ ,  $I = 20 \text{ pA}$ . The line-profiles in (e) were taken along the direction of the white dashed line in (b) and (d).

of  $\sim 185$  K or when it is exposed to Au(111) to produce low coverages at temperatures up to 300 K [44, 166].  $\text{CH}_3\text{SH}$  binds weakly to the surface, and an isolated  $\text{CH}_3\text{SH}$  molecule undergoes tip-induced hindered rotation around the Au-S bond when imaged by STM. This produces a flower-shaped STM image (e.g. Fig. 3.2) with six petals on the perimeter corresponding to the most probable positions of the  $\text{CH}_3$  group during molecular rotation. Based on symmetry considerations and DFT calculations, it was concluded that  $\text{CH}_3\text{SH}$  binds through the S-atom to an atop Au-site [166, 176].

$\text{CH}_3\text{SSCH}_3$  also adsorbs non-dissociatively on Au(111) at low temperatures. The S-S bond dissociates when the surface temperature reaches 200 K [250], which is why all the experiments presented here were done at  $T < 40$  K. The STM image of a single  $\text{CH}_3\text{SSCH}_3$  molecule is shown in Fig. 7.1. It has an elliptical shape with two bright lobes of the same apparent height (see the line scans along the dashed blue line in Fig. 7.1b). A similar STM image was reported for  $\text{CH}_3\text{SSCH}_3$  adsorbed on the Cu(111) surface [251]. The major axis of the elliptical image corresponding to the  $\text{CH}_3\text{SSCH}_3$  molecule assumes one of six orientations, each of which is inclined  $\sim 10^\circ$  from the close-packed direction of the underlying Au lattice. Figure 7.1c schematically shows the adsorption configuration of the  $\text{CH}_3\text{SSCH}_3$  molecule on the Au(111) surface.

### 7.3 ELECTRON-INDUCED DISSOCIATION OF $\text{CH}_3\text{SSCH}_3$ AND $\text{CH}_3\text{SH}$

In order to dissociate either  $\text{CH}_3\text{SSCH}_3$  or  $\text{CH}_3\text{SH}$  adsorbed molecules at 5K, the STM tip is positioned close to the center of the topographic image and a 1-100  $\mu\text{s}$  voltage/current pulse is passed through the tunneling junction. The threshold voltage for  $\text{CH}_3\text{SSCH}_3$  dissociation was  $\sim 700$  mV (at tunneling current  $< 10$  nA) and that for  $\text{CH}_3\text{SH}$  was  $\sim 2.5$  V. Since these values are outside of the energy range of molecular vibrations ( $E < 400$  mV), the dissociation is likely to be initiated via electronic rather than vibrational excitation of the molecule. Both molecules, when pulsed with voltages smaller than the respective dissociation threshold energies, are observed to diffuse away from the tip-Au junction due to the excitation of vibrational and frustrated translational modes of adsorbed molecules by inelastic scattering of tunneling electrons [252].

The products of electron-induced dissociation of  $\text{CH}_3\text{SH}$  and  $\text{CH}_3\text{SSCH}_3$  are compared in Fig. 7.2. The topography of the products is nearly identical in STM, although the line profiles of the two species (Fig. 7.2e) are slightly different because the STM images were obtained with different tips. The yield of the product is 1 species per  $\text{CH}_3\text{SH}$  molecule and 2 species per  $\text{CH}_3\text{SSCH}_3$  molecule, which unambiguously identifies the species in each case as  $\text{CH}_3\text{S}$ . Although  $\text{CH}_3\text{SH}$  produces two fragments upon dissociation, only one ( $\text{CH}_3\text{S}$ ) is imaged. The hydrogen atom is probably too weakly bound to the surface to be imaged by STM at such a low coverage. Another particular feature of the  $\text{CH}_3\text{SH}$  dissociation is that the tip-induced rotation of the  $\text{CH}_3\text{SH}$  molecule is frozen upon deprotonation as shown in Fig. 7.3. The same effect was reported for the tip-induced deprotonation of a chlorinated benzenethiol adsorbed on the  $\text{Cu}(111)$  surface [178]. This fact will be used to emphasize the significant difference in the bonding energy (and geometry) between  $\text{CH}_3\text{SH}$  and  $\text{CH}_3\text{S}$ .

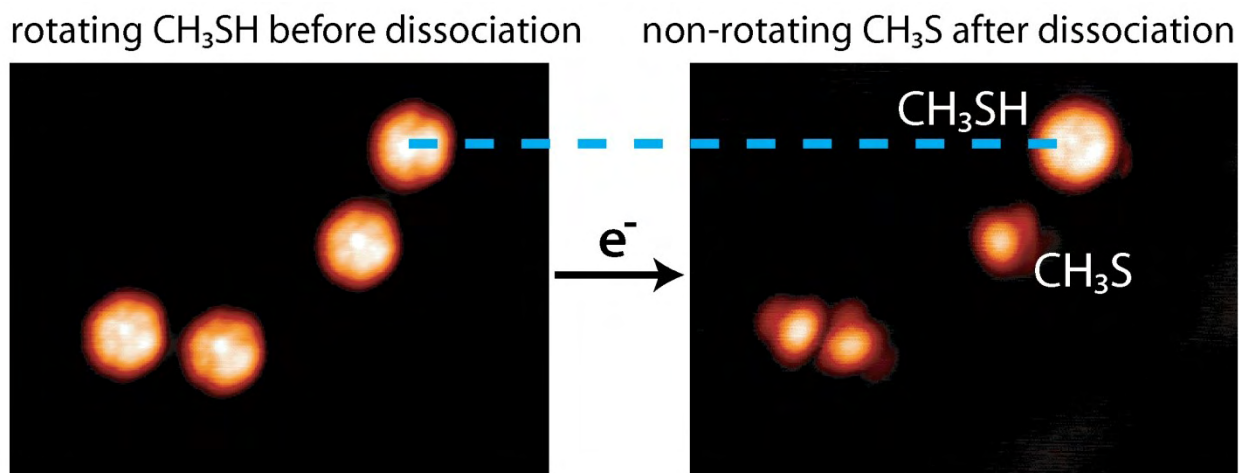


**Figure 7.3.** STM images of several single  $\text{CH}_3\text{SH}$  molecules before and after tip-induced deprotonation, showing that the tip-induced rotation of  $\text{CH}_3\text{SH}$  stops after reaction. Scale:  $6.14 \times 3.9 \text{ nm}^2$ ,  $U = -0.010 \text{ V}$ ,  $I = 40 \text{ pA}$ . The blue dashed line marks the rotating  $\text{CH}_3\text{SH}$  molecule that was not pulsed.

The STM image of the chemisorbed  $\text{CH}_3\text{S}$  species (Figs. 7.2) has two well-resolved lobes, one lobe having both larger size and larger apparent height than the other one. Often a slight dark halo is observed around the small lobe. Both of these topographic features allow us to assign the larger lobe to the  $\text{CH}_3$  group and the smaller lobe to the S-headgroup. The dark halo around the sulfur headgroup was also reported for the dissociated benzenethiolate molecule on  $\text{Cu}(111)$ , and was attributed to be due to the S-Cu charge transfer [178]. The direction from the

large-lobe to the small lobe coincides with the  $[1\bar{1}0]$  closepacked direction of the Au(111) surface. A total of six equivalent orientations of the  $\text{CH}_3\text{S}$  species are observed.

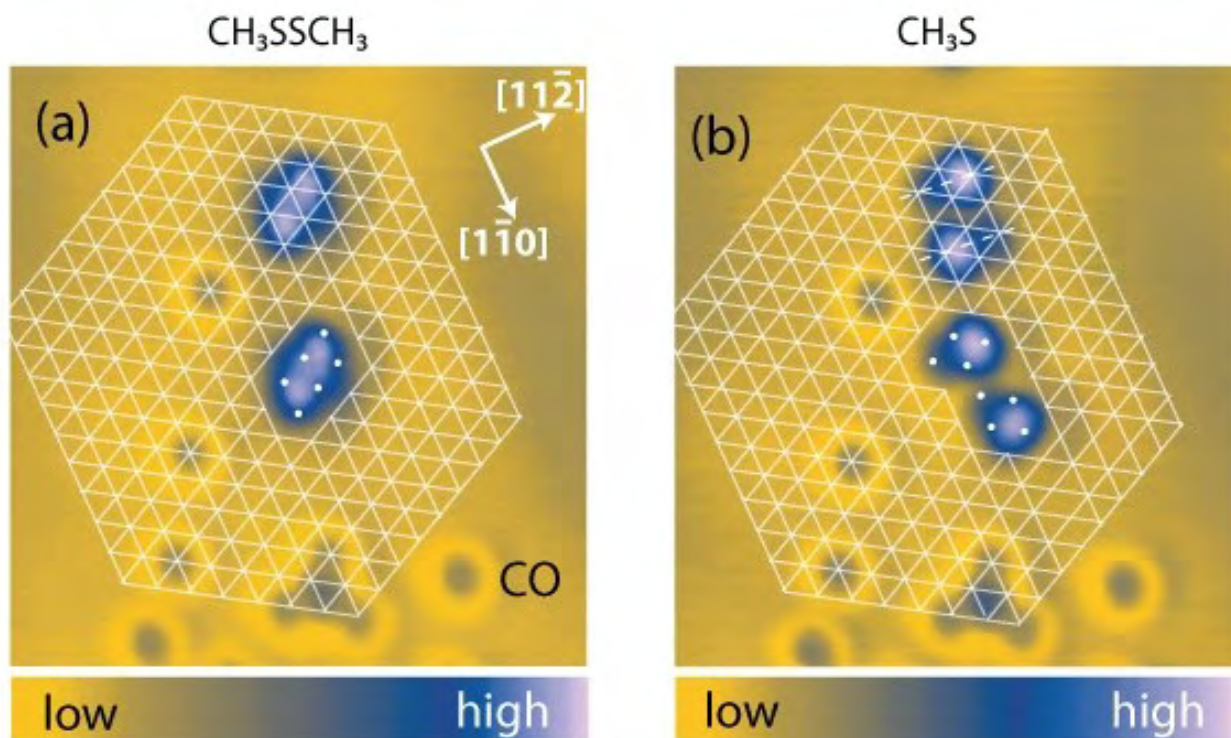


**Figure 7.4.** Triangulation of  $\text{CH}_3\text{S}$  produced from  $\text{CH}_3\text{SSCH}_3$  by tip-induced dissociation at 5K. Scale:  $4.8 \times 5.2 \text{ nm}^2$ ;  $U = -0.04 \text{ V}$ ;  $I = 20 \text{ pA}$ . (a) STM image of  $\text{CH}_3\text{SSCH}_3$  molecules before dissociation. The lattice mesh was derived using co-adsorbed CO molecules as markers for the Au atoms in the surface lattice. (b) Each  $\text{CH}_3\text{SSCH}_3$  molecule in (a) was dissociated using a 1 sec pulse at 1.0 V. White dots mark the position of Au atoms in the mesh for clarity. White dashed lines indicate the azimuthal direction of the S- $\text{CH}_3$  bond in  $\text{CH}_3\text{S}$  (a)

To establish the location of the  $\text{CH}_3\text{S}$  species relative to the Au(111) lattice, a small number of CO molecules were co-adsorbed on the surface. The CO molecules act as markers of the Au atoms is shown in Fig. 7.4. All the  $\text{CH}_3\text{S}$  species produced by dissociation of  $\text{CH}_3\text{SSCH}_3$  molecules assume the same position with respect to the underlying Au lattice. The key fact is that the separation line between the large and the small lobes in the STM image of a single  $\text{CH}_3\text{S}$  species is always located above the bridge site between two Au atoms (Fig. 7.4b).

## 7.4 ADSORPTION ENERGETICS OF THE CH<sub>3</sub>S SPECIES BY DFT CALCULATIONS

Table 7.1 summarizes the binding energies and representative geometric parameters obtained for different adsorption configurations of the CH<sub>3</sub>S species on the unreconstructed Au(111) surface. The corresponding structural models are presented in Figs. 7.5 and 7.6. The CH<sub>3</sub>S adsorption energy is defined as

$$E_{ads} = E_{molec} + E_{slab} - E_{molec+slab}$$

where  $E_{molec}$  is the spin polarized energy of the optimized gas-phase CH<sub>3</sub>S radical,  $E_{slab}$  is the total energy of the surface slab and  $E_{molec+slab}$  is the total energy of the adsorbate/slab system. The energy of the gas-phase CH<sub>3</sub>S was determined from calculations performed on a single molecule in a cubic cell with sides of 10 Å. The same Brillouin-zone sampling was used in all calculations.

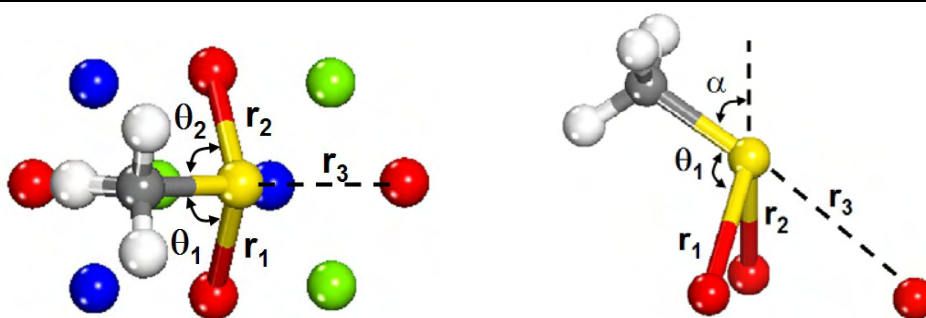
As seen in Table 7.1, CH<sub>3</sub>S binding energy decreases in the following order: bridge-sites > hollow sites >> atop sites. In the most stable configuration, *br-fcc* (*br* stands for *bridge*, Fig. 7.6a), CH<sub>3</sub>S is adsorbed on the Au-Au bridge site with the surface-projected position of the S-atom slightly shifted toward the neighbor fcc hollow site. The S-atom makes “two” bonds with the Au(111) surface with the total adsorption energy of 43.4 kcal/mol. The rotational conformation of the CH<sub>3</sub> group with one H atom pointing to the surface is preferential by ~0.6 kcal/mol compared to configurations having two H atoms pointing toward the surface.

The hollow site configurations, *fcc-t* (*t* for *tilted*, Fig. 7.6b) and *fcc-v* (*v* for *vertical*, Fig. 7.6c), have an adsorption energy of 41.8 kcal/mol and 42.0 kcal/mol correspondingly. The *fcc-v* configuration involves a three-fold coordinated S-Au bonding with the S-C bond oriented along the surface normal, while the *fcc-t* CH<sub>3</sub>S is slightly tilted toward the surface with an angle of 26.4° relative to surface normal (Fig. 7.5).

The binding energy of CH<sub>3</sub>S in the singly-coordinated atop-site configurations (Fig. 7.5 and Fig. 7.6d) decreases by a maximum of 7 kcal/mol relative to the bridge and hollow sites. The S-C bond is tilted off-normal by about the same angle as in the bridge-bonded configurations. Overall these results are in close agreement with the previous theoretical calculations on the CH<sub>3</sub>S/Au(111) system, which suggest the *br-fcc* site to be most stable adsorption configuration and the *atop* site to be the least stable one [64, 65, 253].

**Table 7.1.** Structures and Adsorption Energies for CH<sub>3</sub>S Adsorbed on the Au(111) Surface at Different Coverages ( $\Theta$ ) Determined from PAW-PW91 Calculations (Top-views of the structures are shown in Fig. 7.5).

Struct.	$\Theta$	r(Au-S) (Å)			r(S-C) (Å)	$\theta$ (Au-S-C) (°)			$\alpha$ (°)	E <sub>ads</sub> (kcal/mol)
		r <sub>1</sub>	r <sub>2</sub>	r <sub>3</sub>		$\theta_1$	$\theta_2$	$\theta_3$		
<i>br-fcc</i>	1/5	2.452	2.467	-	1.834	108.8	110.5	-	52.9	43.4
<i>br-fcc</i>	1/3	2.450	2.454	-	1.835	108.2	109.8	-	53.7	40.9
<i>br-hcp</i>	1/5	2.465	2.467	-	1.831	110.9	110.7	-	56.9	42.5
<i>br-hcp</i>	1/3	2.455	2.450	-	1.830	109.8	111.8	-	55.9	40.3
<i>top(1)</i>	1/5	2.371	-	-	1.823	105.7	-	-	62.9	34.5
<i>top(2)</i>	1/5	2.374	-	-	1.824	106.7	-	-	59.2	34.3
<i>fcc-v</i>	1/5	2.453	2.452	2.456	1.834	125.3	124.9	126.7	1.1	42.0
<i>fcc-v</i>	1/3	2.439	2.438	2.443	1.830	128.7	127.3	126.8	1.1	37.1
<i>fcc-t</i>	1/5	2.445	2.447	-	1.844	115.4	115.7	-	26.3	40.6
<i>hcp-v</i>	1/5	2.479	2.479	2.481	1.834	127.6	128.2	128.6	0.7	37.6



The atoms in red, green and blue are positioned in top, second and third layers, respectively.

## 7.5 ADSORPTION SITE OF THE CH<sub>3</sub>S SPECIES ON THE DEFECT-FREE AU(111) SURFACE

The experimental and several calculated STM images for CH<sub>3</sub>S/Au(111) are shown in Fig. 7.7. The Au(111) lattice and the ball models of the adsorbed CH<sub>3</sub>S species are superimposed on the calculated STM images. From direct comparison of these images the *br-fcc* (or a very similar *br-hcp*) configuration most closely matches the experimental image of CH<sub>3</sub>S. The calculated

images for all the other configurations are significantly different from the experimental STM image and can be ruled out as follows.

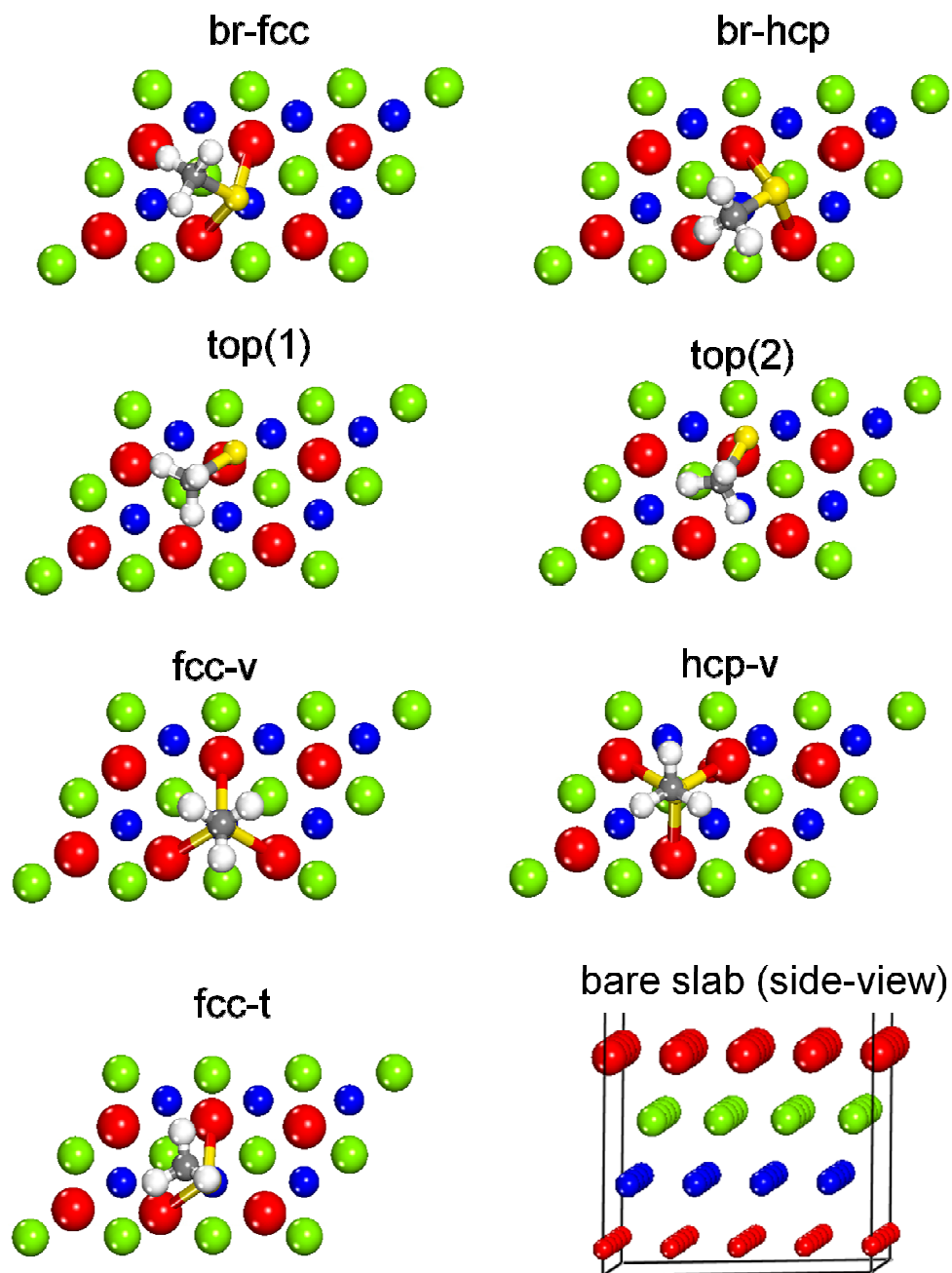


**Figure 7.5.** Top-view ball models of the calculated adsorption configurations of  $\text{CH}_3\text{S}$  described in Table 1. The  $\text{CH}_3\text{S}$  coverage is  $1/5$  ML for each model.

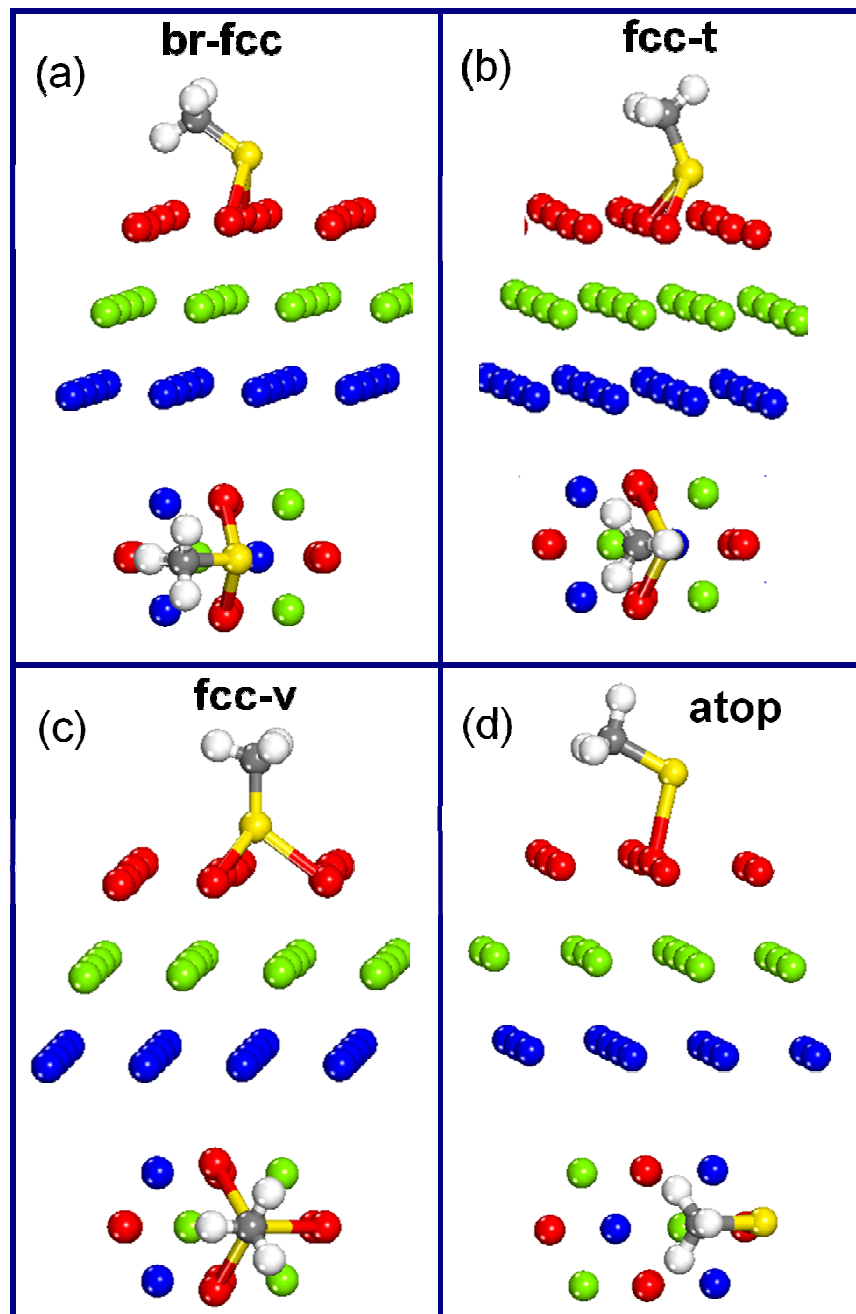


**Figure 7.6.** Structural models of representative adsorption configurations of  $\text{CH}_3\text{S}$  species on the Au(111) surface for which the STM images were calculated. Side and top views are shown for each configuration.

$\text{CH}_3\text{S}$  species adsorbed on the hollow sites (in both *fcc-t* and *fcc-v* configurations) makes a relatively small angle with the normal to the surface ( $\sim 26.3^\circ$  for *fcc-t* and  $0^\circ$  for *fcc-v*, Table 7.1). In this case the STM image is dominated by the  $\text{CH}_3$  group and  $\text{CH}_3\text{S}$  appears as a featureless protrusion (a slight asymmetry of the STM image of the *fcc-t* configuration is

unlikely to be resolved experimentally). However, each experimental  $\text{CH}_3\text{S}/\text{Au}(111)$  image has two lobes on one hand and there are six equivalent orientations with respect to the Au lattice on the other (Fig. 7.4, 7.7). Both of these features imply that  $\text{CH}_3\text{S}$  is strongly tilted towards the surface, which is inconsistent with the hollow site configurations. This conclusion is further supported by a recent observation of the  $\text{CH}_3\text{S}$  species on the  $\text{Cu}(111)$  surface [251], where it is imaged as a round featureless protrusion because of  $\text{CH}_3\text{S}$  adsorption on a three-fold hollow site on the  $\text{Cu}(111)$  surface.

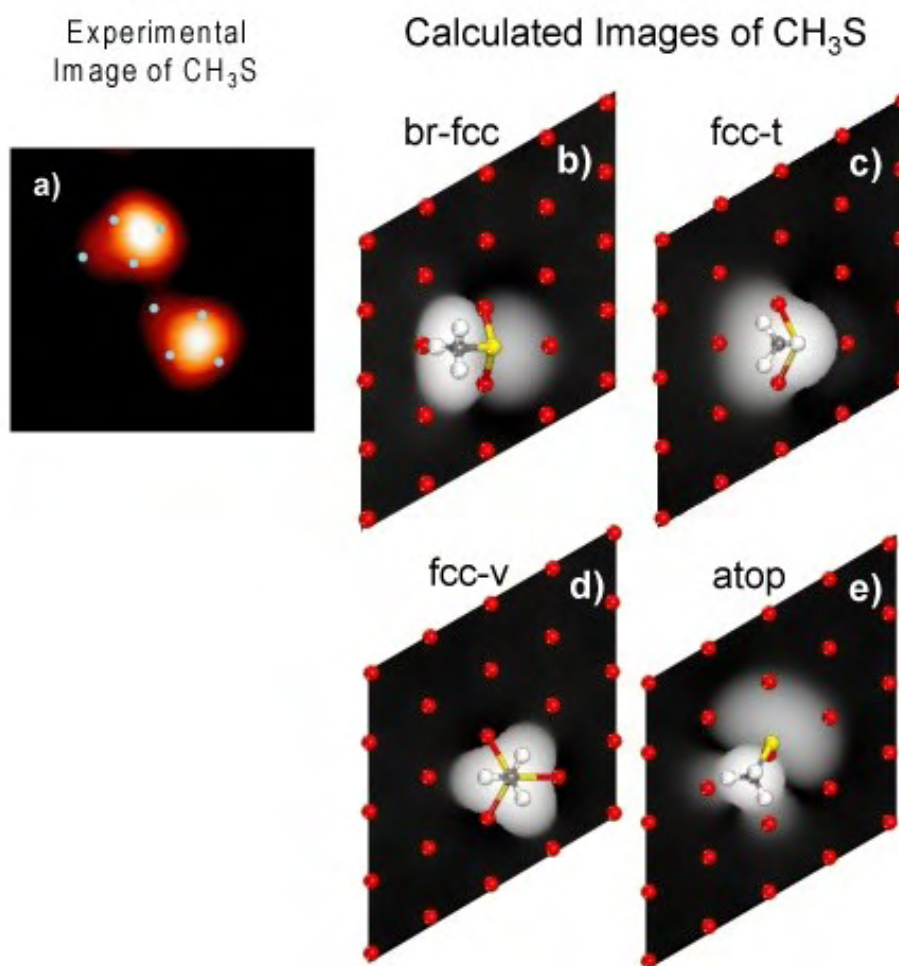


**Figure 7.7.** Experimental and calculated STM images of  $\text{CH}_3\text{S}$  species. Experimental: a)  $\text{CH}_3\text{S}$  species derived from  $\text{CH}_3\text{SSCH}_3$  ( $U = -0.010$  V,  $I = 40$  pA). Calculated: b) *br-fcc*; c) *fcc-t*; d) *fcc-v*; e) *top(1)*. Blue (experimental) and red dots (calculated) mark the position of Au atoms in the lattice.

The atop and bridge-site configurations have very similar two-lobed STM images, because the S-C bond in both configurations is tilted by  $\sim 50^\circ$  relative to the surface normal

(Table 7.1). The higher lobe corresponds to the CH<sub>3</sub>-group and the smaller, more diffuse one originates from the electronic states on the S-atom [254]. However, there is a substantial difference in the spatial location of the STM image of each structure relative to the underlying Au lattice. As seen in Figs. 7.7b and 7.7e, the S-atom is located at the node separating the large and small lobes of the STM image of the CH<sub>3</sub>S species. Thus, the nodal plane in the calculated image is centered above the bridge-site for the *br-fcc* configuration and above a gold atom for the *atop* configuration. Experimentally, it was determined that most of the CH<sub>3</sub>S intensity in the experimental STM image is spatially localized above two neighbor hollow sites (fcc and hcp), and that the separation line between the large and small lobes is located very close to the bridge site between two Au-Au atoms (Fig. 7.4b). This fact agrees well only with the bridge-site configurations, *br-fcc* and *br-hcp*.

In summary, based on the two-lobed shape of the STM image of the chemisorbed CH<sub>3</sub>S species and its spatial position relative to the underlying Au atoms, we conclude that the theoretically predicted bridge-site location of the S-headgroup is most consistent with our experimental measurements for CH<sub>3</sub>S at low coverage on a defect-free Au(111) surface.

## **7.6 LACK OF ROTATIONAL MOTION OF THE BRIDGE-BONDED CH<sub>3</sub>S SPECIES**

Additional evidence against the previously reported atop adsorption configuration of CH<sub>3</sub>S [50, 68, 69] on Au(111) is the freezing the hindered rotation of the CH<sub>3</sub>SH molecule [166] upon its electron-induced deprotonation (Fig. 7.3). We argue that this occurs because the coordination of the S-atom to Au-atoms increases from one to two as a result of the reaction. This would be consistent only with bridge (or hollow) bonded CH<sub>3</sub>S species, because the atop configuration of CH<sub>3</sub>S is singly coordinated similar to CH<sub>3</sub>SH.

### Rotation of CH<sub>3</sub>S on Au(111) – DFT Calculation

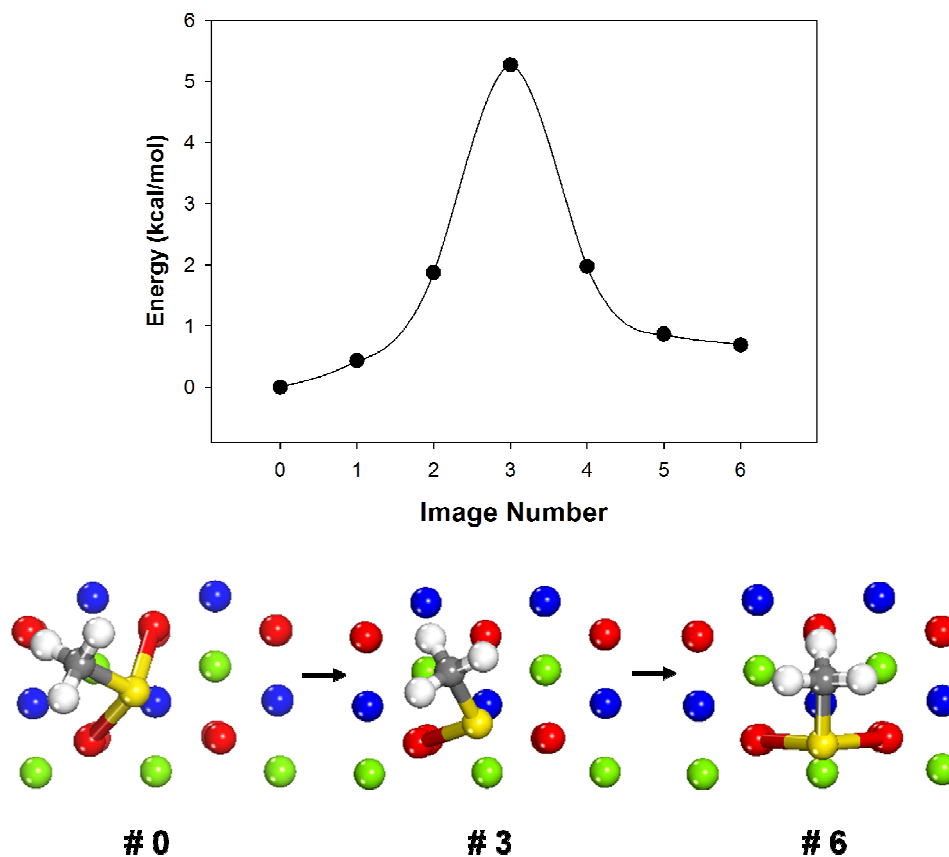


**Figure 7.8.** Barrier to rotation of the *br-fcc* CH<sub>3</sub>S species calculated using DFT/NEB method. The Au atoms are colored according to their vertical position in the slab (Fig. 7.4).

To confirm that addition of extra bonds will produce a larger barrier to rotation, the rotational barrier of the CH<sub>3</sub>S species around the bridge-site in the *br-fcc* configuration was estimated using the Nudged-Elastic Band (NEB) method. The minimum energy path for CH<sub>3</sub>S rotation from a *br-fcc* to a *br-hcp* site is shown in Fig. 7.8. It was determined from a set of 5 NEB images distributed along the reaction pathway between the initial and final equilibrium configurations. As seen in Fig. 7.8, the calculated barrier height is about 5.2 kcal/mol, which is much higher than 0.1 kcal/mol calculated for CH<sub>3</sub>SH. The Boltzmann pre-factor for CH<sub>3</sub>S rotation at 5K is  $\sim 10^{-250}$ , which precludes any thermally activated rotation at this temperature. CH<sub>3</sub>S can, however, be translated and rotated by applying a high current pulse at 0.7-0.8 V.

Our argument is further supported by the similarity of deprotonation of CH<sub>3</sub>SH on the Au(111) and benzenethiol derivatives on the Cu(111) surfaces [178, 255]. The 2,6-

dichlorobenzenethiol molecule on the Cu(111) surface stops rotating, when the S-H bond is dissociated by a current pulse from the STM tip. This occurs because the thiol (RSH) is adsorbed on the atop Cu site and the thiolate (RS) species is adsorbed on the three-fold hollow site on the Cu(111) surface [178].

## 7.7 SUMMARY

1. The products of the STM tip-induced dissociation of CH<sub>3</sub>SH and CH<sub>3</sub>SSCH<sub>3</sub> on the Au(111) surface at 5K are identical, as seen by STM. The product yield is 1:1 for CH<sub>3</sub>SH and 2:1 for CH<sub>3</sub>SSCH<sub>3</sub>, which unambiguously identifies the product in each case as CH<sub>3</sub>S.
2. A high-resolution STM image of an isolated CH<sub>3</sub>S species has a two-lobed shape and six equivalent orientations on the Au(111) surface. Both of these observations imply a strongly tilted adsorption configuration. Based on the comparison of the experimental STM image of the CH<sub>3</sub>S species with the calculated STM images of the CH<sub>3</sub>S species adsorbed on different surface sites, the 2-fold bridge site for the S-headgroup is favored over the 1-fold atop site and the 3-fold hollow site.
3. The assignment of the bridge-site bonded S-headgroup in the chemisorbed CH<sub>3</sub>S species is further verified by observing that the tip-induced rotational motion of the CH<sub>3</sub>SH molecule on the Au(111) surface ceases upon deprotonation. The high barrier to rotational motion of the CH<sub>3</sub>S species originates from the increase in the S-Au bond coordination from one-fold in CH<sub>3</sub>SH adsorbed on the atop site to two-fold in CH<sub>3</sub>S adsorbed on the bridge site.

The STM study presented above is the first one to address a *single* CH<sub>3</sub>S species on the *unreconstructed* Au(111) surface. In this case the agreement between theory and experiment is excellent, indicating standard DFT-calculations provides a sufficiently accurate description of the S-Au bonding. Nevertheless, the preference of the atop bonding of CH<sub>3</sub>S on Au(111) surface was reported a number of times in PhD and NIXSW studies of SAMs prepared at 300K [50, 68, 69] and cannot be disregarded as some kind of experimental error. The difference may, however,

originate from the procedure for CH<sub>3</sub>S synthesis on Au(111) surface: while we are working at low coverages and at low temperatures using tip-induced dissociation of CH<sub>3</sub>SH (CH<sub>3</sub>SSCH<sub>3</sub>) on the unreconstructed Au(111) surface (the herringbone reconstruction can be neglected because of its large length-scale), the spectroscopic studies were done at saturation coverage using thermal dissociation of the thiol or disulfide molecules. This suggests that the discrepancies in assignment of adsorption sites may arise from coverage effects and/or adsorbate-induced surface reconstruction.

Thiolate-induced reconstruction of the Au(111) surface was indeed proposed several times based on indirect evidence [37, 256, 257]. However, no conclusive models were established and therefore this idea was not accepted in the recent literature [16, 22]. It is also clear that alkanethiolate self-assembly *must* induce mass-transport of Au-adatoms across the surface to lift the Au(111) herringbone reconstruction and produce etch-pits on the surface. In all current models of the lifting of the reconstruction [55, 258], it is assumed that the Au-atoms ejected from the reconstructed surface layer migrate to the steps and attach there.

The next chapter presents the first direct and microscopic evidence that *Au-adatoms are embedded into the self-assembled structures of alkanethiolate species*. Furthermore, a quantitative correlation between lifting of the herringbone reconstruction and SAM growth is derived, which implies that the Au-atoms embedded in the SAMS originate from the herringbone reconstruction (at the early stage of SAM growth).

## 8.0 GOLD-ADATOM-MEDIATED BONDING IN SMALL ORGANOSULFUR MOLECULES SELF-ASSEMBLED ON Au(111) SURFACE\*

The evidence for the Au-adatom involvement in the bonding of the alkanethiolate species to the Au(111) surface was obtained from the STM/DFT study of the products of thermal dissociation of  $\text{CH}_3\text{SSCH}_3$ ,  $\text{CH}_3\text{SH}$  and  $\text{C}_3\text{H}_7\text{SH}$  molecules on Au(111). All the studies were done in the low-coverage regime, where alkanethiolate moieties self-assemble into the 2D structures termed the stripe-phase. The stripe-phase is the precursor to saturated 3D-SAMs [16, 59]. The distinct feature of the thiolate stripe-phase is the large tilting angle of the alkane tail relative to the surface normal, which makes the S-Au anchor-bond directly accessible to STM.

In this study a new structural model for the stripe-phase was derived, which involves pairs of RS-species bonded via a Au-adatom (RS-Au-SR). The new model is different from all the previous ones [23, 43, 59], where direct coupling of S-headgroups in the pair-units was assumed (RS-SR). As mentioned above, the spectroscopic analysis of stripe-phase SAMs [68, 69] states the preference of singly-coordinated S-atom adsorbed atop of Au atoms, which contradicts the results of DFT calculations where the preference of the two-fold coordinated S-atoms adsorbed on the bridge-sites is found. However, DFT analysis of the stripe-phase involving Au-adatoms shows that each RS species does indeed form a singly-coordinated bond to the Au(111) surface, reconciling this long-standing controversy.

---

\* Reproduced in part with permission from: P. Maksymovych, D. C. Sorescu, J. T. Yates, Jr., *Physical Review Letters* 97 (146103) 2006. Copyright 2006 American Physical Society.

## 8.1 ADATOM-BONDED STRIPE-PHASE OF METHYLTHIOLATE ON Au(111) SURFACE

Figure 8.1 shows the STM images of three products of  $\text{CH}_3\text{SSCH}_3$  chemistry on the Au(111) surface – the undissociated physisorbed molecule (dosed at 10K) (Fig. 8.1a),  $\text{CH}_3\text{S}$ -species produced by electron-induced dissociation of  $\text{CH}_3\text{SSCH}_3$  at 5K (Fig. 8.1b), and  $\text{CH}_3\text{S}$ -species produced by thermal dissociation of  $\text{CH}_3\text{SSCH}_3$  at 300K (Fig. 8.1c,d). Thermally produced  $\text{CH}_3\text{S}$  forms chains of distinct repeat units (Fig. 8.1d), and the areal profile of each unit is about twice as large as a single  $\text{CH}_3\text{S}$  species in Fig. 8.1b. The chain structure is known as a stripe-phase, and it represents a flat-lying self-assembled layer (with carbon chains of alkyl groups parallel to the surface), which is the precursor to high coverage SAM layers involving upright thiolate species [48]. The stripe-phase chains always grow in the  $[\bar{1}1\bar{2}]$  azimuthal direction with a periodicity of  $\sim 0.47$  nm between repeat units, which is consistent with previous reports [22, 43, 59].

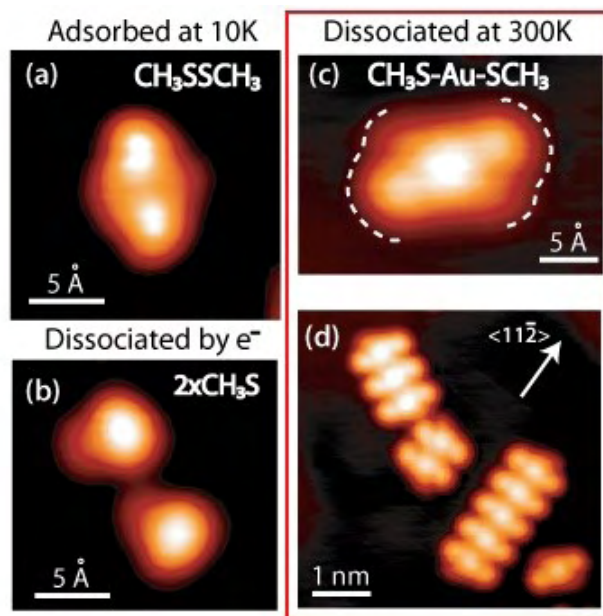


**Figure 8.1.**  $\text{CH}_3\text{SSCH}_3$  chemistry on Au(111) surface. a) Single  $\text{CH}_3\text{S-SCH}_3$  molecule. b) Two  $\text{CH}_3\text{S}$  fragments formed by dissociating  $\text{CH}_3\text{S-SCH}_3$  with a 1.0V pulse at 5K. c) Close-up of a single stripe-phase unit. The asymmetrical boundaries of the  $\text{CH}_3\text{S}$  species are marked by dashed white lines. d) Chains of  $\text{CH}_3\text{S}$  stripe-phase after heating  $\text{CH}_3\text{S-SCH}_3$  on Au(111) to 300K.

In the current models of the stripe-phase [22, 43, 59, 68] the repeat-unit is a pair of RS species, with headgroup-S atoms facing each other and forming an S-S bond (Fig. 8.2). This, however, is inconsistent with the extreme stability of the stripe-phase unit to high tunneling voltage or current as described below.

A  $\text{CH}_3\text{SSCH}_3$  molecule can be stably imaged only at a bias of less than 0.5V, which is consistent with its small calculated adsorption energy of  $\sim 10$  kcal/mol on the Au(111) surface [65]. At higher voltages  $\text{CH}_3\text{SSCH}_3$  undergoes tip-induced motion, and the molecule dissociates above 1.0V producing (at 5K) two  $\text{CH}_3\text{S}$  species bonded to the surface lattice. A single  $\text{CH}_3\text{S}$  species, despite its maximum calculated binding energy of  $\sim 40$  kcal/mol on Au(111) [65], can be translated on the surface by applying pulses of 0.7-1.0V at 1.0 nA. This is likely due to small potential barriers between neighbor  $\text{CH}_3\text{S}$  adsorption sites [65]. The imaging stability of the stripe-phase unit in Fig. 1c is starkly different from both adsorbed  $\text{CH}_3\text{SSCH}_3$  and  $\text{CH}_3\text{S}$ , *as it is virtually indestructible by the tunneling current and voltage*. The unit can be imaged at voltages up to 4.5V (!) without diffusion or decomposition, and it can sustain large imaging currents up to 20 nA.

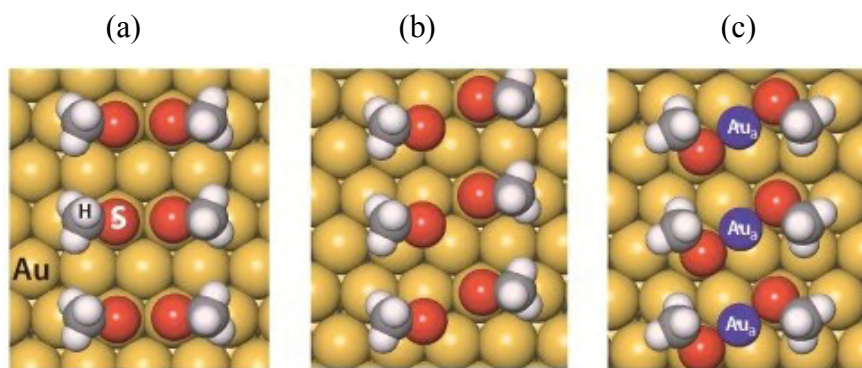


**Figure 8.2.** Alkanethiolate stripe-phase SAM. Top-view models of the  $\text{CH}_3\text{S}$  stripe-phase according to (a) Ref. [68], (b) Ref. [59] and (c) proposed here.  $\text{Au}_a$  is the Au-adatom.

We therefore propose that the thermally-produced thiolate is stabilized by Au-adatoms as shown in Fig. 8.2c. Metal adatoms form spontaneously on a number of metal surfaces at elevated temperatures. Adatom complexes with adsorbate molecules are known to have significantly higher binding energies, and this was also theoretically shown for the  $\text{CH}_3\text{S}$  species on the Au(111) surface [259].

Inclusion of a Au-adatom provides a straightforward explanation of the topographical appearance of the stripe-phase repeat unit. As seen in Fig. 8.1c, high-resolution STM topography of the pair-unit can be divided into two identical asymmetrical features, anti-parallel to each other, separated by a single bright protrusion. Since there are two CH<sub>3</sub>S fragments in each unit, each asymmetrical feature corresponds to a single CH<sub>3</sub>S. Then, the central protrusion can be assigned to the Au-adatom. We have also verified that a similar central bright protrusion exists in the stripe-phases derived from CH<sub>3</sub>SH and from a longer alkanethiol, C<sub>3</sub>H<sub>7</sub>SH. In the stripe-phase models without adatoms (Fig. 8.2(a,b)), the central feature corresponds to a pair of headgroup-S atoms and the CH<sub>3</sub> groups are on the periphery, which makes it difficult to explain the asymmetry of the peripheral features.

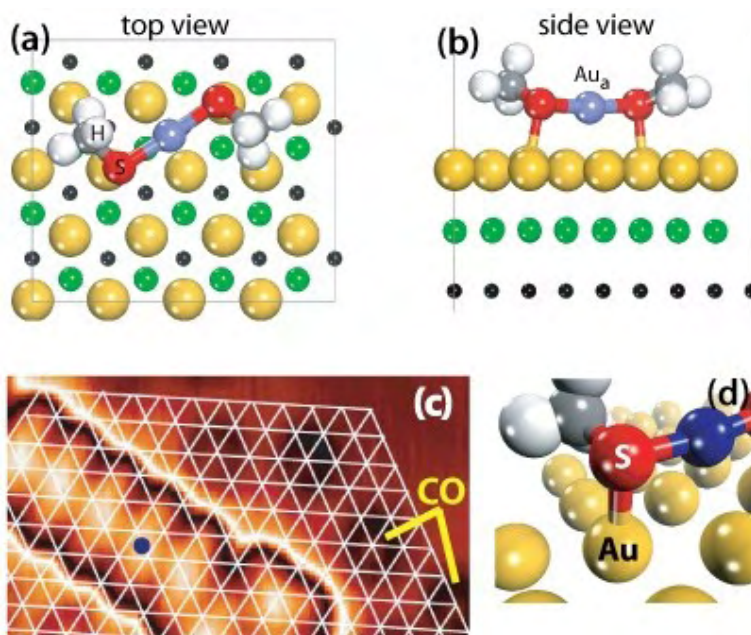


**Figure 8.3.** Structure of CH<sub>3</sub>S-Au-SCH<sub>3</sub> on Au(111). (a), (b) Calculated structure of adatom-bonded pair-unit which forms the CH<sub>3</sub>S stripe-phase. (c) Triangulation of the CH<sub>3</sub>S stripe-phase relative to the underlying lattice using CO molecules as markers of the Au lattice atoms. The off-hollow position of the Au-adatom (blue circle) agrees well with the theoretical predictions presented in this work. (d) Perspective view of the S-atom showing its position above the lattice Au-atom.

The new structural model of the stripe-phase unit (Fig. 8.3) was obtained using DFT calculations. In the input structure the Au-adatom was initially placed above a 3-fold hollow fcc

site, and the two CH<sub>3</sub>S fragments were symmetrically arranged on two hollow sites around the adatom building a structure reminiscent of the STM image. Unexpectedly, the minimization process results in the shift of the Au-adatom from the 3-fold hollow site to the 2-fold bridge-site as shown in Figs. 8.3a,b. At the same time, each CH<sub>3</sub>S species assumes a new adsorption configuration, in which the headgroup-S atom of CH<sub>3</sub>S makes one bond to the Au-adatom and one bond (Fig. 8.3d) to the underlying lattice atom giving  $r(\text{S-Au-adatom})=2.33\text{\AA}$  and  $r(\text{S-Au-lattice})=2.49\text{\AA}$ . The unusual off-hollow position of the Au-adatom in the stripe-phase units is indeed observed by STM as seen in Fig. 8.3c, where the blue dot indicates that the Au-adatom is located on a bridge site above the surface plane. Here the surface Au lattice grid was determined using CO molecules as markers of lattice atoms. As expected, the presence of the Au-adatom in the complex increases the binding energy of a single CH<sub>3</sub>S species to 55.3 kcal/mol compared to the 43.4 kcal/mol binding energy calculated for the most stable CH<sub>3</sub>S configuration on the Au(111) surface. (The binding energy of the adatom-bonded CH<sub>3</sub>S was determined relative to the gas-phase CH<sub>3</sub>S and the Au(111) surface with the Au-adatom on the hollow fcc-site).

The new model of the stripe-phase is also in excellent agreement with recent NIXSW [69] and NEXAFS/PhD [69] studies, where it was found that headgroup-S atom is adsorbed atop of a lattice Au atom forming a singly-coordinated bond. Each S-atom in our calculated model also makes one bond to the lattice Au atom and is located directly above this atom (Fig. 8.3d). Moreover, the calculated bond-length between the S-atom and the lattice Au-atom is 2.49 Å, which agrees well with the values reported for the stripe-phases of long-chain alkanethiolates:  $2.50\pm 0.05\text{\AA}$  measured by NISXW for C<sub>8</sub>H<sub>17</sub>S [69] and  $2.40\pm 0.05\text{\AA}$  measured by PhD for C<sub>6</sub>H<sub>13</sub>S [4]. The spectroscopic signature of the Au-adatom was not reported. However, the adatom-bonded model of the stripe-phase were not tested either in the analysis of the NIXSW [69] and PhD [4] data, which is very sensitive to the choice of the structural model.

## 8.2 HERRINGBONE RECONSTRUCTION – SOURCE OF REACTIVE AU-ADATOMS

Further support for the involvement of Au-adatoms in the thiolate self-assembly comes from the observation of a quantitative correlation between the production of the stripe-phase and the

lifting of the Au(111)  $22\times\sqrt{3}$ -herringbone reconstruction (the latter always occurs in thiolate self-assembly [57]). The herringbone reconstruction is formed by embedding one Au atom per 22 surface atoms into the bulk-terminated surface layer along the  $\langle 1\bar{1}0 \rangle$  direction [56]. The area of the  $22\times\sqrt{3}$  unit cell measured in our atomically resolved images of the Au(111) surface is  $2.8 \text{ nm}^2$ , in agreement with previously reported values [56]. Since there are two embedded Au atoms in the  $22\times\sqrt{3}$  unit cell, the surface density of the embedded Au atoms is  $0.7 \text{ atoms/nm}^2$ .

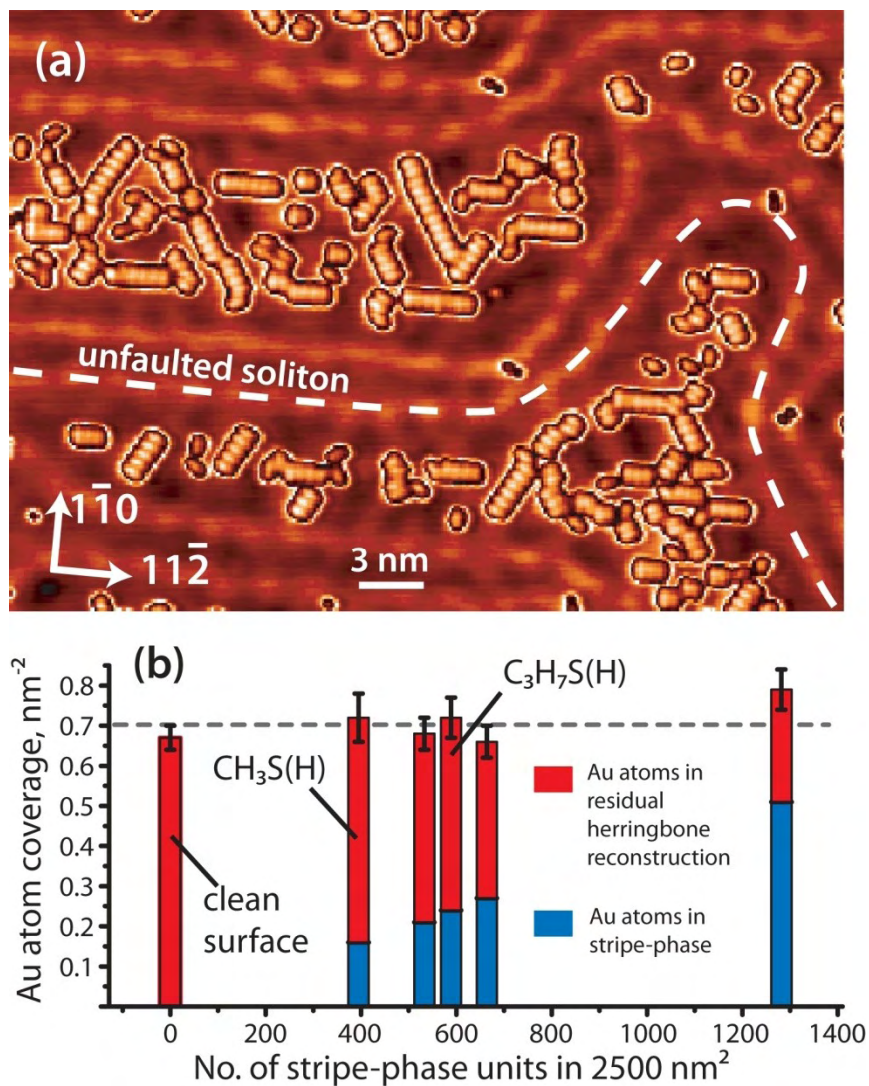


**Figure 8.4.** Correlation between self-assembly of the stripe-phase and lifting of the Au(111) herringbone reconstruction. (a) Typical large-scale sampling area of the Au(111) surface used for counting. Dashed line is the unfaulted soliton line. (b) Distribution of Au atoms (embedded herringbone atoms plus adatoms in the stripe-phase) as a function of stripe-phase coverage for stripe-phases produced from  $\text{CH}_3\text{SSCH}_3$ ,  $\text{CH}_3\text{SH}$  (marked) and  $\text{C}_3\text{H}_7\text{SH}$  (marked).

The number of remaining embedded Au-atoms in the herringbone reconstruction was determined after it is partially lifted by the stripe-phase of methyl- and propylthiolate. The  $22\times\sqrt{3}$  unit cell has one fcc- and one hcp-stacked lattice region along the  $\langle 1\bar{1}0 \rangle$  direction, which are separated by two solitons [260] (regions of faulted vertical stacking). The number of the remaining reconstructed unit cells (each involving two embedded Au atoms) can therefore be conveniently estimated by measuring the total length of the unfaulted soliton lines (Fig. 8.4) in the STM image and dividing it by 0.47 nm, which is the measured periodicity of the  $22\times\sqrt{3}$  unit cell along the  $\langle 11\bar{2} \rangle$  direction of the soliton.

Surprisingly, the number of newly formed repeat units of the stripe-phase is equal (within statistical error) to the number of embedded Au atoms which have disappeared during thiolate self-assembly. This is shown in Fig. 8.4b, where a bar graph shows the distribution of the embedded Au-atoms in the herringbone reconstruction and the bound Au-adatoms in the stripe-phase as a function of the stripe-phase coverage. The total coverage of the Au-atoms (embedded and complexed) remains nearly constant ( $\sim 0.7$  Au/nm<sup>2</sup>) at low and intermediate coverages of the stripe-phase. This conclusion is valid for the stripe-phases obtained from all the molecules studied: CH<sub>3</sub>SSCH<sub>3</sub>, CH<sub>3</sub>SH and C<sub>3</sub>H<sub>7</sub>SH.

Such a correlation quantitatively supports our stripe-phase model, where each repeat-unit contains one Au-adatom. Furthermore, it suggests that the herringbone reconstruction can provide reactive Au-adatoms by ejecting them locally where the stripe-phase is formed. Most likely, lifting of the herringbone reconstruction proceeds at the elbow sites [56] (see below), although the detailed mechanism may involve creation of extended line vacancies [99].

The above correlation begins to break down at a higher stripe-phase coverage, because the number of stripe-phase units exceeds the number of embedded atoms in the herringbone reconstruction (at near-saturation stripe-phase unit density is as high as 1.2 nm<sup>-2</sup>). In this case random atomic steps, and ultimately the top bulk-terminated layer, become the source of Au-adatoms. This is consistent with step-etching and etch-pit creation on the terraces [48, 258] that accompany thiolate self-assembly at high surface coverage.

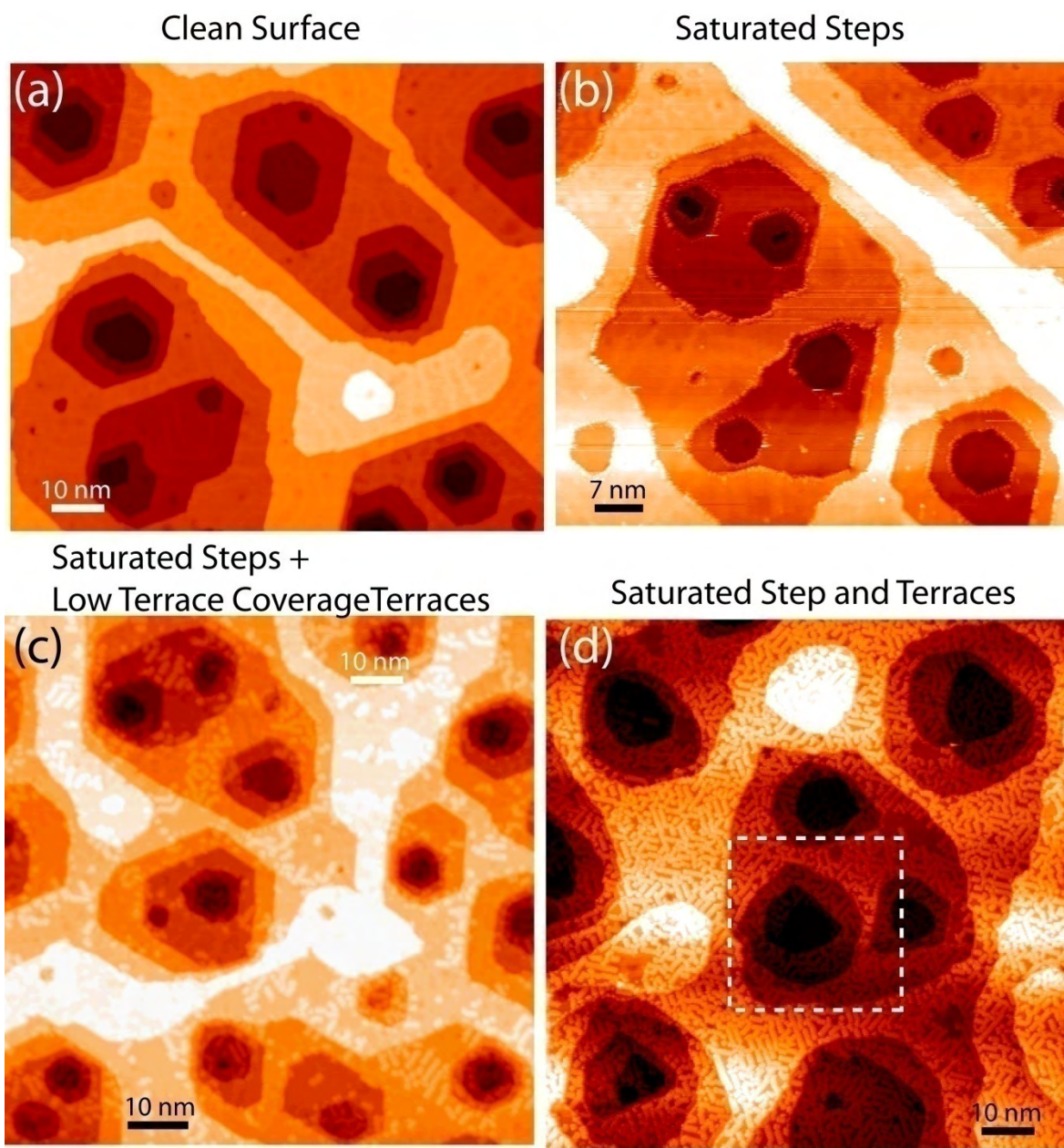
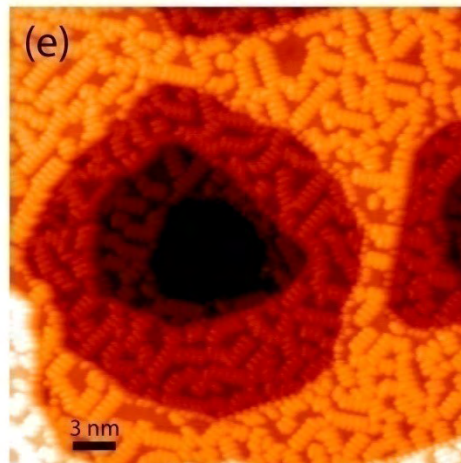


**Figure 8.5.** Step-etching by alkanethiolate self-assembly. (a) Au(111) surface with hexagonal etch-pits decorated by single-atom steps running along  $[1\bar{1}0]$  directions. (b) After dosing a small amount of  $\text{CH}_3\text{SSCH}_3$  at room temperature. (c) Further dosing produces low-coverage of  $\text{CH}_3\text{S-Au-SCH}_3$  stripe-phase on the terraces. Step-morphology is hardly changed in (b) and (c). (d) STM images of high  $\text{CH}_3\text{S-Au-SCH}_3$  stripe-phase coverage on the terraces: substantial erosion of previously hexagonal pits is observed. (e) Enlarged area inside the dashed square in (d).



It is desirable to confirm that step etching is caused by methylthiolate self-assembly at a higher surface coverage. Real-time tracking of the morphology of single-atomic steps during self-assembly is challenging in the LT-STM because of the high temperature required to dissociate  $\text{CH}_3\text{SSCH}_3$ . Instead, the morphology of artificial hexagonal pits was compared before and after stripe-phase growth to verify (qualitatively) that the steps were involved in the process of stripe-phase formation.

An array of etch-pits was first created on the clean Au(111) surface by gentle sputtering at  $\sim 500\text{K}$  [261]. Each pit is one atom deep, and it is decorated by six atomic steps along the close-packed directions  $[1\bar{1}0]$  producing a nearly-symmetric hexagonal shape Fig. 8.5a. After depositing a certain amount of  $\text{CH}_3\text{SSCH}_3$ , the surface was heated to  $\sim 250\text{K}$  in order to form the stripe-phase.

The pit morphology is noticeably changed by the stripe-phase growth (Fig. 8.5d). Pits become rounded, eroded, losing most of their initial hexagonal shape. The crystallographic orientation of many steps significantly deviates from the equilibrium  $[1\bar{1}0]$  direction.

In general, the atomic step-morphology may be changed by molecular adsorption on the step itself, because each step-orientation exposes certain adsorption sites and some of these sites may bind adsorbates stronger than the other [262]. However, this is not the case for the methylthiolate. As seen in Fig.8.5 (b,c), the morphology of the steps saturated with the thiolate species is the same as that on the clean surface. Therefore, the observed changes at high coverage of the stripe-phase are associated with the growth of the thiolate SAM *on the terrace*. In this case, the Au-adatoms are removed from the steps and embedded in the SAM layer. The morphology of the steps thus assumes a non-equilibrium shape. The lowest-energy pathway to restore the equilibrium step orientation is to allow Au-adatoms (or vacancies) to diffuse along the step-edge. On the clean Au(111) surface the activation barrier of adatom diffusion along the step is  $\sim 0.3$  eV [263], which would make the process feasible at 250K on the time-scale of the experiment. Apparently the thiolate adsorbed on the steps increases this barrier preventing equilibration of the step orientation back to  $[1\bar{1}0]$  directions.

### 8.3 CONCLUSIONS

We have presented the first microscopic evidence for the adatom-mediated bonding in the self-assembly of alkanethiolate species on Au(111). The involvement of Au-adatoms resolves the current controversy around the the S-Au anchor bond in the low-coverage stripe-phase SAM, and explains the morphological changes of the Au(111) surface, such as the lifting of the herringbone reconstruction. Although the involvement of the Au-adatoms in the higher coverage 3D-self-assembled layers remains to be established, the results obtained here call upon a significant revision of the currently accepted mechanisms for the nucleation of the 2D stripe-phase and the subsequent 2D to 3D transition of the SAM. The Au-adatoms are also likely to influence the electronic properties of the molecules in the SAM. In addition, adatom-mediated chemistry on gold surfaces, and the role of the herringbone reconstruction as a source of chemically reactive Au-adatoms, is anticipated to have general implications for the field of heterogeneous catalysis and beyond.

## **9.0 IMPLICATIONS OF AU-ADATOM BONDING IN ALKANETHIOLATE AND ARYLTHIOLATE SAMS ON AU(111)**

To emphasize the importance of Au-adatoms for alkanethiol self-assembly, I present preliminary results indicating that Au-adatoms may be crucial in other aspects of self-assembly, including dissociation of the parent molecules and the topology of self-assembled structures.

### **9.1 AU-ADATOMS IN DISSOCIATION OF S-S AND S-H BONDS ON AU(111)**

In the previous chapter Au-adatoms were found to bond self-assembled  $\text{CH}_3\text{S}$ -species to the Au(111) surface. A challenging question is whether Au-adatoms also participate in the dissociation of the precursor molecules (RSH or RSSR). The involvement of Au-adatoms in initiating thiolate self-assembly is indicated by the similar temperatures needed to produce the stripe-phase RS-H and RS-SR molecules. Both  $\text{CH}_3\text{SSCH}_3$  and  $\text{CH}_3\text{SH}$  dissociate to form the stripe-phase near 200K (this work and Refs. [16, 250, 264]). In all cases the stripe-phase is identical. The S-H bond in the gas-phase  $\text{CH}_3\text{SH}$  is  $\sim 1.0$  eV stronger than S-S bond in the gas-phase  $\text{CH}_3\text{SSCH}_3$  [265]. These facts can be consistently correlated by assuming that Au-adatoms are involved in the breaking of the corresponding bonds, and that Au-adatom creation is the limiting kinetic step for molecular dissociation and self-assembly (at low adsorbate coverages used in our experiments).

Direct evidence to support this assumption was obtained by heating the Au(111) surface with a small coverage of  $\text{CH}_3\text{SSCH}_3$  to  $\sim 180\text{K}$ , so that the rate of molecular dissociation is very low and preferential sites of stripe-phase nucleation can be observed. Since in-situ observations at this temperature in the Omicron LT-STM are somewhat complicated, the experiment was done in heating cycles; each time the surface reaches a desired temperature the crystal is quenched to

5K and inspected by STM. Below 160K (with  $\sim 10$ K error), there is absolutely no thermally induced chemistry of  $\text{CH}_3\text{SSCH}_3$  molecules even after many consecutive annealing cycles.

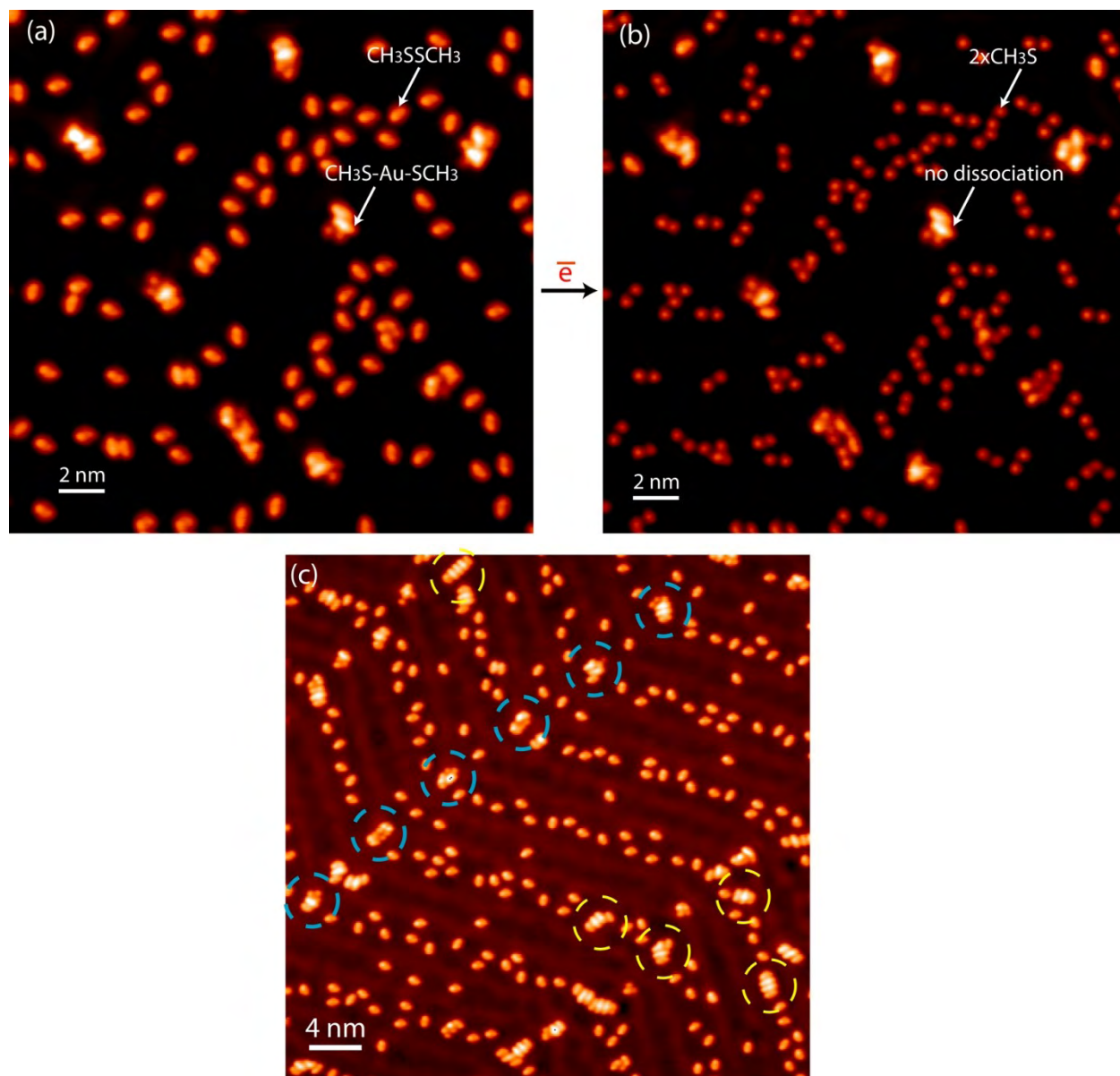


**Figure 9.1.** Slow conversion of  $\text{CH}_3\text{SSCH}_3$  to  $\text{CH}_3\text{S-Au-SCH}_3$  on Au(111) at  $\sim 180$ K. (a) STM image obtained after one annealing cycle.  $\text{CH}_3\text{S-Au-SCH}_3$  is observed to nucleate exclusively on the elbows. (b) STM image of (a) after applying a 2.5V pulse in the center of the image (see Chapter 12), which causes  $\text{CH}_3\text{SSCH}_3$  molecules to dissociate. The adsorbates on the elbows do not change, which confirms that they are  $\text{CH}_3\text{S-Au-SCH}_3$ . (c) STM image obtained after prolonged annealing (10 cycles). Stripe-phase appears on the terraces as well.

Above  $\sim 200\text{K}$ , complete dissociation is achieved and all the molecules present on the surface are self-assembled into Au-adatom-bonded complexes. This observation already suggests that molecular dissociation and self-assembly involving Au-adatoms are correlated processes.

Figure 9.1 shows STM images of the Au(111) surface with  $\text{CH}_3\text{SSCH}_3$  obtained after heating the crystal to  $180\text{K}$  for one time interval of several seconds (Fig. 9.1a) and 5-6 time-intervals of several seconds (Fig. 9.1c). Most of the  $\text{CH}_3\text{SSCH}_3$  molecules are still un-dissociated in Fig. 9.1c. Judging by the topographic appearance of the majority of adsorbates and the ability to dissociate them using electron pulses from the STM-tip (Fig. 9.1b). However, the elbow-sites of the herringbone reconstruction are decorated with what appears to be a single unit of the stripe-phase, i.e.  $\text{CH}_3\text{S-Au-SCH}_3$ . These species do not dissociate by electron pulsing. After prolonged annealing (Fig. 9.1c), more stripe-phase units appear and they start to aggregate in chains. Most of the stripe-phase units are observed on the elbow sites of the herringbone reconstruction, but they can also be found in the fcc-regions of the herringbone reconstruction. The chains on the elbows rarely grow to more than 3 units long in contrast to those on the terraces.

A logical conclusion from these observations is that  $\text{CH}_3\text{SSCH}_3$  dissociation occurs preferentially on under-coordinated (defective) elbow sites, and that the Au-adatom is pulled out from the elbow either by the dissociated  $\text{CH}_3\text{S}$ -radicals at the elbow or during  $\text{CH}_3\text{SSCH}_3$  dissociation. After formation, the  $\text{CH}_3\text{S-Au-SCH}_3$  unit may diffuse away from the elbow onto the terrace.

## **9.2 AU-ADATOMS IN SELF-ASSEMBLY OF BENZENETHIOL ON THE AU(111) SURFACE**

Because of the large steric and chemical difference between the organic tail of aromatic thiols and alkanethiols, the bonding and self-assembly is expected to be different as well [15]. For example, the binding energy of benzenethiolate ( $\text{PhS}$ ) species on the unreconstructed Au(111) is  $\sim 0.5\text{ eV}$  smaller than found for methylthiolate ( $\text{CH}_3\text{S}$ ) [266]. Thermal dissociation of benzenethiol at low coverage on Au(111) was therefore studied to verify that Au-adatom model

derived for alkanethiols can also be applied to arenethiols, which is an important class of organosulfur molecules, particularly in the field of molecular electronics [28, 267, 268].

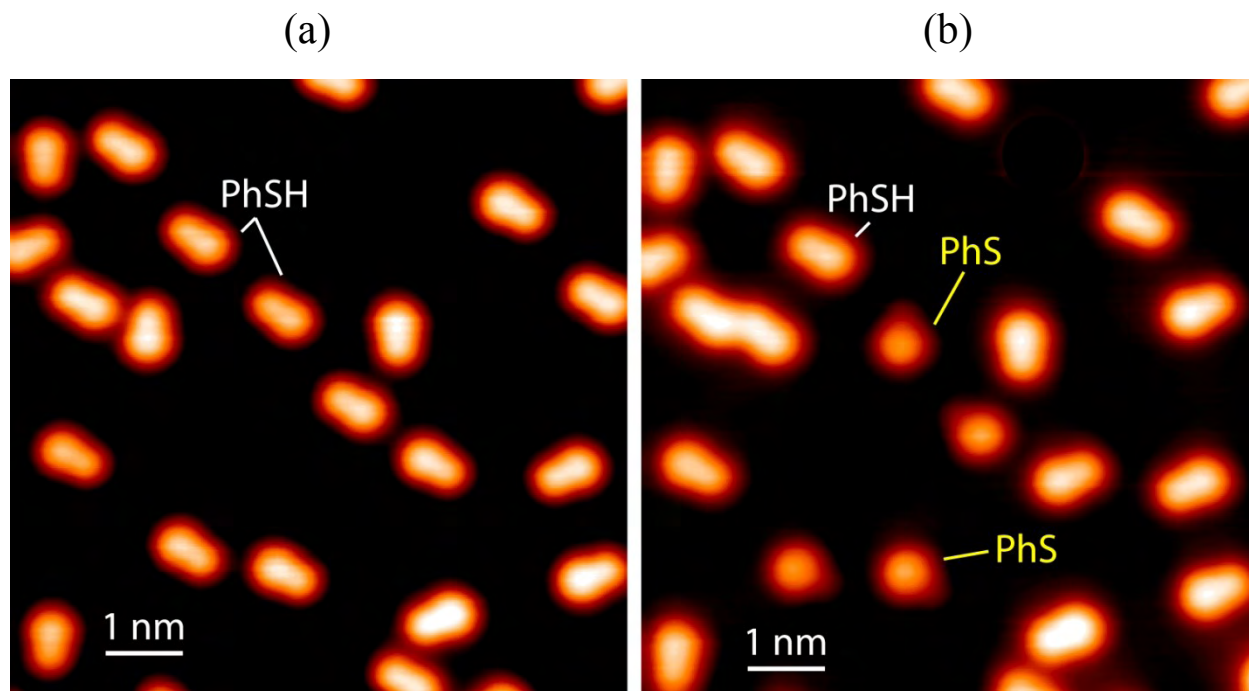


**Figure 9.2.** Phenylthiol (PhSH) and phenylthiolate (PhS) adsorbed on Au(111) at 5K. PhS species in (b) was produced at 5K by applying a 2.7 V pulse on top of PhSH molecules in (a). Au adatoms are not involved in these species because of the low temperature.

Undissociated benzenethiol molecules (deposited on Au(111) at  $T < 70\text{K}$ ) are imaged by STM as dumbbells (FWHM of the STM profile along the length of the molecule is  $9.5 \text{ \AA}$ ) with two lobes of slightly different apparent size and height (Fig. 9.2a). The apparent height of the large lobe is  $\sim 0.12 \text{ \AA}$ . By an obvious chemical analogy, the larger lobe in the image originates from the phenyl group. This assignment is further confirmed in the products of electron-induced dissociation of the S-H bond that is accomplished by applying a voltage pulse of  $> 2.7 \text{ V}$  by the STM-tip above the adsorbed molecule. The only product of this reaction is the PhS species that has one very large lobe ( $\text{C}_6\text{H}_5$ ) with a small tail (Fig. 9.2b) surrounded by a small black halo (not shown). PhS is topographically similar to  $\text{CH}_3\text{S}$  produced by the electron-stimulated dissociation of  $\text{CH}_3\text{SH}$  and  $\text{CH}_3\text{SSCH}_3$  molecules on Au(111) surface at 5K [67]. The large lobe in the  $\text{CH}_3\text{S}$ -species corresponds to the methyl group, while the tail with a halo corresponds to the sulfur

group. First-principles calculations predict adsorption of PhSH with the S-atom on singly-coordinated atop Au sites and the phenyl ring nearly flat and parallel to the surface [269].

Following adsorption of benzenethiol at low temperature, the Au(111) surface was heated to 300K to dissociate benzenethiol molecules thermally and to produce phenylthiolate (PhS) species. As seen in Fig 9.3a, most of the adsorbates are found in the form of species involving

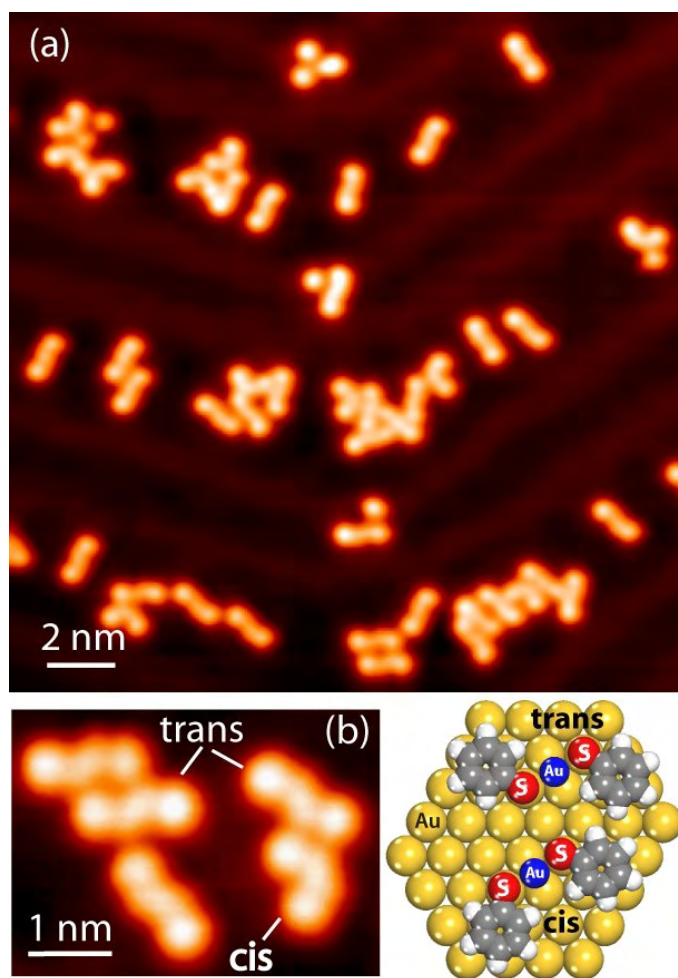


**Figure 9.3.** Dimers of phenylthiolate (PhS-Au-PhS) observed after heating Au(111) with PhSH to 300K. (a) Large scale image showing dimers and the dominance of the dimer in the trans-configuration. (b) Close-up STM image showing trans- and cis-PhS-Au-SPh units. Schematic ball-models are shown on the left (the Au-atom is blue).

two PhS fragments (called dimers) (Fig. 9.3a). The dimer image consists of two symmetric large lobes in cis- or trans-configuration relative to each other (Fig. 9.3b). The apparent height of the lobe is  $\sim 0.12 \text{ \AA}$ , identical to that of the flat-lying undissociated PhSH molecule. The STM profile along the dimer length has  $\text{FWHM} = 1.63 \pm 0.07 \text{ nm}$ , slightly less than two apparent lengths of the STM image of the single adsorbed PhSH molecule (Fig. 9.2a). The trans-dimer is dominant.

Many dimers are observed to be in close proximity to each other, coalescing into spacious structures most likely due weak hydrogen bonding (e.g. C-H...S) between the neighbor-molecules [270]. Due to steric hindrance between large phenyl groups, the phenylthiolate dimers do not form long compact chains observed for alkanethiolate on Au(111) [48].

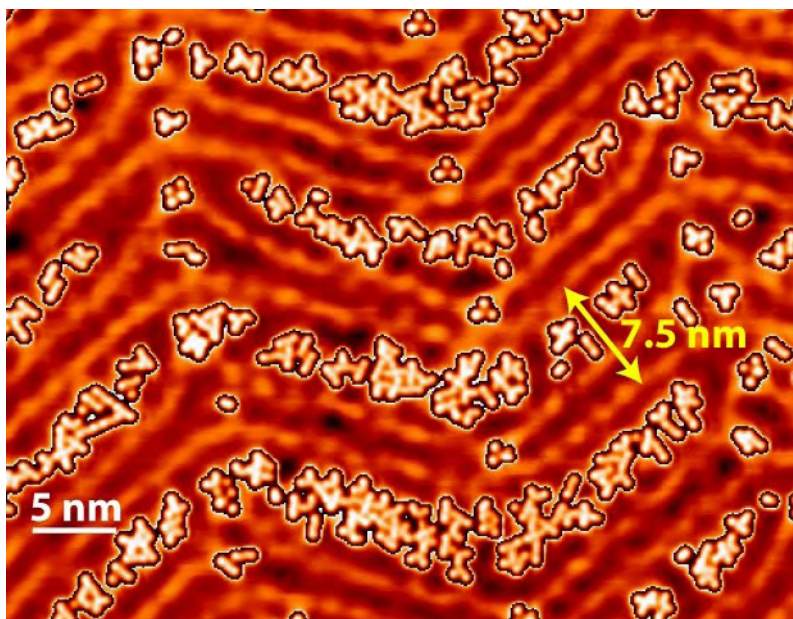


**Figure 9.4.** Formation of PhS-dimers at room temperature causes partial lifting of the herringbone reconstruction: the periodicity of the reconstruction is 7.5 nm along  $[1\bar{1}0]$  direction which is larger than 6.3 nm for the clean Au(111).

The favorable formation of the PhS dimer at high temperatures as well as its STM image imply that the dimer is not the diphenyldithiol molecule (PhS-SPh) with the S-S bond between two PhS fragments. The adsorption energy of this molecule was predicted to be very small [67] and even slightly negative [271] on Au(111). On the contrary, its dissociation is predicted to be facile with a barrier of less than 0.3 eV [67] leading to rapid dissociation at 300K. Furthermore, according to calculations the phenyl-rings in the PhS-SPh molecule adsorbed on the Au(111) surface are oriented nearly normal to the surface [67]. In contrast, the apparent height of the large lobes in the thermally-produced dimer is nearly the same as that in the undissociated PhSH with phenyl rings parallel to the surface. Although the apparent height in STM is only an approximate measure, such a close similarity implies that the conformations of the phenyl groups must also be

similar. One more fact supporting the absence of a S-S bond is the extreme stability of each dimer against high voltage/current pulses from the STM-tip. The dimer does not undergo any observable topographic changes (diffusion, dissociation etc.) even at a pulse voltage as high as 3.5 V and a tunneling current of 100 pA. In contrast, the PhSH molecule with a relatively strong S-H bond dissociates at 2.7 V and above, while the S-S bond in the  $\text{CH}_3\text{S-SCH}_3$  molecule on Au(111) surface dissociates at 1.4 V and above [47, 67].

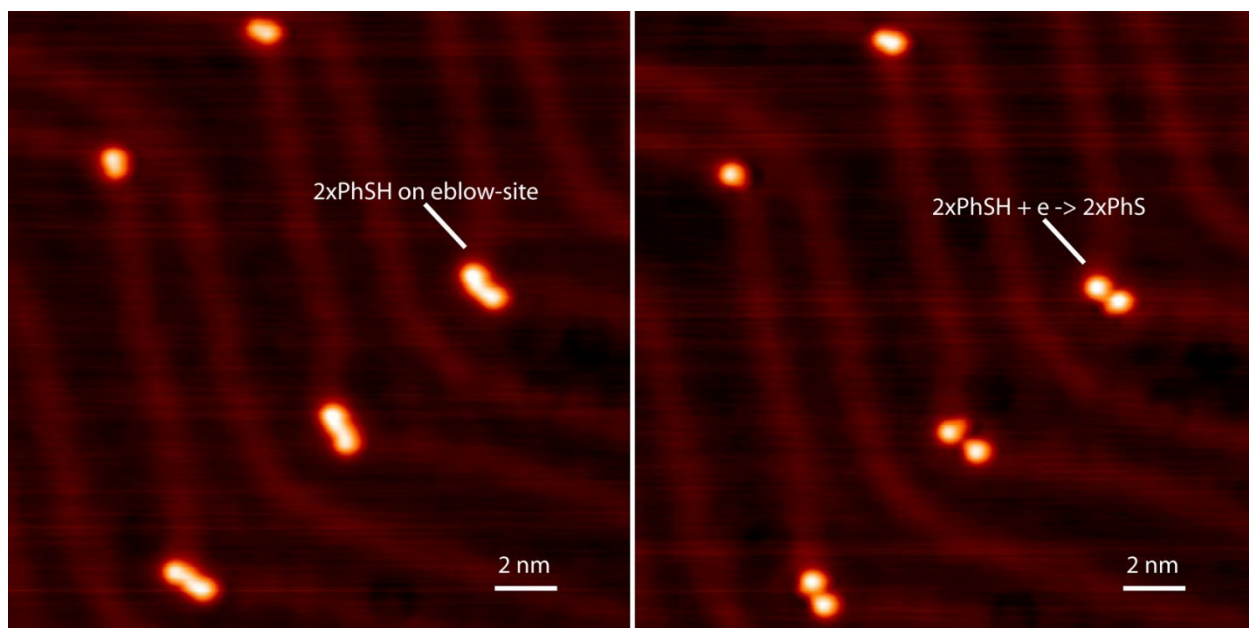


**Figure 9.5.** Pairing of PhSH molecules on the elbow-site at  $T \sim 70\text{K}$ . The S-H groups are facing each-other. The overall geometry of the pair is closely-reminiscent of the PhS-Au-SPh unit formed at higher temperature (Fig. 9.3). Each pair in left panel was pulsed with a 2.7-3.0 V pulse. Pulsing converts PhSH to PhS (right panel) via S-H bond-scission.

The high-temperature dissociation of PhSH at low coverage is accompanied by the partial lifting of the herringbone reconstruction (Fig. 9.4). The periodicity of the soliton lines along the  $[\bar{1}10]$  close-packed directions is  $\sim 7.5\text{ nm}$  in Fig. 9.4, much larger than 6.3 nm observed on the clean Au(111) surface. A statistical analysis of the lifting of the herringbone reconstruction by the self-assembly of methylthiolate on Au(111) was presented in Chapter 8. Following the same procedure here, the extra coverage of Au-atoms embedded in the residual herringbone reconstruction is  $0.55\text{ Au atoms/nm}^2$ , significantly smaller than the  $0.70\text{ Au atoms/nm}^2$  coverage

on a clean Au(111) surface. At the same time, the surface coverage of the phenylthiolate dimers is  $0.16 \text{ units/nm}^2$  in Fig. 9.4. Adding these two numbers restores the value of  $0.71 \text{ atoms/nm}^2$ . These statistics imply that each dimer incorporates one Au-adatom, which was extracted from the reconstructed surface layer of Au(111) [47].

All the observations combined allow us to conclude that the PhS units in the dimers are bonded via Au-adatoms by analogy with self-assembled surface compounds  $\text{CH}_3\text{S}$  at low coverage [47]. Schematic structural models for the Au-adatom bonded PhS-Au-PhS dimers in the cis- and trans-conformations are shown in Fig. 9.3. We assumed that the structure of the sulphur-anchor bond is similar to the  $\text{CH}_3\text{S}$  case, with each S-atom making one bond to the Au-atom in the surface layer and the other bond to the Au-adatom [47].

The detailed mechanism of the S-S and S-H bond dissociation and Au-adatom incorporation into the self-assembled complexes of organosulfur molecules on Au(111) remains to be discovered. The most likely local sources of reactive Au-adatoms at low adsorbate coverage are the elbow sites of the herringbone reconstruction, containing coordinatively unsaturated lattice atoms [47]. An intriguing observation of the elbow-site was made at a very low coverage of PhSH, just at the onset of its thermal dissociation. As seen in Fig. 9.5, virtually no molecules are adsorbed on the defect-free terraces at this coverage. However, all the elbows of the herringbone reconstruction are populated by one or two PhSH molecules. The undissociated state of the PhSH molecules can be readily verified by dissociating the molecules with 2.7 V-3.0 V pulses from the STM-tip (Fig. 9.5), which produces PhS species (similar to Fig. 9.2). When two PhSH molecules are adsorbed on the elbow, they are aligned in a geometry that appears to be very similar to the image of the PhS-Au-SPh dimer in the trans-geometry (Fig. 9.3b). The main difference is a slightly larger separation of the peripheral lobes between two PhSH molecules at the elbow,  $\text{FWHM} = 1.74 \pm 0.04 \text{ \AA}$ . Similar molecule pairs adsorbed on the elbow site were also observed in the case of  $\text{CH}_3\text{SH}$  [166]. These observations suggest that the elbow site (and likely other defects and steps) may act as a template for the RSH dissociation where parent molecules are naturally oriented to achieve a lower activation barrier for S-H bond dissociation. We anticipate that pre-alignment of the RS-H molecules and the subsequent production of the RS-Au-SR species will shed light on the much debated fate of hydrogen atoms in the dissociation of the S-H bond [16, 272]. DFT calculations showed that on a defect-free surface the energy gain due to the dissociation of the S-H bond (forming an adsorbed H-atom) is

very small because of the strength of the S-H bond and weakness of H-bonding to the Au(111) surface [273]. The additional gain of the binding energy due to the Au-adatoms and the possibility of forming an H<sub>2</sub> molecule in the dissociation of the pre-aligned RSH molecules may shift the energetic balance to strongly favor S-H bond dissociation.

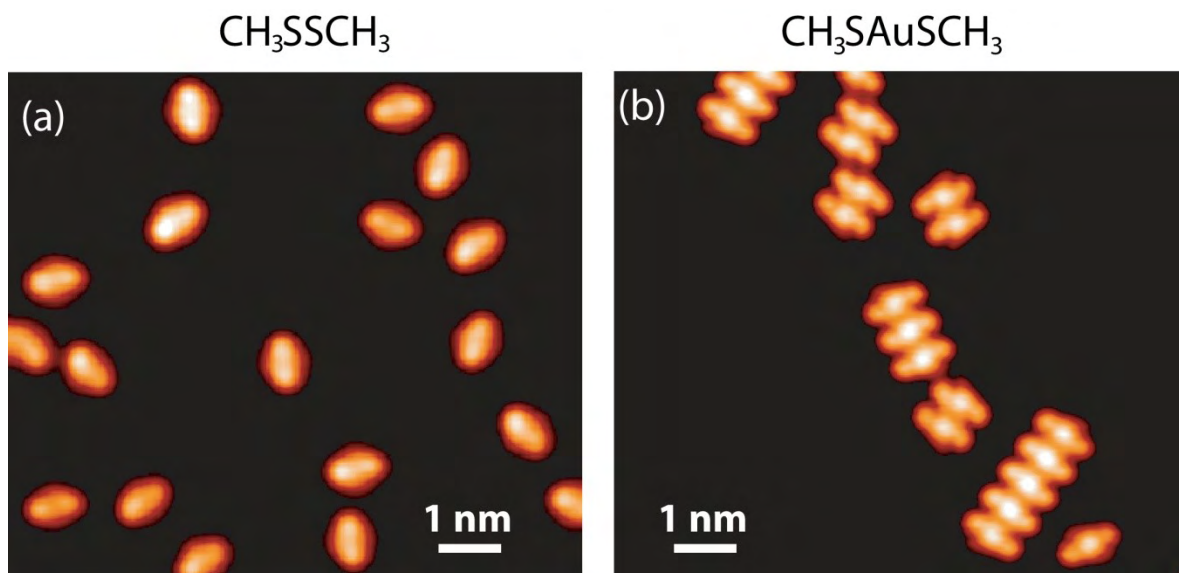


**Figure 9.6.** Intermolecular interactions modified by Au-adatoms. (a) A small coverage of  $\text{CH}_3\text{SSCH}_3$  molecules on Au(111) at  $T < 170$  K. The molecules are isolated indicating repulsive intermolecular interactions. (b) STM image obtained after heating the surface in (a) to 300K. The initial coverage of  $\text{CH}_3\text{SSCH}_3$  molecules is the same for (a) and (b). Most  $\text{CH}_3\text{S-Au-SCH}_3$  units aggregate into chains indicating attractive intermolecular interactions.

### 9.3 AU-ADATOMS MODIFY INTERMOLECULAR INTERACTIONS

Strong modification of thiolate bonding to the Au(111) surface caused by Au-adatoms is likely to influence the self-assembly mechanism of both 2D- and 3D-self-assembled layers. This effect becomes apparent already at a low coverage of methylthiolate or propylthiolate on Au(111) surface.

Intermolecular interaction between  $\text{CH}_3\text{SSCH}_3$  molecules on the Au(111) surface is repulsive. Most of the molecules at a low and intermediate coverage (Fig. 9.6a) are isolated and their distribution on the surface is nearly random. Only at near-monolayer coverage the

molecules start to group into chain-structures. In stark contrast, the stripe-phase units (CH<sub>3</sub>S-Au-SCH<sub>3</sub>) can rarely be found isolated even at the lowest coverage, as seen in the STM image (Fig 9.6b) obtained after annealing the surface shown in Fig 9.6a at ~200K for several minutes. Therefore, Au-adatom bonding reverses the sign of intermolecular interaction between organosulfur species on the surface.

Attractive interaction between the units of the stripe-phase is also verified by DFT calculations. They were done in the unit-cell shown in Fig. 8.3(a,b), inserting the second CH<sub>3</sub>S-Au-SCH<sub>3</sub> unit next to the one already in the cell (considering the periodic boundary conditions, the calculated energies refer to the infinite chain of the stripe-phase). The interaction energy between two units can be calculated as:

$$E_{int} = -\frac{1}{2}(E_{2u} - E_{slab} - 2 * (E_u - E_{slab}))$$

where  $E_{nu}$  is the total energy of the gold-slab and  $n$  CH<sub>3</sub>S-Au-SCH<sub>3</sub> units and  $E_{slab}$  is the total energy of the bare gold slab.  $E_{int}$  is ~2 kcal/mol for methylthiolate, which confirms attractive interaction between the units. The total attractive energy for the CH<sub>3</sub>S-Au-SCH<sub>3</sub> due to interactions with two neighbor-units in the middle of the chain is therefore ~4 kcal/mol. Notably, the van-der-Waals interaction between CH<sub>3</sub>-groups is unlikely to be accounted for in these DFT calculations. Therefore the calculated attractive contribution in methylthiolate is mainly due to the interaction of the S-Au-S headgroups.

## 9.4 CONCLUSIONS AND OUTLOOK

Chapters 8 and 9 present the chemistry and self-assembly of organosulfur compounds from a new perspective of organometallic surface chemistry involving Au-adatoms. Gold-adatoms dramatically change the stability of alkanethiolate species and intermolecular interactions in the 2D-self-assembled layers. The adatom-based model also quantitatively accounts for the lifting of the herringbone reconstruction that accompanies thiolate self-assembly. Conversely, lifting of the

reconstruction can be used as a signature (necessary but not sufficient) of adatom-chemistry on the surface.

Future work in alkanethiolate self-assembly on Au(111) surface will address the mechanism of S-S and S-H bond-breaking, which involves Au-adatoms. Naturally, Au-adatom-bonding in the 2D-SAMs, which are precursors to 3D-SAMs, calls upon significant revision of the structure of the 3D-SAMs and the mechanism of 2D- to 3D-conversion. Within months of our publication on adatom-bonding in self-assembled alkanethiolate species, two new reports stating the Au-adatom-bonding in the 3D-SAMs of methylthiolate were published [37, 53], which further emphasizes the need to revisit many aspects of organosulfur self-assembly on Au(111).

Among other questions of interest is the effect of the Au-adatoms on the electronic properties of thiolate SAMs [268, 274]. Modification of the anchor-group is particularly important for SAMs made of  $\pi$ -conjugated thiols, where the relatively high electronic transparency of the hydrocarbon chain results in a substantial drop of the applied potential at the anchor group [268]. So far this aspect has not been the focus of theoretical work, and the structural models used for calculations were mostly hypothetical. Alignment of electronic levels, charging effects and the conductivity of the S-adatom bond need to be investigated. Yet another adatom perspective is the substitution of the Au-adatoms in SAMs with Ag or Pt adatoms, e.g. by coadsorbing the foreign adatoms with undissociated thiol or dithiol molecules on the gold surface and growing SAMs at lower temperatures. Although such substitution will complicate the SAM growth procedure, it may produce alkanethiolate SAMs with novel or superior properties.

The Au-adatom concept should also be explored in light of the recent interest in alkanethiolate-capped Au-nanoparticles. Passivation of Au-nanoparticles with thiolate SAMs allows some degree of size-selectivity during nanoparticle growth [275]. Significant charge-transfer from the nanoparticle onto the SAM layer was reported [276, 277]. The energy of the surface plasmon resonance [278] of the capped Au-nanoparticle can also be varied by the choice of the alkanethiolate, which is particularly relevant to application of nanoparticles in advanced photonic materials. Since crystalline nanoparticles exhibit a large amount of steps, adatom-bonded scenario is very likely in this case.

Finally, our finding of the herringbone reconstruction of Au(111) being the low-temperature source of adatoms may also be relevant to the surface chemistry on other surfaces and alloys that exhibit the herringbone reconstruction, such as Ag and Cu monolayers on Ru(0001) [99], and other surface reconstructions, such as Au(100) and Pt(100).

**PART IV. ELECTRON-INDUCED SURFACE CHEMISTRY OF  
CH<sub>3</sub>SSCH<sub>3</sub> MOLECULE**

## 10.0 PROPAGATION OF CONFORMATION IN SURFACE-ALIGNED DISSOCIATION OF CH<sub>3</sub>SSCH<sub>3</sub> ON AU(111)\*

### 10.1 INTRODUCTION

Studies of single-molecule reactions on surfaces using scanning tunneling microscopy (STM) provide unprecedented insight into the structure of reactants and products, as well as the reaction pathways [91, 279, 280]. Several previous STM studies detailed the trajectories of atomic fragments produced by electron dissociation of adsorbed molecules [11, 281, 282]. In particular, it was found that if the dissociating bond is aligned with the adsorption sites of the products, the latter are quickly trapped and the bond-geometry of the reactant molecule can be “imprinted” on the surface [281]. However, since the majority of the studied reactions involved the ejection of atomic species, no information about the conformation of the products was accessible.

We have studied the dissociation of the CH<sub>3</sub>SSCH<sub>3</sub> molecule adsorbed on the Au(111) surface using STM. CH<sub>3</sub>SSCH<sub>3</sub> is dissociated by the tunneling current to produce two CH<sub>3</sub>S species [67]. Since CH<sub>3</sub>S is a polyatomic species, it is possible to track the conformational changes involved in the reaction. We find that the ubiquitous geometrical *trans*-conformation of the CH<sub>3</sub> groups in the parent CH<sub>3</sub>SSCH<sub>3</sub> molecule is retained with a high probability as the CH<sub>3</sub>S species are ejected away from each other.

---

\*Reproduced in part with permission from: P. Maksymovych, J. T. Yates, Jr., *Journal of the American Chemical Society*, 128 (2006) 10642. Copyright 2006 American Chemical Society.

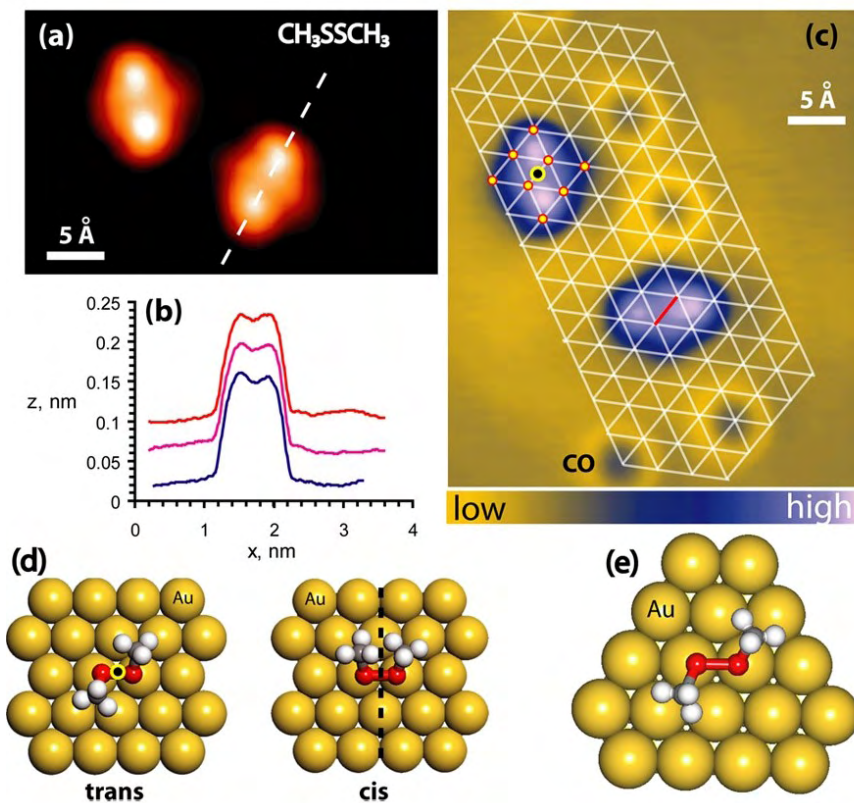


**Figure 10.1.** Conformation of  $\text{CH}_3\text{SSCH}_3$  adsorbed on Au(111) surface. a) STM image of two  $\text{CH}_3\text{SSCH}_3$  molecules on Au(111). Both molecules are trans-conformers (see text); b) Line-profiles of several  $\text{CH}_3\text{SSCH}_3$  molecules taken along the white dashed line in (a); c) Triangulation of  $\text{CH}_3\text{SSCH}_3$  molecules using CO molecules on atop Au sites. The black dot in the upper molecule marks the position of the inversion center; d) Comparison of cis- and trans-symmetry for  $\text{CH}_3\text{SSCH}_3$ . In c) and e) the red line marks the direction of the S-S bond.

## 10.2 RESULTS AND DISCUSSION

Single  $\text{CH}_3\text{SSCH}_3$  molecules (Fig. 10.1a) are imaged as ellipses with two lobes of the same apparent height (see line scans in Fig. 10.1b). The bright lobes originate from the  $\text{CH}_3$ -groups judging by their peripheral position in the STM image [67]. In order to assign *cis*- or *trans*-conformation of the adsorbed  $\text{CH}_3\text{SSCH}_3$  molecule (Fig. 10.1), the position of Au atoms in the surface lattice was determined using isolated CO molecules as markers. The symmetry of the  $\text{CH}_3\text{SSCH}_3$  molecule *combined* with that of the underlying surface lattice (red circles Fig. 10.1c) is described by an inversion center located in the geometrical center of the  $\text{CH}_3\text{SSCH}_3$  image

(black dot in Fig. 10.1c). Such a centrally-symmetric arrangement (molecule+lattice) can be produced only by the *trans*-CH<sub>3</sub>SSCH<sub>3</sub>, because the *cis*-isomer would not have such an inversion center but would have a symmetry plane as shown in Fig. 10.1d. A schematic model of the *trans*-CH<sub>3</sub>SSCH<sub>3</sub> molecule derived from the STM measurements is shown in Fig. 10.1e: the S-S bond is aligned with the close-packed direction on the Au(111) surface, and is located above the Au-Au bridge-site. A similar structure was also proposed theoretically [176].

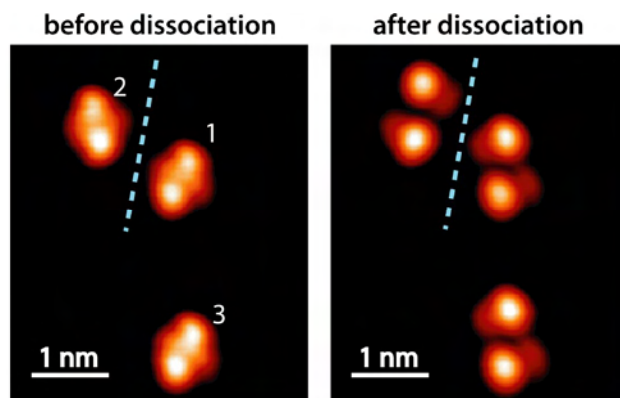


**Figure 10.2.** Electron-induced dissociation of CH<sub>3</sub>SSCH<sub>3</sub> molecules on the Au(111) surface as seen by STM. The products retain the conformation and orientation of the parent molecules: CH<sub>3</sub>SSCH<sub>3</sub> molecules 1 and 3 are identical producing identical CH<sub>3</sub>S *trans*-pairs. Molecules 1 and 2 are offset mirror images of each other, and so are the product *trans*-pairs of CH<sub>3</sub>S-species (dashed blue line is the mirror plane).

Dissociation of a single CH<sub>3</sub>SSCH<sub>3</sub> molecule can be accomplished by applying a low-current pulse with the surface positively biased at a voltage of ~1.4V. The dissociation likely occurs via electronic excitation of the molecule due to the relatively high threshold energy. Surprisingly, the *trans*-conformation of the parent CH<sub>3</sub>SSCH<sub>3</sub> molecule is often reflected in the relative position and alignment of two product CH<sub>3</sub>S species, which are grouped into *trans*-pairs as seen in Fig. 10.2. The orientation of the CH<sub>3</sub>SSCH<sub>3</sub> molecule on the surface (the direction of its S-S bond) is also retained in dissociation, because the *trans*-pairs are related to each other by the same symmetry operations as their parent CH<sub>3</sub>SSCH<sub>3</sub> molecules (Fig. 10.2).

In the detailed study of CH<sub>3</sub>S on the Au(111) surface (Chapter 5), it was established that the CH<sub>3</sub>S species adsorbs with the S-headgroup on the bridge Au-Au site (with a slight shift toward the hollow site) as shown in Fig. 10.3a. Comparison of Fig. 10.3a and 10.3c allows one to determine the adsorption configuration of the *trans*-pair: the CH<sub>3</sub>S species are separated along

the parent direction of the S-S bond by two lattice spacings ( $5.5 \text{ \AA}$ ), and the S-C bond orientation in the  $\text{CH}_3\text{S}$  species match closely those of the parent  $\text{CH}_3\text{SSCH}_3$  molecule. Thus,  $\text{CH}_3\text{SSCH}_3$  dissociation is simultaneously bond-aligned, because the products are ejected along the S-S bond direction, and surface-aligned, because the products are trapped on the surface sites aligned with the breaking bond. This reaction is similar to the *localized atomic reaction* of chlorinated benzene molecules on the Si(111) surface [283].

The probability of the conformation retention in the dissociation of the  $\text{CH}_3\text{SSCH}_3$  molecule was estimated in two separate experiments, involving local and non-local excitation of the adsorbed molecules (non-local excitation is detailed in Chapter 12). The pulsing conditions in the local excitation were adjusted ( $U = +1.4\text{V}$ ,  $I = 20 \text{ pA}$ , pulse duration = 100 ms) to minimize the excitation tunneling current (and therefore decrease the magnitude of the electric field and tip-molecule interaction).

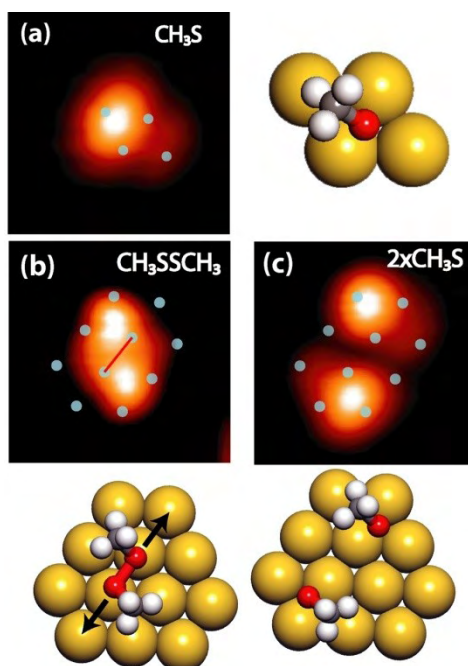


**Figure 10.3.** Propagation of conformation in  $\text{CH}_3\text{SSCH}_3$  dissociation. a) STM image and structural model of isolated  $\text{CH}_3\text{S}$ -species adsorbed on the Au-Au bridge site [67]. Blue dots mark Au atoms in the lattice; b) Undissociated  $\text{CH}_3\text{SSCH}_3$  molecule (red line is the direction of the S-S bond); c) The *trans*-pair of  $\text{CH}_3\text{S}$ -species produced by electron-induced dissociation of (b). The models show the schematic of the surface-aligned dissociation of  $\text{CH}_3\text{SSCH}_3$ .

Out of 485 dissociation events, 358 produced the *trans*-pairs of CH<sub>3</sub>S species with the same conformation as the parent CH<sub>3</sub>SSCH<sub>3</sub> molecules. The probability of such a scenario is therefore 74±4%. This conformational retention is dramatic when considering the large number of possible alternate dissociation scenarios involving in-plane and out-of-plane rotation of the S-C bonds, which will destroy the conformational history of the parent CH<sub>3</sub>SSCH<sub>3</sub> molecule.

The major such alternate scenario (25% of all the events) involved hopping of the CH<sub>3</sub>S-species between several neighbor bridge-sites after the S-S bond is broken. Each multisite hop is followed by a 60° in-plane rotation of the S-C bond. The fairly low probability of this pathway arises from strong binding of the CH<sub>3</sub>S species on the Au(111) surface [65], which quickly get trapped by the surface after dissociation.

Out-of-plane rotation of CH<sub>3</sub> groups around the S-S bond can occur in the transition state of the dissociating CH<sub>3</sub>SSCH<sub>3</sub> molecule. A very small number of dissociation events (<2%) followed this pathway with the out-of-plane rotation of one of the two CH<sub>3</sub> groups. The CH<sub>3</sub>S-pair in this case is imaged in a *cis*-configuration. No events involving rotation of both CH<sub>3</sub> groups out-of-plane were observed. The lack of out-of-plane rotation of CH<sub>3</sub> groups is somewhat unexpected, because bond dissociation is accompanied by substantial vibrational and rotational heating of the product species. A possible explanation is that the surface-alignment of the dissociation process allows the formation of the bridge-bonded CH<sub>3</sub>S-species to be synchronized with the elongation of the S-S bond. The rotation of the CH<sub>3</sub>-group in the transition state will then likely be hindered because of high coordination of the S-headgroup to surface Au atoms along the reaction pathway.

Surface-aligned dissociation of a single CH<sub>3</sub>SSCH<sub>3</sub> molecule transforms into a chain-reaction when the molecules self-assembled into linear chains on Au(111) and Au(100) surfaces. This is presented in the next chapter.

## 11.0 CHAIN REACTION IN A MOLECULAR SELF-ASSEMBLY ON A METAL SURFACE

Self-assembly of  $\text{CH}_3\text{SSCH}_3$  molecules into linear chains on gold surfaces facilitates a new chemical chain reaction which produces  $\text{CH}_3\text{SSCH}_3$  molecules that are mirror images of the reagent molecules. The chain reaction is triggered by electron-induced dissociation of a terminal  $\text{CH}_3\text{SSCH}_3$  molecule and proceeds through as many as 9 molecules along the chain. The mechanism of the reaction involves a radical-like  $\text{CH}_3\text{S}$ -intermediate that reacts with the adjacent  $\text{CH}_3\text{SSCH}_3$  molecule by virtue of the self-assembled molecular alignment. The reaction can be viewed as a surface analog of a free-radical chain reaction in gas-phase involving a substantially reduced potential barrier to S-S bond-breaking.

### 11.1 INTRODUCTION

Self-assembled molecular complexes are building blocks in diverse life forms [20, 284]. This fact inspires the use of self-assembly for the bottom-up construction of functional devices [18, 285, 286]. A most exciting promise of self-assembly is to produce novel functions that are not inherent in the building blocks themselves [17, 287]. Numerous self-assembled molecular complexes and self-assembly mechanisms have been studied on metal and semiconductor surfaces using local probes [235, 288-291], but examples of functional self-assembly are very few. Among them are a one-dimensional polymerization chain reaction [292], the controlled switching of molecular conductance [293] and molecular-electronic gating [294].

We have found that self-assembled chains of 2 to 15  $\text{CH}_3\text{SSCH}_3$  molecules on Au(111) and Au(100) surfaces possess a unique chemical function. If a terminal  $\text{CH}_3\text{SSCH}_3$  molecule is dissociated by tunneling electrons in the scanning tunneling microscope (STM), the whole chain

is observed to react, synthesizing  $\text{CH}_3\text{SSCH}_3$  molecules of in the middle of the chain and leaving dissociated fragments at both termini. STM measurements and theoretical calculations support the reaction mechanism in which  $\text{CH}_3\text{SSCH}_3$  dissociation produces a reactive  $\text{CH}_3\text{S}$ -fragment (hereafter  $\text{CH}_3\text{S}$ -radical), which engages in a substitution reaction with the next  $\text{CH}_3\text{SSCH}_3$  molecule along the chain breaking its S-S bond. The potential barrier to the S-S bond-breaking is substantially lower in this case compared to the dissociation of an isolated  $\text{CH}_3\text{SSCH}_3$  molecule. The surface-bound  $\text{CH}_3\text{S}$ -radical can therefore be viewed as a surface analogue of the gas-phase thyl free-radical [295]. Thyl radicals play an important role in several biological processes [296]. They are also known to react with molecules containing a dithiol bond (S-S) in a variety of radical-substitution reactions [297].

The molecularly-resolved real-space observation of a radical chain reaction represents a dream in the field of chemical reaction kinetics, extending back to the 1920s, when radical chain reactions were first postulated in the gas phase. Using single crystal metal surfaces as templates to control molecular orientation, our study demonstrates that the steric factor in chemical kinetics (as well as possibly electronic factors) can be controlled by self assembly. Such effects were previously observed in bimolecular surface reactions in surface-aligned photochemistry, but not for molecular assemblies [96, 298-300].

## 11.2 RESULTS

Dimethyldisulphide (DMDS) molecules ( $\text{CH}_3\text{SSCH}_3$ ) adsorb at low coverages on the Au(111) surface with a small binding energy of  $\sim 10$  kcal/mol in a structural geometry shown in Fig. 11.1a [301].  $\text{CH}_3$ -groups are located on both sides of the S-S bond, i.e. the adsorbed molecule assumes a *trans*-conformation. Tunneling electrons from the STM-tip (at  $\sim 1.4$ V and above) dissociate a single  $\text{CH}_3\text{SSCH}_3$  molecule, breaking the S-S bond and producing two  $\text{CH}_3\text{S}$ -fragments (Fig. 11.1(a)). The dissociation coordinate is aligned with the S-S bond direction as seen from  $\sim 75\%$  probability of retention of the *trans*-conformation of the parent  $\text{CH}_3\text{SSCH}_3$  molecule in the surface arrangement of the product  $\text{CH}_3\text{S}$ -fragments [301].

At a higher adsorbate coverage, DMDS molecules are observed to self-assemble on Au(111) into epitaxial chains of up to five units at temperatures below 200K. The chains are

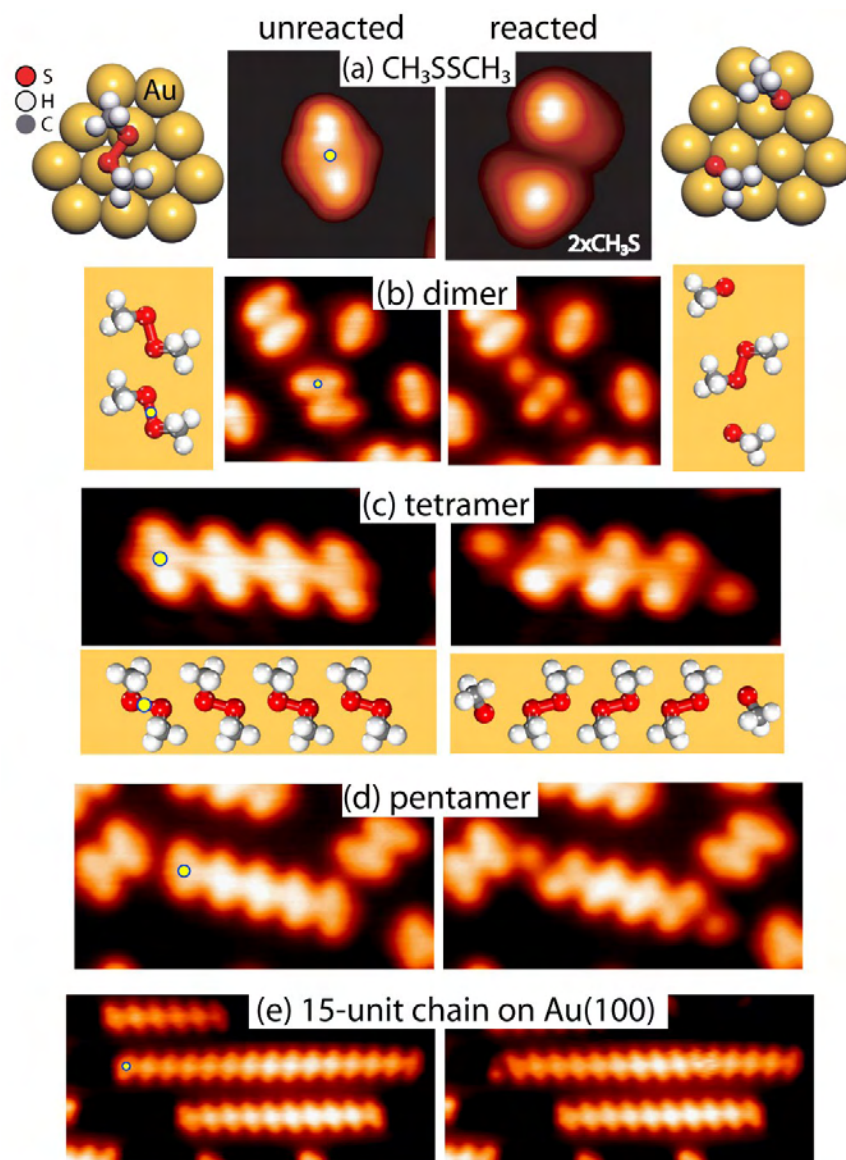


**Figure 11.1.** STM images before and after electron-induced dissociation of a single  $\text{CH}_3\text{SSCH}_3$  molecule and its self-assembled chains on the Au(111) surface. Select structures are shown schematically in ball models (position of  $\text{CH}_3\text{S}$ -fragments in models of chain reactions is one of two equivalent positions). (a) Conformation-retaining dissociation of  $\text{CH}_3\text{SSCH}_3$  [301] producing two  $\text{CH}_3\text{S}$ -fragments by a pulse of tunneling current at 1.4V. (b)-(d) Chain reaction of self-assembled chains of  $\text{CH}_3\text{SSCH}_3$  molecules induced by electron-induced dissociation of the terminal molecule (pulse voltage 0.9V). Voltage pulses were applied at a position marked by yellow circle. (e) Chain reaction of 15  $\text{CH}_3\text{SSCH}_3$  molecules self-assembled on Au(100) surface: the reaction produces 9 flipped molecules.

composed of  $\text{CH}_3\text{SSCH}_3$  molecules of the same orientation stacked along the  $[11\bar{2}]$  crystallographic direction with a periodicity of 0.5 nm. Pulsing a terminal  $\text{CH}_3\text{SSCH}_3$  molecule

by tunneling electrons at 0.8 V causes a surprising reaction *that affects all the molecules in the chain rather than the excited molecule alone*. This is shown in Fig. 11.1b, c and d for the CH<sub>3</sub>SSCH<sub>3</sub> dimer, tetramer and pentamer clusters on Au(111). We have verified that the chain reaction is electron-induced and is not caused by the electric field between the STM-tip and the gold surface using the recently reported technique of non-local electron-induced excitation of adsorbed molecules [302].

The scenario of the CH<sub>3</sub>SSCH<sub>3</sub> chain reaction is unraveled by comparing the STM-topography of DMDS molecules and CH<sub>3</sub>S-fragments produced by the reaction in Fig. 11.2a-e. Both ends of the reacted chains are decorated by *one* CH<sub>3</sub>S-fragment (Fig. 11.2a,b). The images of the interior reaction products closely resemble unreacted CH<sub>3</sub>SSCH<sub>3</sub> molecules (Fig. 11.2a,c) forming a chain that is one molecule shorter than the initial chain. However, the *trans*-conformation of each interior CH<sub>3</sub>SSCH<sub>3</sub> molecule is a mirror image of the reactant molecules with the mirror plane normal to the chain direction (Fig. 11.2d,e). The reaction of the *n*-member chain therefore yields one dissociated CH<sub>3</sub>SSCH<sub>3</sub> molecule and (*n*-1) mirror images of the reactant CH<sub>3</sub>SSCH<sub>3</sub> molecules.

The chain reaction proceeds identically for the self-assembled chains of 2 to 5 molecules on Au(111). The chains with > 5 molecules are very rare on Au(111) because there are six equivalent orientations of the isolated molecule on Au(111), while all the CH<sub>3</sub>SSCH<sub>3</sub> molecules in the chain have to have the same orientation. However, on the Au(100) surface with a pseudo-hexagonal (5x20) reconstruction of the surface layer [12], CH<sub>3</sub>SSCH<sub>3</sub> molecules self-assemble into chains of 9-17 units. Fig. 11.1e shows an exceptional case of a 15-unit chain, where the chain reaction propagates through 10 interior molecules leaving two CH<sub>3</sub>S fragments and 9 isomerized CH<sub>3</sub>SSCH<sub>3</sub> molecules.

It is noteworthy that direct excitation of a CH<sub>3</sub>SSCH<sub>3</sub> molecule using STM cannot transform it into its mirror image on the surface. To flip the molecule, both CH<sub>3</sub>-groups have to be rotated about the S-S bond, which is associated with a substantial barrier. Apparently, inelastic scattering of tunneling electrons does not excite this complex motion directly or indirectly (via anharmonic coupling [303]). In fact, the only reactions induced by STM is the lateral diffusion of the whole CH<sub>3</sub>SSCH<sub>3</sub> molecule on the surface at a tunneling voltage from 0.5 V to 0.8 V, and the dissociation of the S-S bond at higher voltages. *Isomerization of CH<sub>3</sub>SSCH<sub>3</sub> molecules in the chains is made possible solely by their self-assembly.*

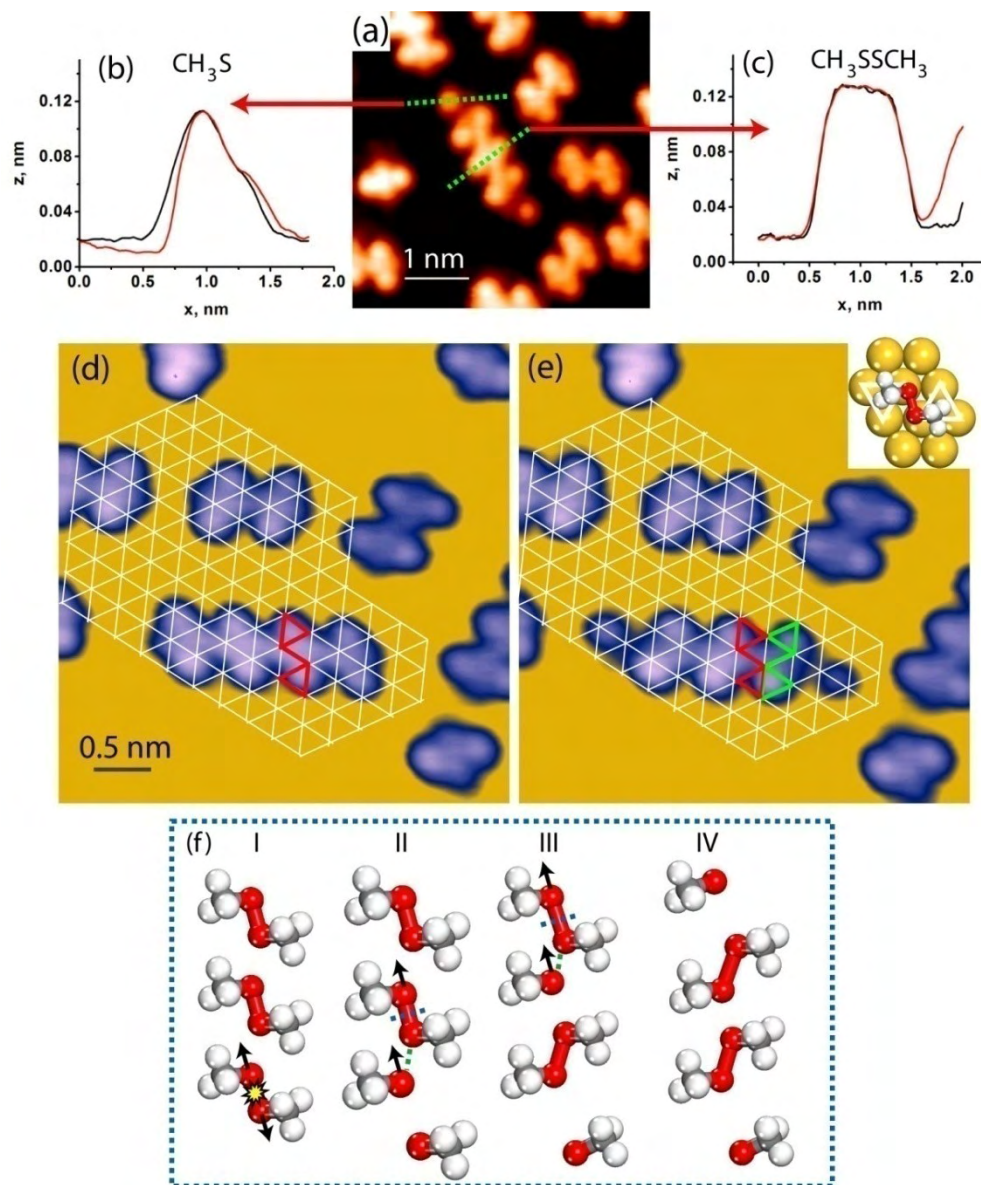


**Figure 11.2.** Chain reaction scenario. (a) STM image of the reacted  $\text{CH}_3\text{SSCH}_3$  tetramer. (b) Line-profiles of isolated  $\text{CH}_3\text{S}$  (black) compared to  $\text{CH}_3\text{S}$  at the end of the reacted chain (red); (c) Line-profiles of isolated  $\text{CH}_3\text{SSCH}_3$  (black) compared to  $\text{CH}_3\text{SSCH}_3$  in the middle of the reacted chain (red); the line-profiles were taken along the corresponding green dashed-lines in (a). (d-e) Triangulation of  $\text{CH}_3\text{SSCH}_3$  tetramer (surface lattice derived from crystallographic directions and known separations between adsorbed molecules). Chirality of  $\text{CH}_3\text{SSCH}_3$  molecules is shown by the red outline connecting lattice atoms (see insert in (e)). Red outline is  $\text{CH}_3\text{SSCH}_3$  molecule before reaction, green - after reaction. (f) Proposed chain reaction mechanism: (I) terminal  $\text{CH}_3\text{SSCH}_3$  is dissociated by tunneling electrons forming kinetically excited  $\text{CH}_3\text{S}$ -fragments. (II) Hot  $\text{CH}_3\text{S}$  fragment reacts with the adjacent  $\text{CH}_3\text{SSCH}_3$  molecule. Green dashed line is S-S bond that is forming, blue dashed line – the S-S bond that is breaking. (III) The decomposition/recombination cycle is repeated until the last  $\text{CH}_3\text{SSCH}_3$  molecule in the chain produces a terminal  $\text{CH}_3\text{S}$ -fragment (IV).

Figure 2f shows a possible mechanism of the chain reaction involving stepwise dissociation/ recombination of  $\text{CH}_3\text{SSCH}_3$  molecules mediated by a hot  $\text{CH}_3\text{S}$ -radical. Excitation of the terminal  $\text{CH}_3\text{SSCH}_3$  molecule creates a kinetically excited  $\text{CH}_3\text{S}$ -radical that propagates along the S-S bond direction. Due to molecular alignment in the chain, the hot  $\text{CH}_3\text{S}$  radical impinges onto the next  $\text{CH}_3\text{SSCH}_3$  molecule in the chain inducing a radical substitution reaction, which produces a flipped  $\text{CH}_3\text{SSCH}_3$  molecule and another  $\text{CH}_3\text{S}$  radical. The latter gains sufficient kinetic energy from the first  $\text{CH}_3\text{S}$  radical (e.g. via collisional energy transfer[304]) to induce the substitution reaction with the next  $\text{CH}_3\text{SSCH}_3$  molecule in the chain, and so forth.

This mechanism accounts for the synthesis of the interior  $\text{CH}_3\text{SSCH}_3$  molecules as well as formation of only *two*  $\text{CH}_3\text{S}$  fragments that are located on the *opposite* termini of the reacted chain. The only other possibility to flip interior  $\text{CH}_3\text{SSCH}_3$  molecules would be to rotate their  $\text{CH}_3$ -groups about the S-S bond. However, the position of the  $\text{CH}_3\text{SSCH}_3$  molecule would not change substantially in that case, which contradicts our observations, where the new S-S bonds are offset from the original ones (Figs. 2d,e)

To investigate the potential barrier for the  $\text{CH}_3\text{S}$  interaction with the  $\text{CH}_3\text{SSCH}_3$  molecule, we have used plane-wave density functional theory (DFT) calculations [170, 305] and periodic slab models. The potential barriers and the transition-state structures for the chain reaction of the  $\text{CH}_3\text{SSCH}_3$  dimer were calculated using the climbing-image nudged elastic band method (CI-NEB) [306]. The calculations were performed for the fundamental ground state of the system. All the atoms were allowed to relax except the Au-atoms in the two bottom layers of the slab that were kept frozen at their bulk optimized positions. Despite the fact that in reality the chain reaction is triggered by the electronic excitation of the molecules, fast de-excitation is expected to take place [307] with subsequent evolution of the chain reaction in the ground electronic state. As a result DFT calculations can capture several chemical motifs which form the basis for the observed chain reaction [308].

The structures of the  $\text{CH}_3\text{SSCH}_3$  dimer before and after the reaction (Fig. 11.3) were inferred from their STM images and by optimized DFT calculations. The insert in Fig. 11.3 shows the variation of the S-S bond length for the upper dissociating (S3-S4), lower dissociating (S1-S2) and the newly forming (S2-S3)  $\text{CH}_3\text{SSCH}_3$  molecules. Each product  $\text{CH}_3\text{S}$ -species is adsorbed on the Au-Au bridge site (Fig.3, NEB image #12), which is the most stable  $\text{CH}_3\text{S}$  configuration on the Au(111) surface [65, 67]. A reference potential energy trace corresponding

to the dissociation of an isolated  $\text{CH}_3\text{SSCH}_3$  molecule on Au(111) was also calculated (Fig. 11.4).

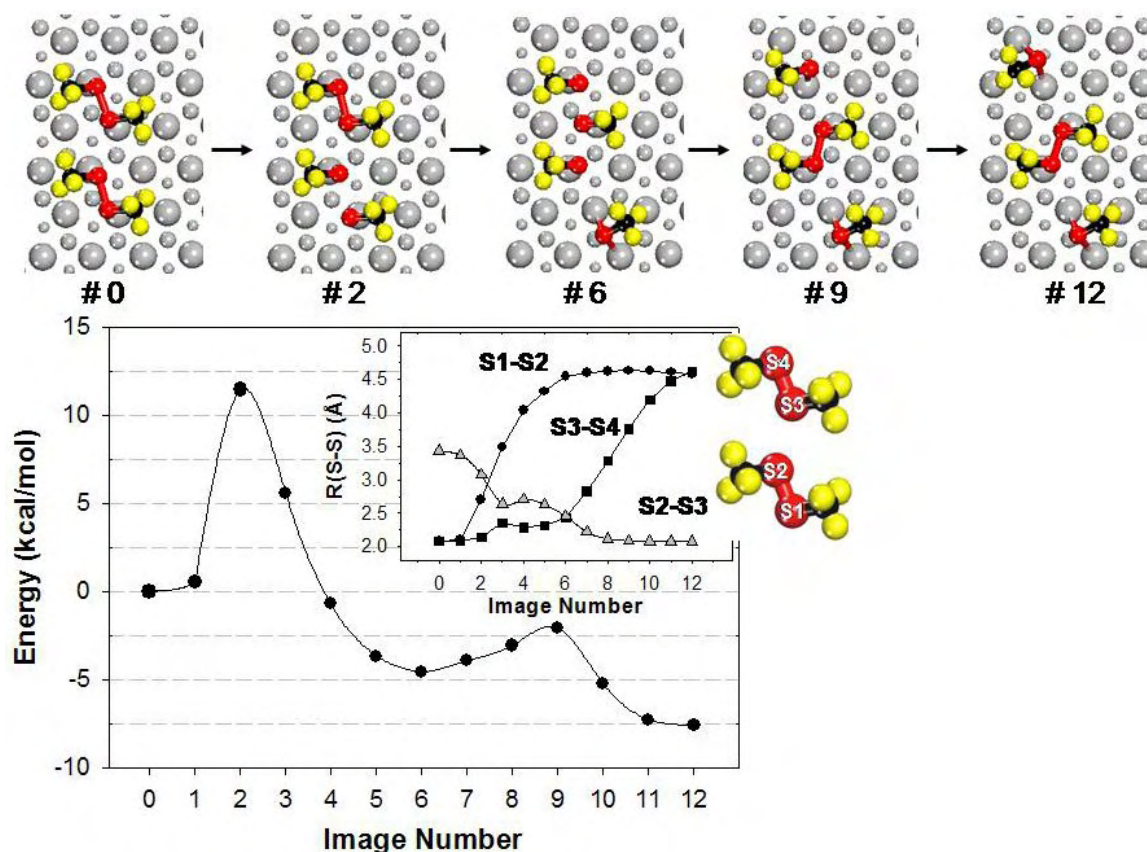


**Figure 11.3.** Potential energy profile for dissociation of the  $\text{CH}_3\text{SSCH}_3$  dimer calculated using DFT CI-NEB method. The insert figure represents the variation of the S-S bond-lengths corresponding to the dissociating molecules (S1-S2, S3-S4) and the newly forming  $\text{CH}_3\text{SSCH}_3$  molecule (S2-S3). The ball models are initial, final and select intermediate optimized configurations along the reaction coordinate. The size of the surface Au atoms (shown in gray) corresponds to their vertical position in the slab, larger atoms being closer to the surface.

The reaction energies calculated for the monomer and dimer reactions are seen to be nearly equal (0.32 eV, Fig. 11.3), because the ultimate result in each case is the dissociation of one  $\text{CH}_3\text{SSCH}_3$  molecule producing two  $\text{CH}_3\text{S}$ -fragments adsorbed on Au-Au bridge-sites. The potential energy surface (PES) for the dimer dissociation has two highly asymmetric barriers of 0.49 eV and 0.11 eV. From the analysis of  $\text{CH}_3\text{S}$ -displacements along the reaction coordinate, the higher barrier in dimer dissociation originates only from the elongation of the S-S bond of the first  $\text{CH}_3\text{SSCH}_3$  molecule (image #2 in Fig. 11.3). The transition-state of on top of this barrier is

very similar to that of the single dissociating  $\text{CH}_3\text{SSCH}_3$  molecule (image # 2 in Fig. 11.4). Its height (0.49 eV) is only slightly smaller than the barrier for the isolated molecule (0.57 eV) due to the influence of the second molecule in the dimer. The second barrier on the dimer PES (image #9 in Fig. 11.3) arises mainly from the motion of the outermost  $\text{CH}_3\text{S}$ -fragment across an energetically unfavorable atop site.

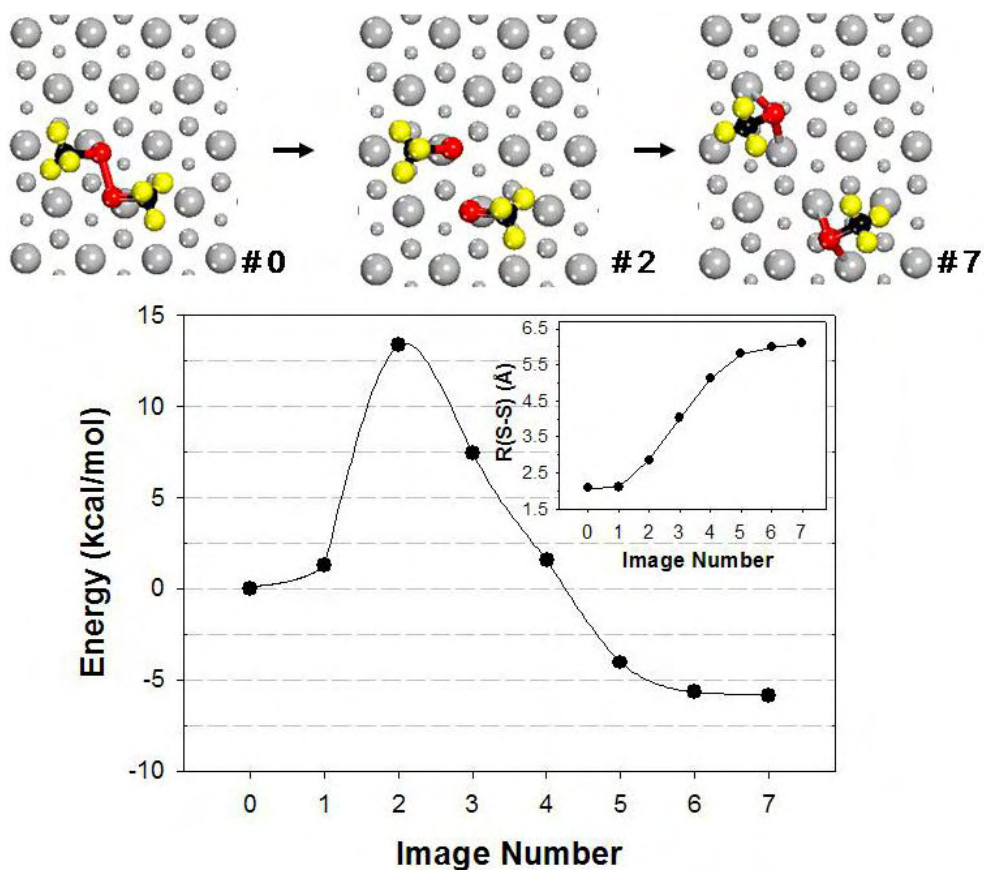


**Figure 11.4.** Potential energy profile for dissociation of the  $\text{CH}_3\text{SSCH}_3$  monomer calculated using DFT CI-NEB method. The insert figure represents the variation of the S-S bond-length. Coloring scheme is the same as in Fig. 11.3.

A surprising feature of the dimer PES is that the potential barrier to the breaking of the *second* S-S bond (between image 4 and image 9) in the “radical-substitution” reaction is very small, and perhaps even negative. The NEB barrier was also calculated specifically for a  $\text{CH}_3\text{S}$ -fragment attacking a  $\text{CH}_3\text{SSCH}_3$  molecule as shown in Fig. 11.5. The potential energy is found to decrease from image #3 to #0 in Fig. 11.5, which corresponds to the partial dissociation of the

S-S bond by the approaching  $\text{CH}_3\text{S}$ -fragment and the formation of the surface complex of three  $\text{CH}_3\text{S}$ -species. This behavior is reminiscent of the formation of the radical-molecule complex in gas-phase reactions [309]. Overall, the energy barrier to the dissociation of the strong S-S bond is lowered by at least a factor of 5 in the  $\text{CH}_3\text{S}$ -mediated chain mechanism (Fig. 11.3). This is caused by the proper alignment of molecules in the self-assembled structure.

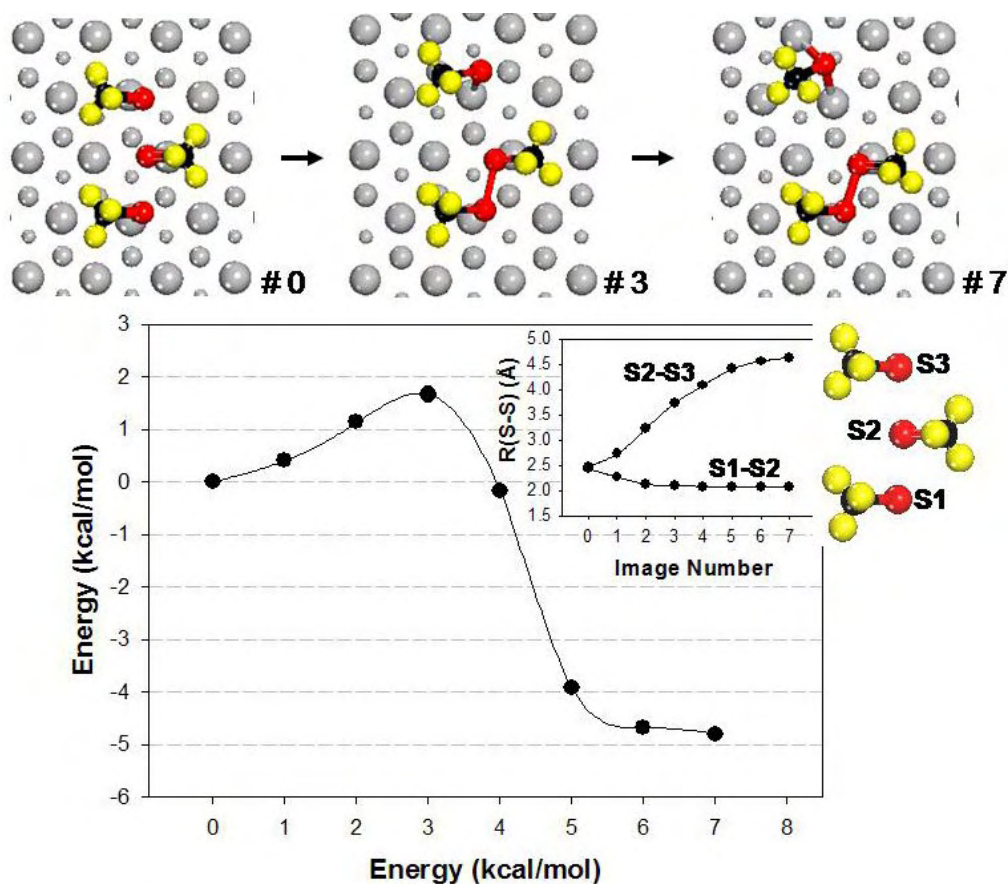


**Figure 11.5.** Potential energy profile for the interaction of the  $\text{CH}_3\text{S}$ -fragment with the  $\text{CH}_3\text{SSCH}_3$  molecule.

The chain reaction relies on the production of  $\text{CH}_3\text{S}$  radicals with a large momentum along the reaction coordinate. A number of mechanisms may be responsible for the dissociation of the terminal  $\text{CH}_3\text{SSCH}_3$  molecule which initiates the chain reaction [78]. The energy threshold of the dissociation is relatively high,  $\sim 0.7$  V at the tunneling current in our experiments. By measuring the dissociation rate of the terminal molecule as a function of tunneling current [11], it was determined that two-electrons at 0.7 V are required to cause the dissociation. Therefore the maximum total energy deposited into the molecule is 1.4 V. Such a high excitation energy

implies that  $\text{CH}_3\text{SSCH}_3$  dissociation proceeds via electronically excited states of the molecule (dissociative electron attachment) rather than by means of vibrational heating of the  $\text{CH}_3\text{SSCH}_3$  molecule in the ground state. Independent experimental evidence supporting this argument comes from the observation that chain reactions can also be triggered by the non-local excitation from the STM-tip [302], which selectively probes the dissociative electron attachment (DEA) reaction. Non-local excitation is caused by a hot-electron that is injected from the STM tip into the metal surface at a large (tens of nanometers) distance from the chain and that propagates parallel to the surface. The energy threshold for the non-local chain dissociation is  $\sim 1.2$  V, which is similar to the total energy of two-electrons required for local dissociation of the terminal  $\text{CH}_3\text{SSCH}_3$  molecule. Within the commonly accepted Antoniewicz model of DEA [76, 310], fast de-excitation of the anionic state will produce a highly vibrationally excited  $\text{CH}_3\text{SSCH}_3$  molecule in the ground electronic state. Subsequent dissociation of the  $\text{CH}_3\text{SSCH}_3$  molecule ejects a  $\text{CH}_3\text{S}$ -radical with a high enough kinetic energy to drive the chain reaction. In addition, the energy must be transferred between the incoming and outgoing  $\text{CH}_3\text{S}$  radicals in the radical substitution reaction. The underlying mechanism is probably collisional energy transfer, reminiscent of that in the “Newton’s cradle” [304]. A similar mechanism was proposed to explain the energy transfer across multilayer films of benzene on Pt(111) [311]. Naturally, energy dissipation to the metal substrate or to molecular vibrations via anharmonic coupling competes with the reaction propagation. For longer chains the reaction may terminate after several substitution reactions as seen for the 15-molecule chain in Fig. 11.1e (10 molecules reacted).

In summary, we have presented a prototype self-assembled reaction on a surface which proceeds via reactive intermediate species akin to free-radicals in the gas-phase. Every aspect of the rather unusual chain reaction of  $\text{CH}_3\text{SSCH}_3$  molecules derives from self-assembly, which aligns the S-S bonds so that the  $\text{CH}_3\text{S}$ -fragment ejected from one  $\text{CH}_3\text{SSCH}_3$  molecule can interact with the next molecule along the chain rather than being trapped on a strongly-binding surface site. The radical-like character of the reaction is manifested in the substantially lowered barriers to the dissociation of the  $\text{CH}_3\text{SSCH}_3$  molecules inside the chains. The reaction products along the chain are  $\text{CH}_3\text{SSCH}_3$  molecules which are mirror images of the reagent  $\text{CH}_3\text{SSCH}_3$  molecules. Such isomerization on the surface is unique to the self-assembled molecules.

## **12.0 NON-LOCAL HOT-ELECTRON SURFACE CHEMISTRY IN SCANNING TUNNELING MICROSCOPE\***

In this chapter a novel approach to surface chemistry studies using Scanning Tunneling Microscopy (STM) is presented. The dissociation of molecules adsorbed on metal surfaces is induced non-locally in a 10-100 nm radius around the STM-tip by hot electrons that originate from the STM-tip and transport on the surface. Non-local molecular excitation eliminates the influence of the STM-tip on the outcome of the electron-induced chemical reaction. The spatial attenuation of the non-local reaction is used as a direct measure of diffusive hot-electron transport on the surface.

### **12.1 INTRODUCTION**

In photochemistry on metal surfaces, most chemical reactions are induced by hot electrons, i.e. electrons photoexcited above the Fermi level of the metal [310, 312]. Scanning tunneling microscopy (STM) has proven to be a powerful method for direct analysis of electron-induced reactions on surfaces, because of its local electron injection and imaging capabilities [313]. Using STM one can analyze the products, kinetics, and intermediate states of a chemical reaction on the surface [11]. The majority of STM studies have focused on single-molecule chemistry,

---

\*Reproduced in part with permission from: P. Maksymovych, D. B. Dougherty, X.-Y. Zhu, J. T. Yates, Jr., Physical Review Letters in press, 2007. Copyright 2007 American Physical Society.

where the molecule located under the STM-tip is locally excited by tunneling electrons [91, 314-316] (see also *Introduction*). An unresolved issue in such studies is the effect of the electric field of the STM-tip and tip-molecule interactions on the local chemical reaction [78].

Here it is shown that electrons tunneling from the tip into a metal surface can also induce dissociation of molecules adsorbed far outside of the tunneling junction, at a lateral distance of up to *100 nm* from the STM-tip. This occurs because hot-electrons injected from the STM-tip can propagate parallel to the surface via surface resonances and then inelastically scatter at adsorbed molecules inducing chemical changes. Exciting molecules non-locally allows one to eliminate tip-artifacts since the tip and the adsorbed molecule are spatially separated. An additional merit of the non-local excitation phenomenon is the ability to monitor the hot-electron transport across the surface using the reaction yield as a measure of the hot-electron current.

Previously, non-local effects due to the tunneling current in STM were observed on silicon surfaces [317, 318], which have pronounced surface states and at least an order of magnitude longer lifetime of hot carriers compared to metal surfaces [319]. On metal surfaces, non-local dissociation of O<sub>2</sub> on Pt(111) in a small radius following a 1.0V pulse [320] was suggested to be due to injected hot electrons but this was not investigated thoroughly. The large-scale isomerization of azobenzene molecules on Au(111) was recently induced by local pulses at 1.2 to 5.0 V, but this was attributed to the effect of the *electric field* between the STM-tip and the sample surface [321]. Therefore, it is not established that non-local hot-electron chemistry can be carried out on a metal surface. In the current study, non-local dissociation of CH<sub>3</sub>SSCH<sub>3</sub> on Au(111) surfaces is found to have unprecedented lateral extent for both silicon and metal surfaces. Two independent quantitative experiments are carried out to confirm the hot-electron origin of this reaction. Finally, non-local reactions are demonstrated for several molecule/surface combinations and some of the perspective applications of the non-local excitation are exemplified.

## 12.2 EXPERIMENTAL

Au(111), Cu(111), Cu(110) and Au(100) surfaces were prepared using Ar sputtering/annealing cycles. Adsorbate molecules were dosed onto metal surfaces from an effusive beam doser at a

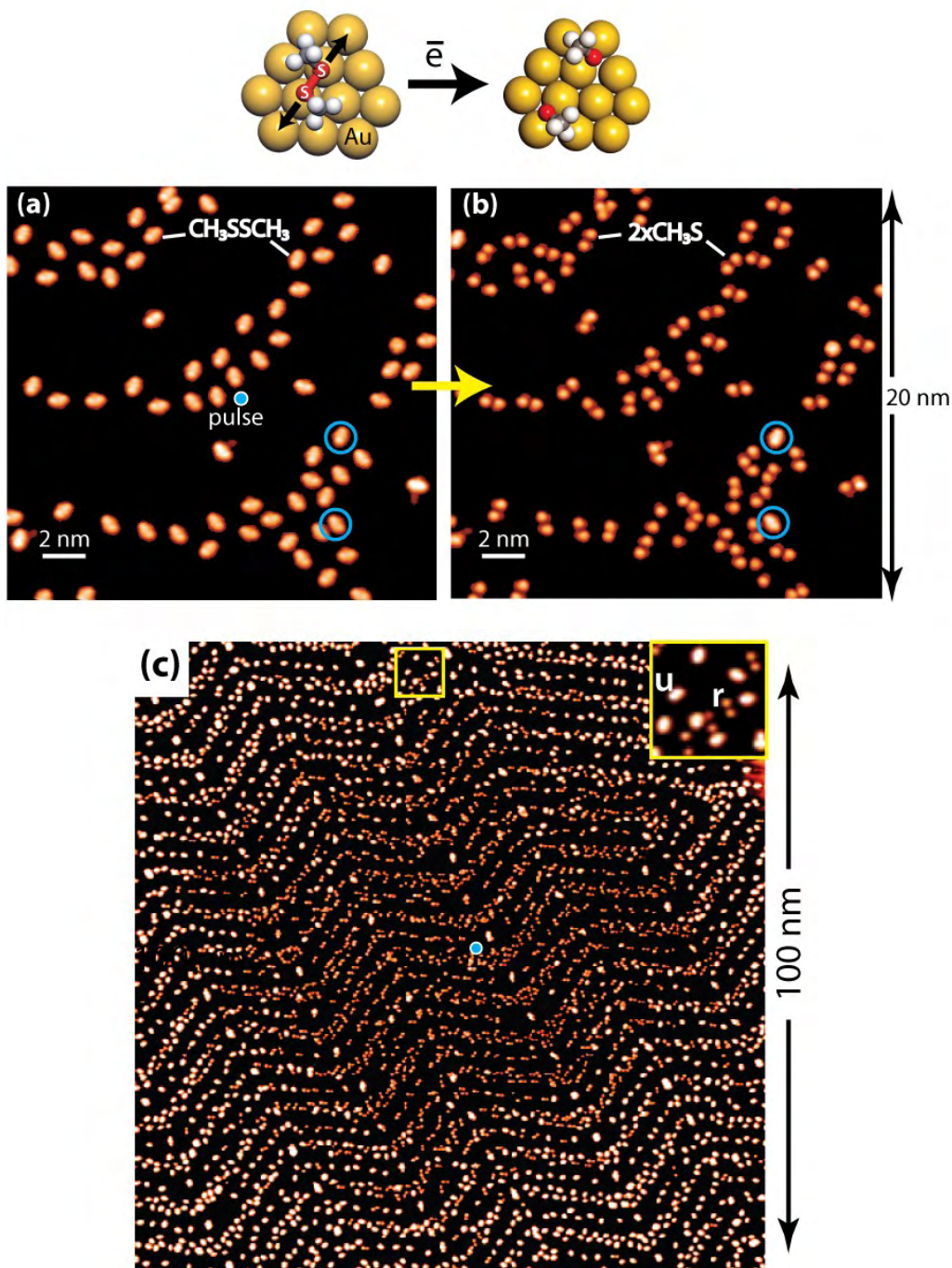


**Figure 12.1.** Non-local electron-induced dissociation of  $\text{CH}_3\text{SSCH}_3$  molecules. Top: structural models of undissociated  $\text{CH}_3\text{SSCH}_3$  molecule on Au(111) and its dissociation products ( $\text{CH}_3\text{S}$ ). Middle: STM images of the same surface area before (a) and after (b) a single pulse of tunneling current (2.0 V/1 nA/100 msec) applied at the marked position (blue circle) on the clean surface. Nearly all the molecules dissociated in the field of view (the undissociated molecules are highlighted). (c) STM image of non-local  $\text{CH}_3\text{SSCH}_3$  dissociation induced by a single 2.5 V/1.0 nA/200 ms pulse at the blue point. The inset shows a surface area (inside yellow square) located  $\sim 46$  nm away from the pulse position. *u* marks unreacted and *r* - reacted  $\text{CH}_3\text{SSCH}_3$  molecules.

crystal temperature of  $< 40\text{K}$ . Current pulses producing non-local chemistry were applied with the feedback engaged to surface regions unoccupied by adsorbate molecules. No dissociation upon adsorption was observed for  $\text{CH}_3\text{SSCH}_3$ ,  $\text{C}_6\text{H}_5\text{SH}$  and  $\text{CH}_3\text{SH}$  molecules on the Au(111) surface (including elbows of the herringbone reconstruction) where most of the present analysis was carried out. Minor dissociation took place on single-atom step-sites, but they are not considered here.

### 12.3 NON-LOCAL MOLECULAR EXCITATION

Electron-induced dissociation of the  $\text{CH}_3\text{SSCH}_3$  molecule on Au(111) [301] ruptures the S-S bond and produces two  $\text{CH}_3\text{S}$  fragments as seen in STM images before dissociation (see Chapter 7 for a detailed discussion). To induce the dissociation reaction, the STM tip need not be positioned right above the  $\text{CH}_3\text{SSCH}_3$  molecule. A pulse of tunneling current at a voltage exceeding  $1.5\text{V}$  causes *non-local* dissociation of the  $\text{CH}_3\text{SSCH}_3$  molecules far from the tunneling junction, as seen in Figure 12.1 (a,b). The efficiency of the reaction is rather spectacular as most  $\text{CH}_3\text{SSCH}_3$  molecules dissociate in a large area around the position of the excitation pulse. The spatial range of the non-local dissociation can be truly dramatic as seen in Fig. 12.1 (c), where about 1000 molecular dissociation events are caused by a single pulse of tunneling current ( $V=2.5\text{ V}$ ,  $3\cdot 10^9$  electrons) applied in the center of the STM image (blue spot). 100% dissociation occurs in a circular area of  $\sim 20\text{ nm}$  in radius. Using even more intense pulses it is possible to dissociate molecules as far as  $100\text{ nm}$  from the injection point.

Because of the large number of molecules dissociated by each pulse, non-local chemistry is statistically reproducible for a given STM-tip and pulse conditions. This is shown in Figure 12.2 (a) where a total number of dissociation events in  $4225\text{ nm}^2$  area was measured for fifteen consecutive pulses (each  $1.8\text{ V}$ ,  $8\cdot 10^8$  electrons) applied to different surface regions partially covered with  $\text{CH}_3\text{SSCH}_3$  molecules. The energy threshold for the non-local reaction was estimated by measuring the total reaction yield as a function of pulse voltage. For  $\text{CH}_3\text{SSCH}_3$  on Au(111) the threshold is  $\sim 1.4\text{ V}$  (sample positive, Figure 12.2(b)), which suggests that the reaction proceeds via electronic excitation of the adsorbed molecules rather than vibrational excitation of the molecules in the ground electronic state [11]. This conclusion is supported by

dissociative electron attachment to  $\text{CH}_3\text{SSCH}_3$  molecules adsorbed on ice which cleaves the S-S bond [322].

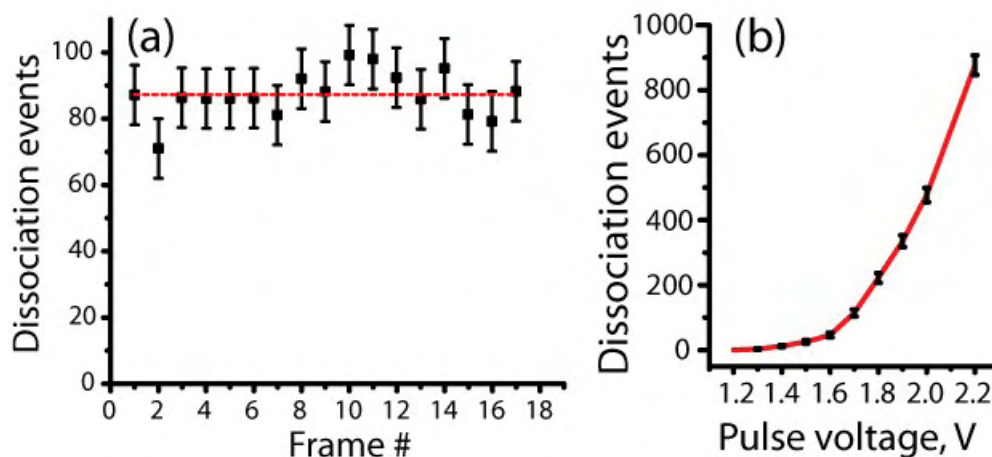


**Figure 12.2.** Reproducibility and energy threshold of non-local  $\text{CH}_3\text{SSCH}_3$  dissociation. (a) Total number of dissociation events per pulse plotted as a function of pulse number. The same current pulse (1.8 V/0.350 nA/150 ms) was repeated in 18 different areas on the surface. The red dashed line is the average number of events. (b) Total number of dissociation events per pulse as a function of pulse voltage. Each pulse is performed at 1.0 nA for 200 ms. The points are connected to guide the eye.

We have observed non-local dissociation of  $\text{CH}_3\text{SSCH}_3$  molecules on the Au(100), Cu(111) and Cu(110) surfaces. In addition, non-local dissociation of the S-H bond in methanethiol ( $\text{CH}_3\text{SH}$ ) and benzenethiol ( $\text{C}_6\text{H}_5\text{SH}$ ) occurs on Cu(111) and Au(111) surfaces, as does dissociation of the C-I bond in iodobenzene ( $\text{C}_6\text{H}_5\text{I}$ ) on Cu(111) and Cu(110). The lateral extent and threshold voltages of the non-local reactions are different in each case. For example, the threshold is as low as 0.8 V for  $\text{C}_6\text{H}_5\text{SH}/\text{Cu}(111)$  and as high as 3.5 V for  $\text{C}_6\text{H}_5\text{SH}/\text{Au}(111)$ . Since the threshold ( $>0.6$  eV) is always much higher than molecular vibrational energies, dissociative electron attachment is the likely reaction mechanism in all cases.

## 12.4 NON-LOCAL REACTION IS DRIVEN BY HOT-ELECTRONS INJECTED FROM THE STM-TIP

The observed non-local chemistry is proposed to be caused by hot electrons which are injected from the STM-tip into the surface. Hot electrons propagate laterally causing dissociation of adsorbed molecules via dissociative electron attachment. Since the radius of the STM-tip is

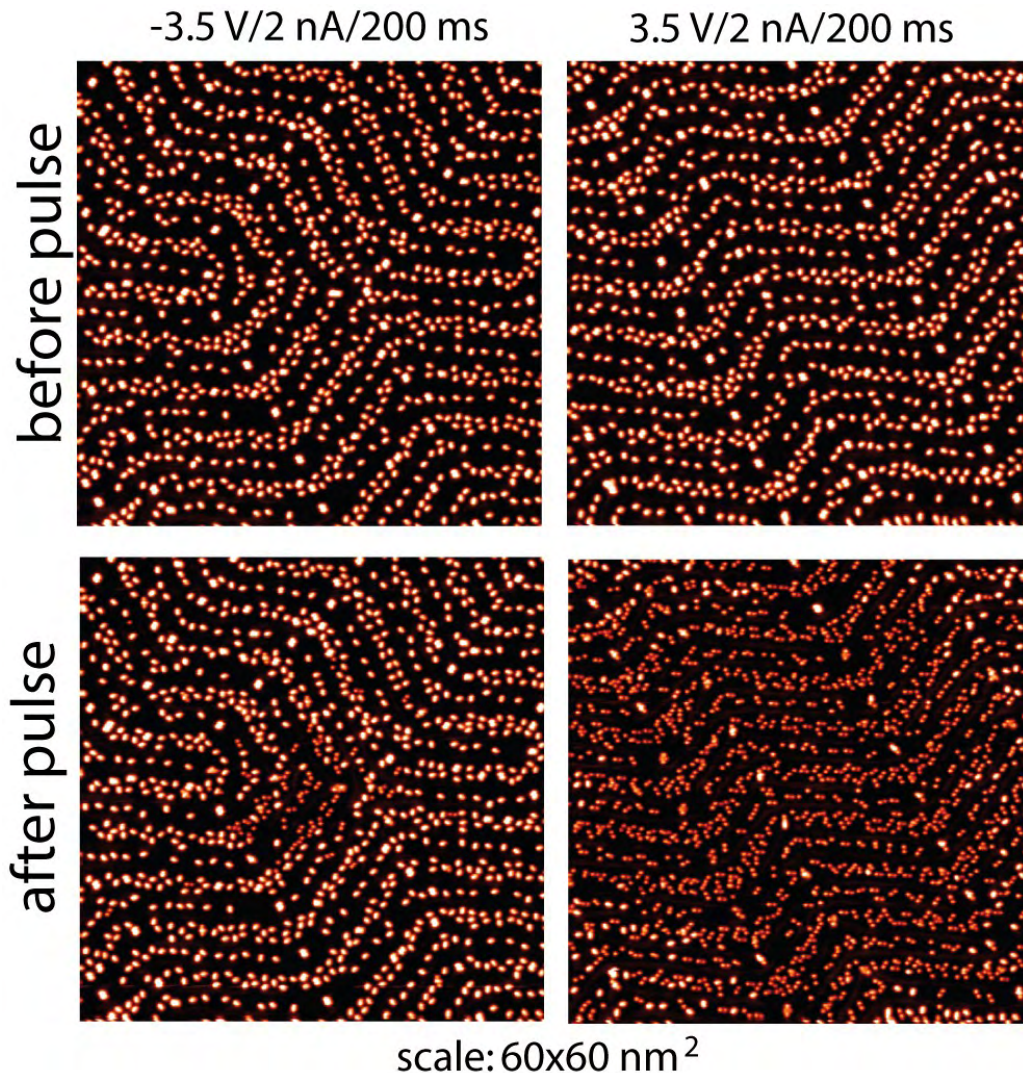


**Figure 12.3.** Dependence of non-local  $\text{CH}_3\text{SSCH}_3$  dissociation on the bias-polarity of the tunneling junction during excitation. Hot-hole injection (left panel) is much less effective than hot-electron injection (right panel) in the non-local reaction.

typically 20-50 nm [323], two plausible alternative origins of the non-local chemistry are the electric field of the STM-tip [321] and the field emission current from random protrusions on the

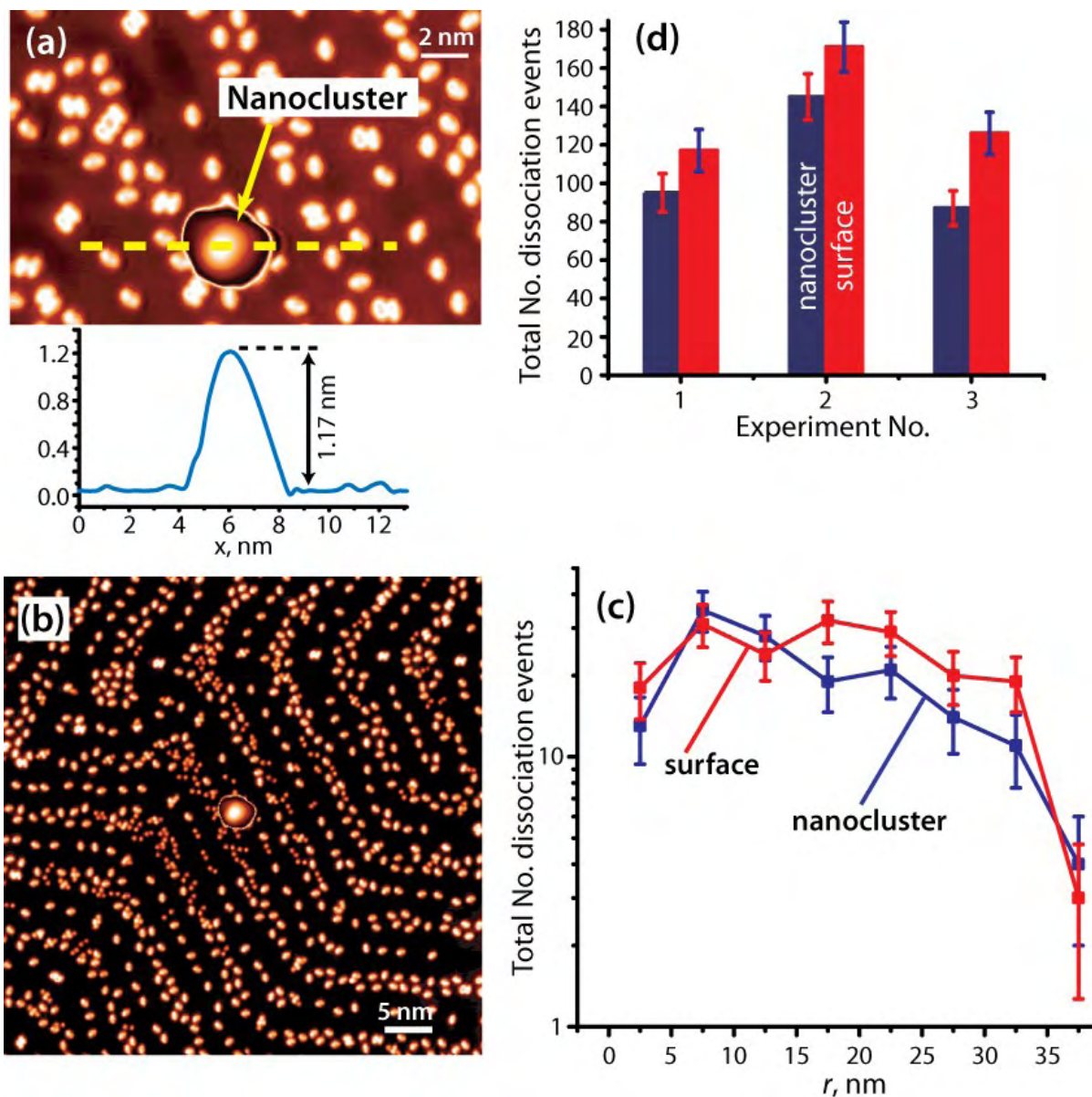


**Figure 12.4.** Non-local reaction from a current pulse applied to a nanocluster. (a) STM image of an artificially created metal cluster. The line-scan below the image was taken along the yellow dashed line. (b) Non-local dissociation of  $\text{CH}_3\text{SSCH}_3$  molecules induced by a current pulse (1.8V/0.5 nA/200 msec) applied to the metal cluster in the center. (c) Histograms of the  $\text{CH}_3\text{SSCH}_3$  dissociation events induced by the same current pulse (1.8V/0.5 nA/200 msec) applied to the cluster and to the Au(111) surface. (d) The effect of the pulse on the cluster and on the surface compared for three different clusters. Pulse conditions are 1.8V/0.5 nA/200 ms for experiment 1 and 2, and 1.8V/0.25 nA/250 ms for experiment 3.

tip surface (microtips) near the tip apex. The effect of the electric field is particularly difficult to address in STM [93, 324] because it is always present and it is non-local.

A most common approach to separate field- and current-induced processes in STM is to detect the asymmetry of the observed effect when switching the bias-polarity of the tunneling junction and reversing the direction of tunneling current. In the present case, the voltage pulses of opposite polarity do indeed produce strong asymmetry of the non-local reaction. Very few non-local dissociation events in a small radius of several nanometers are produced by current pulses of 1.0-2.0 nA in the energy range from -1.8V to -2.0V in contrast to the pulses of opposite polarity. Non-local dissociation of considerable magnitude is observed at  $V > -2.0$  V although pulses of negative polarity are drastically less effective (Figure 10.3).

At negative voltages, hot-holes rather than hot-electrons are injected into the Au(111) surface and the asymmetry could be attributed to the hot-carrier transport and hole-attachment to molecules. However, field-induced processes may also be asymmetric. In addition, neutralization of injected hot-holes proceeds via an Auger process (among others) which produces hot-electrons. Altogether, bias-dependence of the non-local reaction is instructive but not sufficient to rule-out the effect of the electric field.

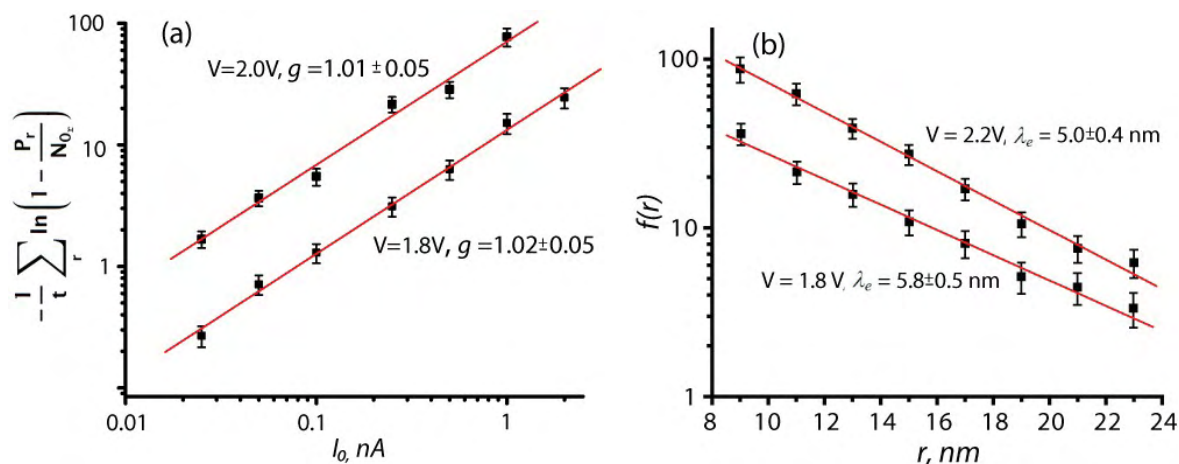


**Figure 12.5.** Statistical analysis of non-local  $\text{CH}_3\text{SSCH}_3$  dissociation.

(a) Linear scaling of non-local reaction rate with excitation current (Eq. 12.2) from two experiments using pulses at 1.8 V and 2.0 V. Each point is an average of two measurements. Red lines are linear fits to the data.

(b) Attenuation function of the non-local chemistry from two experiments using pulses at 1.8 V (average of 15 measurements) and 2.2 V (average of 5 measurements). Red lines are exponential decay fits to the data.

Two statistical experiments were carried out to determine the hot-electron origin of the non-local reaction. In the first experiment, nanometer size clusters were created on the surface by bringing the STM-tip into contact with the Au(111) surface. The STM-tip was first extended into the surface by  $\sim 3$  nm motion ( $V < 1$  mV) and then slowly pulled out by 6-7 nm motion. A typical cluster produced is  $\sim 1.2$  nm high (Fig. 12.4a). When a current pulse is applied to the cluster, the STM-tip is at least 1 nm farther from the surface than when a pulse is applied to the flat surface. The electric field applied to the molecules adsorbed around the cluster is therefore reduced significantly (tip-surface separation in the tunneling regime is  $\sim 0.5$  nm) as is the possible field-emission current from random microtips. Nonetheless, Fig. 12.4b demonstrates that non-local dissociation is also caused by a current pulse on the cluster and its spatial extent is as large as when the same pulse is applied to the flat surface (Fig. 12.4c). This was observed for three different clusters for which 15-30% variation in cluster/surface ratio of dissociation yield exists due to structural variations in the STM tip and between the clusters (Fig. 12.4d). Therefore neither the electric field nor field-emission from microtips causes non-local chemistry around the electron-injection point.

In the second experiment, the non-local reaction was statistically analyzed with a kinetic model. The reaction rate at a distance  $r$  from the electron-injection point is assumed to be given by  $\frac{dP_r}{dt} = k(N_{0_r} - P_r)I_r^g$ , where  $P_r$  is the number of dissociated molecules;  $N_{0_r}$  is the number of reactant molecules;  $k$  is the rate constant for the reaction;  $I_r$  is the surface current of hot electrons at  $r$ ; and  $g$  describes the scaling of the reaction rate with the hot-electron current. This equation is conceptually similar to the one used in the analysis of single-molecule chemistry [92]. The key difference is explicit concentration dependence in the rate equation. In single-molecule chemistry, the tunneling current excites only one molecule in each measurement which makes concentration constant (one molecule). It was further assumed that  $I_r$  is proportional to the tunneling current during the pulse ( $I_0$ ), so that  $I_r = I_0 f(r)$ , where  $f(r)$  is the attenuation function. The integral form of the rate equation is then:

$$-\ln\left(1 - \frac{P_r}{N_{0_r}}\right) = kt(I_0 f(r))^g \quad (12.1)$$

The value of  $g$  was determined from a series of non-local reaction measurements with a variable excitation current ( $I_0$ ). For each electron pulse, the left side of eq. (12.1) was calculated from the number of dissociation events and summed over the radial extent of observed events. With this procedure, eq. (12.1) becomes:

$$-\sum_r \ln\left(1 - \frac{P_r}{N_{0r}}\right) = ktI_0^g \sum_r (f(r))^g \quad (12.2)$$

The right part of eq. (2) is a function of  $I_0$  and  $t$ . The sum of attenuation terms  $f(r)$  is not a function of  $I_0$ , because the average time interval between tunneling electrons is  $\sim 50$  ps at 1 nA, which is much larger than the typical lifetime of hot electrons at  $>1.5$  V (20-40 fs) [325]. The duration of the excitation pulse was chosen to maintain the condition of constant total charge,  $I_0 \cdot t = \text{const}$ , to prevent 100 % dissociation in the scan range at large values of  $I_0$ . As seen in Fig. 12.5a,  $g$  is close to unity, i.e. the rate of the non-local reaction is proportional to the tunneling current of the pulse. This observation provides further quantitative support to our hypothesis that the non-local chemistry is driven by the current of hot electrons injected from the STM-tip.

## 12.5 LATERAL ATTENUATION OF THE NON-LOCAL REACTION

With the experimental determination of  $g=1$ , the attenuation function  $f(r)$  can be determined from Eq. (12.1). As seen in Fig. 12.5b, the attenuation function beyond  $r = 8$  nm behaves as a monoexponential decay,  $f(r) \propto e^{-\frac{r}{\lambda_e}}$ . In the case of the ballistic 2D transport of hot electrons on the surface, the attenuation function includes an additional geometric factor of  $1/2\pi r$ . However, each data point in Fig. 3b is obtained by adding all the dissociation events at a given radius (in the area  $2\pi r \Delta r$ ). Therefore the geometric factor equals unity. The decay length,  $\lambda_e$ , shows little dependence on the STM-tip, the intensity of the hot-electron pulse (hence the range and total yield of non-local dissociation), and the energy of hot electrons (in the range of 1.8 to 2.2 V). The values of  $\lambda_e$  obtained in various experiments over several months were:  $5.4 \pm 0.4$  nm,  $5.4 \pm 0.6$

nm,  $5.2 \pm 0.6$  nm at  $U = 1.8$  V;  $6.5 \pm 0.5$ ,  $5.6 \pm 0.6$  nm at  $U = 2.0$  V; and  $4.9 \pm 0.4$  nm,  $5.9 \pm 0.9$  nm at  $U = 2.2$  V.

The physical meaning of the decay length ( $\lambda_e$ ) at the given energy depends on the transport regime of hot-electrons on the surface [133]. If the cross section for elastic electron scattering by adsorbed molecules is low, the transport is essentially ballistic and  $\lambda_e$  is the inelastic mean-free path of hot-electrons (limited mainly by inelastic electron-electron scattering [326] at the energy of 1.8 V above  $E_f$ ). In the opposite limit of efficient elastic scattering by adsorbed molecules the transport is diffusive, i.e. an electron undergoes multiple elastic scattering by adsorbed molecules before it is inelastically scattered into the bulk (by a molecule or an electron from the Fermi sea). Coverage-dependent measurements of the decay length would help to clarify this issue. Statistical measurement of the non-local chemistry can then be considered a potentially viable approach to measure hot-electron transport on metal surfaces. We anticipate that it will be complementary to the analysis of surface-state scattering on clean metal surfaces that yields phase-relaxation length of hot surface-state electrons [130, 327, 328].

In this work we cannot rigorously assign the origin of the electronic states that carry hot-electron current on the surface. At the energies of hot electrons needed to dissociate  $\text{CH}_3\text{SSCH}_3$  molecules, Au(111) [122] and Cu(111) [329] surfaces have an unoccupied surface state (and the derivative surface resonance) in the  $\bar{\Gamma}$ -centered [329] projected band-gap. Electrons in these states propagate parallel to the surface. On Cu(110), non-local dissociation of  $\text{CH}_3\text{SH}$  is observed at  $V > 0.6$  V ( $> 1.0$  V for  $\text{CH}_3\text{SSCH}_3$ ). However, the lowest empty surface resonance in the  $\bar{Y}$ -centered band-gap crosses the bulk-bands at  $\sim 0.5$  eV above Fermi level [329, 330] (and likely vanishes by analogy with Ag(110) [331]). On the (5x20) reconstructed Au(100) surface, no empty surface resonances below 4.0 V are observed by inverse photoemission in the  $\bar{X}$ -bar centered band-gap [332, 333]. Nevertheless, the onset of the non-local  $\text{CH}_3\text{SSCH}_3$  dissociation on the reconstructed Au(100) is at  $\sim 1.3$  V in our experiments. For these surfaces, the bulk states at the edges of the projected band-gaps may contribute to the hot-electron transport. These states were shown to have enhanced surface LDOS. They produce scattering patterns around defects similar to surface resonances [331], which implies transport parallel to the surface. A “regular” bulk state on any surface is unlikely to be involved, because an electron in these states has a large perpendicular momentum, causing it to quickly leave the surface region along the normal or slightly off-normal trajectory [334, 335].

## 12.6 ELIMINATING TIP-ARTIFACTS

Surface-resonance-mediated electronic excitation of adsorbed molecules makes non-local chemistry distinctly different from the local excitation under the STM-tip, where electronic states of the tip directly couple to molecular resonances. In this regard non-local chemistry closely resembles surface photochemistry, where photo-generated hot-carriers in the electronic states of the surface excite adsorbed molecules [336]. Non-local excitation also eliminates the effects of the STM-tip on the chemical reaction by exciting molecules at a large distance from the tunneling junction. This fact can be illustrated by contrasting the probability of conformation retention in the dissociation of  $\text{CH}_3\text{SSCH}_3$  on the Au(111) surface obtained by the local and non-local excitation.

The detailed analysis of the electron-induced dissociation of  $\text{CH}_3\text{SSCH}_3$  on Au(111) was presented in Chapter 10. The “trans”-conformation of the  $\text{CH}_3\text{SSCH}_3$  molecule can be retained in the geometrical arrangement of the reaction products. The highest probability of conformation-retention ( $75\pm 5\%$ , in  $\sim 500$  molecules studied) is observed in the non-local dissociation of  $\text{CH}_3\text{SSCH}_3$  molecules (pulse: 1.8 V/1 nA/100 ms). In stark contrast, the probability of conformation-retention is observed to be as low as  $10\pm 5\%$  (in  $\sim 100$  molecules studied) when the molecules are excited directly under the tip (pulse: 1.4 V/1 nA/100 ms), and the reaction is influenced by the electric field of the STM-tip or by direct tip-molecule interactions. The high yield of conformation-retention ( $\sim 65\%$ ) for local excitation was found to restore by increasing the tip-surface distance (decreasing the pulse current to 10 pA) [301].

## 12.7 CONCLUSIONS

Based on quantitative analysis of the STM images it is established that adsorbed molecules can be caused to dissociate at large distances (up to 100 nm) from the STM-tip by hot electrons that are injected from the tip and transport laterally on the surface. This effect is observed for several molecules and metal surfaces. Non-local molecular excitation provides unique opportunities to eliminate STM tip-artifacts in the analysis of electron-induced chemical reactions on surfaces, to

study diffusive hot-electron transport on surfaces in the presence of adsorbates, and to connect STM-induced chemistry to the photochemistry of adsorbed molecules.

## APPENDIX A

### STM STUDY OF WATER ADSORPTION ON $\text{TiO}_2(110)$ -(1X2) SURFACE WITH UV-INDUCED DEFECTS\*

Titanium dioxide ( $\text{TiO}_2$ ) is the most investigated single-crystalline system in the surface science of metal oxides. One reason for that is a wide range of its applications.  $\text{TiO}_2$  is traditionally used in heterogeneous catalysis as a component in mixed vanadia/titania catalyst [337]. It was shown that finely dispersed Au particles supported on  $\text{TiO}_2$  oxidize CO at low temperature [338]. Since the 1970's [339] the bulk of experimental and applied work was focused on the photocatalytic properties of  $\text{TiO}_2$ . By far the most effort is dedicated the use of photo-assisted degradation of organic molecules by  $\text{TiO}_2$ , which has direct applications in wastewater purification [340], bactericidal [341], and self-cleaning/antifogging [342, 343] coatings. In addition,  $\text{TiO}_2$  can be applied potentially in solar cells for production of hydrogen and oxygen from water; it is also being viewed as one of the most promising candidates for substitution of  $\text{SiO}_2$  as a gate insulator in microelectronics [344]. On the other hand  $\text{TiO}_2$  is ideally suited for experimental research. The polished single crystal wafers are readily available from commercial sources. The crystals can be reduced by heating in vacuum, which conveniently prevents charging of the surface and allows one to study  $\text{TiO}_2$  using techniques that require the conductive substrates (such as STM).

---

\* Reproduced in part with permission from: P. Maksymovych, S. Mezhenny, J. T. Yates, Jr., *Chemical Physics Letters* 382 (2003) 270. Copyright 2003 Elsevier.

## A.1 BULK STRUCTURE OF TITANIUM DIOXIDE

TiO<sub>2</sub> crystallizes in three major structures (Fig. A.1): rutile – tetragonal unit cell ( $a = b = 4.584 \text{ \AA}$ ,  $c = 2.953 \text{ \AA}$ ), anatase – tetragonal unit cell ( $a = b = 3.782 \text{ \AA}$ ,  $c = 9.502 \text{ \AA}$ ), and brookite – rhombohedral unit cell ( $a = 5.436 \text{ \AA}$ ,  $b = 9.166 \text{ \AA}$ ,  $c = 5.135 \text{ \AA}$ ). Rutile and anatase are of primary practical interest, and most of the experimental studies were done on rutile. The building blocks of all the three structures are slightly distorted octahedrons, where Ti is coordinated by six O-atoms.

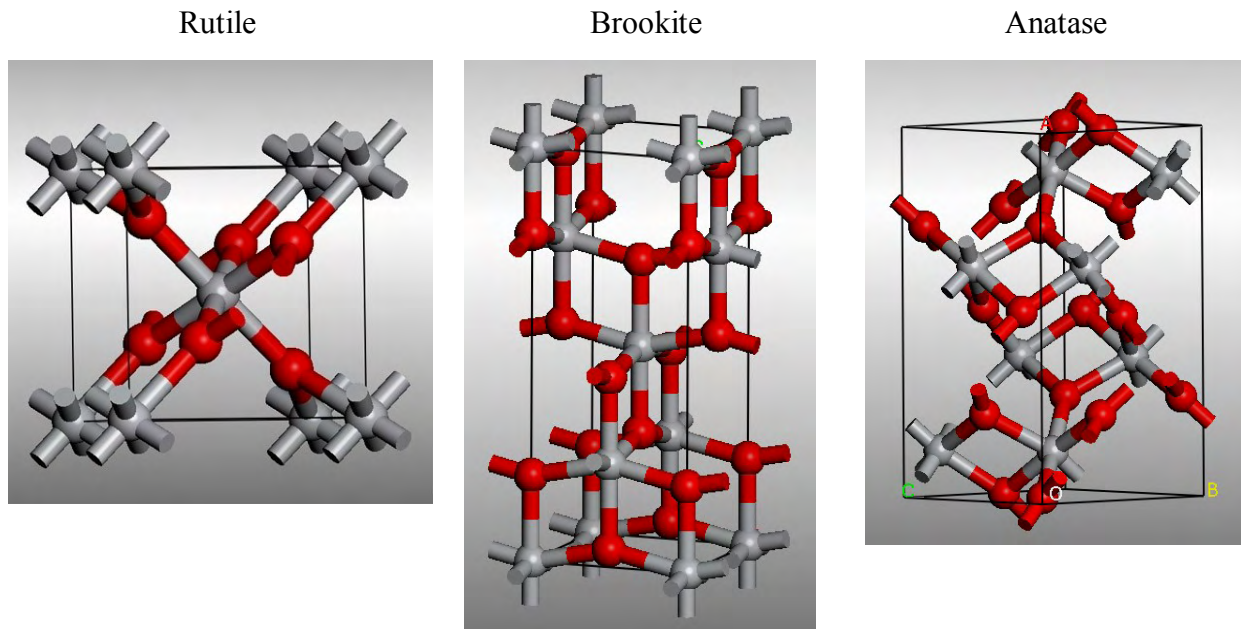


**Figure A.1.** Three crystal structures of TiO<sub>2</sub>. Ti is grey, O – red.

TiO<sub>2</sub> is a semiconductor with a wide band gap of 3.0 eV. However, the crystal can be self-doped by annealing, during which bulk reduction and creation of intrinsic defects (which are n-type dopants) occur. The process is accompanied by a substantial increase of the electrical conductivity and a dramatic change of the color of the crystal. Bulk defects play a major role in any phenomena occurring at elevated temperatures, such as bulk-assisted reoxidation, reconstruction of the surface etc.

## A.2 TiO<sub>2</sub>(110)-(1x1) SURFACE

TiO<sub>2</sub>(110) surface termination is the most stable for a rutile crystal [345]. Figure A.2 shows a ball-and-stick model of the TiO<sub>2</sub>(110)-(1x1) surface. According to Tasker's classification [346], it is a Type 2 surface, where a plane with Ti and O atoms, having a net positive charge, is followed by two planes consisting of only O atoms, having a negative charge. Overall the dipole moment perpendicular to the surface is zero, which means that the surface is thermodynamically stable.

Three most important atomic species on the (1x1) surface are: the six fold coordinated Ti, the five-fold coordinated Ti atoms and the bridging oxygen atoms above the six-fold Ti atoms (Fig. A.2). The in-plane oxygen atoms possess the bulk coordination, while the bridging O-atoms are undercoordinated, and can be easily removed during annealing with the formation of oxygen vacancies.

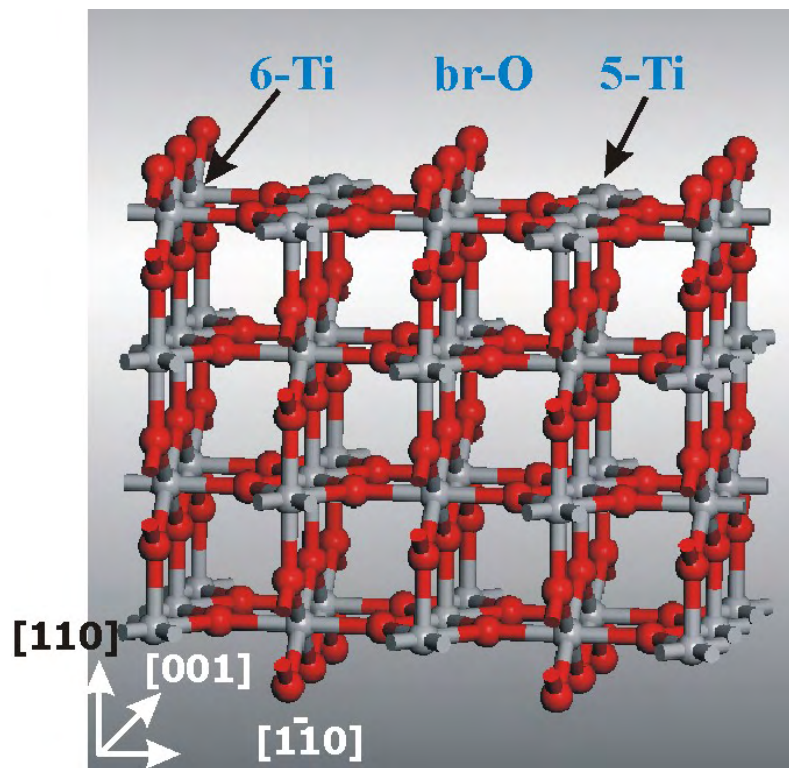


**Figure A.2.** TiO<sub>2</sub>(110)-(1x1) surface: n-Ti corresponds to the n-fold coordinated Ti atom; br-O is the bridging O-atom.

STM images of  $\text{TiO}_2$  surfaces are mostly obtained at a positive bias on the sample (+2.0-+2.5V), so that the empty states are imaged.  $\text{TiO}_2(110)-(1 \times 1)$  surface is seen as alternating bright and dark rows in the  $[001]$  direction with a periodicity of  $\sim 6.3 \text{ \AA}$  (Fig. A.3-4). Since the crystal has to be partially reduced to become sufficiently conductive for STM measurements, the surfaces always have a substantial number of point defects, which are seen as bright spots on dark rows.

The dominant tunneling site on the  $\text{TiO}_2(110)-(1 \times 1)$  surface was subject to some debate in recent years. The uncertainty was as to whether the geometric or the electronic corrugation of the surface contributes to the contrast of the STM images, i.e. whether the bright rows in the image (Fig. A.4) correspond to the rows of the 5-fold coordinated Ti-atoms, or to the bridging O-atoms.

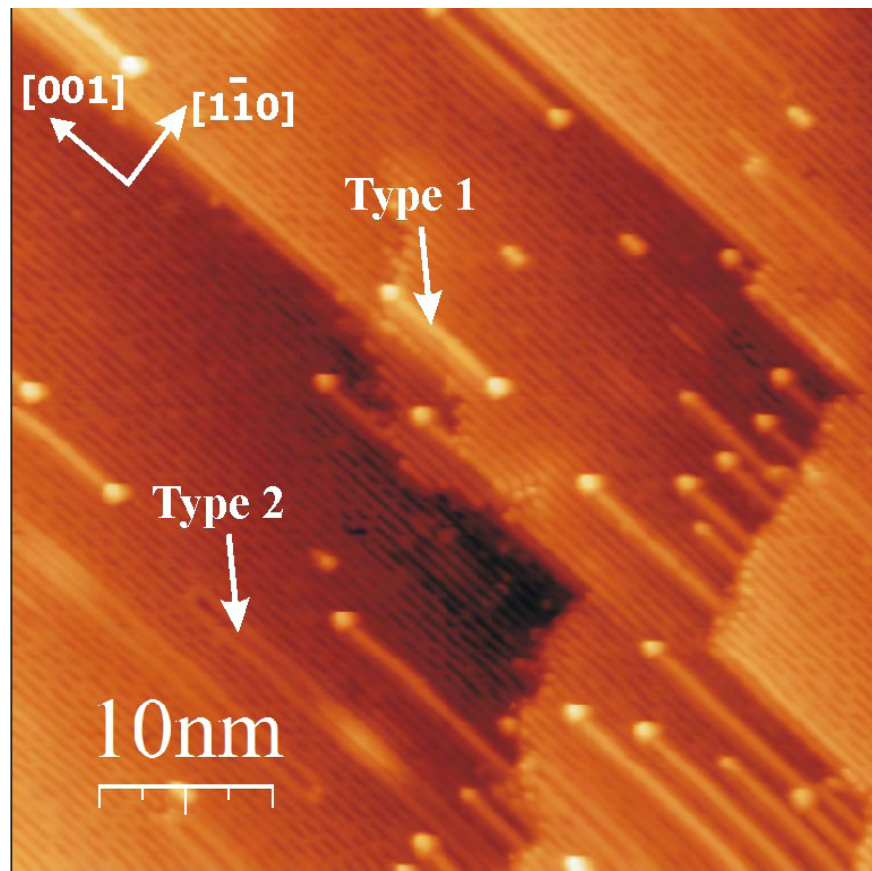


**Figure A.3.** STM image of a clean  $\text{TiO}_2(110)-(1 \times 1)$  surface showing the two types of line defects.  $U=+1.9\text{V}$ ,  $I=0.035 \text{ nA}$ .

In the reduced  $\text{TiO}_2$  crystals (bandgap  $\sim 3.0$  eV), the Fermi level is located closer to the conduction band minimum (CBM), so at biases of  $\sim +2.0$  V the electrons tunnel into the conduction band which has a strong Ti-3d character [347] (the valence band states are dominated by O-2p orbitals). On the other hand the bridging oxygen atoms protrude above the surface and the STM image could be just a reflection of the geometrical corrugation on the surface. The proof that rows of 5-fold coordinated Ti atoms not the bridging O-rows are imaged bright in empty-state STM images is based on a number of experimental and theoretical arguments. (1) Adsorption of nucleophilic sulfur occurs on top of bright rows at room temperature [348]. (2) Surface images taken with non-contact AFM with conducting tips show the 180 phase difference between the electronic and geometric corrugation of the surface [349]. (3) The bright spots on dark rows are very abundant on the surface and their density can be changed by the annealing conditions employed. Finally, theoretical calculations show that the contours of the density of states in the conduction band have protrusions centered on top of the 5-fold coordinated Ti species and the missing bridging oxygen atoms [350].

### A.3 STRUCTURAL DEFECTS ON THE $\text{TiO}_2(110)-(1 \times 1)$ SURFACE

#### Line defects

STM images of the  $\text{TiO}_2(110)-(1 \times 1)$  surface often show presence of two types of bright strands propagating along the [001] direction (Fig. A.3). The strands of the first type have an apparent height of  $\sim 0.28$  nm, terminate with bright spots and are centered above a row of 5-fold coordinated Ti atoms. A large number of these strands grow out of terraces. The strands of the second type (Fig. A.4) have a smaller apparent height ( $\sim 0.1$  nm), and they are also centered above the 5-fold coordinated Ti-row. The origin of the strands, especially that of the first type, was explained in Ref. [351] by observing the reaction of the (1x1) surface with oxygen at  $\sim 600$  K. The authors suggest that both types of strands are the areas of the (1x2) reconstruction (which is described further), since they have a double periodicity in the [110] direction. However the higher strands are described by the model of Pang et. al [352] (stoichiometry  $\text{TiO}_2$ ), while the lower strands correspond to the model of Onishi and Iwasawa [353] (stoichiometry  $\text{Ti}_2\text{O}_3$ ).

## Point defects

Point defects are the most abundant type of defect on the  $\text{TiO}_2(110)-(1 \times 1)$  surface. They appear in STM as bright protrusions elongated in the  $[\bar{1}\bar{1}0]$  direction and located in registry with the dark rows, which correspond to the positions of the bridging oxygen atoms (Fig. A.4). The number of such protrusions decreases when the surface is exposed to oxygen, which is a solid evidence for their being the bridging oxygen vacancy sites.

After the standard surface preparation procedure by sputtering and annealing, the concentration of oxygen vacancies is 3-7 at. % on the surface. The vacancy sites always appear isolated with no apparent short-range ordering, which is the evidence for the repulsive interaction between them [354]. DFT calculations show that when a bridging oxygen atom is removed from the surface, the excess electron density is not localized on the underlying Ti atom, which was directly bound to the removed O-atom, but is instead delocalized over several atoms, including the 5-fold coordinated ones in the neighboring rows [355]. The oxygen vacancies form a defect state in the band gap of  $\text{TiO}_2$ , which is located  $\sim 0.9$  eV below the Fermi edge as evidenced from photo-emission spectra [356].

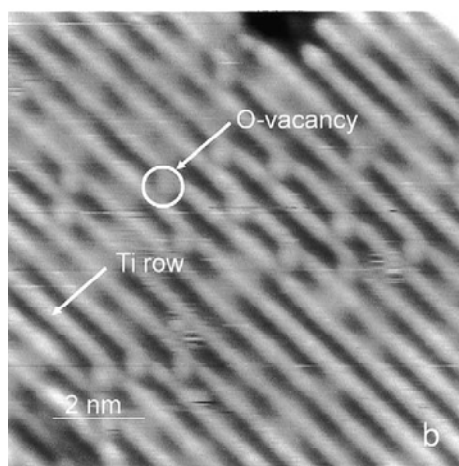


**Figure A.4.** Close-up STM image of clean  $\text{TiO}_2(110)-(1 \times 1)$  surface displaying oxygen vacancies ( $10 \times 10 \text{ nm}^2$ ,  $U=2.5 \text{ V}$ ,  $I=0.035 \text{ nA}$ ).

The oxygen vacancies are responsible for the most of the reactivity of the  $\text{TiO}_2(110)-(1 \times 1)$  surface. It is now a well-proven fact that they are the sites for water dissociation on the surface, although the dissociation mechanism is still a matter of very active debate [357]. They were also shown to be the adsorption sites for gold nanoparticles [358].

#### A.4 $\text{TiO}_2(110)$ -(1x2) SURFACE

The  $\text{TiO}_2(110)$  - (1x2) reconstruction can be obtained using either a special surface preparation procedure or a heavily reduced rutile crystal. The double periodicity of the (1x2) surface is in the  $[1\bar{1}0]$  direction. Here we deal with the so-called Type-2 surface, obtained by high-temperature annealing of the  $\text{TiO}_2(110)$ -(1x1) surface at 1200K for 10-20 minutes. The STM image of this surface is shown in Fig. A.5.

The distinct feature of this surface is a superlattice of links, which join  $[001]$  oriented rows (Fig. 1) with a periodicity of  $\sim 12$  unit cells along the  $[001]$  direction. That is why Type 2 reconstruction is often referred to as the (12x2) reconstruction. According to Ref. [359], the links are formed when the trough between the  $[001]$  added rows is first filled with oxygen, and then with Ti atoms from the neighboring rows. One Ti-atom forms a single link and two Ti-atoms in

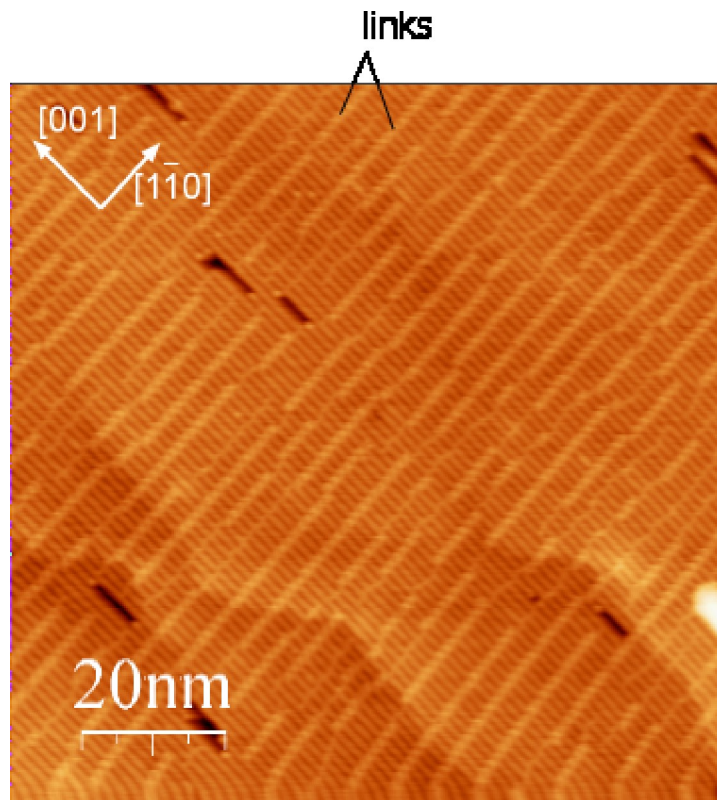


**Figure A.5.** STM images of the  $\text{TiO}_2(110)$ -(1x2) surface with links, obtained under the *reducing* conditions (UHV, annealing at 1200K).  $U=+3.05\text{V}$ ,  $I=0.040\text{nA}$

the trough – double- or cross-links (the name reflects their shape). The links are believed to relieve the surface strain, which arises due to partial reduction of the added rows (Fig. A.6).

The structural model of the (12x2) surface was proposed by Pang et. al. [352], Fig. A.6. In this model the (1x2) surface termination is formed by the Ti-Ox added-rows with a stoichiometry of  $\text{Ti}_3\text{O}_5$  if the bridging oxygen species is removed from the middle of the added row or  $\text{TiO}_2$  if it is not. The ESDIAD pattern of the (1x2) surface obtained under reducing conditions consists of two well separated beams of  $\text{O}^+$  ions [360]. These can be due to the O atoms on the sides of the added [001] row (Fig. A.6), which are tilted upwards due to lattice relaxation. The bridging oxygen species in the center of the added row would add the third, normal beam to the ESDIAD pattern. Therefore the original model of Pang et. al [352] with  $\text{Ti}_3\text{O}_5$  rows is assumed here.

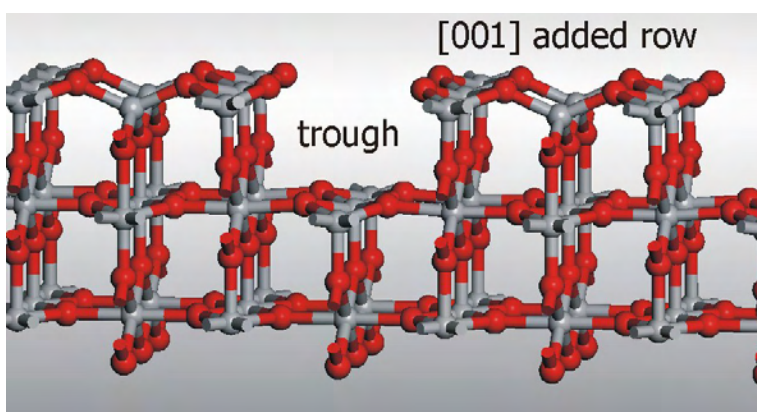


**Figure A.6.** DFT relaxed geometry [379] of the added-row model for the  $\text{TiO}_2(110)-(12 \times 2)$  reconstructed surface. The stoichiometry of the added row is  $\text{Ti}_3\text{O}_5$  (according to Pang et.al. [352]) Ti atoms are grey, O-atoms – red.

## **A.5 INTERACTION OF WATER WITH $\text{TiO}_2(110)$ SURFACE: THE PHENOMENON OF PHOTOINDUCED HYDROPHILICITY**

The importance of understanding the behavior of water on  $\text{TiO}_2$  surfaces stems from  $\text{TiO}_2$  applications where water plays an important role, such as photocatalysis in hydrous environments, self-cleaning  $\text{TiO}_2$ -coated glass based on the UV-induced hydrophilicity etc. Adsorption of water has been most extensively studied on the  $\text{TiO}_2(110)$  surface [361]. At the

time of the experiments presented here, the issue of water dissociation on the  $\text{TiO}_2(110)-(1 \times 1)$  surface was still actively debated, because theoretical calculations predicted dissociation of  $\text{H}_2\text{O}$  on the stoichiometric (vacancy free) surface, which is in stark contrast to experimental observations [362].

The experimental proof for dissociative adsorption of  $\text{H}_2\text{O}$  on the  $\text{TiO}_2(110)-(1 \times 1)$  surface was given by Henderson [363] and Hugen Schmidt et al. [364]. The authors interpreted a high-temperature ( $\sim 430\text{K}$ ) desorption peak to be due to recombinative desorption of OH radicals producing  $\text{H}_2\text{O}$  from the surface. Because of the low-intensity of the thermal-desorption peak, it was suggested that water dissociates only on the defect sites. A convincing proof of  $\text{H}_2\text{O}$  dissociation on the oxygen vacancy sites, and lack of dissociation on the defect-free surface, was presented in the recent VT-STM studies by Schaub, et al. [365].

Wang et. al. [366, 367] proposed that water dissociation on oxygen vacancy sites is the basis for the UV-induced hydrophilicity of  $\text{TiO}_2$ .  $\text{TiO}_2$  surfaces are oleophilic and hydrophobic, i.e., water does not wet the surface but oil does. However, after a  $\text{TiO}_2$  sample is exposed to UV light, the contact angle of water droplets decreases dramatically. Storing such amphiphilic surfaces in the dark restores the hydrophobicity of the original surface. This effect was attributed to the creation of oxygen vacancies by UV-light that dissociate water and form microscopic hydrophilic domains on the surface [343]. To address the issue we studied the effect of UV-radiation on the  $\text{TiO}_2(110)-(1 \times 1)$  surface and found no evidence of defect formation. Therefore the validity of the of the vacancy-based explanation is arguable.

An alternative mechanism was proposed by White et. al [368]. The authors suggested that the UV-induced hydrophilicity is simply a consequence of photo-oxidation of organic compounds on the surface of  $\text{TiO}_2(110)$ . They observed *hydrophilic* behavior of a UHV clean  $\text{TiO}_2(110)$  surface and a hydrophobic behavior of the clean surface with a monolayer of trimethylacetate, which is a molecule with a saturated organic tail. Trimethylacetate could be easily removed from the surface by photooxidation using a UV-light source, restoring the surface hydrophilicity.

The mechanism of trimethylacetate photooxidation was further explained by Henderson et. al. [369]. It was proposed that the UV-generated holes react with the carboxylic group causing its dissociation, while the electrons are trapped by the 6-fold coordinated  $\text{Ti}^{4+}$  cations with reduction to the  $3+$  state. The bridging oxygen atoms are converted to bridging OH-groups in this

process which were directly observed by STM after the photo-oxidation reaction. Hydroxyl groups will certainly makes the surface hydrophilic. The photocatalytic origin of the UV-induced hydrophilicity of  $\text{TiO}_2$  was recently proven by direct measurements carried out in the Surface Science Center [370].

## **A.6 STM STUDY OF WATER ADSORPTION ON THE $\text{TiO}_2(110)-(1\times 2)$ SURFACE**

The photocatalytic properties of  $\text{TiO}_2$  [343], in which UV-irradiation induces hydrophilicity, make it a useful material for anti-fogging and self-cleaning coatings.  $\text{TiO}_2$  may be used for photochemical hydrogen production from water [339], and it was shown to be an effective biocompatible implant [371]. In these applications the surface properties of  $\text{TiO}_2$  towards water play an important role. While water chemistry  $\text{TiO}_2(110)-(1\times 1)$  surface is well-understood,  $\text{H}_2\text{O}$  adsorption on a less common  $\text{TiO}_2(110)-(1\times 2)$  surface (Fig. A.7) has received little attention [372, 373]. The  $\text{TiO}_2(110)-(1\times 2)$  surface is oxygen depleted, and it may be produced from the  $(1\times 1)$  surface by annealing in vacuum to 1200K.

Here the first STM study of water adsorption on the  $\text{TiO}_2(110)-(1\times 2)$  surface is presented. At 300K  $\text{H}_2\text{O}$  adsorbs preferentially on the crosslinks of the  $\text{TiO}_2(110)-(1\times 2)$  surface. Cooling down the surface to 110K during  $\text{H}_2\text{O}$  exposure results in adsorption on the crosslinks and the other surface sites, presumably the 5-fold coordinated Ti-atoms. The reaction products, observed as bright protrusions at positive sample bias, are attributed to hydroxyl groups due to  $\text{H}_2\text{O}$  dissociation. In addition, it was found that the UV-induced line-defects on the  $\text{TiO}_2(110)-(1\times 2)$  [374] surface do not interact with  $\text{H}_2\text{O}$  as seen by STM.

### **A.6.1 Experimental**

Experiments were conducted with a room temperature STM (Omicron) operating in UHV (background pressure  $<5.0\times 10^{-11}$  Torr). The  $\text{TiO}_2(110)-(1\times 2)$  reconstructed surface was formed after annealing the crystals at 1200 K for 45 minutes in UHV. Water used in the adsorption studies was purified using several freeze-pump-thaw cycles. In order to investigate the effect of

UV-induced defects [374] on water adsorption on the  $\text{TiO}_2(110)-(1\times 2)$  surface, the samples were irradiated with the full arc of a focused 500 W high pressure mercury lamp giving photon energies from 1.6 eV to 5.6 eV (Oriental Corporation, Model 66033) for 4 hours. This results in an average fraction of the surface covered by UV-induced defects of about 12%.

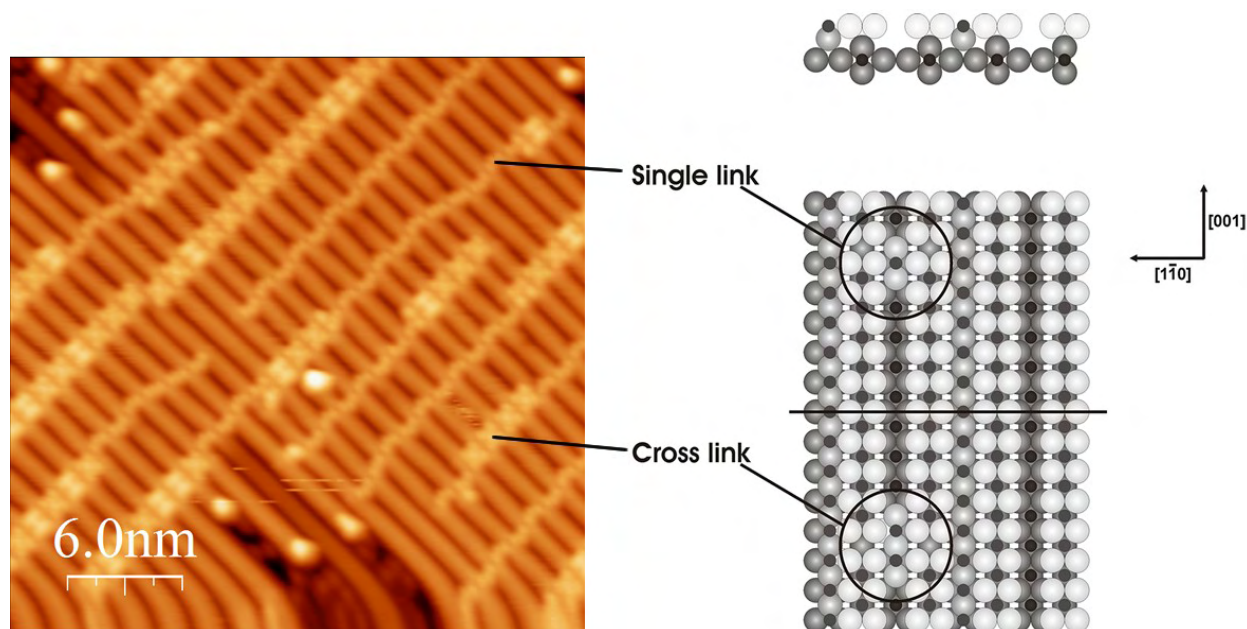


**Figure A.7.** The structure of the crosslinks on the  $\text{TiO}_2(110)-(1\times 2)$  surface. The STM image on the left was acquired at  $U=+3.2\text{V}$ ,  $I=0.040\text{ nA}$ . The model on the left is adopted from Ref. [352]. Small black circles correspond to Ti atoms, large grey circles correspond to O atoms. The correspondence between the grey shading and the type of O atom is shown in the cross section of the model.

## A.6.2 Results and Discussion

It's well known that water adsorbs both molecularly and dissociatively on the  $\text{TiO}_2(110)-(1\times 1)$  surface (Ref. [375] and references therein) below room temperature and at submonolayer coverages. Dissociation takes place on the bridging oxygen vacancies [365, 376]. When the surface is heated to room temperature, the molecular form of  $\text{H}_2\text{O}$  either desorbs, as evidenced by a TPD peak at 290K [363], or dissociates on the vacancy sites forming hydroxyl groups. The hydroxyl groups can desorb from the surface recombinatively, giving rise to a water desorption peak around 490K.

As a structural model for the  $\text{TiO}_2(110)-(1\times 2)$  surface reconstruction, we accept the added row model proposed by Pang *et al.* (Fig. A.6). Although the  $(1\times 2)$  reconstruction is

structurally rather different from the (1×1) phase, one should expect certain similarities in the behavior of water on these two surfaces [377].

Water adsorption was studied using two different experimental procedures. In the first procedure the surface was exposed to water at 300K, and successive STM images of the same surface area were recorded at different H<sub>2</sub>O exposures. In the second procedure the surface was cooled down to 110K before H<sub>2</sub>O exposure, and was brought back to 300K for imaging in STM; therefore, different regions of the surface were sampled by STM before and after adsorption in this case.

### **A.6.3 Adsorption of H<sub>2</sub>O on the TiO<sub>2</sub>(110)-(1×2) surface at 300K**

The empty-state image of the clean TiO<sub>2</sub>(110)-(1×2) surface is shown in Fig. A.7. The (1×2) structure is stabilized by linking [351]. Two kinds of links are observed – single links of V or inverted-V shape and double links, which are formed when the V and the inverted V single links merge [351]. The double links are commonly referred to as crosslinks due to their shape. The schematic model of the links is shown in Fig. A.7. The single links and the crosslinks consist of one and two coordinatively unsaturated Ti atoms in the trough, which originate from the neighboring string [359].

Figure A.8a shows the STM image of the TiO<sub>2</sub>(110)-(1×2) surface after 4-hour UV-irradiation in which a fluence of  $2.2 \times 10^{22}$  photons×cm<sup>-2</sup> was employed. The only substantial difference between the irradiated and the clean surface is a low coverage (~12%) of UV-induced line defects running in the <001> direction [374]. The defects appear as bright rows, which are darker than the unaffected <001> rows, and terminate at the crosslinks. The number of additional features on the surface that could be attributed to adsorption of residual gases during UV irradiation, including water, is negligible. Figures A.8(b-d) show the same surface area as in Figure A.8a after consecutive water exposures of 0.3L, 3L and 180L (1 L =  $1 \times 10^{-6}$  Torr·sec, using an uncorrected ionization gauge). The STM tip was retracted ~1μm away from the surface during dosing to prevent shadowing effects. After dosing, the tip was repositioned above the area on Fig. A.8a using a large surface defect in the center of the scanned frame as a reference point.

The most substantial change in the STM images, obtained after different H<sub>2</sub>O exposures, is the occurrence of bright protrusions (bumps) on the crosslinks with an apparent height of ~1Å

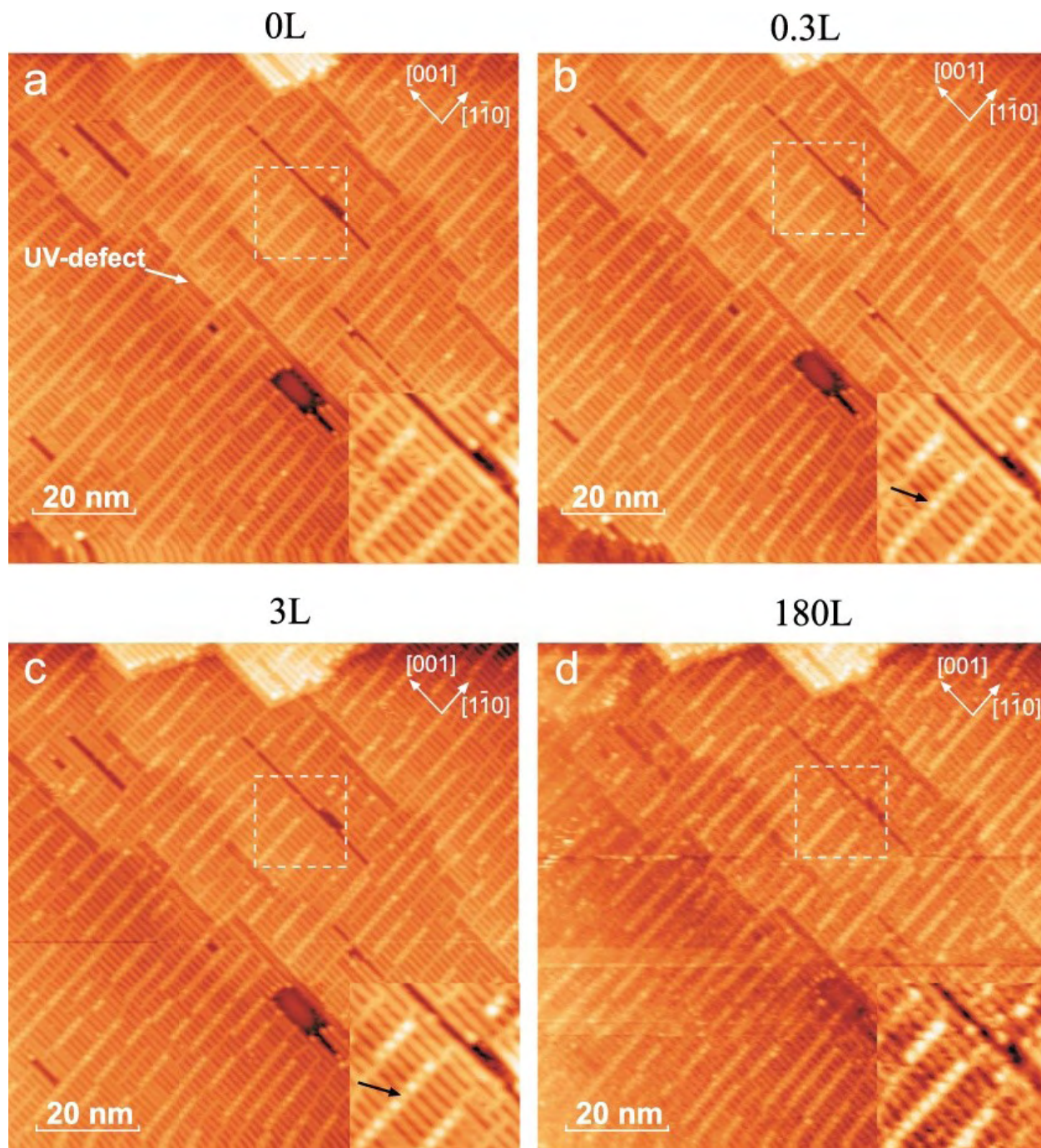


**Figure A.8.** STM images of the same  $100 \times 100 \text{ nm}^2$  area of the  $\text{TiO}_2(110)-(1 \times 2)$  surface after consecutive  $\text{H}_2\text{O}$  exposures at room temperature (scanning conditions for all images are  $U = 3.15 \text{ V}$ ,  $I = 0.035 \text{ nA}$ ): (a) clean surface after UV-irradiation before  $\text{H}_2\text{O}$  exposure (arrow points to a UV-induced line defect); (b), (c) and (d), surface after  $\text{H}_2\text{O}$  exposures of 0.3, 3 and 180 L correspondingly. The insets show the area within the dashed square. The black arrow in the insets (b) and (c) points to the same crosslink.

relative to the crosslinks (insets of Figs. A.8a-d). The number of the bumps gradually increases with H<sub>2</sub>O exposure. The saturation of the crosslinks by the bumps is observed at a H<sub>2</sub>O exposure of 3L (inset of Fig. A.8d). In addition, some of the bumps are frequently observed to move or disappear in subsequent scans (see the disappearing bump on the crosslink marked by an arrow on the insets of Figures 4.2b and 4.2c), most likely due to tip-induced motion.

The TPD spectrum of water on the TiO<sub>2</sub>(110)-(1×2) surface [377] has a desorption peak at 300K, which the authors assign to molecularly adsorbed water on the basis of modulated molecular beam measurements. Since the STM measurements were performed at ~300K, we should not expect the molecularly adsorbed water to be the predominant species on the surface in these conditions. On the basis of these arguments, the bright features on the crosslinks are tentatively assigned to hydroxyl species formed as a result of dissociative adsorption of H<sub>2</sub>O on these sites. The observed hopping of the bright features in the subsequent scans might be due to tip-induced diffusion or desorption. However, it should be mentioned that the structure of the TiO<sub>2</sub>(110)-(1×2) reconstructed surface is sensitive to the preparation conditions. It might occur that the molecular form of water can be bound to the crosslinking sites strongly enough to be present on the surface even at 300K and above. A controlled study with clear structural characterization and TPD, for example, would be required to resolve the issue. The preferential adsorption on the crosslinks is in accord with the recent study of adsorption of formic acid on the TiO<sub>2</sub>(110)-(1×2) surface [378], where a similar effect was observed.

The appearance of the bright <001> rows on the TiO<sub>2</sub>(110)-(1×2) surface at all H<sub>2</sub>O exposures remains largely unchanged, except at very large exposures when a small number of protrusions centered on the rows is observed (see below). The topology of the UV-induced defects does not undergo any noticeable changes after water exposures, indicating that these sites, unlike oxygen vacancies on TiO<sub>2</sub>(110)-(1×1) surface, are not active sites of water dissociation.

#### **A.6.4 Adsorption of H<sub>2</sub>O on the TiO<sub>2</sub>(110)-(1×2) surface at 110K**

Figure A.9 shows a room temperature STM image, which was obtained after exposing the UV-irradiated surface, cooled down to 110K, to 0.04L of water. Many crosslinks contain bright protrusions, indicating that Ti atoms in the crosslinks act as sites for water adsorption, as was

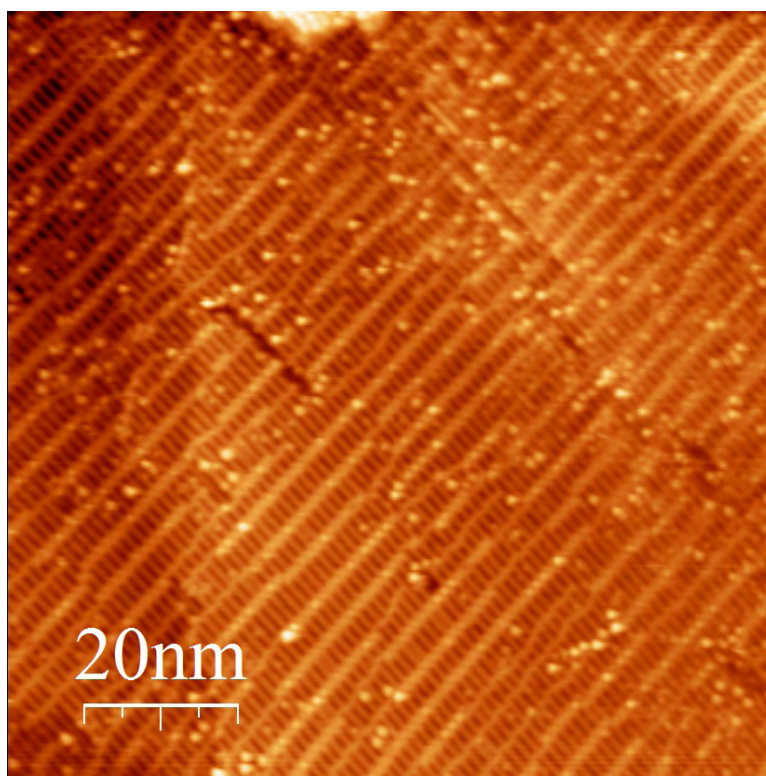


**Figure A.9.** A room temperature STM image taken after exposing a clean UV-irradiated surface to 0.04L of H<sub>2</sub>O at 110K. (size 100×100 nm<sup>2</sup>, U=+3.5 V, I=0.035 nA)

seen for H<sub>2</sub>O adsorption at 300K. However, in contrast to the case of adsorption at 300K, a number of bright protrusions are also observed on top of the bright <001> rows of the (1×2) phase. All of the new features can be separated into three major groups (Fig. A.10). Group I includes protrusions located on *either side* of the bright <001> row (inset (a) of Fig. A.10) with an apparent height of 1.2Å relative to the row. Group II includes protrusions *centered* on the <001> row with an apparent height of 2.0-2.2Å (inset (b) of Fig. A.10), and group III comprises bumps centered on the <001> row with an apparent height of 3.3-4.0Å (inset (c) of Fig. A.10).

Very few features are observed on the bright <001> rows when water is adsorbed at 300K even at exposures above 3L. We postulate that the large changes on the bright <001> rows when adsorption occurs at low exposures and at 110K may be due to efficient adsorption of H<sub>2</sub>O on the <001> rows below its desorption temperature, whereas adsorption on the rows at 300K, near the desorption temperature, is relatively inefficient. It is possible that on TiO<sub>2</sub>(110)-(1×2) surface water dissociation occurs via a molecular mobile precursor species. If the lifetime of this species at 300K is very short, little dissociation will be observed at low exposures used in these

experiments. On the other hand, there exists a temperature regime between 110K and 300K where the mobile precursor has long lifetime and H<sub>2</sub>O dissociation is facile.

### STM image of TiO<sub>2</sub>(110)-(1×2) surface after water adsorption at 110K

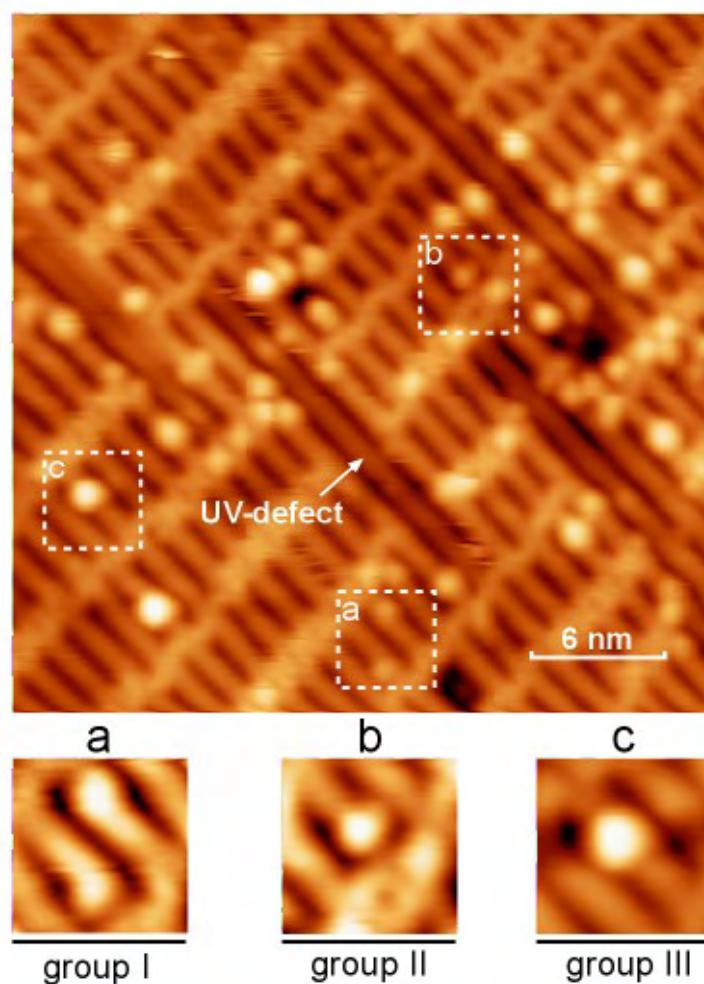


**Figure A.10.** A higher magnification STM image of the surface in Fig. A.9 (size 30×30 nm<sup>2</sup>, U=+3.5 V, I=0.035 nA). Shown in the insets are protrusions of group I (inset a), group II (inset b) and group III (inset c). Arrow points to the UV-induced line defect.

The assignment of the features observed in STM is not straightforward at this point. We expect that a majority of them are hydroxyl groups formed as a result of water dissociation.

According to the model of Pang et. al. [352] the added rows of the  $\text{TiO}_2(110)-(1 \times 2)$  surface consist of the 4 and 5-fold coordinated Ti atoms. It is also known that the 5-fold coordinated Ti atoms on the  $(1 \times 1)$  surface do not act as sites for water dissociation [372]. However, the 5-fold coordinated sites in the  $(1 \times 2)$  reconstructed surface are rather different from those in the  $(1 \times 1)$  surface. The oxygen atoms on the edges of the strands (Fig. A.6) are 2-fold coordinated rather than 3-fold coordinated in the  $(1 \times 1)$  surface, which makes them more reactive. In addition, preliminary DFT calculations show significant lattice relaxations in the  $(1 \times 2)$  strands, in which the 5-fold coordinated Ti atoms are depressed. All these factors make the 5-fold coordinated Ti-atom potentially more reactive site for water dissociation. Indeed, the calculations [379] show that water binds to these sites in the equilibrium geometry that favors formation of hydrogen bonds to the O-atoms on the edges.

#### **A.6.5 Conclusions**

We have shown that at 300K adsorption of water takes place preferentially on the crosslinks of the  $\text{TiO}_2(110)-(1 \times 2)$  surface. At 110K, adsorption of  $\text{H}_2\text{O}$  occurs at much lower exposures, and although the crosslinks are affected in the same way as at 300K, water is also observed to interact with other surface sites, namely those on the  $\langle 001 \rangle$  rows of the  $\text{TiO}_2(110)-(1 \times 2)$  surface. It is likely that dissociative chemisorption of water occurs on both the crosslinks and the  $\langle 001 \rangle$  row sites. In addition, we have not observed any evidence of interaction of the UV-induced defects on the  $\text{TiO}_2(110)-(1 \times 2)$  surface with  $\text{H}_2\text{O}$ , which is consistent with the previous assignment of the origin of these defects [374] to oxygen removal from the surface by UV-light, causing partial reduction of the  $\text{Ti}^{4+}$  ions. Little or no activity towards water dissociation in this case may be due to both geometric (e.g. absence of 2-fold coordinated O-atoms on the sides of the row) and electronic factors (more reduced state of Ti cations).

## APPENDIX B

### IMPROVED CRYSTAL GRINDING AND POLISHING HOLDER FOR METAL SINGLE CRYSTAL PREPARATION\*

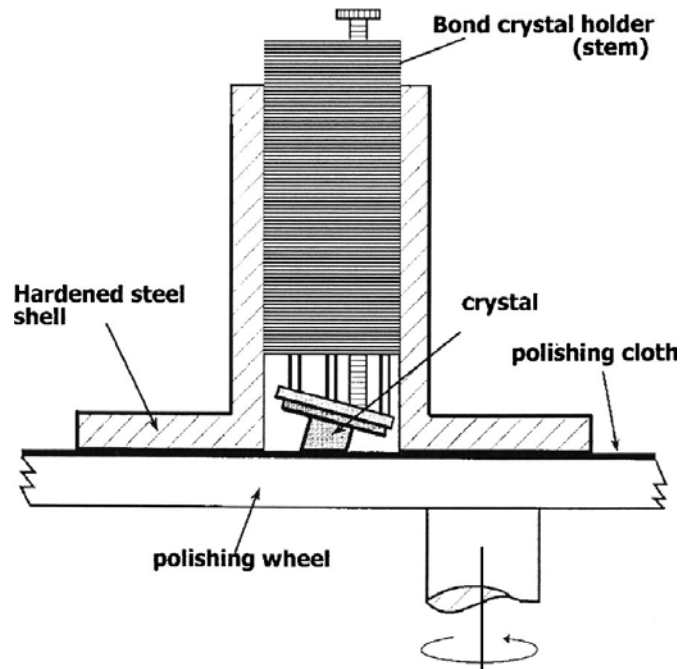
A mechanical holder for easy grinding and polishing of a single crystal on an automatic crystal polishing machine was designed and tested. The holder alleviates human involvement in the long periods of time commonly required to achieve optimal results. In a previous article [380] we reported on the surface flatness achieved using a manual grinding and polishing procedure on a horizontal rotary polishing wheel. It was found that 1.5-cm-diam single crystal disks of Pt could be ground and polished to give surfaces with 2–3  $\mu$ m radius. The degree of curvature was measured by observing Fizeau interference fringes [381] between the crystal surface and a quartz optical flat, using 546 nm light from a filtered mercury lamp. This article shows that equivalent results may be achieved by an automatic method using a new holding device. Crystal radii of the order of 3  $\mu$ m may be achieved minimizing the atomic step density due to crystal curvature.

Figure B.1 shows a Bond Barrel holder [382] with a single crystal cemented to its adjustable plate. The Bond Barrel crystal holder is free to move up and down in a hardened steel shell which provides a smooth sliding fit for the holder, so that the crystal face is pressed down by the holder weight as the grinding or polishing wheel moves. The bottom hardened steel face of

---

\*Reproduced with permission from: P. Maksymovych, T. Gasmire, S. Ohno, J. T. Yates, Jr., *Journal of Vacuum Science and Technology A* 23 (2005) 362. Copyright 2005 American Institute of Physics.

the shell is accurately perpendicular to the axis of the Bond Barrel holder. Commonly one applies force by hand to maintain smooth contact with the polishing cloth and its abrasive. Best results are achieved if the force is applied to the lower part of the hardened steel shell to prevent tipping.



**Figure B.1.** Schematic of crystal polishing equipment on a rotary polishing wheel. The crystal is glued to the adjustable plate of the Bond Barrel holder and oriented to the desired crystallographic direction using x-ray back reflection. The abrasive is supported on a cloth, which is attached to the polishing wheel.

An aluminum fixture to automatically grind and polish a crystal is shown in Fig. B.2. The fixture is designed to provide force at the base of the hardened steel shell. The fixture operates as a mechanical hand, and is connected to the shaft of the polishing machine, which may be set to oscillate with various periods and amplitudes as the polishing wheel turns. Three ball bearings make contact with the bottom circular section of the hardened steel shell, and the pressure exerted inwards by the bearings may be adjusted using sliders. We found in trials with other designs that it is essential for the force between the shaft and the steel shell to be applied low on the shell as in this design. As the polishing table rotates, the crystal holder will rotate inside the ball bearings, achieving isotropic polishing action on the crystal face.

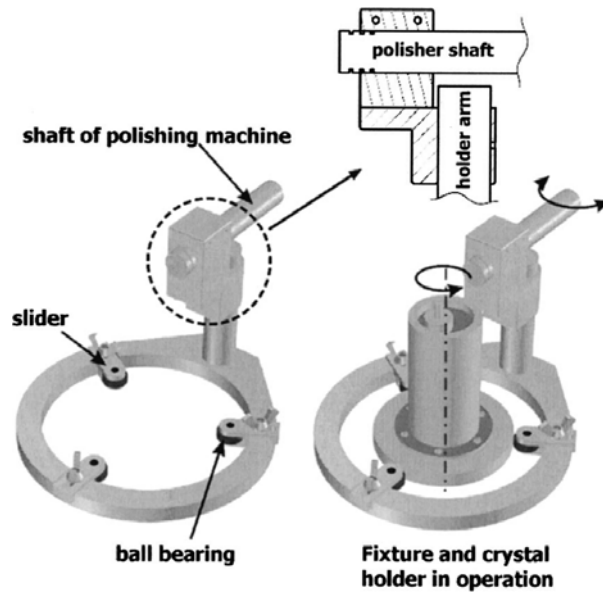


**Figure B.2.** Schematic drawing of the fixture for automatic crystal polishing with the Bond Barrel holder used to orient and hold the crystal.

The performance of the fixture was tested on an aluminum single crystal. The procedure was as follows: (1) fine grinding on SiC abrasive paper (320 grit) using tap water as lubricant; (2) rough polishing using a sequence of diamond pastes on separate Buehler fabric polishing cloths (9; 3; 1  $\mu\text{m}$  abrasive grain sizes) using lapping oil as lubricant; (3) final polishing using 0.05  $\mu\text{m}$  alumina in its suspension.

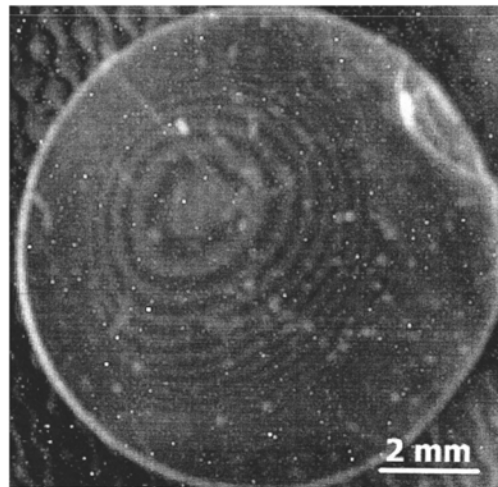


**Figure B.3.** Interference pattern for an Al crystal polished using the designed fixture,  $\lambda=546\text{ nm}$ .

The flatness of the crystal was measured using the procedure described in Ref. [380]. A photograph of the Fizeau interference pattern is given in Fig. B.3. A roughly spherical surface is observed. The average surface curvature, determined from the interference patterns, is measured in Fig. B.4, where the fringe spacings were averaged over three different directions across the pattern. We observe that the minimum radius near the center of the pattern is 3.4 m, and that as one moves away from the center of curvature the radius becomes larger.

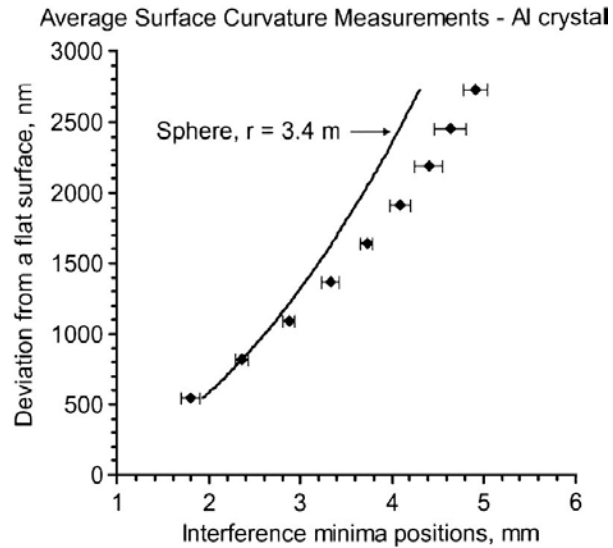


**Figure B.4.** Plot of air film thickness vs interference minima positions as determined from Fig. B-3. The error bars represent the standard deviation of the interference minima measurements along three different trajectories in Fig. B-3. The fitted curve around the 2 mm position corresponds to a 3.4 m radius, which increases to larger values as one moves toward the crystal edge.

If the goal is to minimize the average atomic step density caused by curvature of a single crystal, one may see from Fig. B.4 that in a distance of 4 mm across the crystal, the departure from flatness is about 2500 nm. This corresponds to one atomic step approximately every 2000 atom lengths across the crystal.

## BRIEF VITA

### Peter Maksymovych

Born: April 12, 1981

B.Sc., Kiev Taras Shevchenko University, 2001.

Ph. D. University of Pittsburgh, Pittsburgh, PA, USA, 2007.

#### Awards

Eugene P. Wigner Fellowship, Oak Ridge National Laboratory, Oak Ridge, TN, 2007

Morton M. Traum Award from the Surface Science Division of the American Vacuum Society – 2006.

Soros Scholarship – Kiev Taras Shevchenko University, Kiev, Ukraine – 1998.

#### Peer Review Publications

1. P. Maksymovych, D. C. Sorescu, J. T. Yates, Jr., “*Chain Reaction in a Molecular Self-Assembly on Metal Surface*”, in preparation for **Science**.
2. P. Maksymovych, J. T. Yates, Jr., “*Au-adatoms in the self-assembly of benzenethiol on the Au(111) surface*”, in preparation for **Journal of American Chemical Society**.
3. P. Maksymovych, D. C. Sorescu, J. T. Yates, Jr., “*Site-Selective Molecular Adsorption on the Herringbone Reconstruction: CO, CH<sub>3</sub>SH and CH<sub>3</sub>SSCH<sub>3</sub> molecules on Au(111)*”, in preparation for **Journal of Physical Chemistry C**.
4. P. Maksymovych, D. B. Dougherty, X.-Y. Zhu and J. T. Yates, “*Non-Local Dissociative Chemistry of Adsorbed Molecules Induced by Localized Electron-Injection into Metal Surfaces*”, **Physical Review Letters** in press.
5. P. Maksymovych, D. B. Dougherty, “*The Structure and Real-time Evolution of CH<sub>3</sub>SH Monolayer on the Au(111) Surface: Influence of Anisotropic Surface Lattice on Molecular Self-assembly*”, submitted to **Surface Science**.

6. D. B. Dougherty, P. Maksymovych, J. Lee, and J.T. Yates, Jr., “*Local Spectroscopy of Image Potential-Derived States: from Single Molecules to Monolayers of Benzene on Cu(111)*”, **Physical Review Letters** 97 (2006) 236806.
7. P. Maksymovych, D. C. Sorescu, J. T. Yates, Jr.: “*Gold Adatom-mediated Bonding in Self-assembled Short-chain Alkanethiolate Species on the Au(111) Surface*”, **Physical Review Letters**, 97 (2006) 146103. Also published in *Virtual Journal of Nanoscale Science & Technology*, vol. 14, Oct. 16 2006.
8. P. Maksymovych, D. C. Sorescu, J. T. Yates, Jr.: “*Methanethiolate Adsorption Site on Au(111): A Combined STM/DFT Study at the Single Molecule Level*”, **Journal of Physical Chemistry B** 110 (2006) 21161.
9. P. Maksymovych, J. T. Yates, Jr.: “*Propagation of Conformation in Surface-Aligned Dissociation of Single CH<sub>3</sub>SSCH<sub>3</sub> Molecules on Au(111)*”, **Journal of American Chemical Society**, 128 (2006) 10642.
10. D. B. Dougherty, P. Maksymovych, J. T. Yates, Jr.: “*Direct STM Evidence for Cu-Benzoate Surface Complexes on Cu(110)*”, **Surface Science**, 600 (2006) 4484.
11. P. Maksymovych, J. T. Yates, Jr.: “*Unexpected Formation of Spontaneous CO Clusters on the Au(111) Surface*”, **Chemical Physics Letters**, 421 (2006) 473.
12. T. Suzuki, P. Maksymovych, J. Levy, J. T. Yates, Jr.: “*Formation of carbon-induced dimer vacancy defects on Si(001)-2x1 by thermal decomposition of organic molecules-lack of dependence on the molecules' structure*”, **Surface Science** 600 (2006) 366.
13. P. Maksymovych, D. C. Sorescu, J. T. Yates, Jr.: “*Adsorption and Dynamics of CH<sub>3</sub>SH on Au(111)*”, **Journal of Physical Chemistry B**, 109 (2005) 22463; cover story.
14. I. Rzeznicka, J. Lee, P. Maksymovych, J. T. Yates, Jr.: “*Non-dissociative Chemisorption of Short Chain Alkanethiols on Au(111)*”, **Journal of Physical Chemistry B**, 109 (2005) 15992.
15. P. Maksymovych, T. Gasmire, S. Ohno, J. T. Yates, Jr.: “*Improved Crystal Grinding and Polishing Holder for Metal Single Crystal Preparations*”, **Journal of Vacuum Science & Technology A**, 23 (2005) 362.
16. P. Maksymovych, S. Mezhenny, J. T. Yates, Jr.: “*STM Study of Water Adsorption on the TiO<sub>2</sub>(110)-(1x2) surface*”, **Chemical Physics Letters**, 382 (2003) 270.
17. L. Thompson, J. G. Lee, P. Maksymovych, J. Ahner, J. T. Yates, Jr.: “*Construction and Performance of an Ultrahigh Vacuum-compatible High Temperature Vapor Dosing System for Low Vapor Pressure Compounds*”, **Journal of Vacuum Science & Technology A**, 21 (2003) 491.
18. S. Mezhenny, P. Maksymovych, T. L. Thompson, O. Diwald, D. Stahl, S. D. Walck, J. T. Yates, Jr.: “*STM Studies of Defect Production on the TiO<sub>2</sub>(110)-(1x1) and TiO<sub>2</sub>(110)-(1x2) Surfaces Induced by UV Irradiation*”, **Chemical Physics Letters**, 369 (2003) 152.

19. S. Mezhenny, D. C. Sorescu, P. Maksymovych, J. T. Yates, Jr.: “*Dissociation of CH<sub>3</sub>I on the Al(111) surface - An STM and Density Functional Theory Study*”, **Journal of the American Chemical Society**, 124 (2002) 14202.
20. J. G. Lee, J. Ahner, P. Maksymovych, J. T. Yates, Jr.: “Molecular triangulation - finding the conformation of adsorbed self-assembled organic monolayers”, **Chemical Physics Letters** 340 (2001) 21-25.

## BIBLIOGRAPHY

- [1] G. Binnig, H. Rohrer, C. Gerber, and E. Weibel, *Physical Review Letters* **49**, 57 (1982).
- [2] G. Binnig, H. Rohrer, C. Gerber, and E. Weibel, *Physical Review Letters* **50**, 120 (1983).
- [3] G. Binnig, and H. Rohrer, *IBM Journal of Research and Development* **44**, 279 (2000).
- [4] G. Binnig, and H. Rohrer, *Reviews of Modern Physics* **59**, 615 (1987).
- [5] J. A. Stroscio, and W. J. Kaiser, *Scanning Tunneling Microscopy (Experimental Methods in the Physical Sciences)* (Academic Press, 1994).
- [6] T. Jung, Y. W. Mo, and F. J. Himpsel, *Physical Review Letters* **74**, 1641 (1995).
- [7] R. M. Feenstra, J. Y. Lee, M. H. Kang, G. Meyer, and K. H. Rieder, *Physical Review B* **73** (2006).
- [8] L. Burgi, H. Brune, O. Jeandupeux, and K. Kern, *Journal of Electron Spectroscopy and Related Phenomena* **109**, 33 (2000).
- [9] P. Wahl, L. Diekhoner, G. Wittich, L. Vitali, M. A. Schneider, and K. Kern, *Physical Review Letters* **95**, 166601 (2005).
- [10] R. Wolkow, and P. Avouris, *Physical Review Letters* **60**, 1049 (1988).
- [11] W. Ho, *Journal of Chemical Physics* **117**, 11033 (2002).
- [12] S. Titmuss, A. Wander, and D. A. King, *Chemical Reviews* **96**, 1291 (1996).
- [13] J. V. Lauritsen, and F. Besenbacher, *Advances in Catalysis* **50**, 97 (2006).
- [14] K. Morgenstern, *Physica Status Solidi B-Basic Solid State Physics* **242**, 773 (2005).
- [15] F. Schreiber, *Progress in Surface Science* **65**, 151 (2000).
- [16] J. C. Love, L. A. Estroff, J. K. Kriebel, R. G. Nuzzo, and G. M. Whitesides, *Chemical Reviews* **105**, 1103 (2005).
- [17] N. Lorente, R. Rurali, and H. Tang, *Journal of Physics-Condensed Matter* **17**, S1049 (2005).

- [18] C. H. Jiyun, *Smart Materials and Structures* **12**, 264 (2003).
- [19] V. Humblot, S. M. Barlow, and R. Raval, *Progress In Surface Science* **76**, 1 (2004).
- [20] G. M. Whitesides, and B. Grzybowski, *Science* **295**, 2418 (2002).
- [21] S. Stepanow, M. Lingenfelder, A. Dmitriev, H. Spillmann, E. Delvigne, N. Lin, X. B. Deng, C. Z. Cai, J. V. Barth, and K. Kern, *Nature Materials* **3**, 229 (2004).
- [22] C. Vericat, M. E. Vela, G. A. Benitez, J. A. M. Gago, X. Torrelles, and R. C. Salvarezza, *Journal of Physics-Condensed Matter* **18**, R867 (2006).
- [23] C. Vericat, M. E. Vela, and R. C. Salvarezza, *Physical Chemistry Chemical Physics* **7**, 3258 (2005).
- [24] J. Mathiyarasu, S. S. Pathak, and V. Yegnaraman, *Corrosion Reviews* **24**, 307 (2006).
- [25] D. J. Fuchs, and P. S. Weiss, *Nanotechnology* **18**, 044021 (2007).
- [26] M. T. Cygan, T. D. Dunbar, J. J. Arnold, L. A. Bumm, N. F. Shedlock, T. P. Burgin, L. Jones, D. L. Allara, J. M. Tour, and P. S. Weiss, *Journal of the American Chemical Society* **120**, 2721 (1998).
- [27] S. Hong, R. Reifengerger, W. Tian, S. Datta, J. I. Henderson, and C. P. Kubiak, *Superlattices and Microstructures* **28**, 289 (2000).
- [28] L. A. Bumm, J. J. Arnold, M. T. Cygan, T. D. Dunbar, T. P. Burgin, L. Jones, D. L. Allara, J. M. Tour, and P. S. Weiss, *Science* **271**, 1705 (1996).
- [29] R. L. McCreery, *Chemistry of Materials* **16**, 4477 (2004).
- [30] M. E. Anderson, C. Srinivasan, J. N. Hohman, E. M. Carter, M. W. Horn, and P. S. Weiss, *Advanced Materials* **18**, 3258 (2006).
- [31] T. Ishida, N. Choi, W. Mizutani, H. Tokumoto, I. Kojima, H. Azebara, H. Hokari, U. Akiba, and M. Fujihira, *Langmuir* **15**, 6799 (1999).
- [32] C. D. Lindstrom, M. Muntwiler, and X. Y. Zhu, *Journal of Physical Chemistry B* **109**, 21492 (2005).
- [33] X. Y. Zhu, *Surface Science Reports* **56**, 1 (2004).
- [34] P. Fenter, P. Eisenberger, and K. S. Liang, *Physical Review Letters* **70**, 2447 (1993).
- [35] X. Torrelles, C. Vericat, M. E. Vela, M. H. Fonticelli, M. A. D. Millone, R. Felici, T. L. Lee, J. Zegenhagen, G. Munoz, J. A. Martin-Gago, and R. C. Salvarezza, *Journal Of Physical Chemistry B* **110**, 5586 (2006).

- [36] G. S. Parkinson, A. Hentz, P. D. Quinn, A. J. Window, D. P. Woodruff, P. Bailey, and T. C. Q. Noakes, *Surface Science* **601**, 50 (2007).
- [37] M. Yu, N. Bovet, C. J. Satterley, S. Bengio, K. R. J. Lovelock, P. K. Milligan, R. G. Jones, D. P. Woodruff, and V. Dhanak, *Physical Review Letters* **97**, 166102 (2006).
- [38] F. Thery-Merland, C. Methivier, E. Pasquinet, L. Hairault, and C. M. Pradier, *Sensors and Actuators B-Chemical* **114**, 223 (2006).
- [39] X. M. Ding, K. Moumanis, J. J. Dubowski, L. Tay, and N. L. Rowell, *Journal of Applied Physics* **99**, 054701 (2006).
- [40] M. Zharnikov, and M. Grunze, *Journal of Physics-Condensed Matter* **13**, 11333 (2001).
- [41] C. S. C. Yang, L. J. Richter, J. C. Stephenson, and K. A. Briggman, *Langmuir* **18**, 7549 (2002).
- [42] N. Camillone, T. Y. B. Leung, P. Schwartz, P. Eisenberger, and G. Scoles, *Langmuir* **12**, 2737 (1996).
- [43] S. B. Darling, A. W. Rosenbaum, Y. Wang, and S. J. Sibener, *Langmuir* **18**, 7462 (2002).
- [44] I. I. Rzezinicka, J. S. Lee, P. Maksymovych, and J. T. Yates, Jr., *Journal of Physical Chemistry B* **109**, 15992 (2005).
- [45] T. H. Lin, T. P. Huang, Y. L. Liu, C. C. Yeh, Y. H. Lai, and W. H. Hung, *Journal of Physical Chemistry B* **109**, 14079 (2005).
- [46] R. G. Nuzzo, B. R. Zegariski, and L. H. Dubois, *Journal of the American Chemical Society* **109**, 733 (1987).
- [47] P. Maksymovych, D. C. Sorescu, and J. T. Yates, Jr., *Physical Review Letters* **97**, 146103 (2006).
- [48] G. E. Poirier, *Chemical Reviews* **97**, 1117 (1997).
- [49] G. E. Poirier, *Langmuir* **15**, 1167 (1999).
- [50] H. Kondoh, M. Iwasaki, T. Shimada, K. Amemiya, T. Yokoyama, T. Ohta, M. Shimomura, and S. Kono, *Physical Review Letters* **90**, 066102 (2003).
- [51] D. P. Woodruff, *Surface Science Reports* **62**, 1 (2007).
- [52] D. P. Woodruff, *Reports on Progress in Physics* **68**, 743 (2005).
- [53] R. Mazzarello, A. Cossaro, A. Verdini, R. Rousseau, L. Casalis, M. F. Danisman, L. Floreano, S. Scandolo, A. Morgante, and G. Scoles, *Physical Review Letters* **98**, 016102 (2007).

- [54] G. E. Poirier, and E. D. Pylant, *Science* **272**, 1145 (1996).
- [55] G. E. Poirier, *Langmuir* **13**, 2019 (1997).
- [56] J. V. Barth, H. Brune, G. Ertl, and R. J. Behm, *Phys. Rev. B.* **42**, 9307 (1990).
- [57] W. P. Fitts, J. M. White, and G. E. Poirier, *Langmuir* **18**, 2096 (2002).
- [58] M. Toerker, R. Staub, T. Fritz, T. Schmitz-Hubsch, F. Sellam, and K. Leo, *Surface Science* **445**, 100 (2000).
- [59] R. Staub, M. Toerker, T. Fritz, T. Schmitz-Hubsch, F. Sellam, and K. Leo, *Langmuir* **14**, 6693 (1998).
- [60] L. H. Dubois, and R. G. Nuzzo, *Annual Review of Physical Chemistry* **43**, 437 (1992).
- [61] S. H. Ke, H. U. Baranger, and W. T. Yang, *Journal of the American Chemical Society* **126**, 15897 (2004).
- [62] D. Q. Andrews, R. Cohen, R. P. Van Duyne, and M. A. Ratner, *Journal of Chemical Physics* **125**, 174718 (2006).
- [63] Y. Q. Xue, and M. A. Ratner, *Physical Review B* **69**, 085403 (2004).
- [64] J. Gottschalck, and B. Hammer, *Journal of Chemical Physics* **116**, 784 (2002).
- [65] Y. Yourdshahyan, and A. M. Rappe, *Journal of Chemical Physics* **117**, 825 (2002).
- [66] F. P. Cometto, P. Paredes-Olivera, V. A. Macagno, and E. M. Patrito, *Journal Of Physical Chemistry B* **109**, 21737 (2005).
- [67] P. Maksymovych, D. C. Sorescu, and J. T. Yates, Jr., *Journal of Physical Chemistry B* **110**, 21161 (2006).
- [68] T. Shimada, H. Kondoh, I. Nakai, M. Nagasaka, R. Yokota, K. Amemiya, and T. Ohta, *Chemical Physics Letters* **406**, 232 (2005).
- [69] M. G. Roper, M. P. Skegg, C. J. Fisher, J. J. Lee, V. R. Dhanak, D. P. Woodruff, and R. G. Jones, *Chem. Phys. Lett.* **389**, 87 (2004).
- [70] M. Gruebele, and R. Bigwood, *International Reviews in Physical Chemistry* **17**, 91 (1998).
- [71] D. Menzel, and R. Gomer, *Journal of Chemical Physics* **41**, 3311 (1964).
- [72] P. Readhead, *Canadian Journal of Physics* **42**, 886 (1964).
- [73] P. Feulner, D. Menzel, H. L. Dai, and W. Ho, *Laser spectroscopy and photochemistry on metal surfaces* (World Scientific, River Edge, NJ, 1995).

- [74] R. Treichler, W. Wurth, E. Riedl, P. Feulner, and D. Menzel, *Chemical Physics* **153**, 259 (1991).
- [75] J. G. Lee, J. Ahner, P. Maksymovych, and J. T. Yates, Jr., *Chemical Physics Letters* **340**, 21 (2001).
- [76] P. R. Antoniewicz, *Physical Review B* **21**, 3811 (1980).
- [77] H. Guo, P. Saalfrank, and T. Seideman, *Progress in Surface Science* **62**, 239 (1999).
- [78] A. J. Mayne, G. Dujardin, G. Comtet, and D. Riedel, *Chemical Reviews* **106**, 4355 (2006).
- [79] R. S. Becker, G. S. Higashi, Y. J. Chabal, and A. J. Becker, *Physical Review Letters* **65**, 1917 (1990).
- [80] E. T. Foley, A. F. Kam, J. W. Lyding, and P. Avouris, *Physical Review Letters* **80**, 1336 (1998).
- [81] B. C. Stipe, M. A. Rezaei, W. Ho, S. Gao, M. Persson, and B. I. Lundqvist, *Physical Review Letters* **78**, 4410 (1997).
- [82] J. I. Pascual, *European Physical Journal D* **35**, 327 (2005).
- [83] I. R. McNab, and J. C. Polanyi, *Chemical Reviews* **106**, 4321 (2006).
- [84] H. J. Lee, and W. Ho, *Science* **286**, 1719 (1999).
- [85] J. R. Hahn, and W. Ho, *Physical Review Letters* **87**, 166102 (2001).
- [86] L. J. Lauhon, and W. Ho, *Faraday Discussions* **117**, 249 (2000).
- [87] S. W. Hla, and K. H. Rieder, *Annual Review of Physical Chemistry* **54**, 307 (2003).
- [88] L. J. Lauhon, and W. Ho, *Physical Review Letters* **85**, 4566 (2000).
- [89] A. J. Heinrich, C. P. Lutz, J. A. Gupta, and D. M. Eigler, *Science* **298**, 1381 (2002).
- [90] J. I. Pascual, N. Lorente, Z. Song, H. Conrad, and H. P. Rust, *Nature* **423**, 525 (2003).
- [91] M. Lastapis, M. Martin, D. Riedel, L. Hellner, G. Comtet, and G. Dujardin, *Science* **308**, 1000 (2005).
- [92] B. V. Rao, K.-Y. Kwon, A. Liu, and L. Bartels, *Proceedings of National Academy of Sciences* **101**, 17920 (2004).
- [93] M. Cranney, A. J. Mayne, A. Laikhtman, G. Comtet, and G. Dujardin, *Surface Science* **593**, 139 (2005).
- [94] R. Otero, F. Rosei, and F. Besenbacher, *Annual Review of Physical Chemistry* **57**, 497 (2006).

- [95] F. Chiaravalloti, L. Gross, K. H. Rieder, S. M. Stojkovic, A. Gourdon, C. Joachim, and F. Moresco, *Nature Materials* **6**, 30 (2007).
- [96] C. E. Tripa, and J. T. Yates, Jr., *Nature* **398**, 591 (1999).
- [97] H. Bulou, and C. Goyhenex, *Physical Review B* **65**, 045407 (2002).
- [98] C. B. Carter, and R. Q. Hwang, *Physical Review B* **51**, 4730 (1995).
- [99] K. Thurmer, C. B. Carter, N. C. Bartelt, and R. Q. Hwang, *Physical Review Letters* **92**, 106101 (2004).
- [100] J. P. Hirth, and J. Lothe, *Theory of Dislocations* (Krieger, Malabar, FL, 1992).
- [101] F. C. Frank, *Physica - Amsterdam* **15**, 131 (1949).
- [102] S. Narasimhan, and D. Vanderbilt, *Physical Review Letters* **69**, 1564 (1992).
- [103] C. Wöll, S. Chiang, R. J. Wilson, and P. H. Lippel, *Physical Review B* **39**, 7988 (1989).
- [104] I. D. B. J. A. Meyer, E. Kopatzki, R. J. Behm, *Surface Science Letters* **365**, L647 (1996).
- [105] S. M. Driver, T. F. Zhang, and D. A. King, *Angewandte Chemie-International Edition* **46**, 700 (2007).
- [106] S. G. Davison, and M. Steslicka, *Basic Theory of Surface States* (Oxford University Press, New York, 1992).
- [107] C. J. Chen, *Introduction to Scanning Tunneling Microscopy* (Oxford University Press, New York, 1993).
- [108] S. Elliott, *The Physics and Chemistry of Solids* (John Wiley & Sons, West Sussex, 1998).
- [109] J. Repp, F. Moresco, G. Meyer, K.-H. Rieder, P. Hyldgaard, and M. Persson, *Physical Review Letters* **85**, 2981 (2000).
- [110] N. Memmel, and E. Bertel, *Physical Review Letters* **75**, 485 (1995).
- [111] S. Lukas, G. Witte, and C. Wöll, *Physical Review Letters* **88**, 028301 (2001).
- [112] G. A. Mulhollan, K. Garrison, and J. L. Erskine, *Physical Review Letters* **69**, 3240 (1992).
- [113] L. Guillemot, and V. A. Esaulov, *Physical Review Letters* **82**, 4552 (1999).
- [114] L. Burgi, O. Jeandupeux, A. Hirstein, H. Brune, and K. Kern, *Physical Review Letters* **81**, 5370 (1998).
- [115] S. Shiraki, H. Fujisawa, M. Nantoh, and M. Kawai, *Physical Review Letters* **92**, 096102 (2004).
- [116] I. E. Tamm, *Z. Phys.* **76**, 849 (1932).

- [117] I. E. Tamm, Phys. Z. Sowjet **1**, 733 (1932).
- [118] R. Matzdorf, Surface Science Reports **30**, 153 (1998).
- [119] L. C. Davis, M. P. Everson, R. C. Jaklevic, and W. Shen, Physical Review B **43**, 3821 (1991).
- [120] Y. Hasegawa, and P. Avouris, Physical Review Letters **71**, 1071 (1993).
- [121] J. Kliewer, R. Berndt, E. V. Chulkov, V. M. Silkin, P. M. Echenique, and S. Crampin, Science **288**, 1399 (2000).
- [122] D. P. Woodruff, W. A. Royer, and N. V. Smith, Physical Review B **34**, 764 (1986).
- [123] P. Avouris, I. W. Lyo, and P. Molinas-Mata, Chemical Physics Letters **240**, 423 (1995).
- [124] T. Jamneala, V. Madhavan, W. Chen, and M. F. Crommie, Physical Review B **61**, 9990 (2000).
- [125] N. Nilius, T. M. Wallis, and W. Ho, Science **297**, 1853 (2002).
- [126] C. P. Lutz, and D. M. Eigler, Nature **363**, 524 (1993).
- [127] L. Burgi, Ph. D. thesis, EPFL, Switzerland, 1999).
- [128] L. Burgi, H. Brune, and K. Kern, Physical Review Letters **89**, 176801 (2002).
- [129] L. Burgi, L. Petersen, H. Brune, and K. Kern, Surface Science **447**, L157 (2000).
- [130] L. Burgi, O. Jeandupeux, H. Brune, and K. Kern, Physical Review Letters **82**, 4516 (1999).
- [131] F. J. Garcia-Vidal, P. L. de Andres, and F. Flores, Physical Review Letters **76**, 807 (1996).
- [132] K. Reuter, P. L. de Andres, F. J. Garcia-Vidal, D. Sestovic, F. Flores, and K. Heinz, Physical Review B **58**, 14036 (1998).
- [133] S. Datta, *Electronic Transport in Mesoscopic Systems* (Cambridge University Press, Cambridge, 1995).
- [134] G. Grimvall, *The Electron-Phonon Interaction in Metals* (Benjamin, New York, 1981).
- [135] L. Esaki, Reviews of Modern Physics **46**, 237 (1974).
- [136] I. Giaever, Reviews of Modern Physics **46**, 245 (1974).
- [137] R. Young, J. Ward, and F. Scire, Physical Review Letters **27**, 922 (1971).
- [138] T. v. Hofe, Ph. D. thesis, University of Kiel, Germany (2005).
- [139] J. Bardeen, Physical Review Letters **6**, 57 (1961).
- [140] J. Tersoff, and D. R. Hamann, Physical Review Letters **50**, 1998 (1983).

- [141] J. Tersoff, and D. R. Hamann, *Physical Review B* **31**, 805 (1985).
- [142] L. V. Keldysh, *Sov. Phys. JETP* **20**, 1018 (1965).
- [143] J. Cerdá, M. A. Van Hove, P. Sautet, and M. Salmeron, *Physical Review B* **56**, 15885 (1997).
- [144] C. Rogero, J. A. Martin-Gago, and J. I. Cerda, *Physical Review B* **74**, 121404 (2006).
- [145] C. I. Carlisle, D. A. King, M. L. Bocquet, J. Cerda, and P. Sautet, *Physical Review Letters* **84**, 3899 (2000).
- [146] S. Corbel, J. Cerda, and P. Sautet, *Physical Review B* **60**, 1989 (1999).
- [147] J. Cerda, M. A. Van Hove, P. Sautet, and M. Salmeron, *Surface Science* **409**, 145 (1998).
- [148] N. D. Lang, *Physical Review Letters* **56**, 1164 (1986).
- [149] N. D. Lang, *Physical Review Letters* **58**, 45 (1987).
- [150] S. Mezhenny, D. C. Sorescu, P. Maksymovych, and J. T. Yates, Jr., *Journal of the American Chemical Society* **124**, 14202 (2002).
- [151] G. V. Nazin, X. H. Qiu, and W. Ho, *Science* **302**, 77 (2003).
- [152] M. Roth, M. Weinelt, T. Fauster, P. Wahl, M. A. Schneider, L. Diekhoner, and K. Kern, *Applied Physics a-Materials Science & Processing* **78**, 155 (2004).
- [153] D. B. Dougherty, P. Maksymovych, J. Lee, and J. T. Yates, *Physical Review Letters* **97**, 236806 (2006).
- [154] M. Liu, D. B. Dougherty, J. Lee, and H. Petek, private communication.
- [155] M. K. S. Katano, private communication.
- [156] L. Thompson, J. G. Lee, P. Maksymovych, J. Ahner, and J. T. Yates, Jr., *Journal of Vacuum Science & Technology A* **21**, 491 (2003).
- [157] A. J. Melmed, *Journal of Vacuum Science & Technology B* **9**, 601 (1991).
- [158] O. L. Guise, J. W. Ahner, M. C. Jung, P. C. Goughnour, and J. T. Yates, Jr., *Nano Letters* **2**, 191 (2002).
- [159] S. Mezhenny, Ph. D. thesis, University of Pittsburgh (2003).
- [160] V. A. Ukraintsev, and J. T. Yates, Jr., *Surface Science* **346**, 31 (1996).
- [161] L. Olesen, E. Laegsgaard, I. Stensgaard, F. Besenbacher, J. Schiøtz, P. Stoltze, K. W. Jacobsen, and J. K. Nørskov, *Physical Review Letters* **72**, 2251 (1994).
- [162] L. Bartels, G. Meyer, and K. H. Rieder, *Applied Physics Letters* **71**, 213 (1997).
- [163] E. Niemi, and J. Nieminen, *Chemical Physics Letters* **397**, 200 (2004).

- [164] J. Clavilier, R. Faure, G. Guinet, and R. Durand, *Journal of Electroanalytical Chemistry* **107**, 205 (1979).
- [165] B. Voigtlander, U. Linke, H. Stollwerk, and J. Brona, *Journal of Vacuum Science & Technology A: Vacuum, Surfaces, and Films* **23**, 1535 (2005).
- [166] P. Maksymovych, D. C. Sorescu, D. B. Dougherty, and J. T. Yates, Jr., *Journal of Physical Chemistry B* **109**, 22463 (2005).
- [167] M. Schmid, W. Hebenstreit, P. Varga, and S. Crampin, *Physical Review Letters* **76**, 2298 (1996).
- [168] J. U. Kliewer, Ph. D. Thesis, University of Aachen (2000).
- [169] J. G. Zhou, and F. Hagelberg, *Physical Review Letters* **97**, 045505 (2006).
- [170] G. Kresse, and J. Furthmüller, *Physical Review B* **54**, 11169 (1996).
- [171] P. E. Blochl, *Physical Review B* **50**, 17953 (1994).
- [172] G. Kresse, and D. Joubert, *Physical Review B* **59**, 1758 (1999).
- [173] J. P. Perdew, and Y. Wang, *Physical Review B* **45**, 13244 (1992).
- [174] H. J. Monkhorst, and J. D. Pack, *Physical Review B* **13**, 5188 (1976).
- [175] M. Methfessel, and A. T. Paxton, *Physical Review B* **40**, 3616 (1989).
- [176] W. Andreoni, A. Curioni, and H. Gronbeck, *International Journal of Quantum Chemistry* **80**, 598 (2000).
- [177] Y. Morikawa, T. Hayashi, C. C. Liew, and H. Nozoye, *Surface Science* **46**, 507 (2002).
- [178] B. V. Rao, K. Y. Kwon, A. W. Liu, and L. Bartels, *Journal of Chemical Physics* **119**, 10879 (2003).
- [179] G. Mills, H. Jonsson, and G. K. Schenter, *Surface Science* **324**, 305 (1995).
- [180] G. Mills, and H. Jonsson, *Physical Review Letters* **72**, 1124 (1994).
- [181] M. Brandbyge, J.-L. Mozos, P. Ordejón, J. Taylor, and K. Stokbro, *Physical Review B* **65**, 165401 (2002).
- [182] G. S. Kottas, L. I. Clarke, D. Horinek, and J. Michl, *Chemical Reviews* **105**, 1281 (2005).
- [183] J. S. Koehler, and D. M. Dennison, *Physical Review* **57**, 1006 (1940).
- [184] M. D. Alvey, K. J. Uram, and J. T. Yates, Jr., *Journal of Chemical Physics* **87**, 7221 (1987).
- [185] P. Atkins, and R. Friedman, *Molecular Quantum Mechanics* (Oxford University Press, New York, 2005).

- [186] J. Smoliner, D. Rakoczy, and M. Kast, *Reports on Progress in Physics* **67**, 1863 (2004).
- [187] H. Over, *Prog. Surface Science* **58**, 249 (1998).
- [188] D. C. Meier, V. Bukhtiyarov, and A. W. Goodman, *Journal of Physical Chemistry B* **107**, 12668 (2003).
- [189] H. J. Zhai, and L. S. Wang, *Journal of Chemical Physics* **122** (2005).
- [190] M. Gajdos, A. Eichler, and J. Hafner, *Journal of Physics-Condensed Matter* **16**, 1141 (2004).
- [191] M. Valden, X. Lai, and D. W. Goodman, *Science* **281**, 1647 (1998).
- [192] M. Haruta, *Catalysis Today* **36**, 153 (1997).
- [193] P. J. Feibelman, B. Hammer, J. K. Norskov, F. Wagner, M. Scheffler, R. Stumpf, R. Watwe, and J. Dumesic, *Journal of Physical Chemistry B* **105**, 4018 (2001).
- [194] M. K. Rose, T. Mitsui, J. Dunphy, A. Borg, D. F. Ogletree, M. Salmeron, and P. Sautet, *Surface Science* **512**, 48 (2002).
- [195] R. Brako, and D. Sokcevic, *Surface Science* **469**, 185 (2000).
- [196] J. A. Steckel, A. Eichler, and J. Hafner, *Physical Review B* **68**, 085416 (2003).
- [197] L. Bartels, G. Meyer, and K.-H. Rieder, *Surf. Sci.* **432**, L621 (1999).
- [198] L. Piccolo, D. Loffreda, F. Aires, C. Deranlot, Y. Jugnet, P. Sautet, and J. C. Bertolini, *Surface Science* **566**, 995 (2004).
- [199] C. H. Shue, L. Y. O. Yang, S. L. Yau, and K. Itaya, *Langmuir* **21**, 1942 (2005).
- [200] M. Kulawik, H. P. Rust, N. Nilus, M. Heyde, and H. J. Freund, *Physical Review B* **71** (2005).
- [201] G. Meyer, J. Repp, S. Zöphel, K.-F. Braun, S. W. Hla, S. Fölsch, L. Bartels, F. Moresco, and K. H. Rieder, *Single Molecules* **1**, 79 (2000).
- [202] L. Bartels, G. Meyer, K. H. Rieder, D. Velic, E. Knoesel, A. Hotzel, M. Wolf, and G. Ertl, *Physical Review Letters* **80**, 2004 (1998).
- [203] G. Witte, *Surface Science* **502-503**, 405 (2002).
- [204] E. J. Moler, S. A. Kellar, W. R. A. Huff, Z. Hussain, Y. F. Chen, and D. A. Shirley, *Physical Review B* **54**, 10862 (1996).
- [205] M. Mavrikakis, B. Hammer, and J. K. Norskov, *Physical Review Letters* **81**, 2819 (1998).
- [206] A. Van der Pol, A. Van der Avoird, and P. E. S. Wormer, *Journal of Chemical Physics* **92**, 7498 (1990).

- [207] M. Gsell, P. Jakob, and D. Menzel, *Science* **280**, 717 (1998).
- [208] F. Komori, S.-y. Ohno, and K. Nakatsuji, *Progress in Surface Science* **77**, 1 (2004).
- [209] F. Calleja, V. M. Garcia-Suarez, J. J. Hinarejos, J. Ferrer, A. L. V. de Parga, and R. Miranda, *Physical Review B* **71**, 125412 (2005).
- [210] R. Otero, F. Calleja, V. M. Garcia-Suarez, J. J. Hinarejos, J. de la Figuera, J. Ferrer, A. L. V. de Parga, and R. Miranda, *Surface Science* **550**, 65 (2004).
- [211] W. D. Xiao, P. Ruffieux, K. Ait-Mansour, O. Groning, K. Palotas, W. A. Höfer, P. Groning, and R. Fasel, *Journal of Physical Chemistry B* **110**, 21394 (2006).
- [212] P. Ruffieux, K. Palotas, O. Groning, D. Wasserfallen, K. Mullen, W. A. Höfer, P. Groning, and R. Fasel, *Journal of the American Chemical Society*, ASAP (2007).
- [213] M. Bohringer, K. Morgenstern, W. D. Schneider, R. Berndt, F. Mauri, A. De Vita, and R. Car, *Physical Review Letters* **83**, 324 (1999).
- [214] J. Kroger, N. Neel, H. Jensen, R. Berndt, R. Rurali, and N. Lorente, *Journal of Physics-Condensed Matter* **18**, S51 (2006).
- [215] E. C. H. Sykes, B. A. Mantooth, P. Han, Z. J. Donhauser, and P. S. Weiss, *Journal of the American Chemical Society* **127**, 7255 (2005).
- [216] R. Q. Hwang, J. C. Hamilton, J. L. Stevens, and S. M. Foiles, *Physical Review Letters* **75**, 4242 (1995).
- [217] W. L. Ling, J. C. Hamilton, K. Thurmer, G. E. Thayer, J. de la Figuera, R. Q. Hwang, C. B. Carter, N. C. Bartelt, and K. F. McCarty, *Surface Science* **600**, 1735 (2006).
- [218] P. Maksymovych, and J. T. Yates, Jr., *Chemical Physics Letters* **421**, 473 (2006).
- [219] G. Kresse, and J. Hafner, *Physical Review B* **48**, 13115 (1993).
- [220] G. Kresse, and J. Furthmuller, *Computational Materials Science* **6**, 15 (1996).
- [221] G. Kresse, and J. Furthmuller, *Physical Review B* **54**, 11169 (1996).
- [222] P. E. Blöchl, *Physical Review B* **50**, 17953 (1994).
- [223] G. Kresse, and D. Joubert, *Physical Review B* **59**, 1758 (1999).
- [224] J. P. Perdew, and Y. Wang, *Physical Review B* **45**, 13244 (1992).
- [225] M. Kulawik, H. P. Rust, M. Heyde, N. Nilius, B. A. Mantooth, P. S. Weiss, and H. J. Freund, *Surface Science* **590**, L253 (2005).
- [226] A. Khein, D. J. Singh, and C. J. Umrigar, *Physical Review B* **51**, 4105 (1995).

- [227] N. Moll, M. Bockstedte, M. Fuchs, E. Pehlke, and M. Scheffler, *Physical Review B* **52**, 2550 (1995).
- [228] G. Blyholder, *Journal of Physical Chemistry* **68**, 2772 (1964).
- [229] L. Petersen, P. T. Sprunger, P. Hofmann, E. Lægsgaard, B. G. Briner, M. Doering, H. P. Rust, A. M. Bradshaw, F. Besenbacher, and E. W. Plummer, *Physical Review B* **57**, R6858 (1998).
- [230] L. Petersen, P. Laitenberger, E. Lægsgaard, and F. Besenbacher, *Physical Review B* **58**, 7361 (1998).
- [231] W. Luo, and K. A. Fichthorn, *Physical Review B* **72**, 115433 (2005).
- [232] W. A. Höfer, and A. Garcia-Lekue, *Physical Review B* **71**, 085401 (2005).
- [233] F. Schreiber, *J. Phys.: Condens. Matter* **16**, R881 (2004).
- [234] A. Kuhnle, L. M. Molina, T. R. Linderoth, B. Hammer, and F. Besenbacher, *Physical Review Letters* **93**, 086101 (2004).
- [235] G. Pawin, K. L. Wong, K. Y. Kwon, and L. Bartels, *Science* **313**, 961 (2006).
- [236] N. Neel, J. Kroger, and R. Berndt, *Applied Physics Letters* **88**, 163101 (2006).
- [237] N. Neel, J. Kroger, and R. Berndt, *Advanced Materials* **18**, 174 (2006).
- [238] H. Bulou, and C. Goyhenex, *Physical Review B* **65** (2002).
- [239] S. Clair, S. Pons, A. P. Seitsonen, H. Brune, K. Kern, and J. V. Barth, *Journal of Physical Chemistry B* **108**, 14585 (2004).
- [240] M. Bohringer, K. Morgenstern, W.-D. Schneider, and R. Berndt, *Surface Science* **457**, 37 (2000).
- [241] A. Kirakosian, M. J. Comstock, J. W. Cho, and M. F. Crommie, *Physical Review B* **71**, 113409 (2005).
- [242] Z.-X. Xie, Z.-F. Huang and X. Xu, *Physical Chemistry Chemical Physics* **4**, 1486 (2002).
- [243] A. Kirakosian, M. J. Comstock, J. W. Cho, and M. F. Crommie, *Physical Review B* **71** (2005).
- [244] N. Neel, J. Kroger, and R. Berndt, *Advanced Materials* **18**, 174 (2006).
- [245] T. Dretschkow, D. Lampner, and T. Wandlowski, *Journal of Electroanalytical Chemistry* **458**, 121 (1998).
- [246] S. M. Barlow, and R. Raval, *Surface Science Reports* **50**, 201 (2003).
- [247] M. Giesen, *Progress in Surface Science* **68**, 1 (2001).

- [248] G. R. Desiraju, and T. Steiner, *The Weak Hydrogen Bond In Structural Chemistry and Biology* (Oxford University Press, Oxford, UK, 1993).
- [249] Our preliminary DFT calculations (courtesy of D. C. Sorescu) show that in most relative orientations the interaction will be repulsive. The degree of repulsiveness will depend on the relative orientation of the S-C axis of the neighbor CH<sub>3</sub>SH molecules. .
- [250] V. D. Renzi, R. Rousseau, D. Marchetto, R. Biagi, S. Scandolo, and U. d. Pennino, *Physical Review Letters* **95**, 046804 (2005).
- [251] M. Ohara, Y. Kim, and M. Kawai, *Langmuir* **21**, 4779 (2005).
- [252] M. Ohara, Y. Kim, and M. Kawai, *Chemical Physics Letters* **426**, 357 (2006).
- [253] C. Masens, M. J. Ford, and M. B. Cortie, *Surface Science* **580**, 19 (2005).
- [254] B. Li, C. Zeng, Q. Li, B. Wang, L. Yuan, H. Wang, J. Yang, J. G. Hou, and Q. Zhu, *Journal of Physical Chemistry B*. **107**, 972 (2003).
- [255] K. L. Wong, K. Y. Kwon, and L. Bartels, *Applied Physics Letters* **88**, 183106 (2006).
- [256] S. J. Stranick, A. N. Parikh, D. L. Allara, and P. S. Weiss, *Journal of Physical Chemistry* **98**, 11136 (1994).
- [257] M. J. Esplandiu, M. L. Carot, F. P. Cometto, V. A. Macagno, and E. M. Patrito, *Surface Science* **600**, 155 (2006).
- [258] G. H. Yang, and G. Y. Liu, *Journal of Physical Chemistry B* **107**, 8746 (2003).
- [259] L. M. Molina, and B. Hammer, *Chemical Physics Letters* **360**, 264 (2002).
- [260] U. Harten, A. M. Lahee, J. P. Toennies, and C. Wöll, *Physical Review Letters* **54**, 2619 (1985).
- [261] M. P. Everson, L. C. Davis, R. C. Jaklevic, and S. Weidian, *Journal of Vacuum Science and Technology B* **9**, 891 (1991).
- [262] C. Tao, T. J. Stasevich, T. L. Einstein, and E. D. Williams, *Physical Review B* **73**, 125436 (2006).
- [263] R. Ferrando, and G. Treglia, *Physical Review B* **50**, 12104 (1994).
- [264] D. J. Lavrich, S. M. Wetterer, S. L. Bernasek, and G. Scoles, *Journal Of Physical Chemistry B* **102**, 3456 (1998).
- [265] B. S. Jursic, *International Journal of Quantum Chemistry* **62**, 291 (1996).
- [266] M. J. Ford, R. C. Hoft, and J. D. Gale, *Molecular Simulation* **32**, 1219 (2006).
- [267] L. Romaner, G. Heimel, M. Gruber, J. L. Bredas, and E. Zojer, *Small* **2**, 1468 (2006).

- [268] G. Heimel, L. Romaner, J. L. Bredas, and E. Zojer, *Surface Science* **600**, 4548 (2006).
- [269] J. Nara, S. i. Higai, Y. Morikawa, and T. Ohno, *Journal of Chemical Physics* **120**, 6705 (2004).
- [270] G. R. Desiraju, *Accounts of Chemical Research* **35**, 565 (2002).
- [271] A. Bilic, J. R. Reimers, and N. S. Hush, *Journal of Chemical Physics* **122**, 094708 (2005).
- [272] M. Hasan, D. Bethell, and M. Brust, *Journal of the American Chemical Society* **124**, 1132 (2002).
- [273] H. Basch, and M. A. Ratner, *Journal of Chemical Physics* **120**, 5771 (2004).
- [274] P. C. Rusu, and G. Brocks, *Physical Review B* **74**, 073414 (2006).
- [275] Y. Negishi, Y. Takasugi, S. Sato, H. Yao, K. Kimura, and T. Tsukuda, *Journal of Physical Chemistry B* **110**, 12218 (2006).
- [276] H. Häkkinen, R. N. Barnett, and U. Landman, *Physical Review Letters* **82**, 3264 (1999).
- [277] I. L. Garzón, C. Rovira, K. Michaelian, M. R. Beltrán, P. Ordejón, J. Junquera, D. Sánchez-Portal, E. Artacho, and J. M. Soler, *Physical Review Letters* **85**, 5250 (2000).
- [278] M. A. Garcia, J. de la Venta, P. Crespo, J. Llopis, S. Penades, A. Fernandez, and A. Hernando, *Physical Review B* **72**, 241403 (2005).
- [279] M. Z. Hossain, H. S. Kato, and M. Kawai, *Journal of the American Chemical Society* **127**, 15030 (2005).
- [280] C.-S. Tsai, J.-K. Wang, R. T. Skodje, and J.-C. Lin, *Journal of the American Chemical Society* **127**, 10788 (2005).
- [281] P. H. Lu, J. C. Polanyi, and D. Rogers, *Journal of Chemical Physics* **111**, 9905 (1999).
- [282] P. A. Sloan, and R. E. Palmer, *Nature* **434**, 367 (2005).
- [283] S. Dobrin, K. R. Harikumar, C. F. Matta, and J. C. Polanyi, *Surface Science* **580**, 39 (2005).
- [284] S. Zhang, *Nature Nanotechnology* **1**, 169 (2006).
- [285] J. C. Love, L. A. Estroff, J. K. Kriebel, R. G. Nuzzo, and G. M. Whitesides, *Chemical Reviews* **105**, 1103 (2005).
- [286] S. Zhang, *Nature Biotechnology* **21**, 1171 (2003).
- [287] O. Ikkala, and G. ten Brinke, *Science* **295**, 2407 (2002).
- [288] M. Corso, W. Auwärter, M. Muntwiler, A. Tamai, T. Greber, and J. Osterwalder, *Science* **303**, 217 (2004).

- [289] G. R. Newkome, P. Wang, C. N. Moorefield, T. J. Cho, P. P. Mohapatra, S. Li, S.-H. Hwang, O. Lukoyanova, L. Echegoyen, J. A. Palagallo, V. Iancu, and S.-W. Hla, *Science* **312**, 1782 (2006).
- [290] N. Lin, S. Stepanow, F. Vidal, K. Kern, M. S. Alam, S. Stromsdorfer, V. Dremov, P. Muller, A. Landa, and M. Ruben, *Dalton Transactions* **23**, 2794 (2006).
- [291] J. V. Barth, G. Costantini, and K. Kern, *Nature* **437**, 671 (2005).
- [292] Y. Okawa, and M. Aono, *Nature* **409**, 683 (2001).
- [293] P. G. Piva, G. A. DiLabio, J. L. Pitters, J. Zikovsky, M. Rezeq, S. Dogel, W. A. Höfer, and R. A. Wolkow, *Nature* **435**, 658 (2005).
- [294] K. R. Harikumar, J. C. Polanyi, P. A. Sloan, S. Ayissi, and W. A. Höfer, *Journal of the American Chemical Society* **128**, 16791 (2006).
- [295] V. Martin-Diaconescu, and P. Kennepohl, *Journal of the American Chemical Society* **129**, 3034 (2007).
- [296] M. van Gastel, W. Lubitz, G. Lassmann, and F. Neese, *Journal of the American Chemical Society* **126**, 2237 (2004).
- [297] A. Faucitano, A. Buttafava, M. Mariani, and C. Chatgililoglu, *ChemPhysChem*, **6**, 1100 (2005).
- [298] J. C. Polanyi, and Y. Zeiri, *Laser Spectroscopy and Photochemistry on Metal Surfaces* (World Scientific, Singapore, 1995).
- [299] J. C. Polanyi, and H. Rieley, *Dynamics of Gas-Surface Interactions* (Royal Society of Chemistry, Cambridge, 1991).
- [300] E. B. D. Bourdon, P. Das, I. Harrison, J. C. Polanyi, J. Segner, C. D. Stanners, R. J. Williams, and P. A. Young, *Faraday Discussions of Chemical Society* **82**, 343 (1986).
- [301] P. Maksymovych, and J. T. Yates, Jr., *Journal of the American Chemical Society* **128**, 10642 (2006).
- [302] P. Maksymovych, D. B. Dougherty, X.-Y. Zhu, and J. T. Yates, Jr., *Physical Review Letters* in press (2007).
- [303] H. Ueba, T. Mii, N. Lorente, and B. N. J. Persson, *Journal of Chemical Physics* **123** (2005).
- [304] G. Roberts, *Physical Review A* **64**, 042903 (2001).
- [305] G. Kresse, and J. Furthmüller, *Physical Review B* **54**, 11169 (1996).

- [306] G. Henkelman, B. P. Uberuaga, and H. Jonsson, *Journal of Chemical Physics* **113**, 9901 (2000).
- [307] P. Saalfrank, *Chemical Reviews* **106**, 4116 (2006).
- [308] H. Lesnard, M. L. Bocquet, and N. Lorente, *Journal of the American Chemical Society* **129**, 4298 (2007).
- [309] J. C. Hansen, and J. S. Francisco, *ChemPhysChem* **3**, 833 (2002).
- [310] J. W. Gadzuk, *Physical Review Letters* **76**, 4234 (1996).
- [311] H. Arnolds, C. Rehbein, G. Roberts, R. J. Levis, and D. A. King, *Journal of Physical Chemistry B* **104**, 3375 (2000).
- [312] X. Y. Zhu, *Annual Review of Physical Chemistry* **45**, 113 (1994).
- [313] J. K. Gimzewski, and C. Joachim, *Science* **283**, 1683 (1999).
- [314] M. L. Bocquet, H. Lesnard, and N. Lorente, *Physical Review Letters* **96**, 096101 (2006).
- [315] S. W. Hla, L. Bartels, G. Meyer, and K. H. Rieder, *Physical Review Letters* **85**, 2777 (2000).
- [316] J. Henzl, M. Mehlhorn, H. Gawronski, K. H. Rieder, and K. Morgenstern, *Angewandte Chemie-International Edition* **45**, 603 (2006).
- [317] Y. Nakamura, Y. Mera, and K. Maeda, *Physical Review Letters* **89**, 266805 (2002).
- [318] R. Nouchi, K. Masunari, T. Ohta, Y. Kubozono, and Y. Iwasa, *Physical Review Letters* **97**, 196101 (2006).
- [319] J. R. Goldman, and J. A. Prybyla, *Physical Review Letters* **72**, 1364 (1994).
- [320] B. C. Stipe, M. A. Rezaei, and W. Ho, *Journal Of Chemical Physics* **107**, 6443 (1997).
- [321] M. Alemani, M. V. Peters, S. Hecht, K. H. Rieder, F. Moresco, and L. Grill, *Journal of the American Chemical Society* **128**, 14446 (2006).
- [322] H. Abdoul-Carime, and L. Sanche, *Journal of Physical Chemistry B* **106**, 12186 (2002).
- [323] A. S. Lucier, H. Mortensen, Y. Sun, and P. Grutter, *Physical Review B* **72**, 235420 (2005).
- [324] M. A. Rezaei, B. C. Stipe, and W. Ho, *Journal of Chemical Physics* **110**, 4891 (1999).
- [325] J. Cao, Y. Gao, H. E. Elsayed-Ali, R. J. D. Miller, and D. A. Mantell, *Physical Review B* **58**, 10948 (1998).
- [326] E. V. Chulkov, A. G. Borisov, J. P. Gauyacq, D. Sanchez-Portal, V. M. Silkin, V. P. Zhukov, and P. M. Echenique, *Chemical Reviews* **106**, 4160 (2006).

- [327] L. Vitali, P. Wahl, M. A. Schneider, K. Kern, V. M. Silkin, E. V. Chulkov, and P. M. Echenique, *Surface Science* **523**, L47 (2003).
- [328] K. F. Braun, and K. H. Rieder, *Physical Review Letters* **88**, 096801 (2002).
- [329] A. Goldmann, V. Dose, and G. Borstel, *Physical Review B* **32**, 1971 (1985).
- [330] P. Cortona, and C. Sapet, *International Journal of Quantum Chemistry* **99**, 713 (2004).
- [331] J. I. Pascual, A. Dick, M. Hansmann, H. P. Rust, J. Neugebauer, and K. Horn, *Physical Review Letters* **96**, 046801 (2006).
- [332] F. Ciccacci, S. Derossi, A. Taglia, and S. Crampin, *Journal of Physics-Condensed Matter* **6**, 7227 (1994).
- [333] F. J. Himpsel, and J. E. Ortega, *Physical Review B* **46**, 9719 (1992).
- [334] K. Reuter, P. L. de Andres, F. J. Garcia-Vidal, D. Sestovic, F. Flores, and K. Heinz, *Physical Review B* **58**, 14036 (1998).
- [335] A. Schneider, M. Wenderoth, K. J. Engel, M. A. Rosentreter, A. J. Heinrich, and R. G. Ulbrich, *Applied Physics A -Materials Science & Processing* **66**, S161 (1998).
- [336] C. D. Lindstrom, and X. Y. Zhu, *Chemical Reviews* **106**, 4281 (2006).
- [337] C. N. Satterfield, *Heterogeneous Catalysis in Industrial Practice* (McGraw-Hill, 1991).
- [338] M. Ando, T. Kobayashi, and M. Haruta, *Catalysis Today* **36**, 135 (1997).
- [339] A. Fujishima, and K. Honda, *Nature* **238**, 37 (1972).
- [340] A. Mills, R. H. Davies, and D. Worsley, *Chemical Society Reviews* **22**, 417 (1993).
- [341] P. C. Maness, S. Smolinski, D. M. Blake, Z. Huang, E. J. Wolfrum, and W. A. Jacoby, *Applied and Environmental Microbiology* **65**, 4094 (1999).
- [342] Y. Paz, Z. Luo, L. Rabenberg, and A. Heller, *Journal of Materials Research* **10**, 2842 (1995).
- [343] R. Wang, K. Hashimoto, A. Fujishima, M. Chikuni, E. Kojima, A. Kitamura, M. Shimohigoshi, and T. Watanabe, *Nature* **388**, 431 (1997).
- [344] S. A. Campbell, H. S. Kim, D. C. Gilmer, B. He, T. Ma, and W. L. Gladfelter, *Ibm Journal of Research and Development* **43**, 383 (1999).
- [345] M. Ramamoorthy, D. Vanderbilt, and R. D. King-Smith, *Physical Review B* **49**, 16721 (1994).
- [346] P. W. Tasker, *Journal of Physics C* **12**, 4977 (1979).
- [347] A. T. Paxton, and L. Thien-Nga, *Physical Review B* **57**, 1579 (1998).

- [348] E. L. D. Hebenstreit, W. Hebenstreit, and U. Diebold, *Surface Science* **461**, 87 (2000).
- [349] K. Fukui, H. Onishi, and Y. Iwasawa, *Physical Review Letters* **79**, 4202 (1997).
- [350] U. Diebold, J. Lehman, T. Mahmoud, M. Kuhn, G. Leonardelli, W. Hebenstreit, M. Schmid, and P. Varga, *Surface Science* **411**, 137 (1998).
- [351] R. A. Bennett, P. Stone, N. J. Price, and M. Bowker, *Physical Review Letters* **82**, 3831 (1999).
- [352] C. L. Pang, S. A. Haycock, H. Raza, P. W. Murray, G. Thornton, O. Gulseren, R. James, and D. W. Bullett, *Physical Review B* **58**, 1586 (1998).
- [353] H. Onishi, and Y. Iwasawa, *Surface Science* **313**, L783 (1994).
- [354] R. Schaub, E. Wahlstrom, A. Ronnau, E. Laegsgaard, I. Stensgaard, and F. Besenbacher, *Science* **299**, 377 (2003).
- [355] C. Di Valentin, G. Pacchioni, and A. Selloni, *Physical Review Letters* **97**, 166803 (2006).
- [356] I. D. Cocks, Q. Guo, R. Patel, E. M. Williams, E. Roman, and J. L. deSegovia, *Surface Science* **377**, 135 (1997).
- [357] S. Wendt, R. Schaub, J. Matthiesen, E. K. Vestergaard, E. Wahlstrom, M. D. Rasmussen, P. Thostrup, L. M. Molina, E. Laegsgaard, I. Stensgaard, B. Hammer, and F. Besenbacher, *Surface Science* **598**, 226 (2005).
- [358] D. Matthey, J. G. Wang, S. Wendt, J. Matthiesen, R. Schaub, E. Laegsgaard, B. Hammer, and F. Besenbacher, *Science* **315**, 1692 (2007).
- [359] P. Stone, R. A. Bennett, and M. Bowker, *New Journal of Physics* **1**, 8 (1999).
- [360] Q. Guo, I. Cocks, and E. M. Williams, *Physical Review Letters* **77**, 3851 (1996).
- [361] M. A. Henderson, *Surface Science Reports* **46**, 5 (2002).
- [362] F. Allegretti, S. O'Brien, M. Polcik, D. I. Sayago, and D. P. Woodruff, *Physical Review Letters* **95**, 226104 (2005).
- [363] M. A. Henderson, *Langmuir* **12**, 5093 (1996).
- [364] M. B. Hugen Schmidt, L. Gamble, and C. T. Campbell, *Surface Science* **302**, 329 (1994).
- [365] R. Schaub, R. Thostrup, N. Lopez, E. Laegsgaard, I. Stensgaard, J. K. Norskov, and F. Besenbacher, *Physical Review Letters* **87**, 266104 (2001).
- [366] T. Watanabe, A. Nakajima, R. Wang, M. Minabe, S. Koizumi, A. Fujishima, and K. Hashimoto, *Thin Solid Films* **351**, 260 (1999).

- [367] R. Wang, N. Sakai, A. Fujishima, T. Watanabe, and K. Hashimoto, *Journal of Physical Chemistry B* **103**, 2188 (1999).
- [368] J. M. White, J. Szanyi, and M. A. Henderson, *Journal of Physical Chemistry B* **107**, 9029 (2003).
- [369] M. A. Henderson, J. M. White, H. Uetsuka, and H. Onishi, *Journal of the American Chemical Society* **125**, 14974 (2003).
- [370] T. Zubkov, D. Stahl, T. L. Thompson, D. Panayotov, O. Diwald, and J. T. Yates, Jr., *Journal of Physical Chemistry B* **109**, 15454 (2005).
- [371] B. Kasemo, and J. Gold, *Advances in Dental Research* **13**, 8 (1999).
- [372] U. Diebold, *Surface Science Reports* **48**, 53 (2003).
- [373] I. M. Brookes, C. A. Muryn, and G. Thornton, *Physical Review Letters* **87**, 266103 (2001).
- [374] S. Mezheny, P. Maksymovych, T. L. Thompson, O. Diwald, D. Stahl, S. D. Walck, and J. T. Yates, Jr., *Chemical Physics Letters* **369**, 152 (2003).
- [375] A. L. Linsebigler, G. Q. Lu, and J. T. Yates, Jr., *Chemical Reviews* **95**, 735 (1995).
- [376] O. Bikondoa, C. L. Pang, R. Ithnin, C. A. Muryn, H. Onishi, and G. Thornton, *Nature Materials* **5**, 189 (2006).
- [377] D. Brinkley, M. Dietrich, T. Engel, P. Farrall, G. Gantner, A. Schafer, and A. Szuchmacher, *Surface Science* **395**, 292 (1998).
- [378] R. A. Bennett, P. Stone, R. D. Smith, and M. Bowker, *Surface Science* **454**, 390 (2000).
- [379] D. C. Sorescu, unpublished (2003).
- [380] C. E. Tripa, and J. T. Yates, Jr., *Journal of Vacuum Science and Technology A* **14**, 2544.
- [381] E. Hecht, *Optics* (Addison–Wesley, Reading, MA, 1987).
- [382] W. L. Bond, *Journal of Scientific Instrumentation* **38**, 63 (1961).